

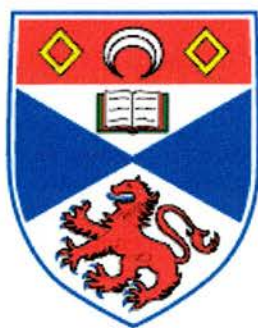
# University of St Andrews



Full metadata for this thesis is available in  
St Andrews Research Repository  
at:

<http://research-repository.st-andrews.ac.uk/>

This thesis is protected by original copyright



**The University of St Andrews**

**School of Chemistry**

# **Electrode Modification**

**Ian Thom**



**Thesis submitted in accordance with the  
requirements of the University of St Andrews for  
the degree of Doctor of Philosophy**

**September 2004**

TK E716

---

## ABSTRACT

Thiol and selenol self assembled monolayers (SAMs) on gold electrodes are studied using cyclic voltammetry with in-situ second harmonic generation. Properties including reductive desorption potential, desorption charge and peak shape are examined for a variety of SAM systems, furthermore, the charge of desorption is correlated with coverage determined by second harmonic generation.

Alkane thiols, the simplest case of thiol SAMs are compared with SAMs containing a rigid biphenyl unit. For a homologue series of molecules  $\omega$ -CH<sub>3</sub>-C<sub>6</sub>H<sub>4</sub>-C<sub>6</sub>H<sub>4</sub>(CH<sub>2</sub>)<sub>n</sub>SH, BPn n=1-6, a distinct odd-even effect in desorption peak potential, desorption charge and peak shape is observed. The effect is reversed on silver substrates indicating that the effect is due to the hybridisation of the sulfur. SAMs containing a hydroxyl or carboxyl tail group are less stable than the methyl analogue whereas SAMs containing a thiol tail group are more stable than the methyl analogue. Selenol SAMs are considerably more stable than their thiol analogues. SAMs of molecules containing multiple anchor points, dipod and tripod, were investigated. Increased hydrogen evolution currents suggest that there is considerable surface disruption during film assembly.

The coverage determined by SHG is linearly proportional to the charge for the desorption of hexadecane thiol despite the presence of a double peak. A desorption mechanism based on pair interactions is proposed based on the cyclic voltammetry and in-situ second harmonic generation of alkane thiols and biphenyl thiols.

Selective metal deposition on patterned SAM modified gold electrodes is illustrated. Using an acidic copper sulfate electrolyte, copper is deposited selectively on biphenyl thiol modified regions, while hexadecane thiol blocks copper deposition. A detachment procedure is applied that allows formation of copper deposits with a flatness comparable to the underlying gold substrate. This technique is a versatile and facile method suited to producing well defined nano structures.

## ACKNOWLEDGEMENTS

First and foremost I would like to express my immense gratitude to my supervisor Dr Manfred Buck, whose enthusiasm for science has been an inspiration and encouragement has been tremendously valuable, and for continued patience in the days when experiments work and more importantly on the days when experiments didn't work.

I would like to thank Dr Piotr Cyganik for expert instruction on use of the STM and for helpful and stimulating discussions on various technical aspects of surface science.

Thanks to Professor Neville Richardson and the whole Surface Science group who have fostered a pleasant and co-operative working environment and organised several enjoyable social events over the past three years, including skiing, hill walking, Christmas nights out, curry nights out and so on and so forth.

Thanks to Dr Chris Baddeley for not making a fuss about the rather extended loan of the glove box.

Thanks to James Wilton-Ely, John Wallace, Michael Zharnikov, Steve Francis and Wendy Crocker for providing chemicals.

Thanks to the technical staff, Ian (undergraduate laboratories), Bobby and George (mechanical workshop), Colin (glassblower), Derek and Brian (electronics workshop) and Marjory (stores) for invaluable support.

Thanks to my friends in and out of the chemistry department who have made the past three years an enjoyable time.

Finally I would like to thank my parents and the rest of my family for all of their belief, encouragement and support for my entire time at University.

## DECLARATIONS

- (i) I, Ian Thom, hereby certify that this thesis, which is approximately 42000 words in length, has been written by me, that it is the record of work carried out by me and that it has not been submitted in any previous application for a higher degree.

date 20/10/04 signature of candidate .

- (ii) I was admitted as a research student in September, 2001 and as a candidate for the degree of Doctor of Philosophy in September, 2004; the higher study for which this is a record was carried out in the University of St Andrews between 2001 and 2004.

date 20/10/04 signature of candidate .

- (iii) I hereby certify that the candidate has fulfilled the conditions of the Resolution and Regulations appropriate for the degree of Doctor of Philosophy in the University of St Andrews and that the candidate is qualified to submit this thesis in application for that degree.

date 20/10/04 signature of

- (iv) In submitting this thesis to the University of St Andrews I understand that I am giving permission for it to be made available for use in accordance with the regulations of the University Library for the time being in force, subject to any copyright vested in the work not being affected thereby. I also understand that the title and abstract will be published, and that a copy of the work may be made and supplied to any *bona fide* library or research worker.

date 20/10/04 signature of candidate ..

---

**TABLE OF CONTENTS**

preliminaries .....	1-6
<b>CHAPTER 1 INTRODUCTION .....</b>	<b>7</b>
<b>1.1 GENERAL ASPECTS OF SELF ASSEMBLED MONOLAYERS (SAMs).....</b>	<b>7</b>
<b>1.2 ELECTRODE MODIFICATION .....</b>	<b>10</b>
<b>1.3 STRUCTURAL PROPERTIES .....</b>	<b>13</b>
<b>1.4 AIMS AND OBJECTIVES .....</b>	<b>14</b>
<b>CHAPTER 2 BACKGROUND.....</b>	<b>17</b>
<b>2.1 THIOL MONOLAYERS ON GOLD.....</b>	<b>17</b>
2.1.1 Introduction .....	17
2.1.2 Substrate Surface .....	19
2.1.3 Molecules .....	22
2.1.4 Substrate-Molecule Interactions.....	24
2.1.5 Domain Size .....	26
<b>2.2 ELECTROCHEMISTRY.....</b>	<b>28</b>
2.2.1 Electrochemistry Theory.....	28
2.2.2 Three Electrode Cell.....	30
2.2.3 Cyclic Voltammetry (CV).....	34
<b>2.3 SECOND HARMONIC GENERATION (SHG).....</b>	<b>39</b>
<b>2.4 SCANNING TUNNELLING MICROSCOPY (STM).....</b>	<b>43</b>
<b>CHAPTER 3 EXPERIMENTAL .....</b>	<b>46</b>
<b>3.1 SAM PREPARATION.....</b>	<b>46</b>
<b>3.2 TECHNIQUES .....</b>	<b>47</b>
3.2.1 Introduction .....	47

---

3.2.2	<i>Cyclic Voltammetry (CV)</i> .....	48
3.2.3	<i>Second Harmonic Generation (SHG)</i> .....	49
3.2.4	<i>Scanning Tunnelling Microscopy (STM)</i> .....	52
<b>3.3</b>	<b>SYSTEM CHARACTERISATION</b> .....	<b>52</b>
3.3.1	<i>Data Acquisition</i> .....	52
3.3.2	<i>Surface Area Determination</i> .....	53
3.3.3	<i>Influence of Oxygen</i> .....	60
3.3.4	<i>Data Evaluation</i> .....	61
3.3.5	<i>Detector Linearity Range</i> .....	63
3.3.6	<i>SHG Increase Reproducibility</i> .....	64
 <b>CHAPTER 4 RESULTS</b> .....		<b>68</b>
<b>4.1</b>	<b>HOMOLOGOUS SERIES: SPACER GROUP INFLUENCE</b> .....	<b>68</b>
4.1.1	<i>Alkane Thiols</i> .....	68
4.1.2	<i>Biphenyl Thiols</i> .....	78
<b>4.2</b>	<b>TAIL GROUP INFLUENCE</b> .....	<b>89</b>
4.2.1	<i>MC8 / CFS</i> .....	89
4.2.2	<i>MC16 / MHA</i> .....	91
4.2.3	<i>BP1 / DT</i> .....	93
4.2.4	<i>BP2 / PET</i> .....	96
4.2.5	<i>BP3 / HBP3</i> .....	98
4.2.6	<i>BP4 / HBP4 / BP4OH</i> .....	99
4.2.7	<i>Tail Group Summary</i> .....	101
<b>4.3</b>	<b>HEAD GROUP INFLUENCE</b> .....	<b>102</b>
4.3.1	<i>Sulfur / Selenium Head Group</i> .....	103
4.3.2	<i>Molecules with Multiple Binding Points</i> .....	107
<b>4.4</b>	<b>SUBSTRATE INFLUENCE</b> .....	<b>115</b>
4.4.1	<i>Roughness</i> .....	115
4.4.2	<i>Gold / Silver Substrate</i> .....	118
<b>4.5</b>	<b>SUMMARY</b> .....	<b>123</b>

---

<b>CHAPTER 5 DESORPTION MECHANISM.....</b>	<b>127</b>
5.1 <i>BACKGROUND.....</i>	<i>127</i>
5.2 <i>RESULTS.....</i>	<i>131</i>
5.3 <i>PAIR INTERACTION MODEL.....</i>	<i>138</i>
5.4 <i>SUMMARY.....</i>	<i>144</i>
<b>CHAPTER 6 METAL DEPOSITION .....</b>	<b>145</b>
6.1 <i>INTRODUCTION.....</i>	<i>145</i>
6.2 <i>COPPER DEPOSITION AND PATTERNING .....</i>	<i>146</i>
6.3 <i>COPPER DETACHMENT.....</i>	<i>150</i>
<b>CHAPTER 7 CONCLUSIONS.....</b>	<b>154</b>
<b>CHAPTER 8 REFERENCES .....</b>	<b>157</b>
<b>APPENDICES .....</b>	<b>173</b>
<i>APPENDIX 1 BIPHENYL THIOLS UNIT CELLS .....</i>	<i>173</i>
<i>APPENDIX 2 HOME-BUILT SPECTROELECTROCHEMICAL CELL .....</i>	<i>174</i>
<i>APPENDIX 3 STATISTICAL ANALYSIS .....</i>	<i>179</i>
<i>APPENDIX 4 BIPHENYL THIOL ANGLES .....</i>	<i>181</i>

# Chapter 1

## INTRODUCTION

### 1.1 General Aspects of Self Assembled Monolayers (SAMs)

Self assembled monolayers are molecular films one molecule deep, which form spontaneously on a solid surface, typically by adsorption from solution, as a result of molecule-substrate and molecule-molecule interactions. Molecules have a head group which attaches onto the substrate, a tail group which often consists of a functional group and a spacer group, between the head and tail groups which influences the intermolecular interactions, figure 1.1 shows the constituent parts of a generic SAM.

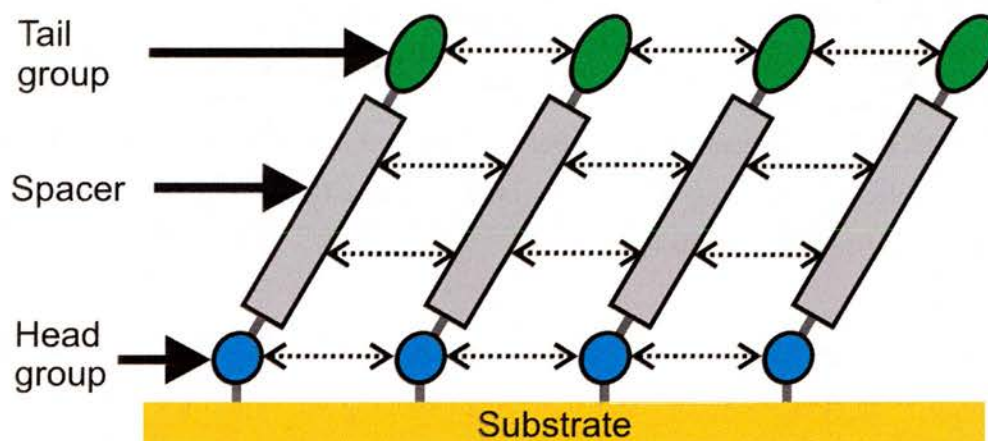


Figure 1.1: A generic SAM. In general, molecules stand upright to achieve close packing of the molecules. Intermolecular interactions, dotted lines, play a significant role in the structure and properties of the self assembled molecules allowing SAMs to achieve well ordered packing.

There are two prerequisites for well ordered SAMs, a sufficient affinity between the head group and the substrate, and intermolecular interactions allowing ordering of the monolayer. The head group connects the molecule to the substrate usually with a covalent or ionic bond. The tail group is of particular interest as this allows the introduction of functionality into the SAM modified surface. The tail group is exposed to the local environment, and therefore, the nature of the tail group can drastically alter the surface properties of the resulting monolayer such as wetting<sup>1</sup>, bio-molecule adhesion<sup>2,3</sup> or friction<sup>4-6</sup>. For example, a SAM with a methyl tail group will have a hydrophobic surface, whereas, a SAM with a carboxyl tail group will have a hydrophilic

surface<sup>1</sup>. SAMs have demonstrated great potential for tailoring surface properties due to the great variety of molecules that can be synthesised. Modification of the SAM by adding functional tail groups are the most attractive part of SAMs, nevertheless, the spacer is a vital part of the SAM influencing the film stability and structure. The spacer length and type have a large influence on the properties of the monolayer. Spacer groups are generally designed to promote intermolecular interactions, typically alkane chains with van der Waals attractions between neighbouring molecules. The spacer unit will influence monolayer stability, longer chains have greater stability and order.

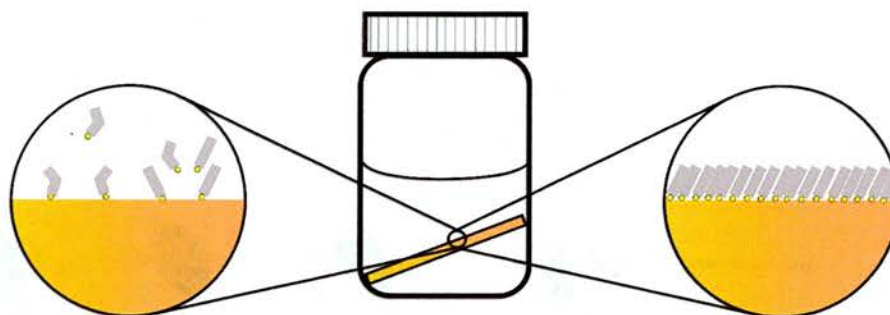


Figure 1.2: Monolayer preparation, a substrate is immersed in a solution containing the desired molecules. Molecules spontaneously adsorb onto the surface (left) and over time, they will rearrange to maximise packing density (right).

SAMs are extremely easy to prepare, a substrate is simply immersed in a solution containing the desired molecule and molecules spontaneously adsorb onto the surface. Substrates are usually immersed overnight giving time for molecules to rearrange and maximise close packing, figure 1.2. Samples are removed from solution and rinsed to remove non-chemisorbed molecules and blown dry with inert gas prior to use. A comprehensive procedure for sample preparation in this project is given in subchapter 3.1.

There are a variety of SAM types, based on the head group–substrate combination described next. The head group-substrate combination defines the type of SAM. Some monolayer classifications are given in table 1.1.

SAM type	Head group	Substrate	references
Thiol (or disulfide)	S	Gold Silver Copper Platinum Palladium Iron Gallium Arsenide Indium Phosphide Mercury	7-9 10,11 12,13 14 15 16-19 20 21 22-24
Sulfide	S	Gold	4,25
Selenol (diselenide)	Se	Gold Silver	26 27
Silane	SiCl <sub>3</sub> / Si(CH <sub>3</sub> O) <sub>3</sub>	Silicon Oxide Tin Oxide Indium Tin Oxide Zinc Selenide	28,29 30 31 32
Isonitriles / Isocyanides	NC	Platinum gold copper	33,34 35 35
Alkanoic acids	COO <sup>-</sup>	Silver Oxide Aluminium Oxide Silicon	36 36,37 38
Alkynes	C≡C	Silicon	39
Alkenes	C=C	Silicon	40

Table 1.1: SAM classifications and corresponding head group substrate combinations.

This thesis focuses on thiol SAMs on gold, which of all the SAM types have received the greatest attention in literature, and to a lesser extent on selenol SAMs on gold and thiol SAMs on silver. Thiol SAMs on gold are particularly attractive due to the inertness of gold and the reliability and reproducibility of high quality film formation. Thiol SAMs were first described by Nuzzo and Allara in 1983 and involved adsorption of disulfide molecules on gold<sup>7</sup>, from then the scale of the research into SAMs in general and thiol SAMs on gold in particular has grown immensely. Thiol SAMs on gold account for a significant proportion of the recent work on SAMs. Figure 1.3 highlights the steady growth in the research into SAMs in the past decade. Selenium based SAMs are becoming attractive candidates for possible molecular electronics applications due to the greater stability<sup>41</sup> and conductivity<sup>42</sup> relative to their sulfur analogues.

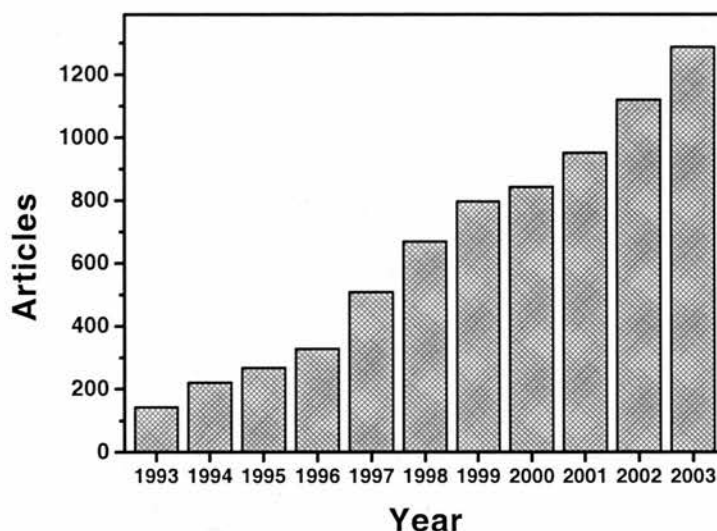


Figure 1.3: Number of publications on self assembled monolayer(s) in the Science Citation Index from 1993 to 2003. During 2003 there were 1288 articles of which 297 included the terms gold and thiol in the title or abstract.

## 1.2 Electrode Modification

Metal surfaces modified using thiol molecules are examined using electrochemistry with an in-situ nonlinear optical technique that probes the surface. Second harmonic generation probes the metal-thiol bond. The adsorption or desorption of molecules, induced by electrochemistry, is monitored using the optical technique. Using the in-situ technique opens up the possibility of studying real-time processes such as the SAM desorption process. There are fundamental and applied aspects to the desorption of SAMs. The fundamental aspects include exploring relations between peak shape and desorption mechanism. For example, relating the occurrence of double peaks to the desorption mechanism. An applied aspect is metal deposition on SAM modified electrodes. The stability of SAMs must extend to at least the equilibrium potential of the metal in order for SAM to influence the metal deposition.

Electrochemical metal deposition,  $M^{z+}_{(aq)} + ze^- \rightleftharpoons M_{(s)}$  is a versatile and facile technique that can be employed to fabricate metal structures on electrodes and SAM modified electrodes. Electrodeposition and dissolution of metal films from solution can be precisely controlled to give well characterised electrode structures. The final structure of the metal deposit can be controlled by adjusting the deposition conditions through

manipulation of variables such overpotential, deposition time, temperature, metal cation concentration and additives. In addition to controlling the deposition conditions, the deposition can be influenced by the presence of SAMs. The blocking property of the SAM allows another level of control over the electrodeposition process. SAMs are a physical barrier to electron transfer and metal deposition on the underlying substrate. The extent of the blocking properties of the SAM are determined its conductivity and structural perfection. Structurally perfect SAMs with low conductivity will present a significant barrier to electrodeposition, whereas SAMs with high conductivity or many defect sites will present a smaller barrier to electrodeposition. The structural perfection can be significantly influenced by the preparation conditions, with better quality SAMs being produced with high temperature preparation or annealing steps. The conductivity is largely dependent on whether the adsorbing molecules contain aliphatic, aromatic or conjugated units. The properties of SAMs containing a biphenyl group are particularly interesting as they contribute to the film stability and structure, while allowing a higher conductivity compared to an alkane thiol SAM of the equivalent thickness<sup>43</sup>. Furthermore, biphenyl thiols demonstrate an odd-even effect with the number of methylene units between the head group and biphenyl unit having a significant influence on the structure and packing of molecules. Molecules with an odd number of methylene units are able to pack closer together than molecules containing an even number of methylene units. Surface patterning of biphenyl thiols using electron beam irradiation has previously been demonstrated<sup>44</sup>. Biphenyl units cross-link under irradiation allowing discrimination between irradiated and non-irradiated regions on the surface. Control over structural perfection and conductivity of the SAM are two factors that are required for a reproducible design of electrode structures.

There are three general ways in which the deposition could proceed, illustrated in figure 1.4. Metal deposition could nucleate at defect sites and grow in a mushroom shape. Alternatively, ions could penetrate through the layer and deposit at the electrode surface forming a buried layer. Lastly, metal could deposit on top of the SAM with charge transfer occurring through the layer. However, this is unlikely, as an extreme degree of SAM perfection would be required. It is highly probable that mushroom type growth prevails due to the preponderance of defects in a typical SAM structure. The extent to which the different growth mechanisms are favoured is expected to depend on the SAM properties. Deposition on disordered SAMs will likely proceed with mushroom type

growth due to the high density of defect sites. Conducting thiols may be more predisposed to on top growth, however, mushroom type growth will still occur at defect sites. Porous SAMs or SAMs containing smaller molecules will be more susceptible to metal penetration and the formation of buried metal layers.

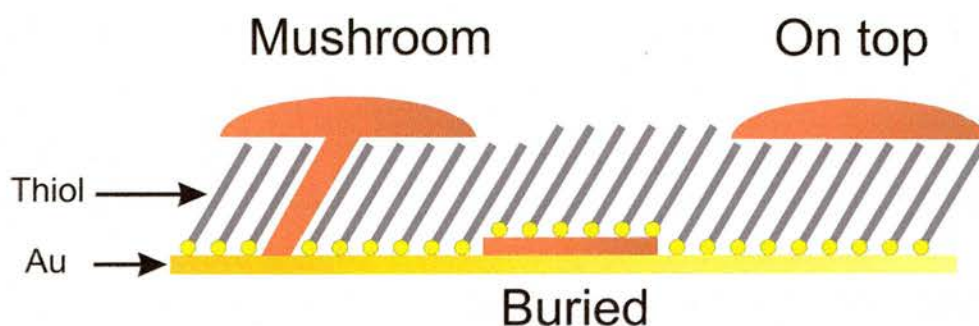


Figure 1.4: Diagram of three different types of metal deposition on thiol modified surfaces. Nucleation and growth from defect sites (left), penetration of copper through the thiol layer (middle) and growth on top the thiol molecules with charge transfer through the SAM (right).

Uniform SAMs or patterned SAMs can be prepared. One particularly attractive feature is selective metal deposition on patterned<sup>45</sup> SAM modified electrodes. There are several techniques to achieve patterning, however the two principal techniques to create surface patterns on thiol modified surfaces are lithography and micro contact printing<sup>45,46</sup>. Lithography involves placing a mask over a sample of thiols on gold and irradiating with photons, ions or electrons. The mask blocks irradiation, which causes some kind of chemical change to the surface molecules, which can then be developed. The second technique, micro contact printing, is used in this project. Thiol molecules are initially stamped onto the metal surface. This is followed by immersion of the substrate in another thiol solution with adsorption preferentially occurring at the bare metal, subchapter 3.1. Electrodes patterned with two SAMs can be developed by deposition on only one of the SAMs, figure 6.4. The contrast is achieved by utilising SAMs with differing degrees of blocking properties<sup>44</sup>. An insulating SAM will resist metal deposition to a high degree while a conducting SAM will impede metal deposition to a much lesser extent.

Controlled and selective deposition of patterned structures on electrode surfaces is dependent on one crucial condition. The SAM must maintain its structural integrity in the potential range where metal deposition occurs. SAMs are stable within a specific

potential range between which the reductive desorption and oxidative desorption processes occur. Each metal has an individual equilibrium potential associated with the  $M_{(s)} | M^{n+}_{(aq)}$  equilibrium, or standard electromotive force of the metal. More active metals have a more negative equilibrium potential. Deposition will proceed when the electrode potential is negative of the equilibrium potential. The deposition of metals on SAM modified electrodes can only occur if the deposition potential for the metal coincides with the thiol stability region. Metals such as copper, nickel, gold, silver, tin, chromium, lead, zinc, iron, palladium and cobalt have all been successfully deposited on bare electrodes<sup>47</sup>. However, not all of these metals will be suited to deposition on SAM modified electrodes due to breakdown of the SAM prior to deposition. In order to achieve the goal of creating well defined metal structures on patterned electrodes the properties of the SAMs must first be established. The main task is to determine the stability of SAMs and understand their structural properties, with a view to establishing the best conditions for deposition of metals. This can be tackled by performing a series of experiments involving the reductive desorption of SAMs. The reductive desorption characteristics of the SAM is informative as several aspects of the SAM properties are probed. The desorption peak potential is a direct indication of the film stability. In addition to the film stability, structural information can be inferred. The desorption charge is related to the packing density of molecules and the desorption peak width can be related to the film uniformity. Once the SAM stability and structural properties are established, specific SAM systems can be tailored for electrodeposition of specific metals. Many challenges exist in this field and the scope is wide and varied.

### 1.3 Structural Properties

Despite the ease of preparation of SAMs, the number of interactions involved in their formation complicates understanding their properties. The SAM properties are a function of the interplay of intramolecular and intermolecular forces dependent on the substrate, head group, spacer and tail group, and the interaction of the SAM with the local environment. The properties of SAMs are dependent on a number of parameters outlined below.

- The strength and type of interaction between the adsorbed molecules and the substrate including the substrate-molecule interaction corrugation.

- The registry between the surface lattice and the adsorbed molecules including any lattice mismatch.
- The intermolecular interactions between adsorbed molecules.
- Steric constraints imposed by the molecular geometry of the adsorbed molecules.
- The interaction of the SAM with the local environment.
- The substrate quality (smoothness and cleanliness)
- The preparation conditions play a role in determining the final structure of the monolayer including; temperature, concentration, adsorption time and any annealing steps.

The first five of these points are intrinsic to SAMs whereas the last two are due to experimental properties such as preparation conditions. The two most important factors governing self assembly are the molecule-substrate and molecule-molecule interactions. These are the factors that drive self assembly of ordered architectures. The final conformation and orientation of molecules largely depend on the intermolecular interactions; this may involve tilting of moieties, alterations to the packing density and steric constraints imposed by the molecular geometry of the adsorbed molecules. The substrate quality refers to the flatness and cleanliness of the substrate at the atomic level. The size of the terraces or the frequency of step edges influences the molecule-substrate and molecule-molecule interactions. SAM properties depend on the tail group, spacer, head group and substrate combination. These factors are explored throughout the thesis and discussed in considerable detail.

A practical design of SAMs for applications or research requires considerable care and attention. Creating a high quality SAM involves using the highest quality substrates and controlling the surface preparation conditions. High quality SAMs have large domains of well ordered molecules. Preparation of high quality SAMs is important for applications such as metal deposition.

## **1.4 Aims and Objectives**

The main objective of this project is to study the electrochemical stability of thiol self assembled monolayers, with a view to understanding the factors that contribute to SAM stability. The specific aims and objectives are as follows.

1. Focus on the structure property relationship for a homologue series of biphenyl based SAMs; comparing established odd-even properties with electrochemical properties such as desorption potential, peak shape and charge transfer. Examine the influence of preparation temperature on the reductive desorption peak and examine the influence of scan rate on the desorption position. Determine the correlation of charge determined electrochemically to coverage determined using nonlinear optical second harmonic generation. Compare the electrochemical and nonlinear optical behaviour of the biphenyl homologue series on gold and silver substrates.
2. Focus on the electrochemical and optical properties for the reductive desorption of a homologue series of alkane thiol SAMs, examining features such as SAM stability, desorption peak shape, desorption charge transfer and readsorption features. Correlate the desorption charge from electrochemistry with coverage from second harmonic generation.
3. Investigate the electrochemical and optical properties of a variety of SAM types exploring influences of tail group, spacer, head group and the substrate. Catalogue the reductive desorption behaviour for a variety of SAM systems, developing an understanding of the relationship between film stability measured by electrochemical desorption peak position and desorption peak shape and peak width with preparation conditions. Determine the correlation between charge measured using electrochemistry and coverage measured using second harmonic generation.
4. Examine the veracity of desorption models in literature contrasting electrochemical and optical results obtained in this project with experimental and theoretical papers. Present a general desorption model that accounts for all of the established features for thiol desorption and is consistent with other systems examined in this thesis.
5. Use surface patterning, via micro contact printing with SAMs to direct metal deposition on electrode surfaces, controlling rate of deposition and achieve a clear definition between deposited and non-deposited regions. Use detachment

procedures to remove the metal deposit from the electrode surface creating novel metal microstructures.

6. The combination of in-situ second harmonic generation with electrochemistry presented a technical challenge, which involved the design and construction of a new electrochemical three electrode cell. The design and construction of the cell was completed and comprehensive documentation for the cell construction procedure is included. Procedures were developed to reliably produce high quality thiol SAMs on gold for electrochemical, optical and microscopic analyses. Procedures for the assembly of the samples into the cell were developed to ensure reproducible and high quality results.

## Chapter 2

### BACKGROUND

#### 2.1 Thiol Monolayers on Gold

This section expands the background on thiol SAMs on gold detailing a few key areas including discussion on the formation and structure of the SAMs, types of molecules used and the interaction between the molecules and substrate. Information on both gold and silver surfaces is given.

##### 2.1.1 Introduction

There is a huge research focus on thiol monolayers on gold due to the formation of well ordered films with relative ease<sup>8</sup> and versatility of these systems for fundamental and applied scientific pursuits. Alkane thiol SAMs on gold are the archetypal SAM system<sup>9</sup>, which have received the greatest attention in literature and have the most well understood properties of all thiol SAMs, and therefore, are used as a reference system in this thesis. Figure 2.1 depicts a hexadecane thiol monolayer on gold.

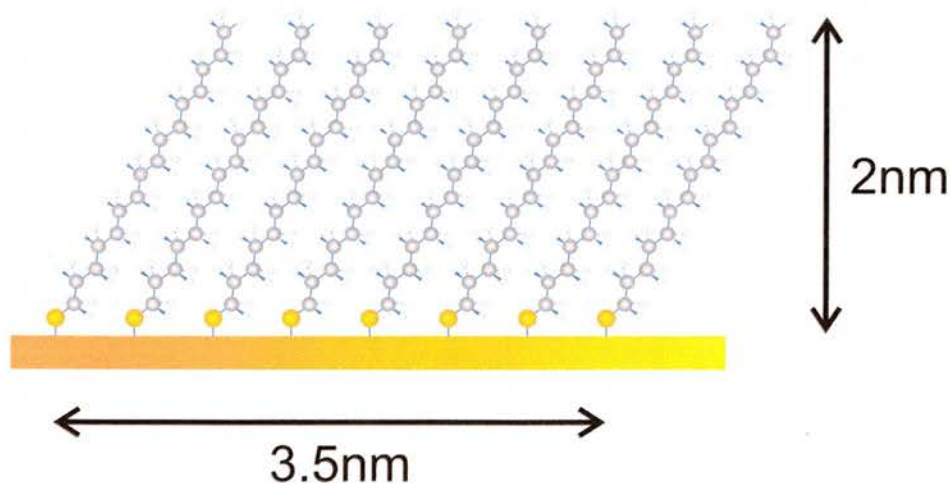


Figure 2.1: Diagram of a hexadecane thiol monolayer on gold with a methyl tail group, a spacer consisting of fifteen methylene units and sulfur head group. The molecular axis is tilted  $30^\circ$  off the surface normal. Approximate dimensions are given.

For gold, the distance between nearest neighbour sulfur atoms is approximately  $5 \text{ \AA}$ , the origin of this distance is explained in subchapter 2.1.4. The gold – sulfur – carbon bond

is consistent with  $sp^3$  hybridisation<sup>48,49</sup>, and is about  $104^\circ$ . The combined effect of the preferred bond angles of carbon atoms in the molecular backbone and head group, the substrate corrugation potential and optimisation of the inter-chain distance imposes a tilt angle of about  $30^\circ$  for the molecular axis from the surface normal. For an all-trans conformation alkane thiol on gold, due to the gold-sulfur-carbon bond angle and bond angle constraints in the carbon backbone the molecular axis will be tilted from the surface normal. In addition to this effect there are intermolecular forces driving a tilting of chains, molecules will tilt from the surface normal. A maximisation of close packing of neighbouring chains with a degree of interlocking of methylene units is thermodynamically favoured<sup>50</sup>. The van der Waals diameter of an alkane chain is  $4.2 \text{ \AA}$ <sup>51</sup>, achieving this interchain distance for SAMs imposes a tilt of  $33^\circ$ . However the interlocking of the chains may still influence this parameter to further optimise the packing of molecules<sup>8</sup> decreasing the tilt to the experimentally observed value of  $30^\circ$ . The influences of the intermolecular interaction and the strong S-Au bond work in a cooperative way, this synergy produces highly stable layers of well ordered thiols. Long chain alkane thiols such as hexadecane thiol produce SAMs that have a comparatively high stability due to having the optimal bond angles and a large degree of van der Waals intermolecular attractions between neighbouring molecules. There is a gradual order / disorder transition around decane thiol<sup>9,48,50,52</sup>, longer molecules produce ordered, crystalline SAMs whereas shorter molecules produce SAMs with less crystalline packing. Hexadecane thiol SAMs have well understood properties and absence of functional groups<sup>11,53-60</sup> and make an ideal reference system with which other SAMs can be compared.

The widely accepted adsorption model is a two step mechanism<sup>1,8,61,62</sup>, although a three step mechanism has also been suggested<sup>63</sup>. There is a quick adsorption step where the majority of the thiols chemisorb onto the gold surface, followed by a slow step where molecules re-arrange to maximise favourable intermolecular interactions, allowing the remainder of the thiols to chemisorb onto the surface. The first step begins as soon as the substrate is immersed in the solution. After a few minutes, at a typical concentration of 1 mM, there is a high surface coverage about 80-90% of thiols in a disordered state. The second step takes place over a number of hours, thiol molecules re-arrange into the lowest energy all-trans conformation, allowing molecules to fill in spaces created by molecules ordering. SAMs with well ordered molecules in large domains are described

as having a high quality. Longer preparation times and elevated preparation temperatures improve the quality of a SAM. Preparing samples at elevated temperatures, such as 60°C or 70°C, increases the domain size of the SAM significantly and the overall uniformity, and hence the coverage and quality<sup>64,65</sup>.

### 2.1.2 Substrate Surface

Gold and silver substrates are used in this thesis. They are in the same group in the d block in the periodic table and are chemically very similar. Although, gold is an inert material forming no stable oxides<sup>48</sup> whereas silver is more reactive spontaneously oxidising in air. Gold is therefore ideal for routine experimental use; silver is only used on a few occasions for a direct comparison with gold. The surface lattice structure of the two metals is a crucial parameter that influences the bonding of molecules, the surfaces used in this work are primarily (111). Gold and silver both form a face centred cubic lattice with a very similar bond distance, 2.88 Angstroms for gold and 2.89 Angstroms for silver. Topographically the surfaces are very similar, however the substrate potential corrugation is very different with silver having a smoother substrate potential corrugation<sup>8</sup>. The bulk truncated (111) surface consists of atoms with hexagonal symmetry, each atom is surrounded by 6 other atoms on the surface plane. Figure 2.2 illustrates the (111) cut on the face centred cubic crystal lattice and the 3-fold symmetry of the (111) surface. Note that due to the abc stacking geometry the sub-surface layer ensures the symmetry is 3-fold not 6-fold symmetry.

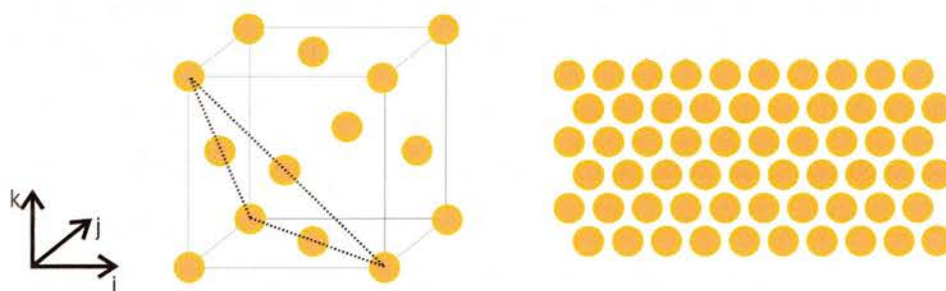


Figure 2.2: gold crystal face centred cubic unit cell showing the (111) plane (left) and the (111) surface (right). Considering the gold surface has abc stacking geometry, half of the three fold hollow sites have a gold atom one layer below the hollow site (hcp), the other half have a gold atom two layers below the surface hollow site (fcc).

An ideal high quality surface would be totally flat and free from any surface contamination, however in reality this is not the case. The quality of a gold surface is

determined by features such as terrace size, step edges, kinks, pits, adatoms and defect regions between domains represented in figure 2.3. Three different types of commercial gold (111) substrates are used in this project<sup>66</sup>; gold single crystal, evaporated gold on mica (Au/mica) and evaporated gold on silicon (Au/Si). The surface quality for these three substrates is not equivalent. Gold single crystals have the highest quality surfaces, however their expense precludes routine use. Au/mica has a quality comparable to gold single crystal in terms of terraces size and is regularly used. Au/Si substrates are the least expensive although the surface is notably rougher than the other two.

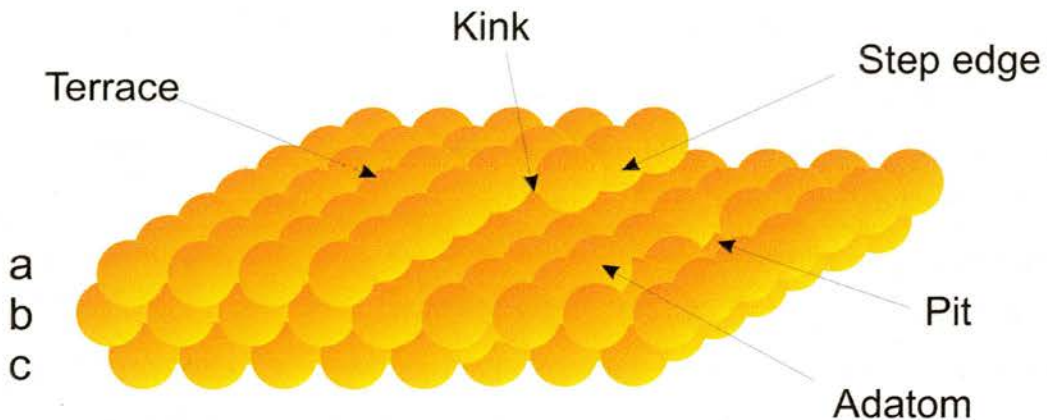


Figure 2.3: Some features of a surface, terraces, step edges, kinks, pits, adatoms. The fcc (111) surface has abc stacking geometry.

The fabrication methods and surface quality for each substrate type are briefly described. Gold single crystal is prepared by the Czochralski method<sup>67</sup>, where a small seed crystal is dipped in molten gold initiating crystallisation. A polishing and x-ray diffraction procedure is applied to obtain the (111) face of the single crystal. These surfaces have 3-fold symmetry with all gold atoms in a fixed azimuthal orientation and are characterised by large flat terraces and have the highest quality surface of all fabrication methods. Epitaxial gold (111) is prepared by evaporation on mica with a heating stage. The axes of the underlying mica substrate determine the gold lattice axes, the azimuthal orientations of all domains are aligned. The surface is polycrystalline in nature with a macroscopic 6-fold symmetry due to domains having two possible azimuthal orientations. Au/mica is characterised by large flat terraces about 150 – 200 nm across<sup>58</sup> and larger have been reported<sup>68</sup>. Au/Si is prepared by evaporation of 100 nm of gold onto a silicon (100) substrate coated with a 5 nm thick titanium adhesion layer. The gold preferentially assumes the lowest energy (111) surface structure. This is a polycrystalline surface characterised by many domains with small terraces and infinite

azimuthal crystal axes orientations. Other faces of gold may form such as (110) and (100) and the surface is typically rougher than the other two substrate types. For Au/mica and gold single crystals, high temperature annealing is normal practise to flatten out planes of atoms. The gold surface quality is crucial for high quality SAMs and the success of any experiment. Since molecules may adsorb with a stronger affinity to the gold surface at step edges or other gold faces altering the film stability locally and disrupting the long range ordering of molecules the substrate quality is an important issue which is examined in subchapter 4.4.

The bulk truncated gold (111) surface naturally reconstructs to a  $(\sqrt{3}\times 23)$  unit cell, due to an anisotropy at the bulk truncated surface<sup>69,70</sup>. The reconstruction forms a herringbone shape and involves a 4.3% uniaxial contraction on the surface relative to the bulk layers. The herringbone reconstruction involves a periodic switching of the stacking geometry from abc to aba stacking. STM clearly shows this reconstructed shape, figure 2.4.

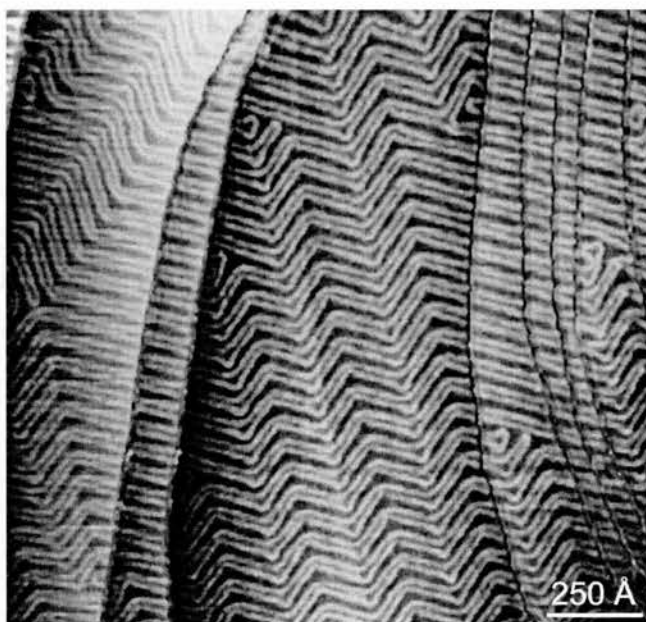


Figure 2.4: Gold (111) Herringbone reconstruction<sup>71</sup>, the periodicity of the herringbone pattern is around 250 Å.

Surface stresses in an electrochemical environment have been shown to cause a distortion of the surface arrangement of atoms dependent on the potential<sup>72</sup>. Furthermore, the  $(1\times 1)$  to  $(\sqrt{3}\times 23)$  surface reconstruction is influenced by the surface potential<sup>73,74</sup>. Negative potentials suit a  $(\sqrt{3}\times 23)$  reconstructed surface while positive

potential suits the 1×1 surface structure. The nature of the gold surface in the presence of an applied potential is complicated by the presence of adsorbates, this is elaborated in subchapter 2.1.4.

### 2.1.3 Molecules

With current synthetic chemistry techniques it is possible to obtain a variety of different and complex molecules with a high purity. There is therefore the possibility to tailor the surface properties of SAM modified substrates with correct selection of the initial molecule. Chemical functionality at a molecular level can drastically alter macroscopic properties of the resulting SAM. In this thesis different SAMs are examined to determine the influences of the tail group, spacer, head group and substrate. The chemical names, abbreviations and structures of molecules used in this thesis are given in table 2.1, abbreviated names are used primarily in the text. A main focus of this thesis is to study SAMs containing a rigid biphenyl unit, a homologue series of SAMs of  $\omega$ -(4'-methyl-biphenyl-4-yl)-alkanethiols ( $\text{CH}_3\text{-C}_6\text{H}_4\text{-C}_6\text{H}_4\text{-(CH}_2\text{)}_n\text{-SH}$ , BP1 to BP6 + BP12) are examined. A distinct odd-even effect is observed for these thiols where an alteration in the tilting of the biphenyl unit is observed depending on whether there is an odd or even number of methylene units in the molecule. This has a notable impact on the packing density of molecules and the resulting film stability. BP(odd) molecules have a smaller tilt and closer packing relative to BP(even) molecules. Previous electrochemical studies of thiol SAMs have overwhelmingly focused on aliphatic thiols<sup>55,56,58,75-83</sup>, in contrast there are few reports on the electrochemical behaviour of aromatic thiol SAMs<sup>43,84-91</sup>. This is surprising as aromatic SAMs offer a number of advantages over aliphatic SAMs. With respect to SAM design there is an increased possibility to achieve a greater degree of control over the structure with the introduction of a rigid biphenyl aromatic unit. Better control over the structure, and ultimately, over defects in SAM, is an aspect of particular importance for electrochemical applications. Together with the significantly higher conductivity of aromatic compared to aliphatic systems<sup>92</sup> aromatic thiol SAMs promise to get around the dichotomy of increasing structural perfection with increasing chain length but at the same time large decrease in conductivity. This allows aromatic SAMs to 'tune' the conductivity by selecting the right combination of aromatic (conducting) and aliphatic (insulating) moieties. Varying the length of the insulating aliphatic moiety will vary the SAMs conductivity.

Chemical Name	Abbreviation	Molecular Structure
Butane thiol	MC4	
Decane thiol	MC10	
Hexadecane thiol	MC16	
Docosane thiol	MC22	
Mercaptohexadecanoic acid	MHA	
4'-Methyl-biphenyl-4-thiol	BP0	
(4'-Methyl-biphenyl-4-yl)-methanethiol	BP1	
2-(4'-Methyl-biphenyl-4-yl)-ethanethiol	BP2	
3-(4'-Methyl-biphenyl-4-yl)-propane-1-thiol	BP3	
4-(4'-Methyl-biphenyl-4-yl)-butane-1-thiol	BP4	
5-(4'-Methyl-biphenyl-4-yl)-pentane-1-thiol	BP5	
6-(4'-Methyl-biphenyl-4-yl)-hexane-1-thiol	BP6	
12-(4'-Methyl-biphenyl-4-yl)-dodecane-1-thiol	BP12	
2-(4'-Methyl-biphenyl-4-yl)-propane-1,3-dithiol	Dipod	
[4-(4'-Methyl-biphenyl-4-yl)-[1,2]dithiolan-4-yl]-methanethiol	Tripod	
(4'-Mercaptomethyl-biphenyl-4-yl)-methanethiol	DT	
2-Phenyl-ethanethiol	PET	
Biphenyl-4-selenol	BPSe	
3,3,4,4,5,5,6,6,7,7,8,8,8-Tridecafluoro-octane-1-selenol	CFSe	
3,3,4,4,5,5,6,6,7,7,8,8,8-Tridecafluoro-octane-1-thiol	CFS	

Table 2.1: Chemical names, abbreviations and chemical structures of a large sample of molecules described throughout this thesis<sup>93</sup>. Alkane thiols have a purity between 92-99% (GC), MC18 (95%), MC16 (92%), MC10 (96%), MC8 and MC7, (97%), MC4 (99%). In general shorter thiols have higher purity. Typical impurities in longer alkane thiol molecules are shorter alkane thiols. NMR and melting point determinations indicate a high purity for biphenyl thiol molecules<sup>94</sup>.

Additionally, dithiol, dipod and tripod biphenyl thiols are examined. These allow an investigation into the SAM-Metal interface, and a more detailed analysis of the bonding between molecules and the substrate. Alkane thiols have no bulky groups unlike biphenyl thiols and lack functionality and are used as a reference system to understand basic film properties. Alkane thiols have received considerable attention in literature and are well understood and characterised. They are used as a reference system to which other SAMs are compared. Additionally, there is some uncertainty in literature about the desorption peaks for long chain alkane thiols which are investigated.

Different molecules are compared with the aim of examining the influence of a specific group or functionality. For example, MC16 SAMs are compared with MHA SAMs, the molecules are identical except for the tail group. Several examinations of this type where there is only one specific difference between the SAMs are performed to build up an understanding of the relative influence of different groups on the overall film stability and properties. Comparing different molecules allows an assessment of the relative impact of the tail group, spacer, head group and substrate on the overall film structure and stability. The interaction of the molecules with the substrate is a crucial factor that influences the structure and stability of SAMs and is discussed in the following subchapter.

#### 2.1.4 Substrate-Molecule Interactions

The strong interaction energy for a gold-sulfur bond, about  $170 \text{ kJ mol}^{-1}$ , drives self-assembly and forms stable structures<sup>8</sup>. High coverage alkane thiol monolayers prepared on gold form the commensurate  $(\sqrt{3} \times \sqrt{3})R30^\circ$  overlayer structure<sup>70</sup> as shown in figure 2.5 with a  $c(4 \times 2)$  superstructure. The area of the overlayer unit cell is three times greater than the underlying gold unit cell, the shapes are identical, but rotated by  $30^\circ$ . The distance between nearest neighbour sulfur atoms is  $\sqrt{3} \times 2.88 \text{ \AA}$ , which is approximately  $5 \text{ \AA}$ . The unit cell is universally accepted, however, as discussed below, there is considerable disagreement in literature over the true adsorption site. In figure 2.5 and for biphenyl systems, illustrated in appendix 1, the position of the sulfur atom with respect to the gold lattice is chosen arbitrarily.

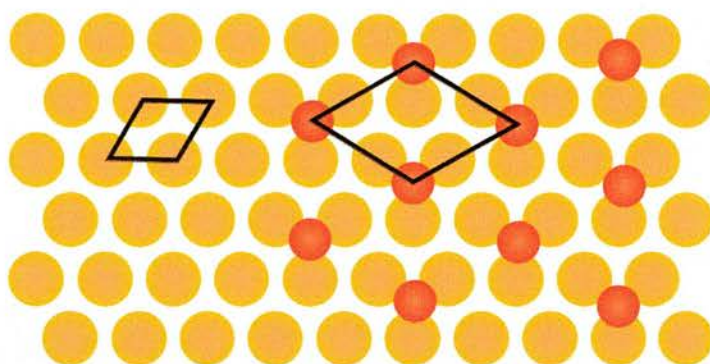


Figure 2.5: Gold atoms are yellow, sulfur atoms are red, only the head group of the SAM is shown. The  $(1 \times 1)$  unit cell for the underlying gold substrate (left) and  $(\sqrt{3} \times \sqrt{3})R30^\circ$  unit cell for the alkane thiol monolayer (right) are shown. The sulfur atoms are in the three fold hollow sites, however, the question of the registry between the overlayer and the underlying lattice is an unsettled issue in literature, the adsorption site in this diagram is selected arbitrarily.

The registry of the molecular unit cell relative to the underlying surface lattice unit cell, and hence the adsorption sites of molecules are described. The interaction of adsorbates with the gold is not uniform across the surface on the nanoscale, due to variations in the local topography and substrate potential corrugation. There are four well defined positions on the gold surface: the on top site, the bridged site, and a face centred cubic (fcc) and hexagonal close packed (hcp) three-fold hollow site. Considering the gold surface has abc stacking geometry, half of the three fold hollow sites have a gold atom one layer below the hollow site (hcp), the other half have a gold atom two layers below the surface hollow site (fcc). The energetics of adsorbates – substrate interactions depends on which of the four positions, on top, bridged, fcc and hcp is concerned. For thiol molecules on gold in the commensurate  $(\sqrt{3} \times \sqrt{3})R30^\circ$  unit cell, various groups have suggested different binding sites, Sellers et al suggest a hollow site<sup>95</sup>, Yourdshahyan et al suggest the fcc position<sup>96</sup>, Beardmore et al suggest the hcp site<sup>97</sup>. Hayashi et al<sup>98</sup> and Vargas et al<sup>99</sup> suggest the bridge site. Kondoh et al<sup>100</sup> and Roper et al<sup>101</sup> suggest the on top position. Despite the discrepancies over the adsorption site, the unit cell, and packing density of molecules is unaffected. To a large extent the true adsorption site for thiols on gold can be ignored for most intents and purposes. However, for one case in particular the adsorption site may be relevant. Assuming the unit cell reflects the positions of the sulfur atoms, then all molecules in the commensurate  $(\sqrt{3} \times \sqrt{3})R30^\circ$  overlayer will have the same adsorption site, whereas, molecules in the BP(even)  $(3 \times 5\sqrt{3})\text{rect}$  unit cell, appendix 1, must have molecules on different adsorption sites. The electrochemical properties for BP(even) SAMs in

particular are interpreted with a consideration of the variety of adsorption sites. Exploring the influence of a thiol monolayer on the properties of a surface is an objective of this thesis.

As discussed in subchapter 2.1.2, the state of the gold-SAM interface or more specifically the structure of the surface layer of gold atoms is not permanently fixed. Two well defined surface states are  $(1\times 1)$  and  $(\sqrt{3}\times 23)$ . The state of the surface structure is dependent on surface adsorbates and applied potentials. Adsorption or desorption of molecules from a substrate can induce a transition between substrate surface structures. The adsorption of molecules influences the surface energy, and may largely restore a  $(\sqrt{3}\times 23)$  reconstructed surface to the  $(1\times 1)$  surface structure. Conversely, the desorption of molecules allows the reconstruction of the gold surface. To complicate the situation further, the surface structure of the underlying substrate may exist in a relaxed state when thiols are adsorbed<sup>101,102</sup>, i.e. other than a  $(1\times 1)$  or  $(\sqrt{3}\times 23)$  structure. It is clear that mobility of surface atoms is a crucial issue. Poirier has investigated the migration of surface gold atoms in relation to the coalescence of gold vacancy island<sup>103,104</sup>. This is unambiguous proof that surface gold atoms in a SAM modified substrate are mobile. However, the precise details of the relaxation phenomenon are only beginning to emerge, and more detailed research is required.

### 2.1.5 Domain Size

As noted in subchapter 2.1.1, preparation of samples at elevated temperatures has the effect of increasing the domain sizes. Figure 2.6 illustrates the difference in domain sizes for BP3 samples prepared at 22°C and 70°C. The average domain size is significantly larger for samples prepared at elevated temperatures<sup>64,65</sup>. At room temperature the majority of domains for BP3 have a size within the range 5-20 nm. At 70°C the average domain size increases substantially and can reach 70-100 nm<sup>65</sup>. A model is developed to highlight the possibility that the domain boundary regions can substantially contribute to the overall packing density of molecules on a substrate. The model assumes square domains are formed, at 22°C the side of the square domain is 15 nm, whereas at 70°C it is 50 nm, figure 2.7 illustrates the model. The spacing of 1 nm between domains is an estimation of the average domain boundary size based on 2 nm long molecules tilting by 30° from the surface normal, with some molecules tilting

towards each other and others tilting away from each other. It is possible that BP(even) SAMs may have a greater spacing than BP(odd) SAMs due to the tilt of the molecules.

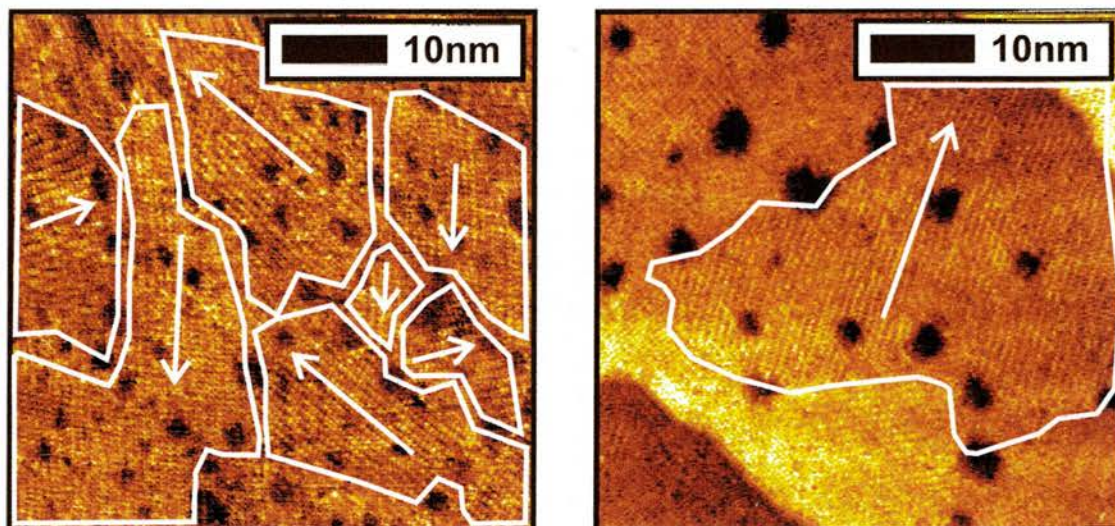


Figure 2.6: STM image of BP3 prepared at 22°C (left) and 70°C (right). Tunnelling conditions: 1.0 V, 500 pA. Domain boundaries and row directions are indicated.

Using the model, at 22°C the coverage is 88% compared to 96% at 70°C. The difference of 8% in the coverage of molecules between samples prepared at 22°C and 70°C is a substantial amount, which is expected to have a clear difference on the charge transfer magnitude for the reductive desorption. The overall uniformity of the layer improves with increased preparation temperatures. Examining the influence of domain size on reductive desorption for the biphenyl thiol homologue series is an objective of this thesis and is examined in subchapter 4.1.2.

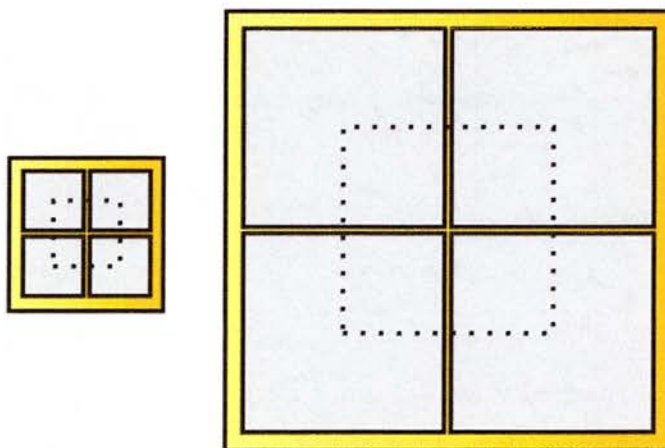


Figure 2.7: Theoretical domains for thiol molecules on gold at 22°C (left) and 70°C (right) with square domains of edge 15 nm and 50 nm respectively. There is an estimated 1nm space between domains. Dotted lines indicate the unit cells for domains.

## 2.2 Electrochemistry

Electrochemistry encompasses several areas including basic research, energy applications (battery and fuel cells), devices (electroanalytical sensors and light emitting devices) and large scale industry (corrosion control and chemical production)<sup>105</sup>. This thesis is concerned with using electrochemistry as a tool to control chemical systems with the aim of understanding fundamental properties such as charge transfer, electrode capacity and adsorbate stability on modified electrode surfaces and metal deposition.

### 2.2.1 Electrochemistry Theory

The process of electron transfer at an electrode is the foundation of electrochemistry, an electron can be transferred from an electrode to a species at the electrode surface (reduction) or an electron can be transferred from a surface species to the electrode (oxidation). The Fermi level in an electrode changes with the applied potential, as the electrode potential is made more negative the Fermi level increases, there is an increased likelihood that electron transfer from the electrode to a surface species will occur, figure 2.8.

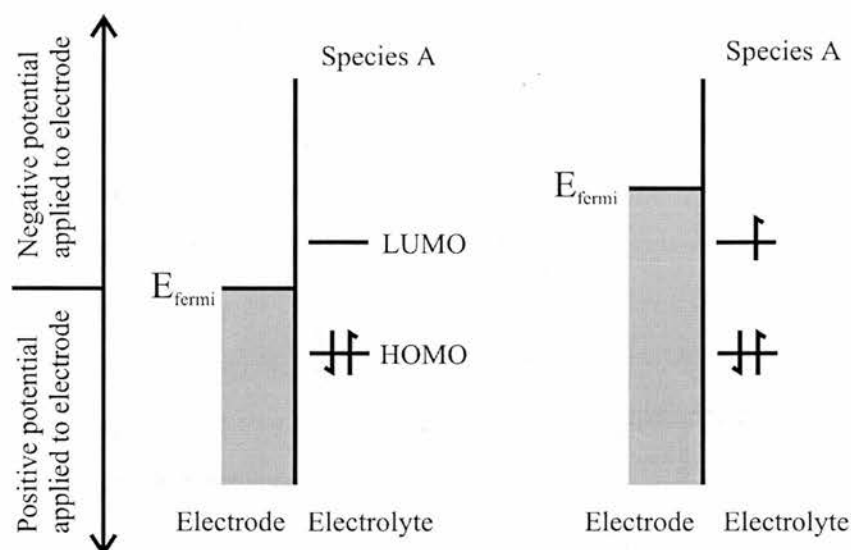


Figure 2.8: A diagram of the reduction process for species A, either surface bound or in solution, as a negative potential is applied to the electrode. When no potential is applied the reduction process will not occur (left). When a negative potential is applied to the electrode such that the Fermi level surpasses the LUMO of species A the reduction of species A will occur (right). If a positive potential was applied such that the Fermi level dropped below the HOMO of species A then the oxidation of species A would occur.

A focus of the work is to determine the stability of SAMs, which is measured by determining the potential at which reductive desorption occurs. Processes involving transfer of electrons are known as faradaic processes, other non-faradaic processes involving charge transfer occur at electrode surfaces, in particular, recharging of the electric double layer are capacitive processes<sup>106</sup>. When a potential is applied to an electrode, ions of the opposite charge in the electrolyte migrate towards the electrode, while ions of the same charge are repelled from the electrode. The electric double layer is the region in the electrolyte where the composition of cations and anions differs from the bulk electrolyte due to the forces exerted by a charged electrode, figure 2.9. Electrode double layer theory has been developed over many years by Helmholtz, Gouy, Chapman and Stern<sup>105</sup>. The edge of the double layer is marked by the double layer boundary, this is the point where the local composition of cations and anions deviates from the bulk composition. The inner Helmholtz plane is defined as the plane intersecting the nuclei of specifically adsorbed ions, whereas the outer Helmholtz plane is the plane intersecting the nuclei of fully solvated ions at their closest point to the electrode surface.

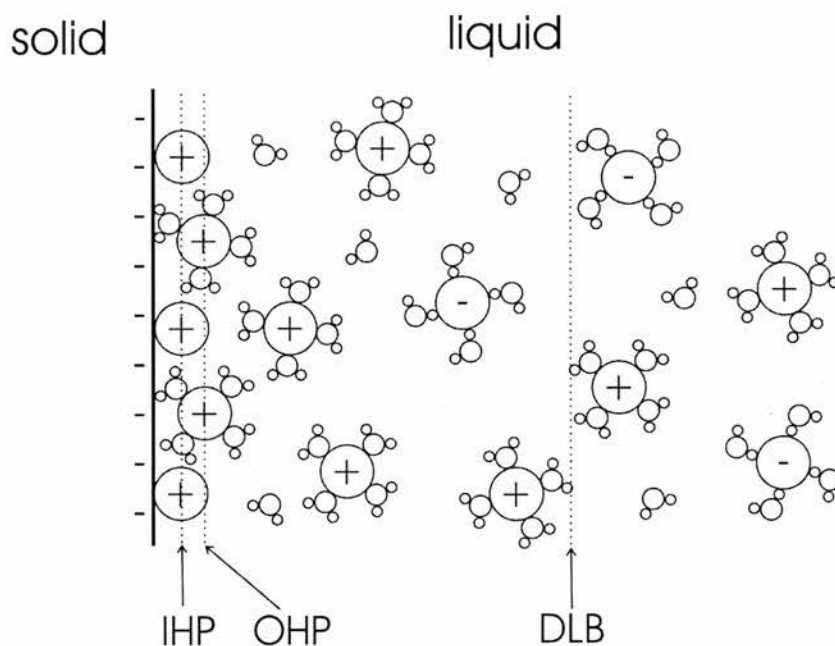


Figure 2.9: The electric double layer occurs when a potential difference between the electrode and electrolyte exists. For a negatively charged electrode ions of the opposite charge will migrate towards the electrode while ions of the same charge are repelled. IHP, OHP and DLB indicate the inner Helmholtz plane, outer Helmholtz plane and double layer boundary respectively, details are given in the text. The diagram is not drawn to scale.

The double layer can be considered equivalent to a capacitor where two metal plates store charge. The capacity of the double layer depends on the presence of any adsorbates. Adsorbates, such as thiol molecules on a gold electrode decrease the capacity of the electric double layer. For long chain alkane thiols a decrease in the capacity by a factor of up to 80 is reported<sup>105</sup>. Upon desorption of molecules a significant capacitive current will flow to recharge the double layer. The total charge for desorption is the sum of the faradaic charge and the capacitive charge. For long chain alkane thiol SAMs the ratio of faradaic charge to capacitive charge is approximately 2:1<sup>76</sup>.

The potential drop over the electrode | electrolyte interface is defined as  $\phi_s - \phi_m$  where  $\phi_s$  is the potential of the solution and  $\phi_m$  is the potential of the metal. On a bare gold electrode the potential drop occurs over the double layer region. On a SAM modified electrode the potential drop occurs over the SAM and to a small extent over the double layer. Figure 2.10 illustrates the potential drop profile for a bare metal and SAM modified metal electrode at different potential values.

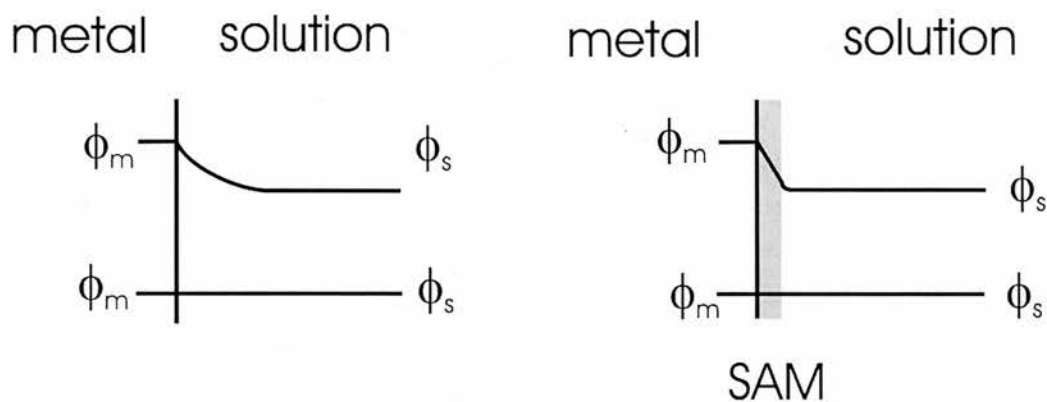


Figure 2.10: Diagram of the potential drop profile across the solid-liquid interface for a bare electrode (left) and a SAM modified electrode (right). The potential drop profile for an electrode negative of the point of zero charge (top) and at the point of zero charge (bottom) is illustrated. For a bare electrode the potential drop occurs over the double layer. On a long chain alkane thiol SAM modified electrode the majority of the potential drop occurs over the SAM.

### 2.2.2 Three Electrode Cell

Electrochemical experiments are performed in an electrochemical cell consisting of three electrodes in a solution connected to a potentiostat, which interfaces the cell with a

computer. In potentiostatic mode, used throughout this project, the potential of the working electrode is controlled and the current is measured. A cell with three electrodes is depicted schematically in figure 2.11, the three electrode cell consists of a working, reference and counter electrode. The potential is measured across the working and reference electrodes while the current flowing between the working and counter electrodes is measured. The vast majority of the current flows between the working and counter electrodes while only a very small current flows between the working and reference electrodes. The reference electrode is at a fixed potential, determined by its open circuit potential. The cell potential is defined as the potential of the working electrode with respect to the potential of the reference electrode. The potential of the counter electrode is undefined, in potentiostatic operation it is continually adjusted through a feedback loop to maintain the desired potential between the working and reference electrodes.

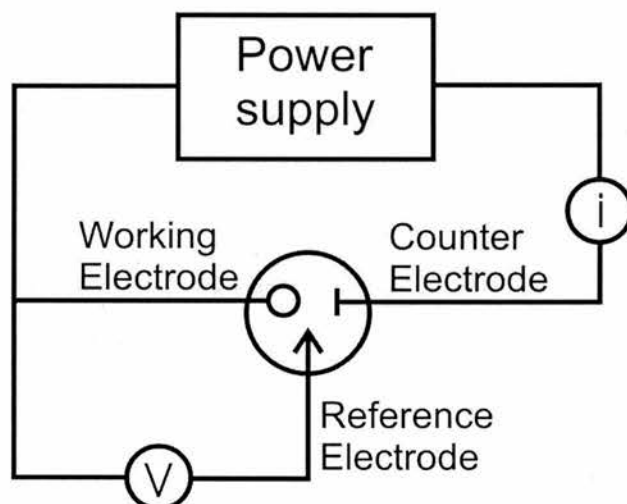


Figure 2.11: Three electrode cell, the cell potential is defined as the potential between the working and reference electrodes. The current is measured between the working and counter electrodes. Feedback loops allow careful control of the potential of the working electrode. The three electrode cell is used rather than the two electrode cell which can not attain both well defined potentials and large currents.

This work involves using working electrodes based on ultra flat polycrystalline gold (111) and silver (111) substrates in native and modified form. The counter electrode has a straightforward function, the only restrictions are that it should in no way dissolve or limit the maximum current density. A platinum wire is used, it is inert and highly suitable as a counter electrode. The reference electrode is the most complicated electrode, figure 2.12, the purpose of the reference electrode is to provide a stable and

well defined potential, to which the working electrode potential can be referenced against. The reference electrode consists of a metal / salt junction in a reference electrolyte.

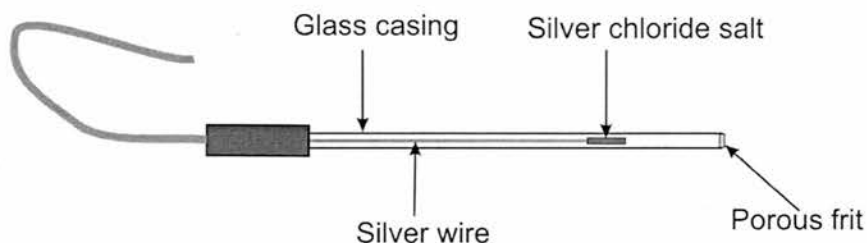
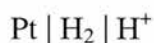
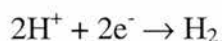


Figure 2.12: Silver / silver chloride reference electrode. Silver wire with a silver chloride precipitate on the end, internal electrolyte is contained inside the glass casing.

Some general principles of reference electrodes and some more specific details relevant to the silver / silver chloride reference electrode utilised throughout this thesis are discussed here. Extremely small currents flow through the reference electrode allowing the cell potential to be defined by the open circuit potential which is determined by the constituent materials of the reference electrode. The salt has metal cations of the same element as the pure metal, and shares a common anion with the electrolyte. The metal, metal salt junction are immersed in a well defined electrolyte, and contained in a glass casing and separated from the main electrolyte typically by a porous frit or glass fibre. The frit allows very small currents to flow without allowing mixing of the internal and external electrolytes either side of the glass casing. An equilibrium is established at the metal | salt | electrolyte junction which determines the cell potential. The equilibrium potential of any reference electrode depends on three factors, the metal | salt junction, the concentration of the reference electrolyte and the electrode temperature. The reference potential of any electrode can be measured with respect to the standard hydrogen electrode for the reaction in a two electrode cell.



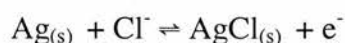
$$E_0 = 0.0000$$

The standard hydrogen electrode (SHE) is a universal system assigned a potential of zero. A comparison of results obtained using different reference electrodes is possible by adjusting the potentials according to the relative differences of their reference electrode potentials with the SHE. Although the SHE forms the basis for determining all

cell potentials, it is not suitable for routine use. The silver / silver chloride reference electrode is a compact and inexpensive electrode that is highly practical for routine use and is well established in the field of electrochemistry.



The overall cell potential is determined by the equilibrium between solid silver and chloride ions.



The concentration of chloride ions is determined:

$$[\text{Cl}^-] = [\text{Cl}^-]_{(\text{AgCl})} + [\text{Cl}^-]_{(\text{KCl})} \approx [\text{Cl}^-]_{(\text{KCl})} \quad (2.1)$$

The chloride ion contribution from AgCl is negligible compared to the contribution from KCl, this allows the well defined KCl concentration to be used for calculations.

The Nernst Equation is applied to give a theoretical cell potential:

$$E_{\text{cell}} = E_{\text{AgCl/Cl}^-} + \frac{RT}{nF} \ln \frac{[\text{AgCl}_{(s)}]}{[\text{Cl}^-][\text{Ag}_{(s)}]} \quad (2.2)$$

The activity of  $\text{AgCl}_{(s)}$  and  $\text{Ag}_{(s)}$  are assigned the value of 1.  $R$  (universal gas constant) =  $8.314 \text{ J K}^{-1} \text{ mol}^{-1}$ ,  $F$  (Faraday Constant) =  $96485 \text{ C mol}^{-1}$ ,  $E_{\text{AgCl/Cl}^-}$  (equilibrium constant)<sup>107</sup> = 0.222,  $n$  (number of electrons transferred) = 1. The above values are inserted into equation 2.2, which is re-arranged and converted to  $\log_{10}$ :

$$E_{\text{cell}} = 0.222 - (T/5039)\log[\text{Cl}^-] \quad (2.3)$$

For a silver / silver chloride reference electrode the two variables influencing the cell potential are temperature and chloride ion concentration, this is seen clearly in equation 2.3. At standard temperature,  $25^\circ\text{C}$ , the equation becomes:

$$E_{\text{cell}} = 0.222 - 0.059\log[\text{Cl}^-] \quad (2.4)$$

In a reference electrolyte, prevented from mixing with the main electrolyte by a frit, the chloride ion concentration is constant. Equation 2.4 can be used to calculate the theoretical cell potential (194 mV). The theoretical cell potential is within 5 mV of the given cell potential (197 mV)<sup>105</sup>. There is a small discrepancy due to the fact that the reference electrode has a 3 M KCl electrolyte concentration and the given value is for a saturated KCl solution. Additionally, there is an extremely small current flowing through the cell that distorts the equilibrium potential from the open circuit value, leading to interfacial potential losses that slightly distort the electrode potential. These factors account for the small differences between the theoretical cell potential and the given cell potential. Despite the uncertainty by a few mV, the reference electrode provides a stable reference potential allowing a comparison of results taken on different days or with different experimental conditions.

### 2.2.3 Cyclic Voltammetry (CV)

Cyclic voltammetry is a technique routinely employed using a three electrode cell. Cyclic voltammetry involves measuring the current while scanning the potential of the working electrode, where the processes of scientific interest are occurring, between two potentials at a constant rate. The experimental conditions are programmed before the experiment can begin. Variables include the starting potential, vertex potential, scan rate and number of cycles. A linear sweep voltammogram is a subset of a cyclic voltammogram (CV), which involves measuring the current while scanning the potential between two potentials then stopping. There are additional complexities that can be added to electrochemical experiments involving CVs. These include adding time periods where a potential is held at a defined value before or between cycles can be introduced, adding more vertices to the CV or adding potential steps. An example of how a CV is acquired is given in figure 2.13.

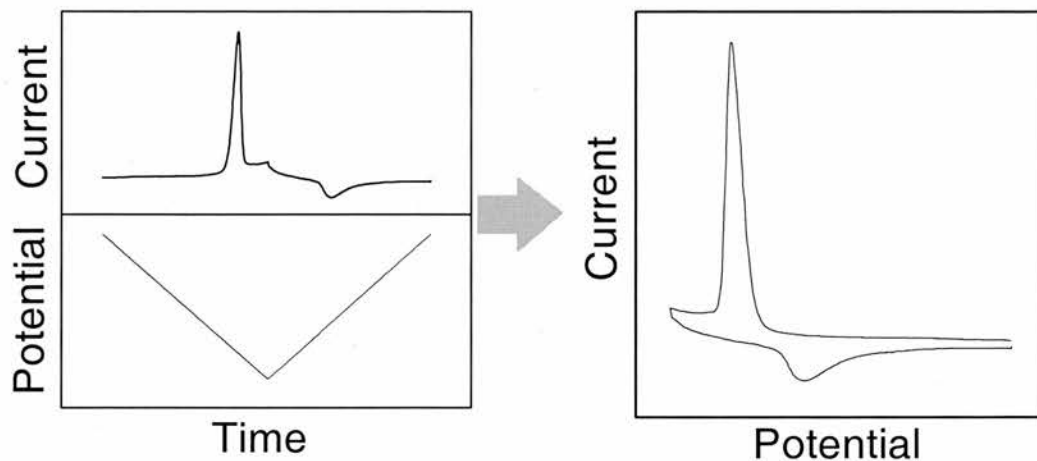


Figure 2.13: Exemplary cyclic voltammogram (CV) with a single cycle. The potential is controlled (bottom left) while the current is measured (top left) with respect to time. The two plots are combined to generate the CV (right).

The electrochemical response can be ascribed to reversible or irreversible electrode processes depending on whether thermodynamic or kinetic factors dictate the electrochemistry. For fully reversible processes the reductive and oxidative peaks occur at the same potential. Reversible processes are characterised by conditions where thermodynamic rather than kinetic factors dictate the redox processes. For a cyclic voltammogram of surface confined species, the desorption and re-adsorption peaks are offset from each other in terms of position so the system must be considered irreversible. There is considerable theory for reversible and irreversible reactions of surface confined redox species<sup>108-113</sup>. In ideal cases, for a desorption reaction kinetic information on the process can be inferred from the peak shape and asymmetry, however, this is more difficult for SAMs. For surface adsorbates the theory is complicated by the non-ideal influences. These included lateral interactions between molecules, potential losses across the molecules, differing penetration across the film and solubility effects. However, due to these reasons there are several deviations from ideal behaviour. Nevertheless, some basic principles can be examined. The scan rate can be related to desorption features including peak potential, maximum current and peak charge. The following conditions are expected for an irreversible redox process<sup>105</sup>. The desorption potential should scale with the logarithm of the scan rate. For surface confined redox species the faradaic contribution to the maximum current should scale

linearly with the scan rate. The total desorption charge should be independent of the scan rate.

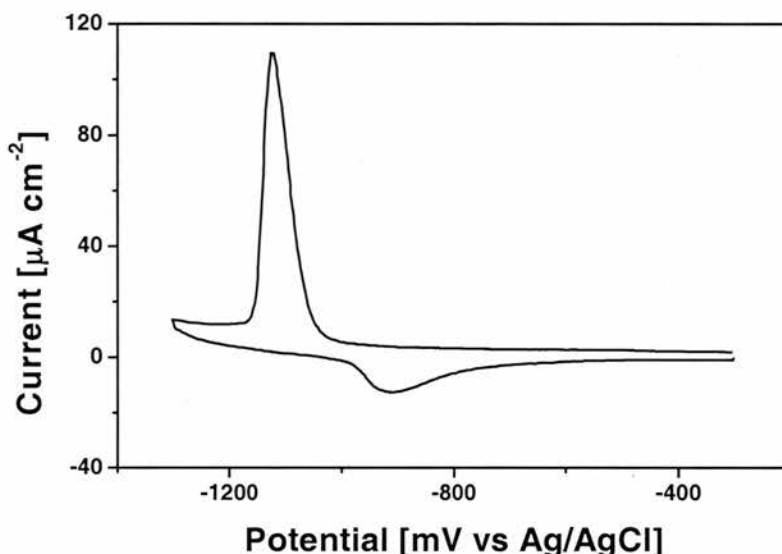


Figure 2.14: Exemplary CV, Au/mica immersed in BP3 at 70°C. Scan range is from -300 mV to -1300 mV with the cycle starting at -300 mV. The desorption peak is observed on the cathodic (negative going) scan between -1000 and -1200 mV, the readsorption peak is observed on the anodic (positive going) scan between -1000 and -600 mV. The separation of potential for desorption and readsorption processes is evidence of an irreversible reaction.

A CV involving the reductive desorption and partial oxidative readsorption of a BP3 SAM prepared at 70°C is shown in figure 2.14. It is noted that the reductive desorption process is assigned a positive current and the oxidative readsorption is assigned a negative current. This assignment goes against the convention for reductive and oxidative currents. However, the assignment makes for a much easier comparison with SHG data for the reductive desorption of SAMs from gold where an SHG increase occurs in parallel with the reductive desorption peak. Three main criteria for evaluating the desorption peak in a cyclic voltammogram are detailed here, they are the desorption peak position, desorption charge and peak shape.

### Position

The peak position or peak potential is simply the potential value where the peak's maximum current is recorded on either the cathodic or anodic scan. For the CV in figure 2.14 the desorption peak position is -1125 mV and the readsorption peak position is -915 mV. The desorption potential is a measure of the film stability with more stable

films capable of sustaining more negative potentials. It is a measure of the strength of the interaction between the molecules and the substrate and the extent of intermolecular interactions with a more negative peak position indicating a more durable SAM. The onset of desorption would be a useful parameter to determine as it indicates the potential at which the film begins to degrade, however, this is not a well defined position and would introduce more uncertainty into interpretations.

## Charge

The reductive desorption charge is the sum of faradaic and capacitive processes. Assuming a one electron desorption process, the faradaic charge depends on the number of molecules bonded to the substrate. The desorption peak charge gives an indication of the packing density of molecules, a larger desorption charge indicates a greater packing density. Determining the charge from the reductive desorption peak for thiol SAMs involves determining the area of the desorption peaks. A baseline is selected to ensure the correct capacitive charging contributions to the voltammogram are included in the peak area determination, and to compensate for effects such as hydrogen evolution. Ideally, voltammetric peaks are resolved from any other electrochemical feature such as hydrogen evolution or substrate oxidation. The baseline is used as a lower boundary for integration of the peak. The charge transfer (charge density),  $Q$  ( $\text{C cm}^{-2}$ ), is calculated from the peak area,  $A_{\text{peak}}$  ( $\text{A V}$ ) using the following relationship:

$$Q = \frac{A_{\text{peak}}}{A_{\text{sample}} \times v} \quad (2.5)$$

Where  $A_{\text{sample}}$  ( $\text{cm}^2$ ) is the area of the sample exposed to the electrolyte and  $v$  ( $\text{V s}^{-1}$ ) is the scan rate.

## Peak Shape

The peak shape assessment involves three parts, it involves qualitative and quantitative aspects. Qualitatively, a general description of the peak shape is given, i.e. whether it is a single peak, a single peak with a shoulder, a double peak or well resolved multiple peaks. The shape of the peak gives insight into various aspects of the desorption

process. Quantitatively, the width of the peak and a measure of the symmetry of the peak are determined. To determine the peak width and symmetry, the baseline created for the charge determination is required. A vertical line between the desorption maximum ( $E_{des.}$ ) and the baseline is drawn, a horizontal line intersecting this line at half its height is drawn. The potentials where the horizontal line intersects the peak on the positive ( $E_{p,FWHM}$ ) and negative ( $E_{n,FWHM}$ ) side are noted. The peak width at half maximum (FWHM) is the difference between  $E_{p,FWHM}$  and  $E_{n,FWHM}$ . The symmetry is defined by equation 2.6 using an asymmetry factor,  $AF$ :

$$AF = \frac{|E_{p,FWHM} - E_{des.}|}{|E_{n,FWHM} - E_{des.}|} \quad (2.6)$$

Therefore, a symmetric peak shape yields  $AF = 1$  and  $AF > 1$  ( $AF < 1$ ) means a broadening of the increasing (decreasing) part compared to the decreasing (increasing) part of the desorption peak.

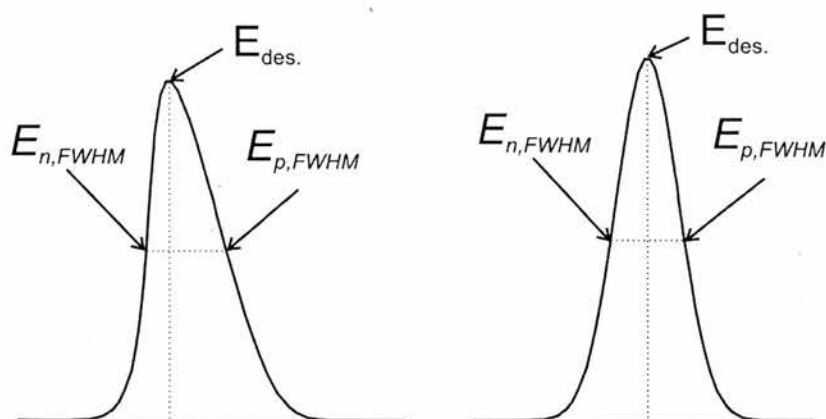


Figure 2.15: Diagrammatic illustration of an asymmetric peak (left) and a symmetric peak (right) in a cyclic voltammogram. See text for details.

Figure 2.15 illustrates the peak shapes for an asymmetric and symmetric peak with asymmetry factors,  $AF$  of 2.4 and 1 respectively. The asymmetry factor of 2.4 indicates that the peak is considerably asymmetric with a sharp fall in the current after the desorption maximum.

## 2.3 Second Harmonic Generation (SHG)

Large electric fields are generated using laser light, the electric fields generated can be comparable to the electric fields observed by electrons in a chemical bond<sup>114,115</sup>, this opens up the new and interesting field of nonlinear optics<sup>116-118</sup>. The interaction of light with materials no longer occurs in a purely linear fashion. When high intensity light interacts with materials a nonlinear optical effect is observed where higher light harmonics are produced. Light is generated with higher frequencies than that of the original laser beam. This nonlinear effect only becomes important when high intensity radiation is used, indeed the first reported instance of SHG was reported Franken et al one year after the first optical laser was built<sup>119</sup>. This field has developed from investigating bulk properties in the sixties to studying interfaces and surfaces in the eighties. In this thesis second harmonic generation is used to monitor desorption and adsorption of thiol containing organic molecules on electrode surfaces.

Impinging light creates a polarisation at the metal surface, which emits light at higher frequencies. A simple case of nonlinear optics is second harmonic generation (SHG) where light at double the frequency of the fundamental beam is emitted. It is a coherent process with the emitted light having a defined direction, frequency and polarisation. SHG is suitable for studying solid-liquid interfaces unlike many other spectroscopic techniques used for surface studies. SHG can only be applied where there is a break in centro-symmetry, this means either non centro symmetric crystals or at the interface of two different centrosymmetric materials. The electrons in the gold surface oscillate with the electric field from the light source creating a polarisation, denoted  $P$  or  $P_i$ . The polarisation has several harmonics:

$$P_i = \epsilon_0 \left( \chi_{ij}^{(1)} E_j + \chi_{ijk}^{(2)} E_j E_k + \chi_{ijkl}^{(3)} E_j E_k E_l + \dots \right) \quad (2.7)$$

Where  $\epsilon_0$  is the free-space permittivity, the terms  $\chi$  are the susceptibility tensors where  $\chi_{ijk}^{(2)}$  is the second order nonlinear susceptibility tensor.  $i, j, k$  and  $l$  denote vector components,  $E$  is the Electric field. The polarisation contains a linear term ( $\chi_{ij}^{(1)}$ ) and nonlinear terms. In equation 2.7 the second and third harmonics represent the nonlinear

terms. The magnitudes of the nonlinear tensors are considerably smaller than linear tensor  $\chi^{(1)}$ . The polarisation for the first nonlinear term in the polarisation is as follows:

$$P^{(2)}(2\omega) = \epsilon_0 \chi^{(2)} E(\omega) E(\omega) \quad (2.8)$$

Where  $E(\omega)$  is the electric field of the incoming fundamental wave and  $\chi^{(2)}$  is the second order susceptibility tensor. The polarisation produces light at the second harmonic ( $2\omega$ ). The intensity of SHG is proportional to the square of the magnitude of the polarisation:

$$I_{SHG} \propto |P^{(2)}|^2 \quad (2.9)$$

The SHG intensity is related to the electric field by substituting equation (2.8) into (2.9):

$$I_{SHG} \propto |\chi^{(2)} EE|^2 \quad (2.10)$$

Equation 2.10 is rearranged and written in terms of the fundamental beam intensity:

$$I_{SHG} \propto |\chi^{(2)}|^2 I_{(1064nm)}^2 \quad (2.11)$$

Equation 2.11 relates the intensity of the second harmonic signal to the intensity of the fundamental beam. For gold surfaces modified with thiol molecules the polarisability of the surface electrons is altered, qualitatively, electrons are localised in a bond with a sulfur atom allowing a discrimination of surfaces based on the extent of coverage. The susceptibility tensor,  $\chi^{(2)}$  contains a background contribution,  $\chi_{Au}$ , and a contribution from the interface proportional to the coverage  $\chi_{int}$ . The surface coverage,  $\theta$ , can be related to the SHG intensity assuming that the interface susceptibility tensor parameter  $\chi_{int}^{(2)}$  scales linearly with the coverage:

$$I_{SHG} \propto |\chi_{Au}^{(2)} + \chi_{int}^{(2)} \theta|^2 \quad (2.12)$$

The coverage of adsorbates can be related to the intensity of the second harmonic signal when the SHG intensity for a bare surface and a completely covered surface are known<sup>118</sup>:

$$\theta(E) = \frac{\sqrt{\frac{I_{SHG}(E)}{I_{SHG}(E_{\theta=0})} - 1}}{b} \quad (2.13)$$

where

$$b = \frac{\chi_{int}^{(2)}}{\chi_{Au}^{(2)}} = \sqrt{\frac{I_{SHG}(\theta = 1)}{I_{SHG}(\theta = 0)} - 1} \quad (2.14)$$

Equation 2.13 is used to determine the coverage of a sample using second harmonic generation. The SHG probes the surface as molecules adsorb onto the gold and desorb off the gold. SHG provides a non-destructive, real-time, in-situ optical technique to investigate buried interfaces. Performing SHG at an electrode surface where there is a continuously changing electrode field,  $E_{DC}$ , introduces an additional third order term,  $\chi_{eff}^{(3)}$  to the polarisation. The polarisation  $P(2\omega)$  giving rise to SHG from an electrode is phenomenologically described by

$$P(2\omega) \propto \chi^{(2)}E(\omega)E(\omega) + \chi_{eff}^{(3)}E(\omega)E(\omega)E_{DC} \quad (2.15)$$

Figure 4.1 reveals that the SHG for a bare gold surface changes as the potential is scanned between  $-300$  and  $-1300$  mV. There is a clear SHG intensity decrease at more negative electrode potentials. Capacitive processes are therefore involved in the SHG intensity changes, however, the effect is small. In the region between  $-800$  and  $-1300$  mV there is 1% decrease in the SHG intensity every 13mV relative to the SHG intensity at  $-1300$  mV. SHG changes due to capacitive processes are compared with the changes for faradaic processes. For a typical desorption peak spanning 100 to 150 mV the SHG decreases due to capacitive processes by about 10% of the intensity relative to the SHG at  $-1300$  mV. The total SHG change due to faradaic and capacitive processes is typically an increase of about 60% relative to the intensity at  $-1300$ mV. The SHG

changes during a desorption process are therefore dominated by faradaic processes by a ratio of 7:1.

Some details of the components of the polarisation terms are now described. The polarisation is defined in terms of x, y and z Cartesian coordinate system where the surface is in plane xy. Tensor elements are defined  $\chi_{ijk}$ , where i is a coordinate describing the  $\omega_1 + \omega_2$  term, j is a coordinate describing the  $\omega_1$  term and k is a coordinate describing the  $\omega_2$  term. For example, the tensor element  $\chi_{xyz}$  describes a component of the generated photon oscillating along the x-axis, the  $\omega_1$  photon oscillating along the y-axis and the  $\omega_2$  photon oscillating along the z-axis. The polarisability can be described by 27 individual tensor elements corresponding to all possible permutations. For second harmonic generation  $\omega_1 = \omega_2$  hence  $\chi_{ijk} = \chi_{ikj}$  so there can be up to 18 independent tensor elements, these are plotted in a matrix.

$$\begin{array}{cccccc} \chi_{xxx} & \chi_{xyy} & \chi_{xzz} & \chi_{xxy} & \chi_{xyz} & \chi_{xzx} \\ \chi_{yxx} & \chi_{yyy} & \chi_{yzz} & \chi_{yyx} & \chi_{yyz} & \chi_{yzy} \\ \chi_{zxx} & \chi_{zyy} & \chi_{zzz} & \chi_{zxy} & \chi_{zyz} & \chi_{zzx} \end{array}$$

Due to symmetry, if a tensor element has inversion symmetry,  $\chi_{ijk} = -\chi_{-i-j-k}$  there is no contribution to second harmonic generation and the tensor vanishes, of eighteen tensor elements, five are non-vanishing<sup>120</sup>.

$$\begin{array}{cccccc} 0 & 0 & 0 & 0 & 0 & \chi_{xzx} \\ 0 & 0 & 0 & 0 & \chi_{yyz} & 0 \\ \chi_{zxx} & \chi_{zyy} & \chi_{zzz} & 0 & 0 & 0 \end{array}$$

Of the five non-zero tensor elements three are independent,  $\chi_{xzx} = \chi_{yyz}$ ,  $\chi_{zxx} = \chi_{zyy}$  and  $\chi_{zzz}$ . The contribution of each tensor depends on the polarisation of the fundamental and second harmonic light. The polarisation is defined for a beam in the xz plane impinging on a surface xy. Light with an electric field oscillating in the zx plane is p polarised, whereas light with an electric field oscillating in the y direction is s polarised. Altering the polarisation of the incoming or detected light can probe the magnitude of different tensor elements. When both fundamental and second harmonic beams are p polarised

(pp polarised) all three independent tensors are probed. When the fundamental is s polarised and the second harmonic in p polarised (sp polarised) only one independent tensor element,  $\chi_{zxx} = \chi_{zyy}$  is probed. For ss and ps polarisations no tensors are probed. In this thesis pp polarised light is always used due to the established relationship between SHG intensity and coverage<sup>121</sup>.

## 2.4 Scanning Tunnelling Microscopy (STM)

STM is a powerful tool that allows nanoscopic imaging of planar conducting surfaces allowing molecular or atomic resolution<sup>122,123</sup>. STM can be operated in a wide range of temperatures, from liquid helium temperatures up to well above room temperature, and pressures from ultra high vacuum to normal atmospheric pressure. It can operate in air or in liquid, opening up the possibility of imaging electrochemical surfaces. Since its discovery in the early eighties<sup>122</sup>, the versatility of the technique has led to its rapid emergence as one of the major techniques employed by surface scientists. The resolution is about 2 Å in the surface plane and 0.1 Å in the direction perpendicular to the surface plane allowing real space atomic resolution. Operation of the STM relies on the principle that two conductors positioned extremely close together but not touching will have overlapping wave functions allowing quantum mechanical tunnelling of electrons across the barrier. A small measurable current will flow when a potential difference is applied. The wave functions extend into vacuum with an inverse exponential decay. The current,  $I$ , is related to the distance,  $d$ , between two conductors<sup>123</sup>:

$$I \propto \exp(-2Kd) \quad (2.16)$$

Where  $K$ , the inverse decay length is defined:

$$K = \frac{2\pi}{h} \cdot \sqrt{2m\phi} \quad (2.17)$$

Where,  $h$  = Planck's constant,  $m$  = electron mass and  $\phi$  = effective local work function. Taking a typical work function,  $\phi = 4$  eV,  $K$  can be calculated to be approximately equal to  $1 \text{ \AA}$ . This means within  $1 \text{ \AA}$ , the wave function magnitude becomes  $1/e$ .

STM has a conducting tip which ideally has a single atom at its apex, figure 2.16. A potential difference is applied between the tip and conducting surface. The tip is brought extremely close to the conducting surface, to a distance of a few Angstroms. The wave functions overlap allowing quantum mechanical tunnelling, figure 2.17. A tunnelling current in the region of pico or nano Amperes can be measured. For a negatively biased tip, electrons flow from the tip to unoccupied states on the sample. The density of the unoccupied states on the surface is mapped as the tip scans across the surface. If the tip is positively biased with respect to the surface it will map the occupied states of the surface as electrons tunnel from the sample to the tip.

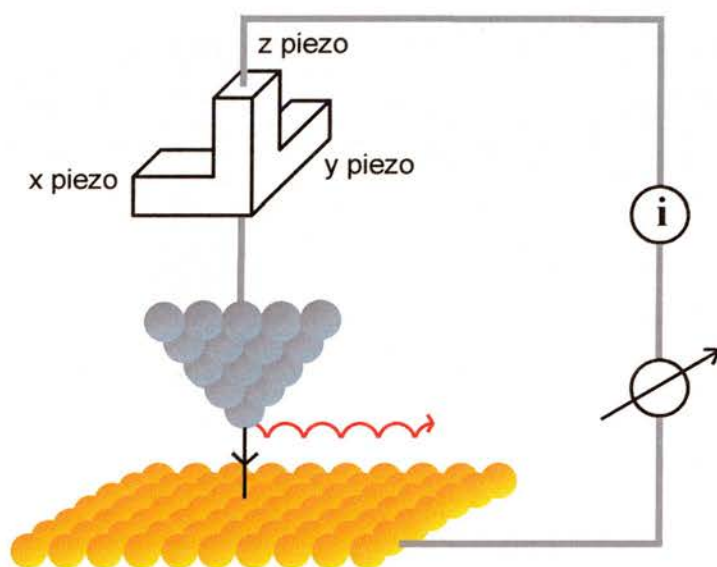


Figure 2.16: Diagram of the STM tip with a single atom at its apex. A potential difference is applied between the tip and surface, the current flow between them is measured. Typically nano or pico Ampere currents are measured. Piezocrystals control the position of the STM tip with respect to the surface. In constant current mode feedback loops control the  $z$  piezo, to maintain a constant current flow between the tip and sample.

The tunnelling current is exponentially sensitive to the distance between the tip and the nearest metal atom on the surface (equation 2.16). As the tip scans across the surface, it will experience a change in tunnelling current as it moves due to local variations in electronic states of atoms or molecules and surface topography. The tip probes

electronic states of atoms or molecules rather than the actual position so images must be carefully interpreted. The technique is sensitive to topographic features such as those indicated in figure 2.3. STM images are a convolution of topographic and electronic surface features.

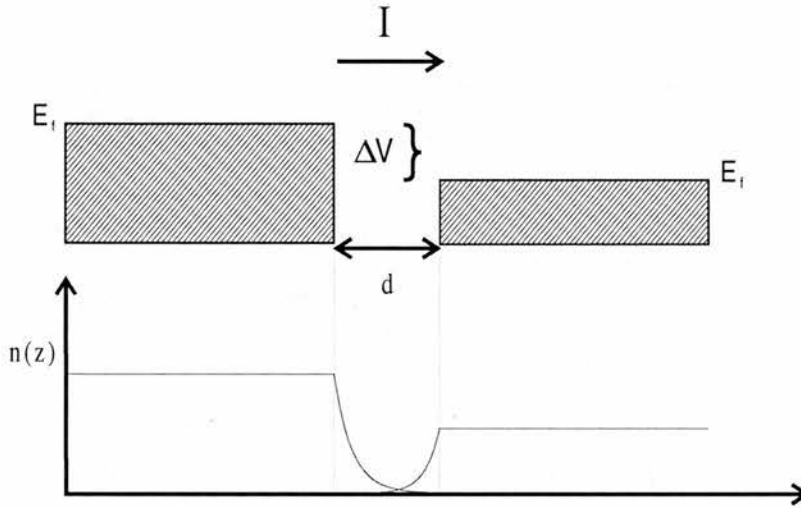


Figure 2.17: A potential difference applied between two metals produces Fermi levels at different magnitudes with respect to each other, this provides a driving force for quantum mechanical tunnelling. The  $x$ -axis represents a distance, electrons on the left in occupied states tunnel to unoccupied states on the right. Two metals very close to each other have overlapping wave functions and small currents can flow.  $I$  is the current,  $E_f$  is the Fermi level,  $\Delta V$  is the potential difference,  $d$  is the distance between the two metals and  $n(z)$  is the electron density. Figure adapted from reference 124.

## Chapter 3

# EXPERIMENTAL

### 3.1 SAM Preparation

Two types of SAM preparation procedure are described; uniform SAMs and patterned SAMs. To prepare a uniform SAM the following procedure was followed. First, 15 ml glass screw top jars were cleaned using a 'piranha solution' which comprises a mixture of hydrogen peroxide and sulfuric acid. 100 volumes hydrogen peroxide was added to a large glass dish. To this, concentrated sulfuric acid was slowly and carefully added. There is a rapid temperature increase on mixing. The jars were immersed in the 'piranha solution' for 10 minutes before careful rinsing with distilled water. The jars were allowed to dry before rinsing with pure ethanol before drying again. Predetermined amounts of thiol crystals were weighed into the jars. 5 ml of ethanol was added to each jar to make a thiol concentration of 1 mM. If necessary the jars were warmed slightly to facilitate dissolution. The gold substrate, stored in a low-pressure chamber, was cut into pieces 12.5 mm by 15 mm and blown clean with inert gas. Au/mica substrates were annealed in a butane / oxygen flame. Each substrate was allowed to cool for 15 seconds before it was immersed in an individual jar, containing the thiol solution. Au/Si substrates were not flame annealed. The jars were sealed and samples were incubated for a period of time, usually overnight. Typically samples would be incubated at either 22°C, or 70°C using a thermostatically controlled oven. After the incubation step, the gold sample was carefully removed from the jar with clean tweezers. Excess solution was allowed to drain off before the sample was thoroughly rinsed in pure ethanol. Finally, the samples were blown dry in inert gas. This sample preparation procedure was strictly followed to reproducibly form high quality SAMs.

Patterned SAMs were also prepared. Patterned samples are of interest for selective desorption or metal deposition experiments. There are several techniques to achieve patterning, however the two principal techniques to create surface patterns on thiol modified surfaces are lithography and micro contact printing<sup>45,46</sup>. The second technique, micro contact printing, is used in this project. Micro contact printing is a facile, inexpensive and versatile technique that involves pressing a polydimethylsiloxane

(PDMS) stamp onto the surface. The surface patterning procedure for routine preparation of patterned samples is outlined in figure 3.1. The first step is to immerse a stamp in a thiol solution then gently blow it dry with inert gas. Molecules remain in the stamp. The stamp is then pressed onto the surface. Molecules transfer from the stamp onto the substrate surface only at the point of contact. The sample can subsequently be developed by immersion in a solution of different thiols, which will preferentially attach at the bare gold.

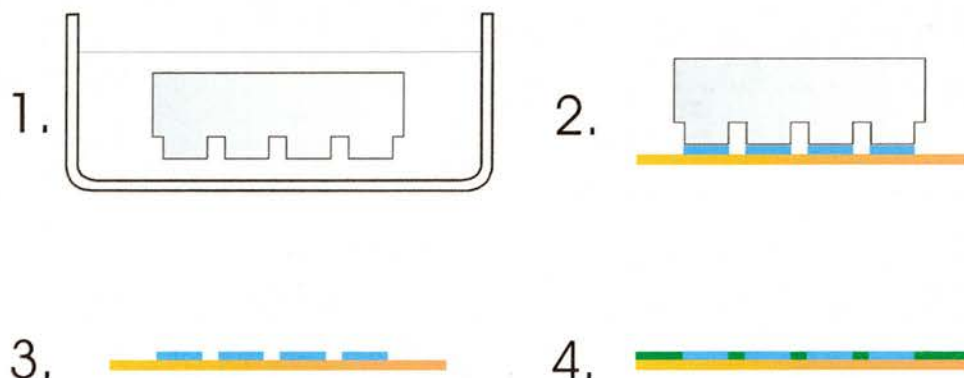


Figure 3.1: Patterning of a gold surface using micro contact printing. The PDMS stamp is immersed in solution containing thiol molecules (1), and then dried. The stamp is gently pressed onto a gold surface and held with gentle pressure for a short period of time typically 30 seconds (2). The stamp is removed leaving thiol molecules bound to gold only in regions where there was contact with the PDMS stamp (3). The sample can be immersed in a solution of a different thiol, adsorption will preferentially occur on the regions of bare gold (4).

Various factors influence the SAM quality such as substrate cleanliness<sup>75</sup>, substrate flatness<sup>58</sup>, thiol type<sup>1</sup>, preparation temperature<sup>65</sup>, immersion time<sup>118,125</sup>, potential control<sup>80,126,127</sup> and annealing<sup>76,128</sup>. Of these factors, substrate flatness, thiol type and preparation temperature are explored in this thesis.

## 3.2 Techniques

### 3.2.1 Introduction

The three scientific techniques performed in this project are electrochemical, spectroscopic and microscopic in nature, they are cyclic voltammetry (CV), second harmonic generation (SHG) and scanning tunnelling microscopy (STM). Cyclic voltammetry is routinely performed using gold surfaces and modified gold surfaces as the working electrode in a three electrode cell. The technique can probe many properties

such as electrode capacity, charge transfer properties and thiol film stability. Cyclic voltammetry is routinely performed with in-situ and real-time SHG. SHG is a complementary technique probing the gold-sulfur bond, the combination of electrochemistry with SHG allows one to follow the faradaic and capacitive processes at the electrode surface during thiol desorption. Electrochemistry measures the combination of faradaic and capacitive processes while SHG predominantly measures faradaic processes, the combination of these techniques brings new insight into phenomena such as the desorption mechanism. The ability to perform cyclic voltammetry with in-situ SHG is not a trivial proposition as a number of technical issues must first be addressed. A suitable spectroelectrochemical cell must be designed and constructed, the software for data acquisition must be written and verified. The design and construction of the spectroelectrochemical cell was a significant part of the project. The design was continually optimised through repeated use and testing, the latest version is described in appendix 2. In order to collect a sufficient number of SHG data points there needs to be collection of several data points each second, the data collection and storage systems needs to be capable of high throughputs.

STM is performed on gold surfaces either prior to or post electrochemical experiments and is capable of nanoscopic imaging with a molecular or atomic resolution. Unit cells adopted by adsorbate molecules can be observed allowing a determination of the packing density of molecules. Theory for the techniques is described in chapter 2 while the experimental details are described in the following subchapters.

### 3.2.2 Cyclic Voltammetry (CV)

An EG&G potentiostat model 283 was used to perform electrochemical measurements. Cyclic voltammetry is performed using a three electrode cell. Typical experimental conditions for cyclic voltammetry using a three electrode cell used in this project are as follows.

Working electrode:	Gold (111) surface / modified gold (111) surface
Counter electrode:	Platinum wire (0.5 mm diameter)
Reference electrode:	Ag / AgCl / KCl (3 M, saturated AgCl)
Electrolyte:	deoxygenated 0.5 M KOH <sub>(aq)</sub> (distilled water)

Scan rate: 20 mV/second  
 Scan range: -300 mV to -1300 mV

The scan rate and scan range are often altered to tailor the experimental conditions for a particular purpose.

### 3.2.3 Second Harmonic Generation (SHG)

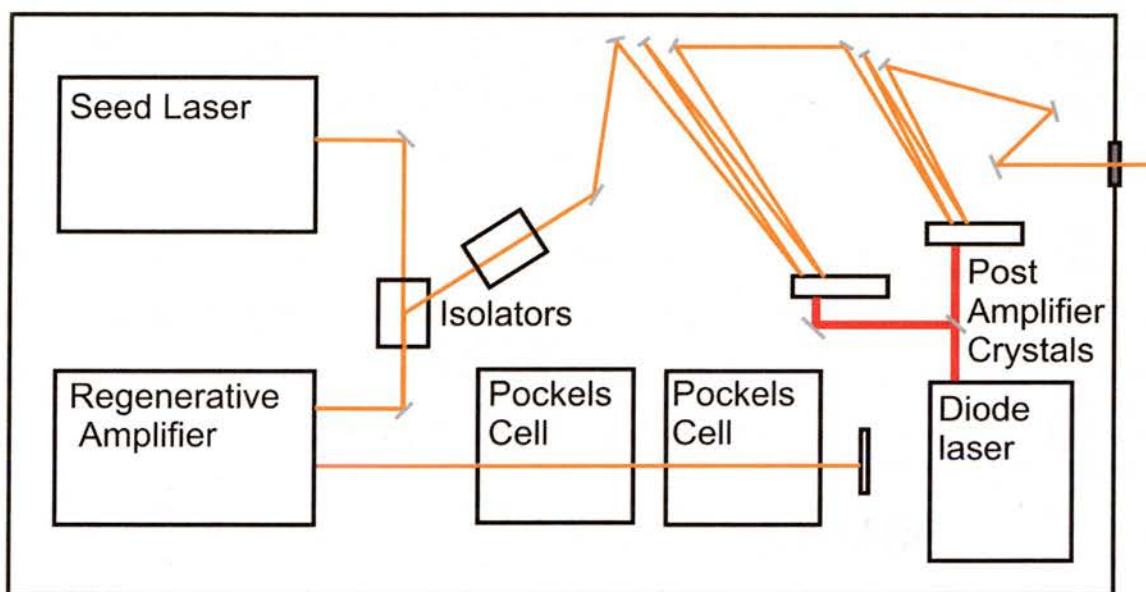


Figure 3.2: Simplified diagram of beam path and components inside the laser system used for this work. Many components are omitted for clarity. The details of the set-up are described in the text. The orange line indicates the 1064 nm laser beam, red line indicates the 808 nm diode laser used to pump the Nd:VAN crystals, there are diode lasers pumping the Nd:VAN crystals in the seed and regenerative amplifier not displayed.

In-situ laser SHG was performed with a 1064 nm diode pumped Nd:Vanadate laser (HighQ Laser). The lasing material is a Vanadate crystal doped with Neodymium (Nd:VAN), the material emits infrared radiation at 1064 nm. A schematic of the laser used in this project is presented in figure 3.2. The laser pulses are initiated at the seed laser, there are several amplification and beam shaping steps before the laser beam passes through the aperture. The seed laser cavity is 1.665 m long producing pulses with a 90 MHz frequency, the seed laser cavity generates pulses every 11.1 nanoseconds. One of the emitted pulses is selected and introduced into the regenerative amplifier. The Pockels Cells use an optical switching mechanism that rotates the polarisation of the light when it first enters the regenerative amplifier preventing it from escaping. In the

regenerative amplifier the single pulse from the seed laser is amplified, the light passes through the lasing material many times building up a high energy. Every millisecond the Pockels Cells rotates the polarisation for a very short time allowing a short burst of pulses to leave the cavity through the isolator in a Q-switching process. Concurrently a new pulse is selected from the seed laser and the process inside the regenerative amplifier is repeated. The pulse train escaping from the regenerative amplifier is shaped using lenses and mirrors and the polarisation is aligned using a half wave plate. The beam is amplified on four more occasions as it passes through both of the diode pumped laser crystals on two occasions each. The beam reflects off several mirrors before it is emitted through the aperture. The beam leaves the laser with a Gaussian distribution beam profile, a well defined pulse train and stable beam power.

The laser system used throughout this work is a special type of pulsed laser, which produces a characteristic pulse train. Every millisecond a burst of pulses is emitted, each pulse train consists of about 8 pulses 11.1 nanoseconds apart. Each pulse within a train has a different intensity. The pulse trains are depicted in figure 3.3.

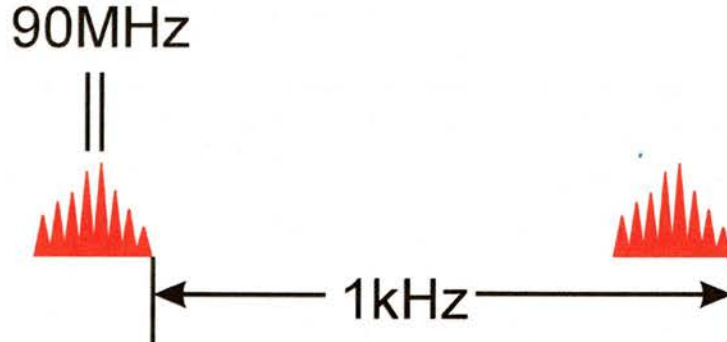


Figure 3.3: Diagram of the pulse trains emitted by the laser (not to scale). Pulse trains are emitted every millisecond, each train consists of around eight pulses 11.1 nanoseconds apart.

Due to the high degree of coherence, and large instantaneous powers, massive electric fields can be generated with lasers. The scale of the electric field generated by laser light is comparable to the electric field present on an electron in a bond<sup>114,115</sup>

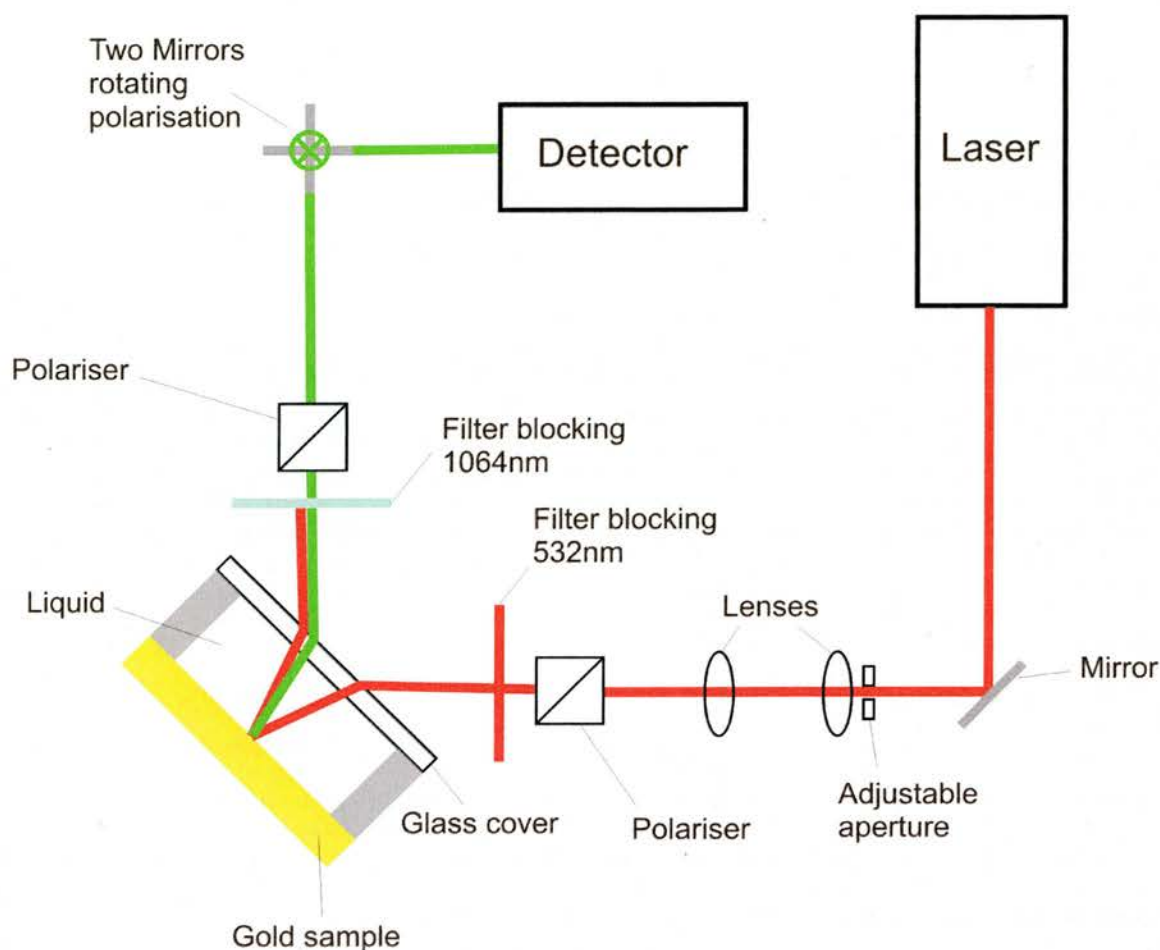


Figure 3.4: Second Harmonic Generation Schematic. The 1064 nm infrared beam is depicted as red, the 532 nm beam is green. The electric field of the laser light is parallel to the table, the beam width is controlled using an aperture and two lenses. P polarised 1064 nm light is selected using a polariser. The incoming beam is at  $45^\circ$  from the surface normal, due to the refractive index of the electrolyte the angle changes to about  $30^\circ$  off the surface normal. The fundamental 1064 nm beam is blocked after the sample. P polarised 532 nm light is selected by a second polariser. The polarisation of the 532 nm light is rotated using two mirrors, one mirror is above the other and rotated  $90^\circ$  around the plane of the table with respect to the lower mirror. The detector measures the second harmonic beam generated at the gold surface.

The average beam power was 100 mW impinging on an area of approximately  $0.5 \text{ mm}^2$ . The fundamental impinged on the cell window at an angle of  $45^\circ$  which corresponds to an angle of incidence onto the SAM coated electrode of  $\sim 32^\circ$ . Figure 3.4 illustrates the experimental set up. In this thesis all SHG experiments are performed using pp polarisation.

### 3.2.4 Scanning Tunnelling Microscopy (STM)

The tip is controlled using piezo crystals, which can expand and contract when a current flows through them (subchapter 2.4). The crystals expand by about 1 Å per mV allowing very high precision. Piezo crystals for each of the x, y and z coordinates can be operated independently. Using the z piezo the tip slowly approaches the surface until a predetermined current is reached. In constant current mode, a current is selected, the tip scans across the surface, feedback loops move the tip up and down maintaining the constant current. The movement of the tip is plotted. The resulting image is a convolution of topographical features and electronic states of the surface.

Vibrations, temperature fluctuations or electronic interference can disturb the STM. These factors must be eliminated in order to achieve good resolution, and high quality images. The instrument used is a Molecular Imaging Pico SPM operated in constant current mode, at room temperature in air. The tip is a Pt/Ir 80/20 wire 0.25 mm diameter cut with sharp pliers. The STM, containing the sample and tip are mounted on a foam covered platform supported by 4 elastic cords. The platform is held inside an insulated box which is operated in a quiet and air conditioned room. Typical starting tunnelling conditions are 1.0 V and 500 pA (tip is positive).

## 3.3 System Characterisation

### 3.3.1 Data Acquisition

In order for electrochemistry to be correlated with nonlinear optics the data acquisition has to be such that the data acquisition for each technique is measured against a common time clock. This was achieved by using a computer with LabVIEW (National Instruments) software, which controls both the potentiostat and SHG data acquisition. The computer runs a time clock while communicating with the potentiostat and SHG detector. Data points for both techniques are collected and referenced against the common time clock. Current and potential data points were recorded at an average interval of 60 ms. SHG data points represent an average of 100 shots each and were recorded at an interval of 220 ms. Where cyclic voltammograms and SHG were recorded in parallel a typical scan rate of 20 mV/second was used to ensure an adequate density of data points of the SHG signal during thiol desorption. Experiments were

performed at a room temperature of 16°C. Relationships such as current over potential, SHG over potential or charge over coverage are calculated from the raw data using Origin (OriginLab Corporation) data evaluation software.

### 3.3.2 Surface Area Determination

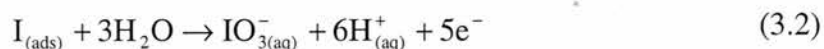
The actual surface area of a metal is always greater than the geometric area when features such as step edges, pits and adatoms are present. This deviation from an ideally flat surface is accounted for by the unitless roughness factor which is defined:

$$\text{Roughness} = \frac{\text{actual sample area}}{\text{geometric sample area}} \quad (3.1)$$

The actual surface area of a sample is an important parameter for the assessment of desorption charges, molecules can adsorb on the surface in 3 dimensions when permitted by the surface morphology. Figure 6.6 highlights the extent to which surfaces, which appear smooth macroscopically, are rough nanoscopically.

Various schemes exist to determine the actual surface area and surface roughness including gold surface oxide reduction<sup>81,129-132</sup>, lead under potential deposition (upd) on gold<sup>76,133</sup>, and on silver<sup>10</sup>, iodine desorption<sup>134,135</sup>, use of radio labelled alkane thiols<sup>136</sup> and STM cross sectional analysis<sup>58,132</sup>.

The potentiometric method, described by Rodriguez et al<sup>134</sup>, involving iodine desorption was employed to calculate the actual surface area and surface roughness of the gold surfaces used in this thesis. The methodology and theory from this paper are outlined here. Samples are immersed in a solution containing iodine, which spontaneously chemisorbs onto the gold surface, chemisorbed iodine covers the surface with a well defined packing. The chemisorption of iodine is limited by the space required to pack the atoms together. It is assumed that the layer contains close-packed but unassociated atoms in a hexagonal arrangement. The charge transfer for the oxidation of chemisorbed iodine is used to determine the surface area:



The average area occupied by a single iodine atom,  $\sigma_{I,calc}$ , is determined using the iodine van der Waals radius ( $r_{vdw}$ ) of 0.215 nm:

$$\sigma_{I,calc} = 2\sqrt{3}r_{vdw}^2 = 0.160 \text{ nm}^2 \quad (3.3)$$

The calculated iodine packing density ( $\Gamma_{I,calc}$ ) is related to  $\sigma_{I,calc}$  by Avogadro's constant ( $N_A$ ):

$$\Gamma_{I,calc} = \frac{1}{N_A \times \sigma_{I,calc}} \quad (3.4)$$

The calculated iodine packing density,  $\Gamma_{I,calc} = 1.04 \text{ nmole cm}^{-2}$ . For a cyclic voltammogram involving the oxidation of a monolayer of iodine atoms, the peak area,  $A_{peak}$ , is integrated, then divided by the scan rate,  $v$ , giving the charge transfer,  $Q$ :

$$Q = \frac{A_{peak}}{v} \quad (3.5)$$

The actual sample area,  $A_{sample}$ , is obtained from the magnitude of the charge transfer for desorption of the layer of iodine atoms:

$$A_{sample} = \frac{Q}{n \times F \times \Gamma_{I,calc}} \quad (3.6)$$

The actual surface area is used to calculate current density values in electrochemical experiments, this assessment is essential to compare electrochemical results for different substrate types with different roughnesses.

The surface areas for both Au/mica and Au/Si surfaces were determined. Samples were prepared by immersing a gold sample in a concentrated iodine / ethanol solution overnight. After removal from solution, samples were rinsed with copious amounts of ethanol and blown dry with an inert gas. Samples were assembled into the electrochemical cell using the procedure detailed in appendix 2. The geometric area of

the electrode exposed to the cell was determined using Vernier Callipers, and is  $54 \pm 3$  mm<sup>2</sup> standard deviation. The electrolyte for the experiments was a 1 M de-oxygenated sulfuric acid solution.

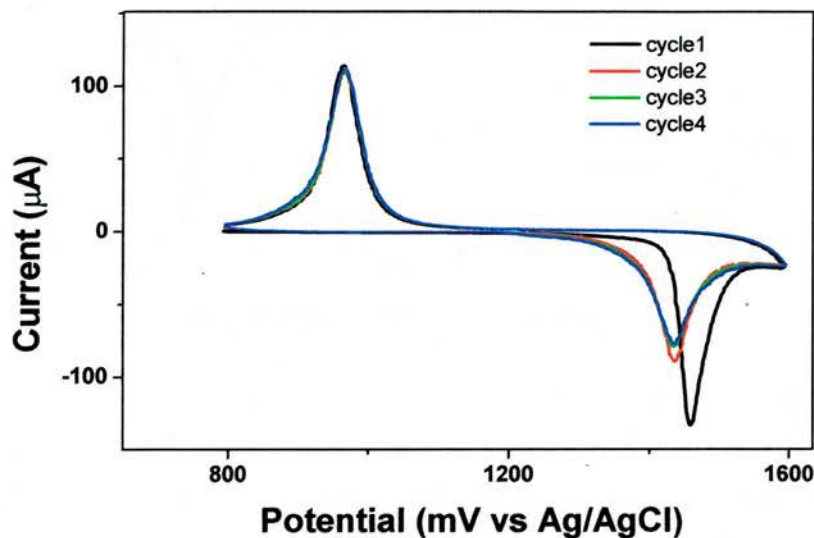


Figure 3.5: Clean Au/mica electrode, 20 mV/second scan rate, 4 cycles from 800 mV to 1600 mV. The gold oxidation peak is on the anodic scan around 1450 mV, the reduction of the gold oxide to gold is on the cathodic scan at 980 mV. Between cycles 1 and 2 the electrochemistry of the gold surface changes irreversibly.

First, a control experiment was performed using a clean Au/mica substrate, the results are depicted in figure 3.5. For cycle 1 there is a gold oxidation peak at 1450 mV and a peak corresponding the reduction of the surface oxide at 980 mV. There is a significant difference in the gold oxidation peaks between cycles 1 and 2 in position and shape. Hamelin et al. have reported that a roughening of a gold (111) surface occurs during the gold oxidation step which disturbs the surface<sup>137</sup>. The proposition is consistent with the results observed here. It is envisaged that the initial gold oxide formation irreversibly alters the surface morphology, this highlights a weakness in the method to determine the surface area using the peak area of the oxide reduction peak.

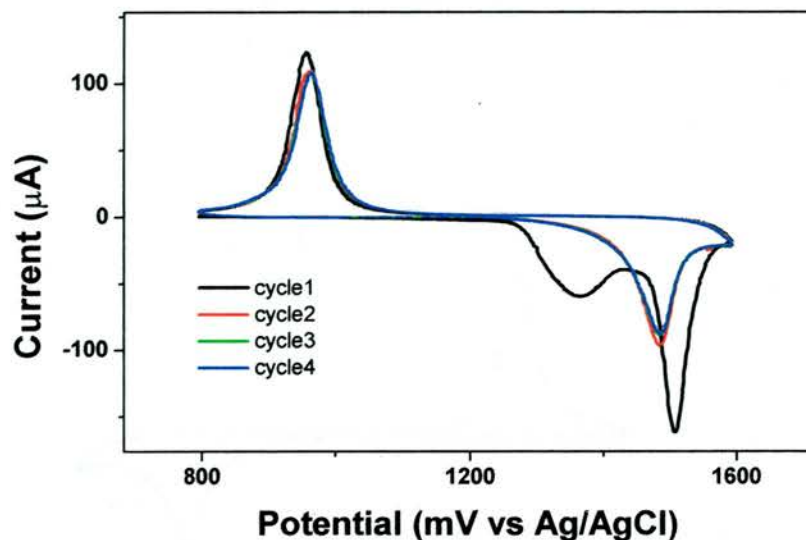


Figure 3.6: Au/mica electrode with chemisorbed iodine layer, 20 mV/second scan rate, 4 cycles from 800 mV to 1600 mV. Iodine desorption in cycle 1 is around 1350 mV, the gold oxidation peak is on the anodic scan around 1450 mV, the reduction of the gold oxide to gold is on the cathodic scan at 980 mV.

Figure 3.6 shows the voltammetric response for an iodine layer on Au/mica. There is an iodine desorption peak on the first cycle around 1350 mV that overlaps with the gold oxidation peak. Rodriguez et al. calculated the area of the iodine desorption peak by subtracting the area of the 'gold oxide' reduction peak in cycle two from the total area of the iodine oxidation and gold oxidation peaks in cycle one. However, due to the irreversible roughening of the surface during gold oxidation, discussed above, this method introduces systematic errors so is not used. An alternative evaluation method is performed. The peak area is first baseline corrected to remove any capacitive charging influences. A Gaussian curve is then fitted to the plot, the area under the curve, using the baseline as the lower boundary for integration, is used to determine the desorption charge. The evaluation method is validated by fitting a Gaussian curve to both the iodine desorption and gold oxidation peaks and ensuring a good fit is achieved, figure 3.7. There is a very good fit using two Gaussian curves.

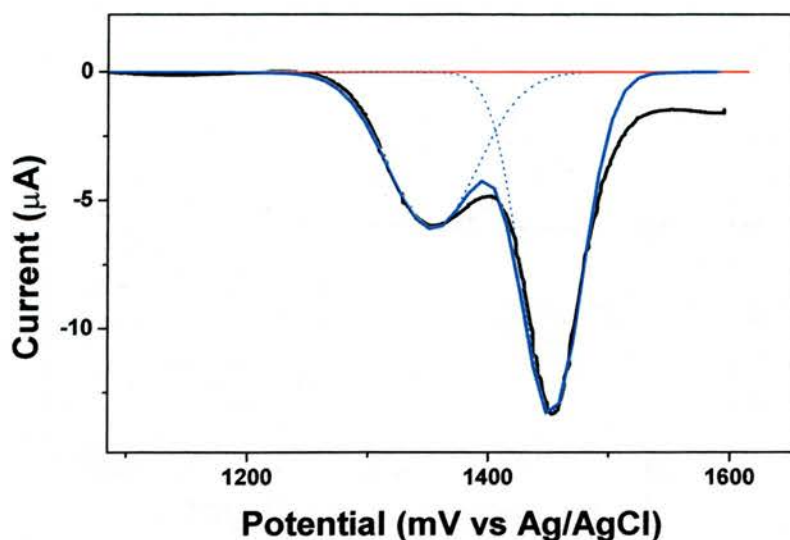


Figure 3.7: Example of an iodine desorption evaluation. The current (black) is baseline corrected (red). Two gaussian peaks (dotted blue) combine (blue) to give a curve that matches very well with the experimental data.

Using equation 3.6 and the evaluation method involving fitting a Gauss curve to the plot, the actual sample areas of four Au/mica samples were determined. They are as follows,  $58 \text{ mm}^2$ ,  $57 \text{ mm}^2$ ,  $55 \text{ mm}^2$  and  $61 \text{ mm}^2$ . The average area is  $58 \pm 2.5 \text{ mm}^2$  standard deviation. Using equation 3.1 the roughness is calculated as  $1.07 \pm 0.07$ .

The same experiments were performed using Au/Si substrate with the aim of determining the actual surface area and the roughness. Figure 3.8 represents two cycles for a Au/Si sample, the oxidation of gold complicates the evaluation of the iodine desorption peak. The presence of faces other than (111) means there is a small gold oxidation peak overlapping with the iodine desorption peak. This can be observed in cycle two in the potential range where iodine desorption occurs. The interpretation of the data to determine the surface area is slightly different due to the overlapping peak. The peak area determined by the Gaussian curve is a combination of two peaks and is therefore systematically greater than the iodine oxidation peak. The area of the Gaussian curve represents the upper limit for the iodine oxidation, the lower limit is a completely flat surface, roughness of unity. The surface area is determined as the mid-point between the upper and lower limits, the error is the maximum and minimum values.

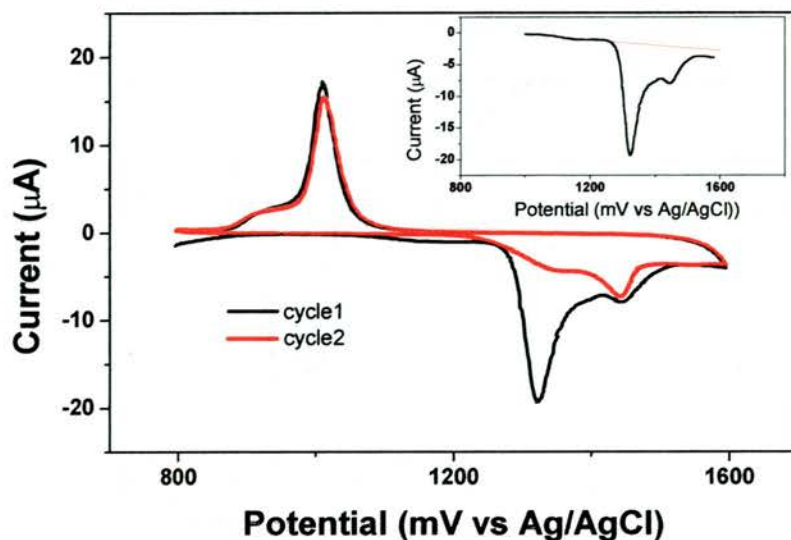


Figure 3.8: Au/Si electrode with chemisorbed iodine layer, 2 mV/second scan rate, two cycles from 800 mV to 1600 mV. Iodine desorption in cycle 1 is around 1350 mV. The gold oxidation peak on the anodic scan around 1450 mV, the reduction of the gold oxide to gold is on the cathodic scan at 1000 mV. The gold oxidation process is more complicated due to the presence of faces other than (111), different faces oxidise at different potentials resulting in overlapping peaks. The inset shows a part of cycle 1 with the baseline used in figure 3.9.

Figure 3.9 represents the baseline corrected peak with the best fit Gaussian curve overlaid. The maximum area, i.e. the area of the Gauss curve corresponds to an area of  $78 \text{ mm}^2$ . An additional experiment for Au/Si, produced a Gauss curve peak area corresponding to an area of  $72 \text{ mm}^2$ , the average of the two results is  $75 \text{ mm}^2$ , this value is considered the actual surface area. Due to the overlapping gold oxidation peak the actual area is expected to be a systematic overestimation. This corresponds to roughness of  $1.4 \pm 0.1$ . The roughness for Au/Si is determined with a lower accuracy and is therefore described with only two significant figures. The actual surface areas for both substrates are summarised in table 3.1.

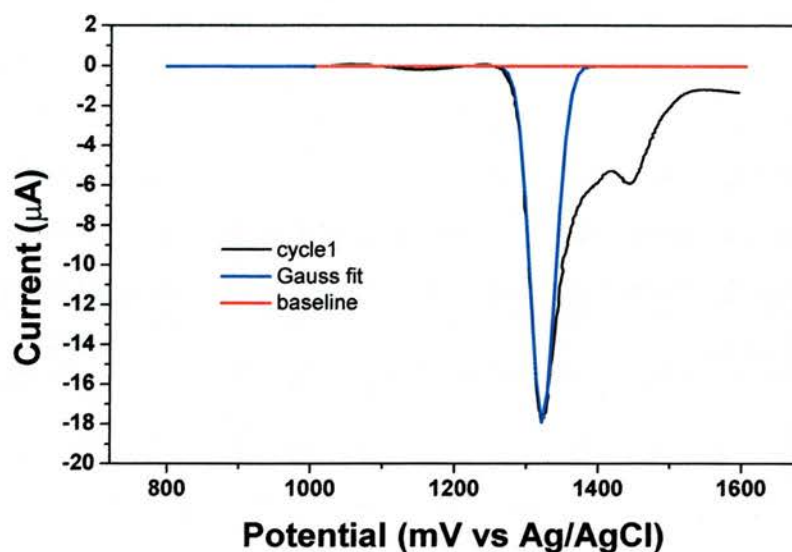


Figure 3.9: Cycle 1 with iodine desorption peak, the best fit Gaussian curve is overlaid.

Surface	area	error	roughness	error
Au/mica	58 mm <sup>2</sup>	2.5 mm <sup>2</sup>	1.07	0.07
Au/Si	75 mm <sup>2</sup>	4 mm <sup>2</sup>	1.4	0.1

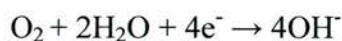
Table 3.1: Summary of peak areas and roughness values for Au/mica and Au/Si.

The Au/mica surface is clearly flatter than the Au/Si surface. The influence of the surface roughness is again compared in subchapter 4.4.1 using cyclic voltammetry and second harmonic generation. The roughness values for annealed Au/mica obtained by other groups using a variety of methods are compared with the values obtained here. Kakiuchi and co-workers report a roughness of  $1.05^{76,133}$ , Porter and co-workers report a roughness of  $1.1 \pm 0.1^{58,135}$ , Tao et al report a roughness of  $1.2^{87}$ , Schlenoff et al report a roughness of  $1.15 \pm 0.05^{136}$  and Losic et al report a roughness of  $1.11 \pm 0.05^{132}$ . The experimentally determined roughness value of  $1.07 \pm 0.07$  for annealed Au/mica is below the average roughness value for similar substrates suggesting a very high quality of substrate. Au/Si surfaces are now examined. Porter and co-workers report a roughness of  $1.5 \pm 0.2$  using iodine desorption and, for the same substrate,  $1.18 \pm 0.05$  using STM<sup>138</sup>. The experimentally determined roughness value of  $1.4 \pm 0.1$  for Au/Si agrees very well with published data. The roughness values for a gold (111) single crystal reported in literature are summarised. Wan et al report a roughness of 1.04 for Au (111) single crystal using a surface oxidation method<sup>84</sup>, Morin and co-workers

report a roughness of  $1.0 \pm 0.1$  for Au single crystal using lead upd<sup>90</sup>, Leopold et al report a roughness of  $1.1 \pm 0.05$  using lead upd<sup>139</sup>. The average roughness for Au single crystal from these three references is 1.05. The roughness value for a gold single crystal is closer to Au/mica than Au/Si, and hence, based on roughness values the surface quality of Au/mica is comparable to a gold single crystal. All current density values and charges reported in this thesis are calculated using the actual surface areas reported here, not the geometric area.

### 3.3.3 Influence of Oxygen

The presence of trace amounts of oxygen in the electrolyte has a deleterious effect on the quality of the resulting cyclic voltammograms due to oxygen reduction producing large currents. Oxygen reacts according to a 4 electron process<sup>140</sup>:



The limiting step is the diffusion of dissolved oxygen to the working electrode surface. Oxygen reduction drives large currents in the same potential range as thiol desorption peaks and can therefore can severely alter thiol reductive desorption peaks.

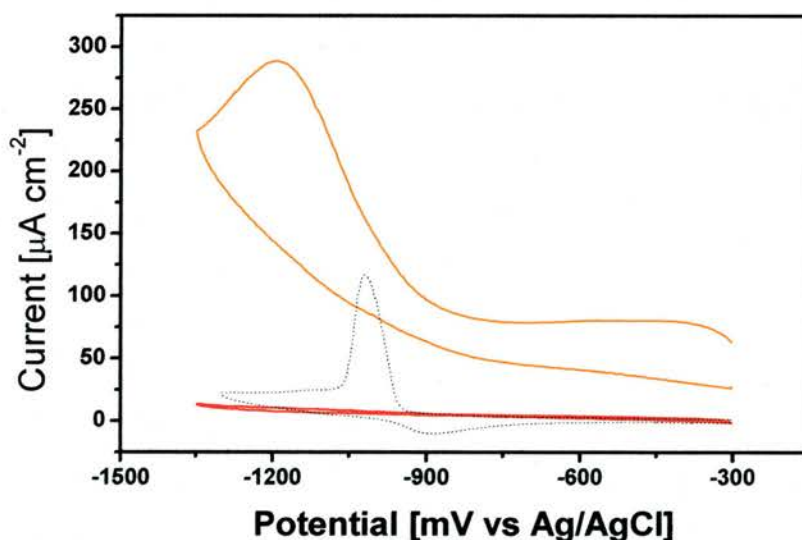


Figure 3.10: CVs for Au/mica substrate at 50 mV/second in the clean state with oxygen purging (orange) and argon purging (red) and a substrate modified with BP4 at 70°C (dotted line). The charging due to oxygen is  $2.9 \text{ mC cm}^{-2}$  for the entire first cathodic scan of the oxygen purged sample, this compares to a charge of approximately  $100 \text{ } \mu\text{C cm}^{-2}$  for the BP4 desorption.

Figure 3.10 compares the cyclic voltammogram of a clean gold substrate in an oxygenated electrolyte with the cyclic voltammogram for a thiol desorption, where the electrolyte is purged with argon for around twenty minutes, and the cell is purged in an inert atmosphere glove box for twenty minutes. The reductive current due to the presence of oxygen on the cathodic scan only is 29 times greater than the desorption peak for a BP4 SAM in a purged electrolyte. For thiol desorption experiments, the desorption peak occurs in the same potential range as the oxygen peak, oxygen influences cannot be distinguished for molecular desorption for this case, clearly oxygen must be eliminated. Prior to injection of purged electrolyte the cell is purged in an inert atmosphere glove box for a minimum of 45 minutes.

### 3.3.4 Data Evaluation

For a thiol reductive desorption peak, the baseline is first fixed at the cathodic side of the peak at a position that is most clearly the point where the peak ends. The other end of the baseline is then brought towards the anodic side of the desorption peak until the baseline becomes a tangent to the cyclic voltammogram, figure 3.11.

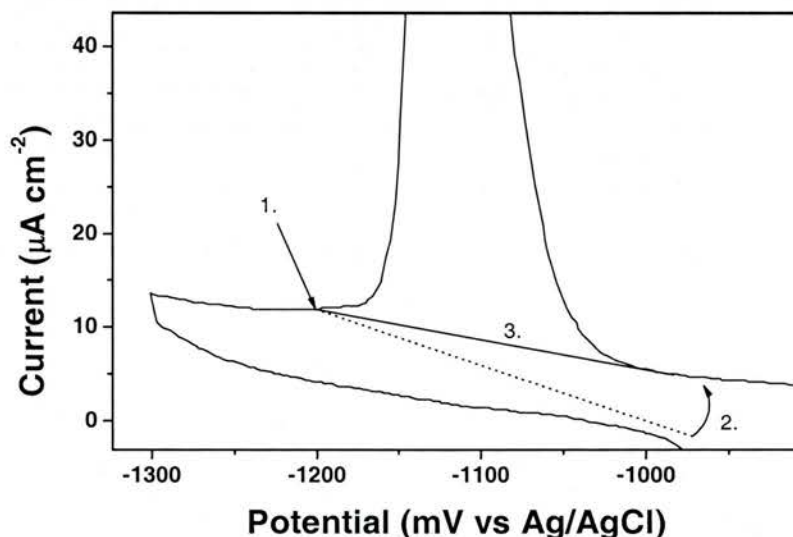


Figure 3.11: Exemplary CV showing steps taken to generate the baseline for a desorption peak. A point is selected on the cyclic voltammogram immediately after the peak (1). The baseline is generated, and is rotated around the selected point (2) until it touches the cyclic voltammogram at a position immediately prior to the desorption (3).

The errors involved in the procedure originating from the selection of the original point at the cathodic side of the peak are examined in figure 3.12. Five points are selected

approximately 25 mV apart as the starting point to generate the baseline. For each baseline the above procedure is applied to fix the anodic end of the baseline to the cyclic voltammogram, the corresponding charges are calculated and reported in table 3.2.

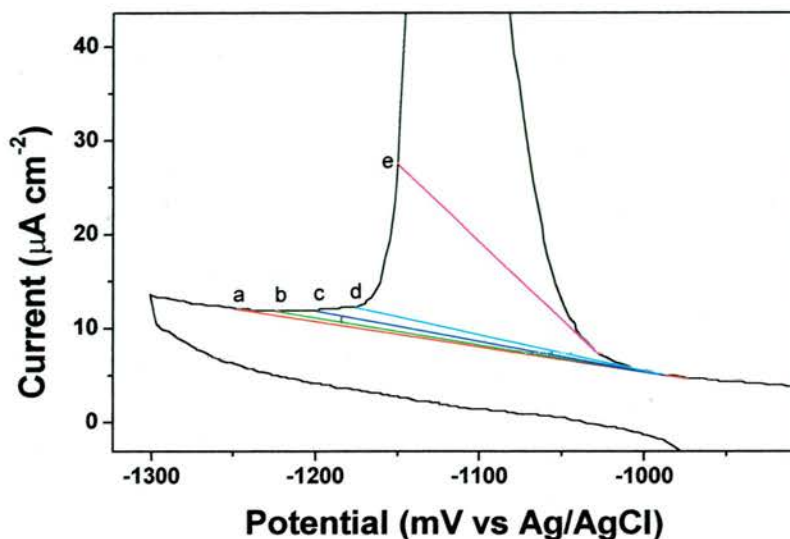


Figure 3.12: CV with five baselines selected for the integration of the peak approximately 25 mV apart.

baseline	left intersect (mV)	right contact (mV)	charge ( $\mu\text{C cm}^{-2}$ )
a	-1248	-974	114.1
b	-1224	-987	112.9
c	-1199	-987	111.1
d	-1175	-991	108.7
e	-1150	-1027	85.5

Table 3.2: Charge transfer for the desorption peak using the five baselines presented in figure 3.12. (The sample is BP3 prepared at 70°C on Au/mica.)

The evaluation relies on a consistent approach for every sample examined and is to some extent a question of judgement. Position 'c' is judged to be the most accurate, for a deviation of 25 mV in either direction along the cyclic voltammogram there is only a 2% change in the peak area. This careful and consistent evaluation gives a high precision allowing comparison of desorption charges for different thiol SAMs. The charge transfer as the desorption progresses is followed for correlation with SHG:

$$q(E) = \int_{E_i}^E \frac{i(E)}{v} dE \quad (3.7)$$

Equation 3.7 relates the coverage determined by SHG with the charge transfer.  $Q$  is the charge,  $i$  the current,  $v$  is the scan rate,  $E$  is the potential. This evaluation procedure is applied to all peak area evaluations throughout this thesis.

### 3.3.5 Detector Linearity Range

The performance of the detector is a crucial factor in the overall performance of the SHG system, the detector consists of a monochromator and a photo multiplier tube. The monochromator selects a specific frequency of photons which then enter into the photo multiplier tube where they are converted into photoelectrons which are amplified in a cascade. An amplification of about six orders of magnitude occurs before a current is measured. The detector is extremely sensitive allowing single photon detection. There is however the possibility that with large currents, the linear relationship between photons entering the detector and the measured signal intensity is broken. This is an obviously undesirable outcome and the detector must be tested to establish the operating conditions where there is no adverse saturation of the photo multiplier tube distorting the results. The linear relationship between photons entering the detector and the measured signal intensity is essential for routine use.

A series of experiments were performed to establish the region where the detector operates in the linear regime. The second harmonic beam intensity is proportional to the square of the impinging laser power, any deviations from this relationship indicate that the photo multiplier tube is becoming saturated. The photo multiplier amplification setting was adjusted to 780 units. The maximum setting of 1000 corresponds to an amplification of 1250 Volts in the photo multiplier tube. The power of the infrared beam impinging on the sample surface was varied while the measured SHG intensity was recorded. The square root of the SHG intensity is plotted against the laser power, figure 3.13. There is a linear relationship between the square root of the SHG and the power of the impinging beam.

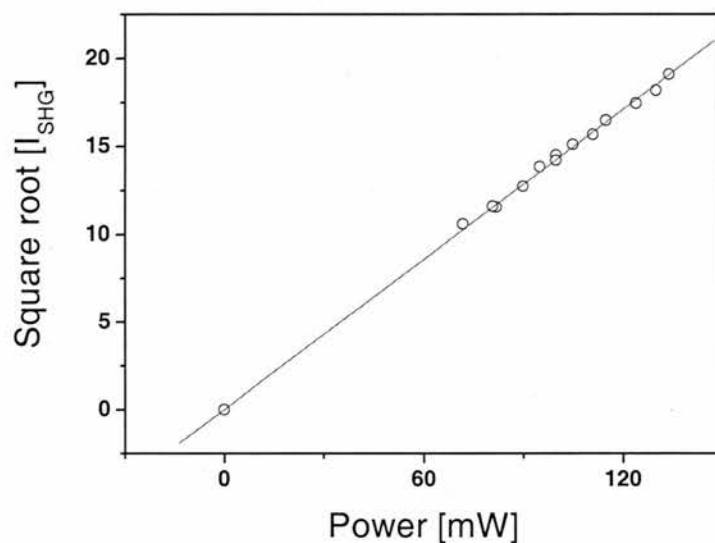


Figure 3.13: Square root of the SHG over the laser power. Photo multiplier amplification is set to 780 units. Line of best fit passing through the origin is displayed. A data point at the origin is included.

For the experiment performed with the photo multiplier amplification set at 780 units, all points were within the range of linearity. The greatest magnitude measured had an intensity of 330 SHG units. The limit of linearity is therefore greater than 330 SHG units. This provides a generous window in which to operate, it was not necessary to probe higher amplifications. All measurements using SHG were kept within the range of linearity, typically the maximum SHG intensity would be around 100 units and the photo multiplier setting was maintained at 750 units.

### 3.3.6 SHG Increase Reproducibility

During cyclic voltammetry with in-situ SHG, the gold electrode is scanned to negative potentials, when the electrode becomes sufficiently negative, adsorbed molecules will desorb, changing the surface polarisability, resulting in an increase in the SHG intensity as described in subchapter 2.3. The reproducibility of the SHG increase is examined for twelve identically prepared hexadecanethiol samples with a view to a rigorous statistical analysis of the variation in SHG signal increase for the desorption process. The average plot of the combined results is then compared with the SHG signal for a bare gold surface to confirm that the SHG response after thiol desorption is identical to the bare gold response.

Due to the different scan rates, the position where the SHG increases varies slightly, however, the starting and final SHG intensities are independent of the scan rate. For all twelve results the cathodic scan was selected and placed in a single graph. The plots were normalised to region where thiols had desorbed because every sample should be identical in this region. There may then be small differences in the initial signal intensity due to small differences in coverage or very slight variations in beam alignment. Individual plots were adjusted by scaling all values up or down using a normalisation function. An average of the twelve plots was generated and overlaid onto the twelve plots as shown in figure 3.14. The individual plots were finely adjusted so that each plot was the best fit with the average line plot in the region after desorption, i.e. from  $-1220$  mV to  $-1300$  mV. The average was then regenerated using the new positions. This iterative process was repeated three to four times until all plots were perfectly aligned in the region from  $-1220$  mV to  $-1300$  mV.

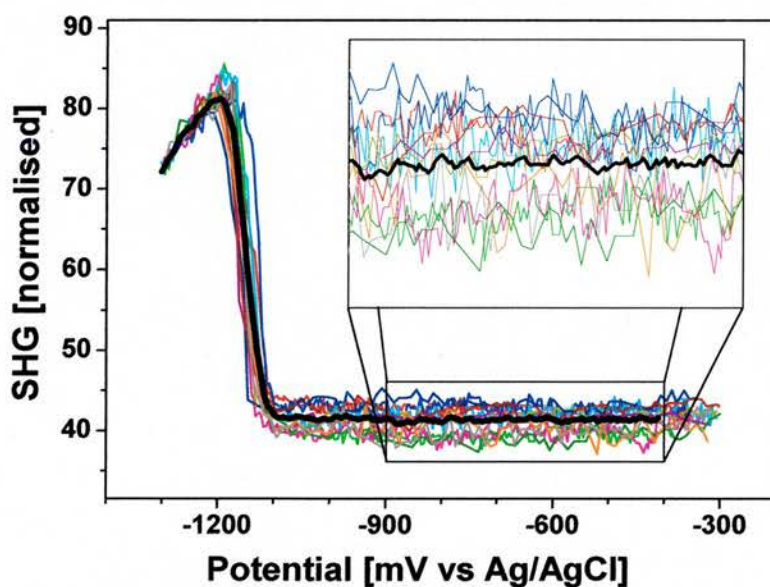


Figure 3.14: The SHG against potential for twelve different MC16 desorption experiments, using  $0.5$  M  $\text{KOH}_{(\text{aq})}$  electrolyte, with scan rates from  $10$  mV/second to  $50$  mV/second all prepared at  $22^\circ\text{C}$  are compared. The bold black line is the average curve. The individual plots were scaled up or down until the data points in the region from  $-1220$  to  $-1300$  mV best fit the average line. The inset shows the region from  $-400$  to  $-900$  mV.

In the region where the monolayer is intact ( $-300$  to  $-1000$  mV) the average intensities are no longer all fitting with the average plot. This may be due to small differences in coverage or very slight variations in beam alignment. The average SHG intensities for

the 12 samples in the region where the monolayer is intact were determined, and are as follows:

$$X_{1-12} = 39.5, 39.6, 39.9, 40.4, 40.4, 41.7, 41.8, 42.1, 42.7, 42.8, 42.9, 43.6.$$

Using the statistical analyses described in appendix 3 the mean value and standard deviation for the starting SHG intensity were calculated:

$$\bar{X}_{12} = 41.4 \quad \text{Standard deviation} = 1.43$$

Standard deviation expressed, as a percentage of the average value is 3.4%. The twelve plots are now represented with a single average plot with error bars  $\pm 3.4\%$  indicating one standard deviation, figure 3.15. The 'b' value (equation 2.14) for this plot is  $-0.28$ .

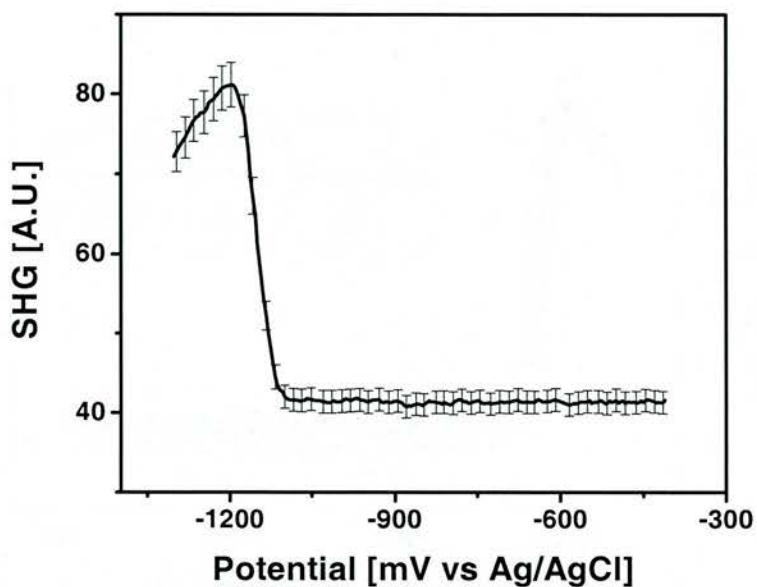


Figure 3.15: Standardised plot representing the desorption of hexadecane thiol from Au/mica prepared at room temperature. The plot is the average of 12 linear sweep voltammograms, error bars are  $\pm 3.4\%$  and indicate one standard deviation.

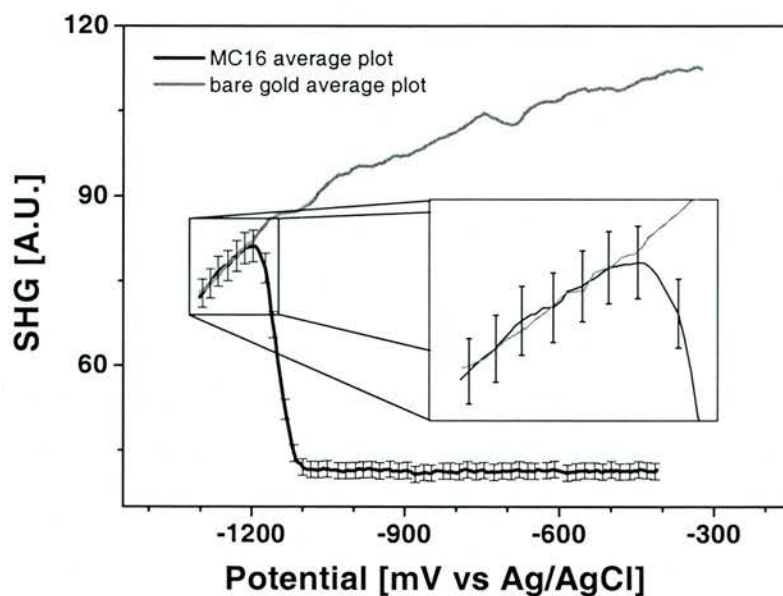


Figure 3.16: Hexadecane thiol is compared with bare gold. The inset shows the region between  $-1150$  mV and  $-1320$  mV. The SHG for the hexadecane thiol in the most negative region is exactly the same as the SHG for a bare gold sample.

The standardised plot for hexadecane thiol on Au/mica prepared at room temperature is compared with bare gold. Figure 3.16 demonstrates that after the thiol molecules desorb, the SHG response is, within the experimental uncertainty, identical to the response for a bare gold surface. In summary, the SHG increase is highly reproducible, with a standard deviation of only 3.4%. The SHG, after molecules have desorbed, is identical to the SHG for a bare gold surface.

---

## Chapter 4

### RESULTS

#### 4.1 Homologous Series: Spacer Group Influence

##### 4.1.1 Alkane Thiols

The alkane thiol homologous series is assessed using cyclic voltammetry with in-situ SHG. Alkane thiols as depicted in table 2.1 are examined. Alkane thiols are the simplest class of molecules that could be investigated, they represent the most fundamental case of SAMs. In the generic SAM model, figure 1.1, containing a head group, spacer and tail group, examining the alkane thiol homologue series represents a systematic study of the spacer group influence on the structure and bonding of alkane thiols.

The CV and SHG for the reductive desorption for selected alkane thiols in the homologue series is shown in figure 4.1. Thiols examined in the range from MC7 to MC22 are displayed. Results for MC2 and MC4, exhibited multiple peak features which are not understood and therefore the results are not displayed. The results display clear differences in peak shape and position. The SHG response parallels the peaks, the SHG increase begins at the onset of the desorption peak and ends at the completion of the peak. A more rigorous assessment of the SHG to electrochemistry correlation is performed after the quantitative assessments of the electrochemical results. The SHG overshoot for MC16 and MC22 is noted, this is systematic for long chain alkane thiols. The peak shape, desorption potential and desorption charge are assessed using the criteria described in chapter 2.2.3, additionally, the readsorption process is examined by determining the readsorption charge. The peak shapes for the alkane thiol series are examined first, considering the simple chemical structure, the peak shape trends are complex, exhibiting three distinct regions. While MC7, MC8 and MC10 all display reasonably symmetrical single peaks, MC16 has a double peak structure. Surprisingly, MC22 has, again, a single peak. The transition between MC10 and MC16 from a single peak to double peaks is established<sup>135</sup>, although the reasons for this are controversial and are discussed in more detail in chapter 5.

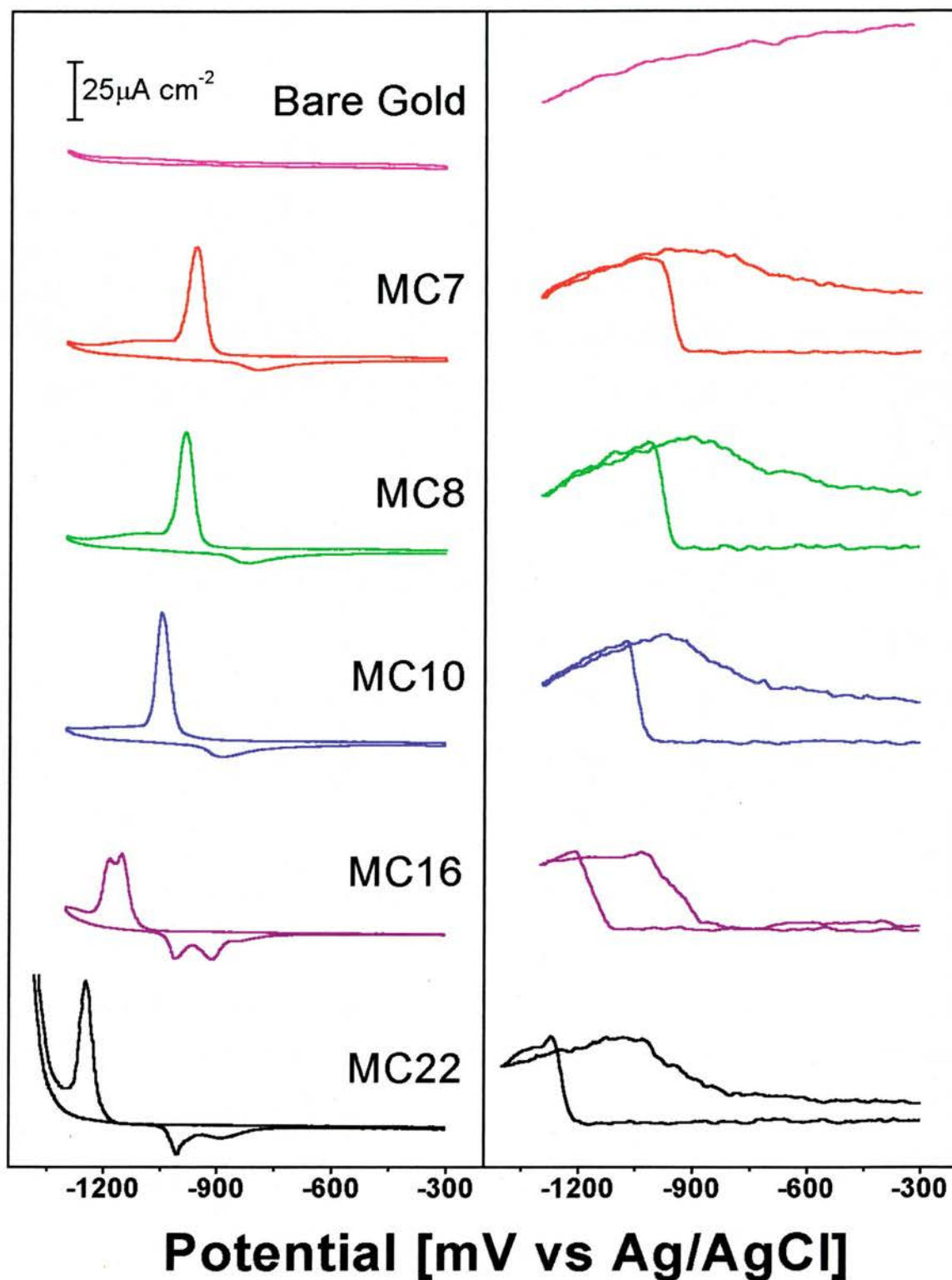


Figure 4.1: CVs (left) and SHG (right) for bare gold, MC7, MC8, MC10, MC16 and MC22 at 20 mV/second. All SHG plots are normalised to the bare gold plot in the region where thiols have desorbed. The starting SHG intensity for all samples lies between 36% and 39% of the SHG intensity for bare gold at  $-300$  mV. Samples were prepared at  $22^\circ\text{C}$  and experiments were performed at  $16^\circ\text{C}$ .

The transition from MC16 to MC22 from double peaks to a single peak is a new and important observation as previous studies in literature have only extended to MC18. A detailed discussion on this phenomenon is given in the following chapter with specific reference to the desorption process that is consistent with these observations. The readsorption peak shapes are of interest. MC7 to MC10 display single readsorption peaks with readsorption position shifting to more negative potentials for longer molecules. MC16 and MC22 have double readsorption peaks. For MC16 the separation of the peaks is about 80-100 mV, whereas MC22 has a separation of about 100-120 mV. Interestingly the first readsorption peak for MC16 and MC22 overlap. The fact that MC22 has a double readsorption feature and a single desorption peak is interesting, and raises questions about the desorption mechanism.

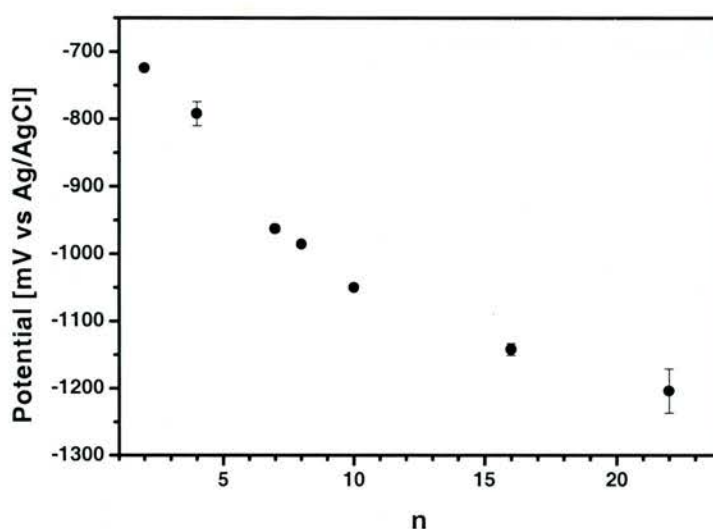


Figure 4.2: Desorption potential for alkane thiols plotted over the number of carbon atoms in the alkane chain. The potentials for the main desorption peak for MC2 and MC4 are included. Error bars indicate one standard deviation.

The desorption peak potential with respect to alkane chain length is examined. There is a general trend for longer molecules to desorb at more negative potentials, figure 4.2. longer molecules are more stable due to greater intermolecular interactions and increased ability to impede ion penetration and screen the electric field. There is a nonlinear relationship between the desorption potential and the number of carbon atoms in the chain. The desorption potential change is 40 mV per methylene unit in the range from MC2 to MC10, in contrast to 13 mV per methylene unit in the range from MC10 to MC22. The interaction between alkane chains stabilises the layer, there are several

factors which enter into the energy balance. There is a greater tendency for shorter molecules to be in a disordered state. Longer molecules form more crystalline layers with a greater degree of order. It is likely that in shorter molecules the disorder of the alkane chain packing is manifested as a less stable desorption. This is an important study, which has conclusions that may be relevant for other molecule systems, which straddle order / disorder regimes.

These results were compared with data from other groups. Kakiuchi et al report a desorption potential change of 40 mV per methylene unit in the range from MC3 to MC10, and 8 mV per methylene unit in the range from MC10 to MC16<sup>76</sup>. The same gold on mica substrate type was used, but preparation conditions were slightly different, samples were annealed in deoxygenated pure water for 5 hours at 70°C. Salvarezza and co-workers, using gold evaporated on glass, report that for three SAMs, MC3, MC6 and MC12 there is a desorption potential change of 35 mV per methylene unit<sup>77</sup>, a close inspection of the plot reveals there is a nonlinear relationship consistent with the observation in figure 4.2. Porter and Zhong report a desorption potential change of 25 mV per methylene unit<sup>135</sup>. Overall there is some variation with the reported values, but considering differences in experimental conditions the general trends are in good agreement. Of these three groups, the data in figure 4.2 best agrees with the recent work by Kakiuchi<sup>76</sup>. The data can be interpreted as a manifestation of the extent of ordering discussed in subchapter 2.1.1. Longer alkane thiols produce SAMs with well ordered, crystalline structures, whereas shorter alkane thiols produce SAMs with less crystalline packing. Extrapolating the desorption potential for zero carbon units using the MC10 to MC22 region, SAMs gives a desorption potential of -920 mV vs. Ag/AgCl. Interestingly Salvarezza and co-workers note that atomic sulfur desorbs at a potential of -920 mV vs. SCE, equivalent to -878 mV vs. Ag/AgCl<sup>77</sup>. The desorption of monatomic sulfur is consistent with the trends for the desorption of well ordered, crystalline SAMs. Despite having potentially very different bonding with the substrate the stability is remarkably close to the extrapolated value for MCn with n = 0.

The charge transfer for the reductive desorption is examined next. The charge transfer comprises faradaic and capacitive components. For a ( $\sqrt{3} \times \sqrt{3}$ ) monolayer, assuming a one electron desorption process, the faradaic charge for a complete coverage is 74  $\mu\text{C cm}^{-2}$ . It must be noted that domain boundary regions have a lower density of molecules

and therefore it is improbable that a faradaic component of  $74 \mu\text{C cm}^{-2}$  would be attained. The capacitive current for each alkane thiol is determined by the difference in capacity between the bare gold and the thiol covered gold. The measured charge for desorption is the sum of the faradaic and capacitive contributions. The charge for each SAM was determined by integrating the desorption peaks using the procedure described in subchapter 3.3.4, the results are presented in figure 4.3.

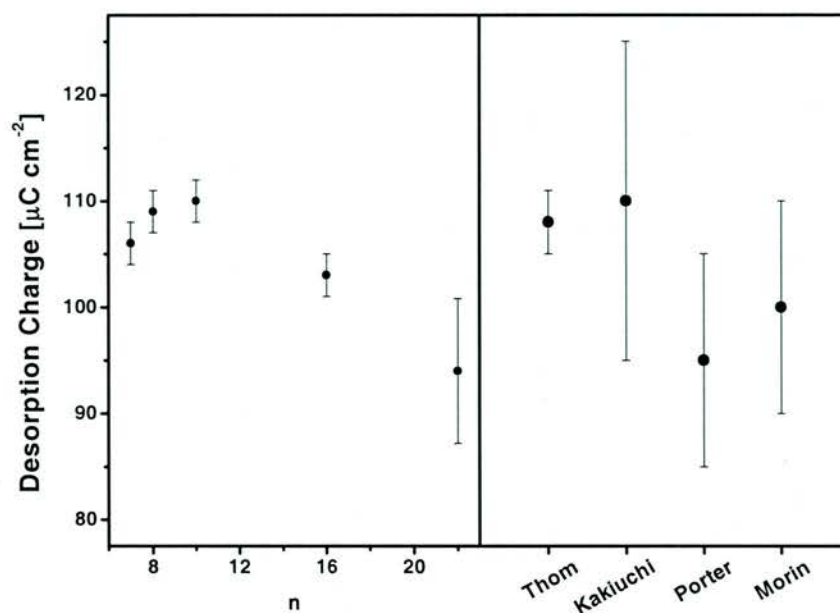


Figure 4.3: Relationship between charge and the number of carbon atoms in the alkane chain for samples prepared at  $22^\circ\text{C}$  (left). The data is compared with charges determined by other groups (right), details are in the text. Error bars are one standard deviation.

Note that MC16 and MC22 desorb in the potential range where hydrogen evolution is a significant factor, there is an additional error in determining the peak areas. There is potential for a systematic error due to the overlapping of two processes as well as the random error. The recorded values for MC16 and MC22 are systematically lower than the values for the shorter SAMs. It is likely that lower charge is due to the baseline selection rather than a real decrease in coverage. The SHG data for these systems are cross-referenced with the CV data to test this hypothesis, figure 4.1. The starting coverage, determined by SHG, for MC16 and MC22 is equivalent to the coverage for MC7, MC8 and MC10. This is clear evidence that the co-evolution of hydrogen introduces errors into the peak area determination, and leads to a systematic underestimation of charge transfer for longer SAMs. For these reasons the average charge transfer magnitude is calculated using data from the shorter SAMs. The charge

transfer magnitude of  $108 \pm 3 \mu\text{C cm}^{-2}$  attained, this is the mean value and standard deviation of MC7, MC8 and MC10 values combined. The charge of  $108 \pm 3 \mu\text{C cm}^{-2}$  is taken as the overall charge transfer for desorption of alkane thiols. The average charge of  $108 \pm 3 \mu\text{C cm}^{-2}$  is compared with results from other groups. Kakiuchi et al report a charge transfer of  $110 \pm 15 \mu\text{C cm}^{-2}$  for a range of alkane thiol molecules<sup>76</sup>, noting that the charge “did not appreciably depend on the chain length”. Porter and Wong cite a charge  $104 \pm 11 \mu\text{C cm}^{-2}$  for MC16<sup>58</sup> although the total is not corrected for the roughness. Correcting for a roughness of 1.1 that they provide gives the value  $95 \pm 10 \mu\text{C cm}^{-2}$ , which is plotted in figure 4.3. Morin and co-workers report a charge transfer of  $100 \pm 10 \mu\text{C cm}^{-2}$  for the reductive desorption of nonanethiol<sup>141</sup> and hexadecane thiol<sup>59</sup>. The charge transfer value of  $108 \pm 3 \mu\text{C cm}^{-2}$  is in excellent agreement with values reported by other groups and the errors are notably smaller.

The total charge is the sum of the faradaic and capacitive contributions. The faradaic charge for a complete coverage is  $74 \mu\text{C cm}^{-2}$ , however, it is not likely that a complete coverage will be achieved due to packing faults at domain boundaries. Comparison of charge transfer values for samples prepared at  $22^\circ\text{C}$  and  $70^\circ\text{C}$  (subchapter 4.1.2) and relating these values to the domain size model, figure 2.7, suggests that the coverage for a sample prepared at  $22^\circ\text{C}$  could be about 90%. The faradaic charge for a sample with 90% coverage will be  $67 \mu\text{C cm}^{-2}$  and the capacitive contribution will be  $41 \mu\text{C cm}^{-2}$ . The capacitive contribution is approximately 38% of the total desorption charge. Kakiuchi reports a capacitive charge of  $42 \mu\text{C cm}^{-2}$  noting that the “double-layer charging current can amount to one-third of the charge calculated from the area of the peak of the reductive desorption”<sup>76</sup>. The results obtained here are in excellent agreement with the literature values. The overall capacitive charge is dominated by the charge of a bare gold electrode, which is about an order of magnitude greater than the differences between different SAMs, so differences in capacity for different length alkane thiols result in overall charge transfer differences that are smaller than the experimental errors.

The peak widths for the reductive desorption for alkane thiols are assessed, full width at half maximum (FWHM) values and asymmetry factor are given in figure 4.4.

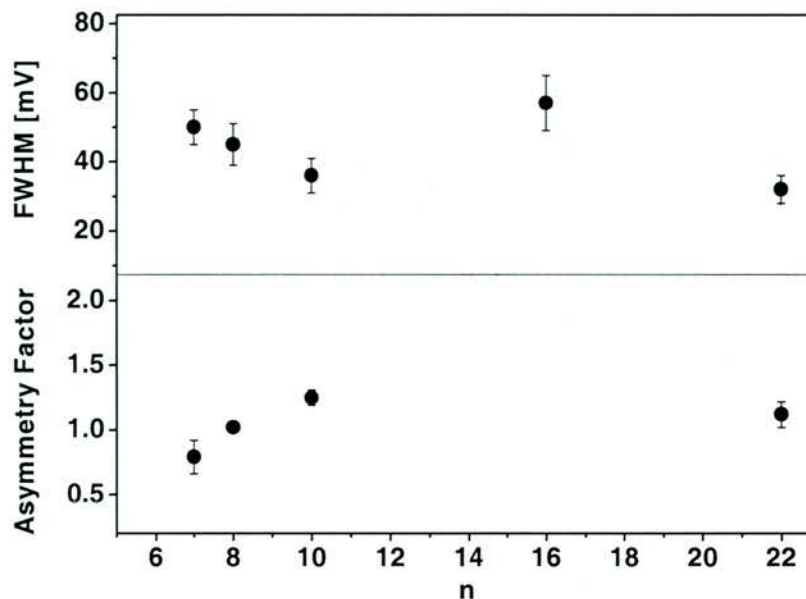


Figure 4.4: FWHM values (top) and asymmetry factor (bottom) for alkane thiols, error bars are one standard deviation.

The FWHM values show a trend of narrowing peaks from MC7 to MC10. MC16 has double desorption peaks, the recorded width is the width of both peaks. MC22 has a narrow single peak, the reasons for the narrowing of the peak are related to the desorption mechanism and are discussed in chapter 5. Within the range of MC7 to MC10, the peak width is a measure of the uniformity of the SAM, narrow peaks are indicative of highly ordered, uniform SAMs. The trend from MC7 to MC16 is an increasing uniformity, due to increasing interactions between alkane chains. MC16 has double peaks, the desorption process is affected by intermolecular interactions increasing the time required for desorption. The FWHM values observed by Kakiuchi et al follow the same trend<sup>76</sup>, for longer molecules to have narrower peaks, from MC3 to MC10 the FWHM approaches 20 mV, from then on it remains constant. The sample preparation involved an annealing step after film preparation, and double peaks were not presented for MC16 so the SAMs are different from the ones examined here. Nevertheless, the general trend is comparable, and the narrower peaks can be due to the different preparation conditions. The peaks examined are reasonably symmetrical, the asymmetry factor is within  $1 \pm 0.25$  for all of the alkane thiol peaks, MC16 is excluded from this because it has double peaks.

The degree of solubility of the series of alkane thiols is partly indicated by the readsorption charge, figure 4.5. In general, the readsorption charge is greater for less soluble molecules.

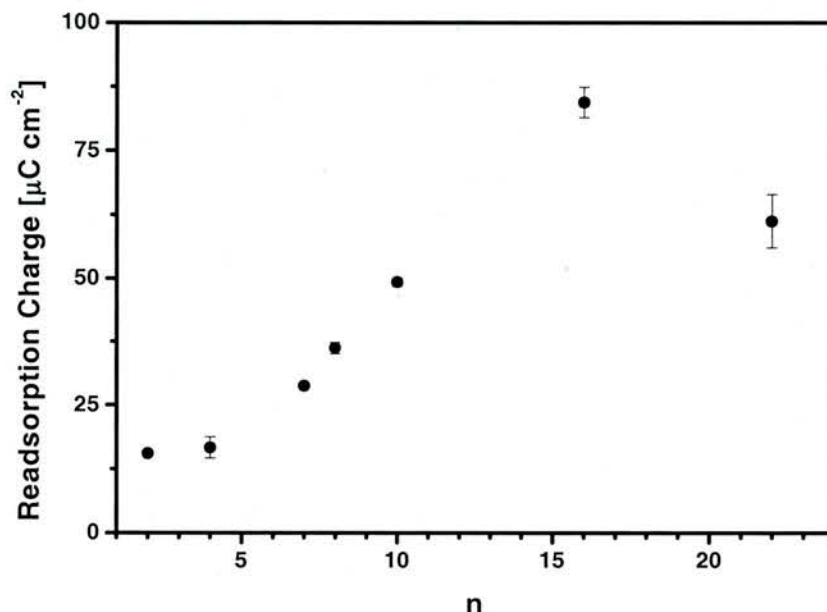


Figure 4.5: The readsorption charge for various length alkane thiols. Error bars are one standard deviation. In some cases the data point hides the error bars.

The readsorption charges are compared with the average desorption charge of  $108 \mu\text{C cm}^{-2}$ . There is a large range of results, MC2 has 16% readsorption compared to 78% for MC16. Between MC2 and MC8 there is an average increase of readsorption ratio of 3% per methylene unit, from MC8 to MC16 the average increase is 4.5%. MC16 has a readsorption of 78% on the first cycle but a readsorption of from 97% to 100% on all subsequent cycles. It is interesting to note that the large readsorption charge is accompanied with the occurrence of double readsorption peaks. Between MC16 and MC22 there is a decrease in the extent of readsorption, MC22 has only 57% readsorption. It could be argued that there was a lower starting coverage for MC22, as depicted in figure 4.3, however using these values for the calculation, the extent of readsorption for MC16 and MC22 is 82% and 65% respectively. Additionally, the SHG points to an incomplete readsorption for MC22. There is an unambiguous difference in the extent of readsorption between MC22 and MC16, with MC16 readsorbing to a greater extent. This points to sterical constraints rather than a partial solubility. The geometry of the cell has some consequences for the experiment, the desorption of a monolayer of molecules into a small volume of electrolyte ( $100 \mu\text{l}$ ) means the

electrolyte has an average concentration of thiols in the solution of the order of 5  $\mu\text{M}$ . Even a completely soluble molecule will readsorb to some extent in these circumstances. So two factors, solubility and diffusion must be considered when interpreting the results. Longer molecules will be less soluble; therefore it is likely that they will readsorb to a greater extent. Different molecules desorb at different potentials, and therefore, due to the constant scan range molecules will remain desorbed for different times. MC4 remains in solution for 54 seconds compared to 33 seconds for MC10. Molecules will have time to diffuse into solution leaving a smaller proportion of molecules close to the electrode surface. The extent of readsorption is a measure of both solubility and diffusion for this fixed scan range, tailoring the scan range for each molecule to standardise the diffusion effect would provide a set of data that measures solubility exclusively. Porter and Zhong report about 30% readsorption for MC12 and smaller sharply increasing for longer molecules<sup>135</sup>. Morin and co-workers report that for repeated cycling (from three to a few hundred cycles) for MC16 on a Gold (111) single crystal there is still  $90 \pm 5\%$  of the layer present<sup>59</sup>.

The in-situ SHG results for MC7, MC10 and MC16 represent a sample selection and are compared with the electrochemical results, the charge for desorption is correlated to the coverage determined by SHG. If the SHG signal change predominantly reflects the breaking of the thiol-Au bond (equation 2.12) i.e. monitors the electron transfer upon the reductive desorption of thiols and, thus, the faradaic contribution, the ratio between the desorption charge measured by CV and the thiol coverage derived from the SHG signal yields information about the distribution of faradaic and capacitive currents. If the ratio between capacitive and faradaic currents is constant over the potential range of the desorption peak a linear relationship between thiol coverage (equation 2.13) and the integrated charge (equation 3.7) should be observed. Conversely, a change of this ratio or even a separation of faradaic and capacitive currents should be reflected in a deviation from the linear correlation. The charge for desorption is plotted against the coverage determined by SHG using equations 2.13 and 3.7 for MC7, MC10 and MC16, figure 4.6. The charge vs. potential and coverage vs. potential data sets are collated. The data sets are of different size so charge and coverage can not be directly compared. Data points for charge are interpolated with respect to the potential in the coverage data set allowing a direct comparison of charge with coverage. The coefficient of determinations for the MC7, MC10 and MC16 are 0.984, 0.992 and 0.993 respectively. For each SAM

type, there is a linear correlation between the charge of desorption and the coverage determined by SHG. MC7 and MC10 have a single desorption peak so this result is not surprising. The result for MC16, which has a double peak is more interesting, despite the double peak structure the charge is linearly correlated to the coverage determined by SHG. This is an interesting observation which is in conflict with a desorption model proposed in literature<sup>53</sup>. The importance of this observation is discussed in the context of the desorption mechanism in chapter 5.

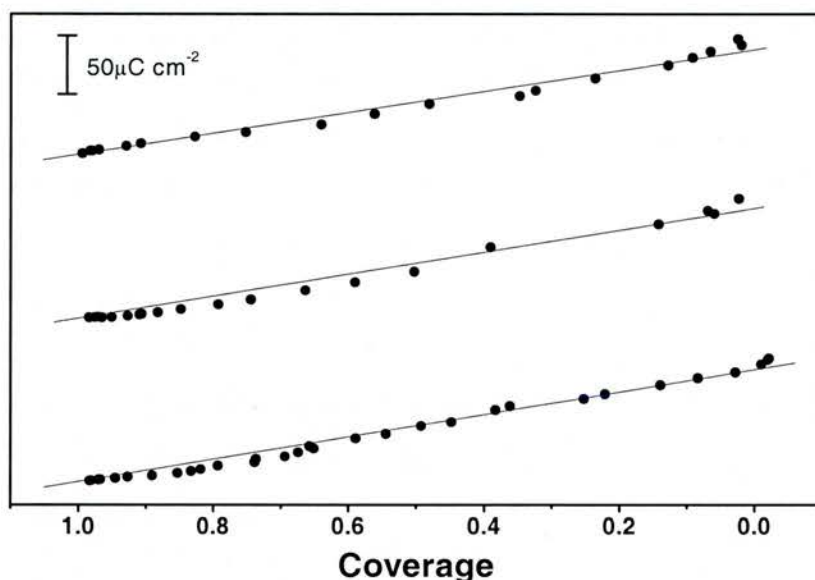


Figure 4.6: Charge to coverage relationship for MC7 (top), MC10 (middle) and MC16 (bottom). The line of best fit through (1,0) is included for each SAM.

Figure 4.6 highlights the linear dependence of desorption charge against the coverage determined by SHG. For alkane thiols where changes in current and SHG signal run always parallel suggest that faradaic and capacitive currents are tightly linked, figure 4.1. This is confirmed by a detailed evaluation shown in figure 4.6 where the integrated charge  $q(E)$  is plotted against the SHG derived coverage  $\theta$ . No significant deviation from linear behaviour is observed for any of the systems. Before continuing the discussion of the  $q/\theta$  relationship the evaluation of the SHG signal has to be addressed since it is based on a number of assumptions. The first assumption is that the potential induced change of the SHG signal does not play a significant role. Looking at the SHG response to a bare gold electrode in figure 4.1, the variation of the potential induced change of the SHG signal from the bare gold surface is about 10% or less over the

potential range of a desorption peak. The second assumption is that aliphatic chains do not influence the SHG. This is justified since, as discussed in the literature<sup>142</sup>, the nonlinear polarisability of the aliphatic chains is negligible compared to the thiol-Au interface signal.

In summary, the alkane thiol homologue series presents a fundamentally simple class of molecule that forms high quality SAMs on gold and is well suited to examine basic properties of films and spacer group influences. The peak shape is determined greatly by the thiol length, short thiols (MC7 to MC10) have a single peak, MC16 has a double peak and MC22 has a single peak. In each case the SHG increases upon desorption, the SHG increase exactly parallels the desorption peak. The desorption position and hence the film stability depends on the length of the molecule, longer molecules form more stable SAMs. The desorption potential change per methylene unit is 40 mV in the range from MC2 to MC10, it is 13 mV in the range from MC10 to MC22. The deviation is likely due to a transition from less ordered to more ordered SAMs. The transition from less ordered to more ordered SAMs from short molecules to long molecules reported in literature<sup>9,48,50,52</sup> is in general agreement with these results where a gradual transition in stability is observed. The charge transfer for the desorption of a layer of alkane thiols is independent of the molecule length within experimental errors, the desorption charge is  $108 \pm 3 \mu\text{C cm}^{-2}$ . The peak width gets narrower from MC2 to MC10, there is an increase for MC16 due to its insolubility. The percentage of readsorption charge gradually increases from MC4 to MC16, linked to the solubility and diffusion of molecules after desorption. The coverage determined by SHG is linearly correlated to the charge for desorption for alkane thiols, despite a double peak structure for MC16 the linear correlation is still observed. The electrochemical and spectroscopic behaviour must be accounted for by a desorption model that is consistent with all of the data, in particular the different desorption regimes evidenced by the peak shapes, and the linear correlation of coverage to charge for the MC16 double peak. Chapter 5 discusses these results in the context of the desorption mechanism.

#### 4.1.2 Biphenyl Thiols

Thiol SAMs containing a rigid biphenyl unit as described in subchapter 2.1.3 and depicted in appendix 4 are examined using CV and SHG. The structure of SAMs

containing a biphenyl unit is markedly different from alkane thiol SAMs due to the presence of the bulky endgroup. There is a distinct odd-even effect with SAMs containing an even number of methylene units having a biphenyl unit with a greater tilt angle than SAMs containing an odd number of methylene units<sup>94</sup>. This corresponds to a lower packing density of BP(even) molecules by 25% relative to BP(odd) SAMs. The BP(even) SAMs are electrochemically less stable than BP(odd) SAMs. Samples are prepared at two different temperatures, 22°C and 70°C. Preparation of SAMs at 70°C produces SAMs with substantially larger domains, this allows an investigation of the domain size on the electrochemistry of the SAMs. The SAM stability, desorption charge and peak shape are examined, as is the correlation of the voltammetry to the SHG for the homologous series. For BP3 and BP4 samples prepared at 22°C the influence of the scan rate on the desorption position is examined.

The evolution of the cyclic voltammograms with increasing  $n$  is shown in figure 4.7 which compiles the complete series both for BP $n$  SAMs prepared at 22°C (figure 4.7 left) and at 70°C (figure 4.7 right). The respective CVs for MC16 are included for comparison. Focussing first on the general trends which are common to both preparation temperatures it is obvious from figures 4.7 to 4.10 that there is a clear odd-even effect in position, width, and charge of the desorption peaks. The BP(odd) thiols desorb at more negative potentials with narrower, larger peaks than BP(even) thiols.

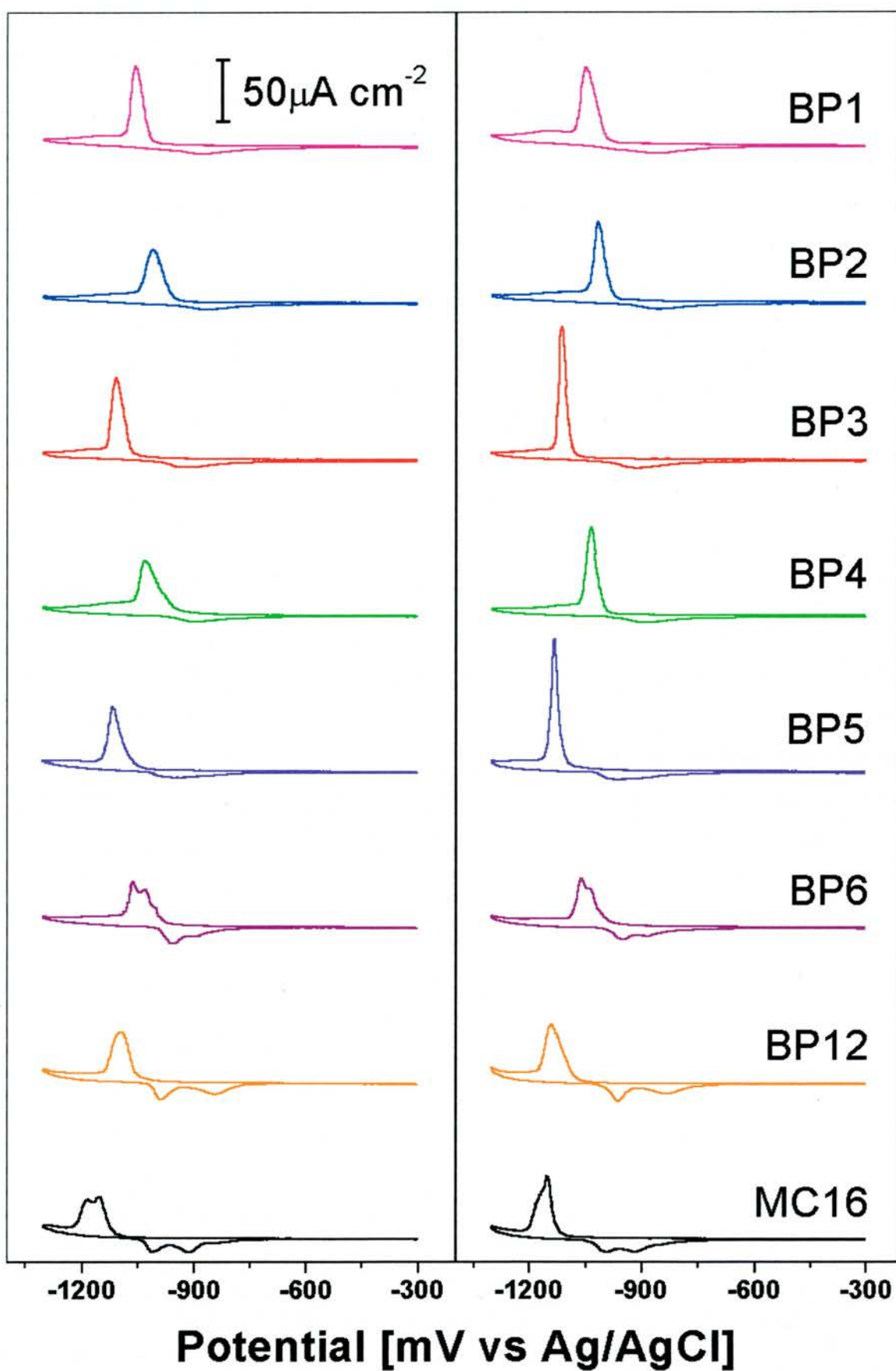


Figure 4.7: Cyclic voltammograms for BP1-6 and 12 and MC16 at 22°C (left) and 70°C (right) on Au/mica, at 20 mV/second.

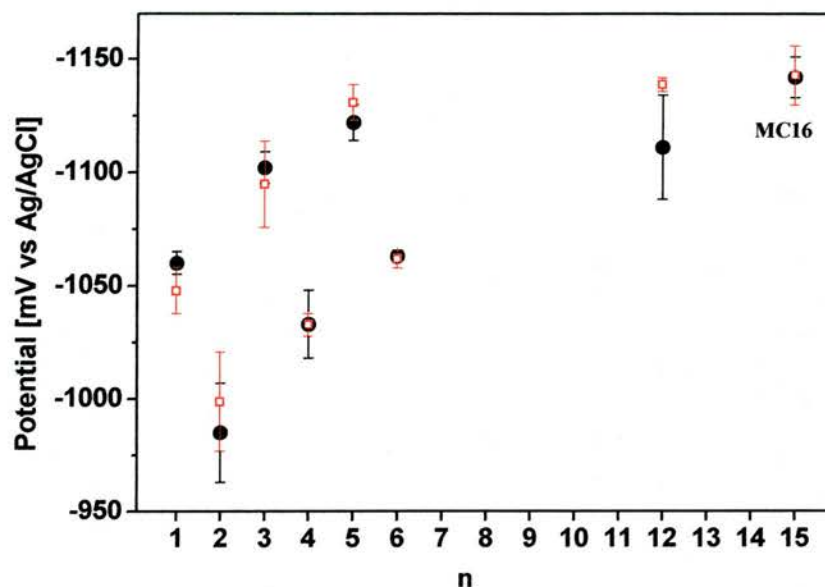


Figure 4.8: Desorption peak potentials for BP1-6 and 12 and MC16 SAMs on Au/mica prepared at 22°C and 70°C. Filled circles and open squares represent SAMs prepared 22°C and 70°C, respectively.

### Position

From the plot of the desorption potentials vs. spacer length, Figure 4.8, it is seen that a continuous shift towards more negative potentials with increasing  $n$  is superimposed onto the odd-even variation. The potential difference due to the odd-even effect is 82 mV in good agreement with the value reported for Au/Si<sup>91</sup>. The average increase per methylene unit, ignoring the odd-even effect is 17 mV/methylene unit in good agreement with values for alkane thiols<sup>143,144</sup>. Interestingly, there is no clear difference in the desorption potentials between the two preparation temperatures. If one assumes that the structural perfection of the BP $n$  SAMs influences the stability this is somewhat unexpected since BP $n$  SAMs prepared at elevated temperature exhibit a higher crystallinity. From STM measurements domain sizes were found to increase from 5-20 nm at room temperature for BP $n$  SAMs with  $n = 1-6$  to a maximum of 70-100 nm for  $n = 1-3$  and 40-60 nm for  $n = 4$  and 5. For  $n = 6$  the situation is different as at elevated temperatures elongated rectangular domains form whose symmetry does not fit to the 3-fold symmetry of the substrate. For BP12 no information on the molecular length scale is available. It is noted that the readsorption potential also shows a clear odd-even effect for  $n = 1$  to 5 but is not observed between  $n = 5$  and 6, possibly due to the insolubility of

BP6. Compared to desorption the odd-even difference in the readsorption potentials amounts to  $\sim 25$  mV and, thus, is significantly smaller.

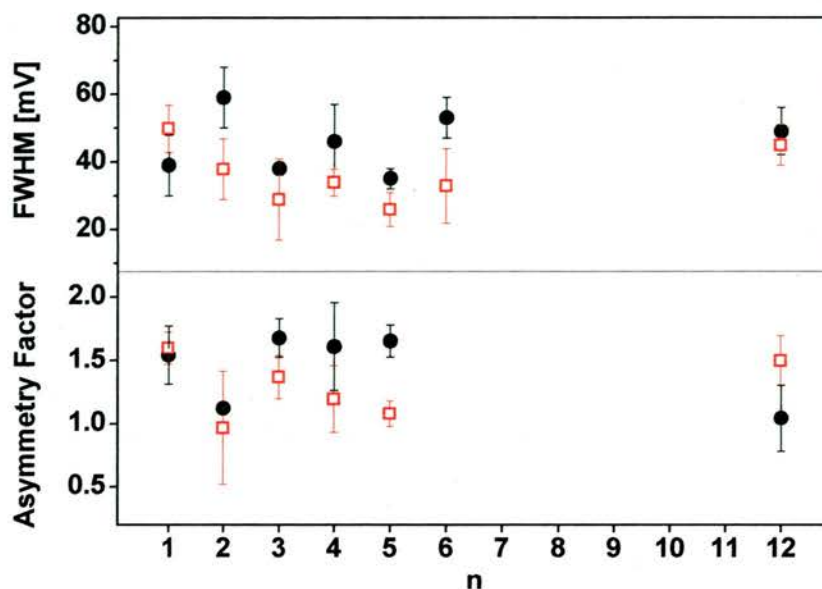


Figure 4.9: Influence of the spacer length of BP $n$  SAMs on Au/mica on the width and symmetry of the desorption peak. Full width at half maximum (FWHM) (top) and asymmetry factor (bottom) as defined in subchapter 2.2.3. For BP6 which exhibits multiple peaks no asymmetry factor was determined.

## Shape

The shape of the desorption peak also reflects odd-even differences as seen qualitatively from figure 4.7 and more quantitatively from figure 4.9 which compiles the full-width at half maximum (FWHM) and the symmetry of the desorption peaks. For BP1-5 all desorption peaks and readsorption peaks are a single peak. For BP6, at 22°C preparation temperatures the desorption peak is a double peak separated by 30 mV with a small shoulder on the anodic side, the readsorption peak is a double peak separated by 60 mV. At 70°C the desorption peaks are separated by 20 mV, readsorption peaks separated by 65 mV. The desorption peak for BP12 is a single peak at both preparation temperatures, however the readsorption peaks are double peaks with a separation of 140 mV at 22°C and 130 mV at 70°C. Subsequent cycles for BP12 display double desorption peaks. For samples prepared at 22°C there is a clear odd-even effect in the peak width, BP(odd) SAMs have narrower peaks by an average of 16 mV. The difference in peak width may be due to differing substrate interactions as BP(even) molecules are likely attached to a range of different adsorption sites, in contrast to BP(odd) molecules which all attach at

the same site. Increasing the preparation temperature from 22°C to 70°C results in the narrowing of all peaks except BP1 which broadens by 10 mV. BP2 and BP6 narrow by about 20 mV, BP3-5 narrow by 10 mV and BP12 narrows by about 3 mV. The behaviour of BP1 is not surprising based on the fact that higher preparation temperatures produce islands on the gold surface, an effect not observed for BP2-6. For the majority of BP<sub>n</sub> SAMs ( $n = 1,3-5$ ) prepared at 22°C an asymmetry of the peak shape is observed, the increasing part of the peak is substantially broader than the decreasing part. Only for BP2 and BP12 no asymmetry is seen. For BP6 at room temperature no asymmetry factor was calculated since multiple peaks are observed.

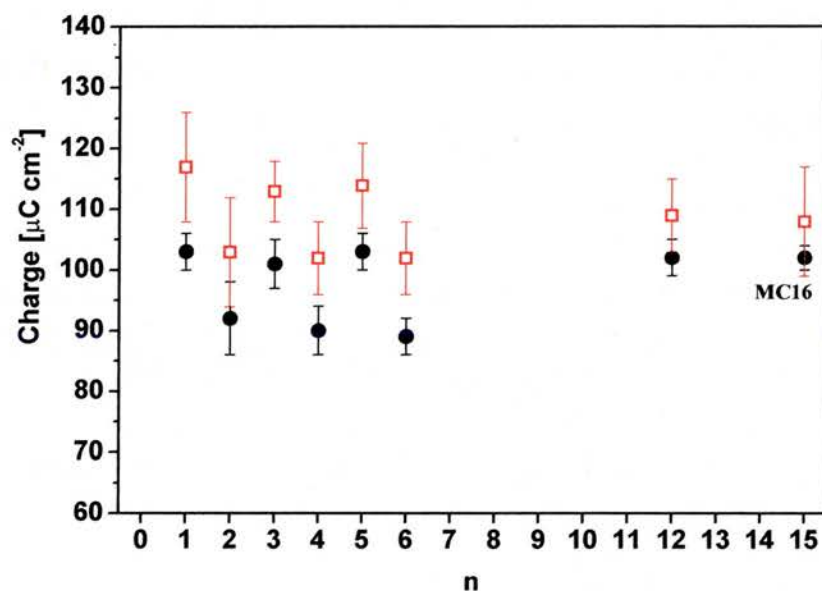


Figure 4.10: Charge integrated over the desorption peak for BP<sub>n</sub> SAMs on Au/mica prepared at 22°C (filled circle) and 70°C (open squares). For comparison the value of hexadecane thiol is displayed at  $n = 15$ . The larger standard deviation for MC16 is due to the fact that the evaluation is more difficult, selecting the position of the end of the lower boundary for the desorption peak where it overlaps with the hydrogen evolution is not trivial. Desorption peaks were integrated with a straight baseline connecting the start and end of the peak as a lower boundary.

## Charge

As known from spectroscopic analysis<sup>94</sup> and STM<sup>65,145</sup> there is a substantial odd-even difference in the packing density. While all odd-numbered BP<sub>n</sub> SAMs have essentially the same packing density as alkane thiols the density for  $n = \text{even}$  is about 20% lower. As figure 4.10 shows this is clearly reflected in the smaller charge for  $n = \text{even}$ . The desorption charges alternate between, on the average, 102 and 90  $\mu\text{C cm}^{-2}$  for samples

prepared at 22°C, and between 115 and 102  $\mu\text{C cm}^{-2}$  for samples prepared at 70°C for BP(odd) and BP(even) respectively. There is a systematic increase in the charge due to higher preparation temperatures and a clear odd-even difference reflecting the odd-even variation in coverage. Since it is known that increasing the preparation temperature improves the quality of the film by increasing domain sizes and increasing the coverage the values obtained at 70°C closer reflect the ideal fully covered sample. The values for these samples are examined in more detail. Looking at the desorption charge in more detail one has to differentiate between the faradaic and capacitive charges. For a one electron process,  $\text{RSAu} + \text{e}^- \rightarrow \text{Au} + \text{RS}^-$ , which was established for the reductive desorption of thiols<sup>79,80</sup>, the faradaic charge for a perfect monolayer with a  $(\sqrt{3}\times\sqrt{3})$  structure such as alkane thiols is calculated to be 74  $\mu\text{C cm}^{-2}$ . For BP(odd) SAMs with a reported  $(2\sqrt{3}\times\sqrt{3})$  structure and two molecules per unit cell<sup>65,145</sup> the same value should result whereas for BP(even) a value of 59  $\mu\text{C cm}^{-2}$  is obtained. Calculating the capacitive charging for the data of BP $n$  SAMs prepared at 70°C by subtracting the theoretical faradaic charge from the measured total charge, values of 41  $\mu\text{C cm}^{-2}$  for BP(odd) and 43  $\mu\text{C cm}^{-2}$  for BP(even) are obtained. Despite preparation of samples at 70°C domain sizes are not infinite so there will be a discontinuity of the molecular packing at domain boundaries with a concomitant reduction in the number of molecules attached to the surface from the theoretical 100% coverage. Using the model detailed in subchapter 2.1.5 the coverage will be about 88% for samples prepared at 22°C and 96% for samples prepared at 70°C. The difference in coverage predicted using the model is substantiated by the average 14% increase observed for the charges for samples prepared at elevated temperatures. Correcting the theoretical faradaic charge from the coverage of 96% gives 71  $\mu\text{C cm}^{-2}$ , and a capacitive contribution of 43  $\mu\text{C cm}^{-2}$  for BP(odd) and 45  $\mu\text{C cm}^{-2}$  for BP(even). The capacitive contribution is therefore about 37% of the total charge for BP(odd) and 44% of the total charge for BP(even). Assuming the capacitive contributions are independent of the packing density of molecules in the SAM the faradaic contributions are in very good agreement with the difference in packing observed by STM. This result indicates that the capacitive charge is similar for alkane thiols and all biphenyl thiols, the capacitive charge is dominated by the capacity of a bare gold electrode, small differences in capacity between different SAMs of a few micro Faradays cannot be distinguished in the CV as the bare gold capacity is about 40  $\mu\text{F cm}^{-2}$ .

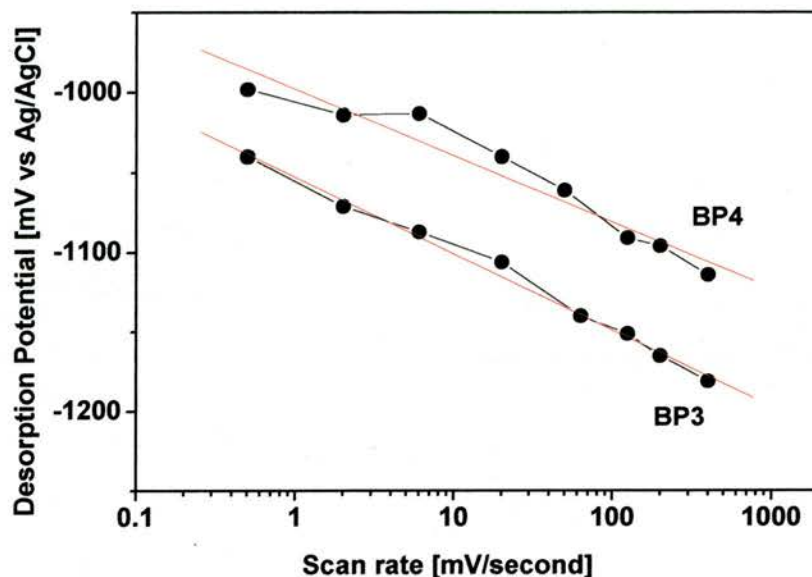


Figure 4.11: Peak potential of the desorption peak for BP3 and BP4 on Au/mica as a function of the scan rate. The x-axis is a  $\log_{10}$  plot.

### Scan Rate

The stability of the layer as a function of the scan rate is depicted in figure 4.11 which compares BP3 and BP4 as examples for odd and even numbered systems. Both SAMs show a linear dependence of the peak potential  $E_{des.}$  on the logarithm of the scan rate which is indicative of an irreversible process, subchapter 2.2. No significant odd-even difference in slope is observed and the shift of  $E_{des.}$  of about 50 mV/decade change in scan rate is in the same range as the 70 mV/decade reported for mercaptohexanoic acid<sup>143</sup> and the 60 mV/decade for mercaptoundecanoic acid<sup>146</sup>. For alkane thiols the values diverge with 60 mV/decade reported for decanethiol<sup>76</sup> and almost no dependence (< 10 mV/decade) for dodecane thiol<sup>146</sup>. For decane thiol in alkaline ethanol solution a value of 44 mV/decade was reported<sup>80</sup>.

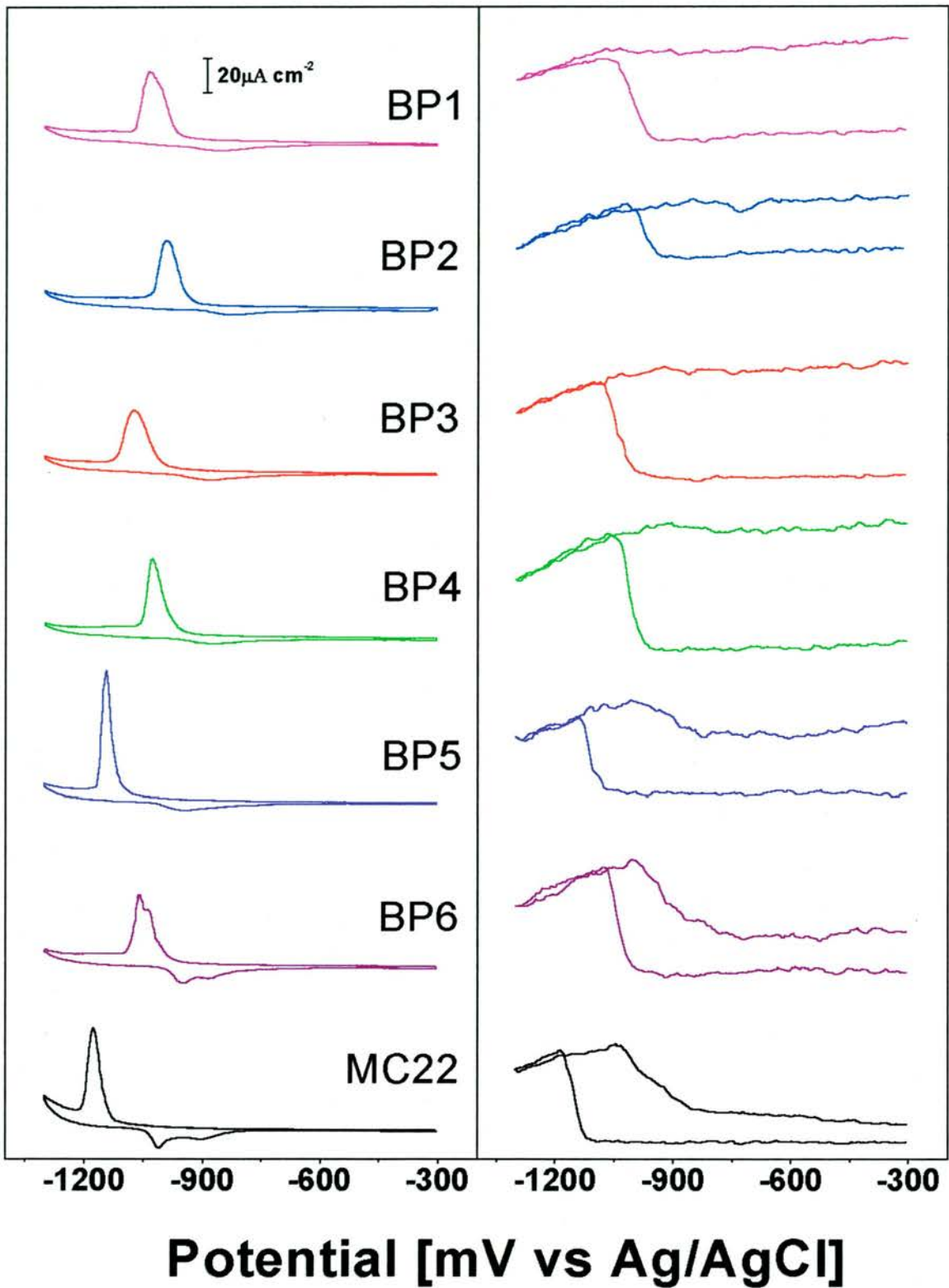


Figure 4.12: CVs (left) and SHG (right) for the series of BP SAMs prepared at 70°C at a scan rate of 20 mV/second. All experiments were performed in the same day with identical conditions. SHG is normalised to region of bare gold, the SHG intensity minimum is 55% of the intensity at -1300 mV.

The CV with in-situ SHG for the biphenyl series is depicted in figure 4.12, SHG is normalised to the signal of the bare gold electrode, an alkane thiol is included for reference. The SHG intensity increases across the desorption peak for every sample, the readsorption peaks are paralleled by a decrease in the SHG intensity. The extent of readsorption indicated by the area of the readsorption peak is in agreement with the SHG intensity change. BP1-4 have very little readsorption and the SHG change on the anodic scan due to readsorption supports this. BP5, BP6 and MC22 have considerably larger readsorption peaks and the extent of the SHG change parallel to the readsorption peak also indicates a greater readsorption. There is a clear trend of gradually increasing readsorption going from BP4 to BP6 observed with both CV and SHG. This is consistent with the trends for alkane thiols between MC2 and MC16, figure 4.5.

Figure 4.13 highlights the linear correlation of charge for desorption with the coverage determined by SHG. This is identical to the results for alkane thiols depicted in figure 4.6, this result is quite remarkable for several reasons. Firstly, the molecular structure seems irrelevant. Neither the aliphatic spacer length nor the difference between the mixed aromatic/aliphatic BPn thiols and the purely aliphatic thiol affects the linear relationship between  $\theta$  and  $q$ . Secondly, the preparation temperature has no effect on  $q$  vs.  $\theta$ . Separate plots for the different temperatures yield the same results as the one shown in figure 4.13 which is the average of all experiments. Thirdly, in contrast to the pronounced odd-even effect of the position, charge, and width of the desorption peak, both types of BPn thiols yield a linear dependence of  $q(E)$  vs.  $\theta$ . Fourthly and most remarkably, the linearity is observed irrespective whether the desorption signal consists of a single peak (BPn,  $n = 1-5, 12$ ) or multiple peaks (BP6, MC16). All this strongly suggests that the SAM structure, i.e. domain size, density of etch pits, and molecular packing density does not have a detectable influence on the ratio between the integrated desorption charge (capacitive plus faradaic) and the faradaic component as measured by SHG.

This linear correlation of charge to coverage is a clear piece of evidence that contradicts the desorption mechanism proposing a clear separation of faradaic and capacitive processes where double peaks are observed, i.e. BP6 and MC16. This is discussed in the following chapter focussing on the desorption mechanism.

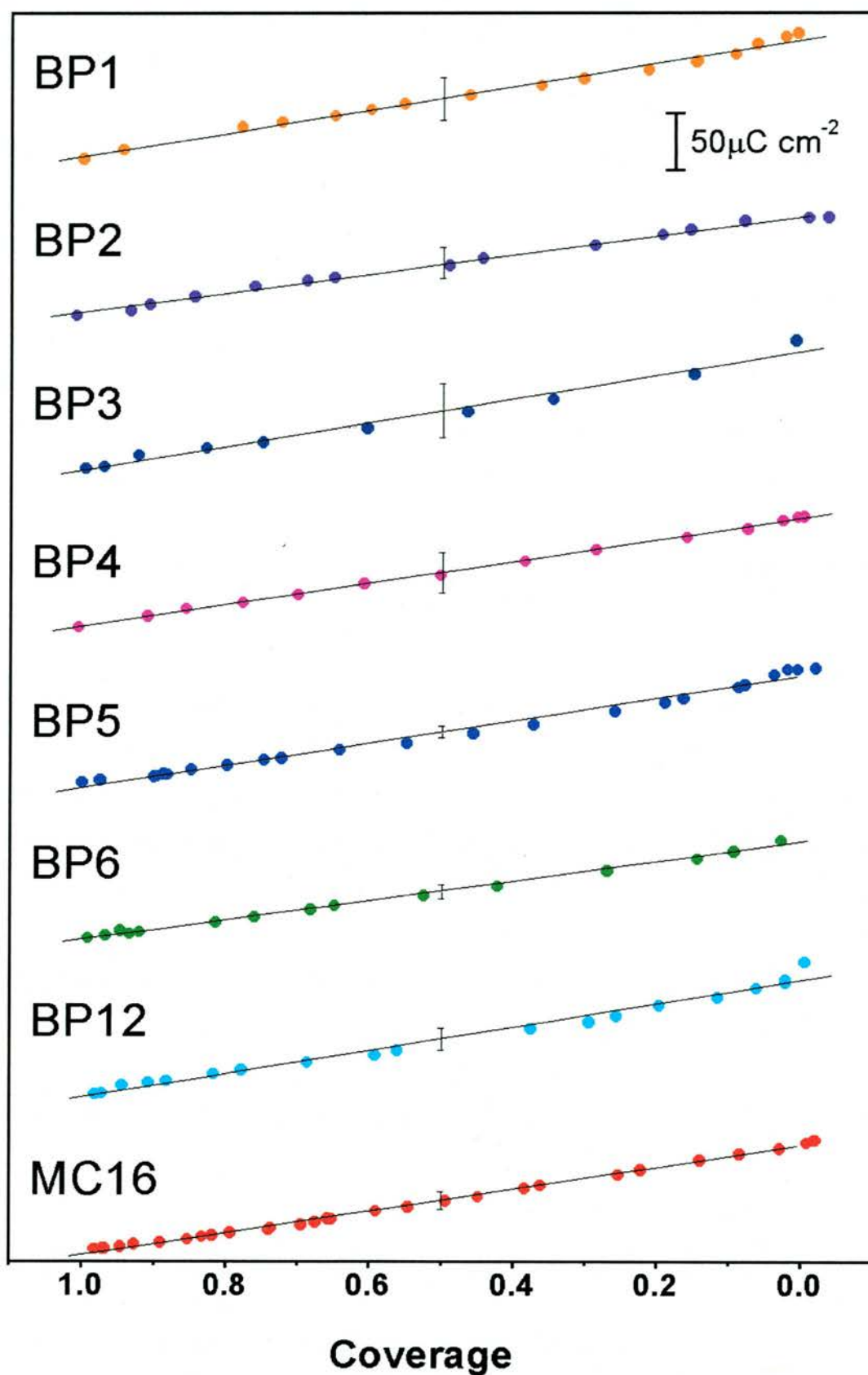


Figure 4.13: Plot of desorption charge density over coverage derived from SHG for BP1-6, and 12 and MC16 on Au/mica. Data are from cyclic voltammograms taken at a scan rate of 20 mV/second. Solid lines are linear least square fits. Error bars are derived from averaging different experiments with samples prepared at 22°C and 70°C.

## 4.2 Tail Group Influence

The tail group is the part of the molecule that is exposed to the local environment and hence, has a central role in determining the surface properties of the SAM modified surface. Tail groups can be introduced to deliberately increase stability or create disorder. Bulky tail groups can be used to reduce coverage. Functional groups can add functionality to surfaces for applications such as tribology or immobilising biological molecules. The tail group can influence the formation and resulting properties of the film, several different comparisons are made to illustrate the variety and extent of the tail group influence. Cyclic voltammetry is performed on a variety of systems with a view to obtaining information on the desorption potential, the desorption peak shape and desorption charge transfer.

### 4.2.1 MC8 / CFS

Octane thiol is compared with a perfluorinated octane thiol molecule, figure 4.14. The perfluorinated thiol has a modified spacer and tail group. This comparison is an appropriate link between the previous subchapter on the spacer and the present subchapter on the tail group. The molecule abbreviated CFS will be revisited in subchapter 4.3.1 comparing the head group influence with its selenol analogue.

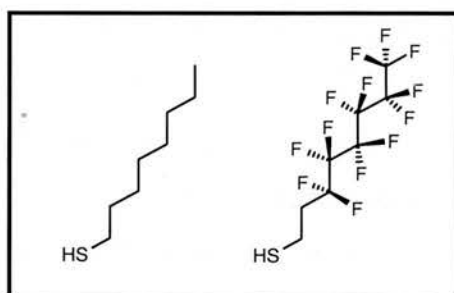


Figure 4.14: MC8 (left) and CFS (right), CFS has 13 fluorine atoms in the molecule. SAMs based on these two molecules are considered to have different spacer and tail groups.

Perfluorinated SAMs are of interest as surface modifiers, they can render a surface chemically inert<sup>147</sup>. Perfluorinated SAMs exhibit superior properties to equivalent alkane thiols in terms of decreased defectiveness and permeability<sup>51</sup>. The van der Waals diameter of the perfluorinated region is 5.6 Å compared to 4.2 Å for the alkane chain<sup>51</sup>. The juxtaposition of the bulky perfluorinated moiety and the alkane moiety has some

impact on the film structure. The tilt angles for the respective fluorinated and non-fluorinated moieties differ with fluorinated parts tilting closer to the surface normal<sup>148</sup>.

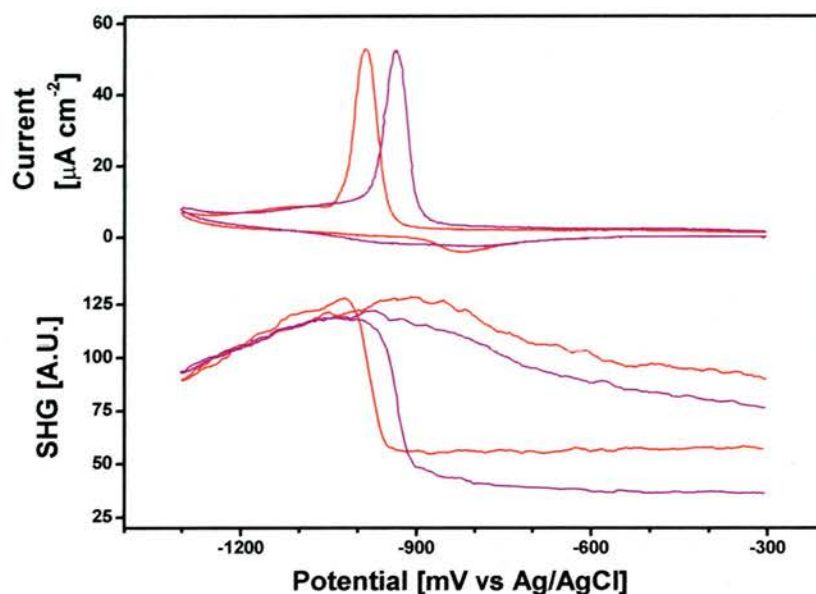


Figure 4.15: CVs (top) and SHG (bottom) for CFS (purple) and MC8 (red). There was an exceptionally high degree of reproducibility for the CVs. SHG is the average of two results. MC8 desorbs at more negative potentials. Samples prepared at 22°C.

Figure 4.15 depicts CVs and SHG for these two SAMs. The desorption potentials are  $-986 \pm 1$  mV for MC8, compared to  $-940 \pm 8$  mV for CFS, MC8 is more stable by 46 mV, this is equivalent to the potential shift observed for one or two methylene units. The fluorine substituted molecule is notably less stable to electrochemical desorption than the pure alkane thiol molecule. The voltammograms all display a very similar single peak shape, the peak widths for MC8 and CFS are almost identical. MC8 has a FWHM of  $47 \pm 4$  mV compared to  $44 \pm 2$  mV for CFS. Notably, the peak heights are almost identical, all falling within a  $3 \mu\text{A cm}^{-2}$  range. CFS has an asymmetry factor of 0.9 compared to 1.0 for MC8, The current onset for CFS is slightly sharper, although the difference is very small. The charge transfer for MC8 is  $109 \pm 2 \mu\text{C cm}^{-2}$ , for CFS it is  $105 \pm 1 \mu\text{C cm}^{-2}$ , the areas of the two peaks differ by only 4%. These values are consistent with expectation as the bulkier perfluorinated molecule would make close packing slightly more difficult. It is likely that the unit cell for the two systems are similar. The SHG for the two systems is compared with the CV, The SHG increase in both cases exactly parallels the desorption peak. The CVs and SHG both indicate that there is only a partial readsorption of molecules. Taking the alkane thiol starting SHG

intensity as the reference point, due to the lack of functionality, it is clear that the CFS starting SHG intensity is lower than the MC8 starting intensity, this suggests the presence of the fluorine atoms influences the SHG. This could be due to a polarising effect. Fluorine could polarise the electrode either directly or through the sulfur. The electronegativity of the perfluorinated moiety is considerably greater than the equivalent aliphatic region in MC8. This phenomenon is examined again in subchapter 4.3.1 where CFS is compared with its selenium analogue.

#### 4.2.2 MC16 / MHA

Hexadecane thiol (MC16) is compared with mercaptohexadecanoic acid (MHA) SAMs, figure 4.16.

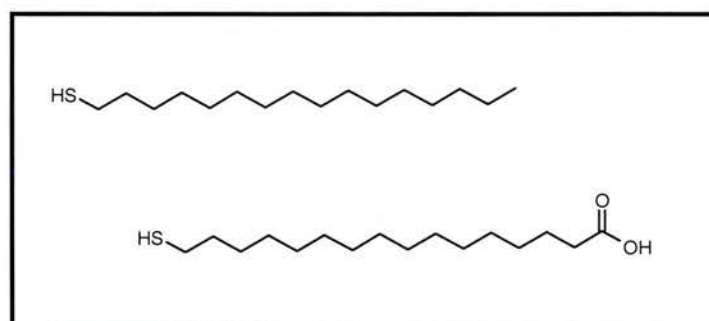


Figure 4.16: MC16 (top) and MHA (bottom), MHA has a carboxyl tail group.

The presence of the carboxyl group complicates the SAM formation and intermolecular interactions. The carboxyl group has a permanent dipole, which results in unfavourable dipole-dipole interactions between the tail groups of neighbouring molecules. The consequence is a lower degree of ordering in the film<sup>143</sup>. Despite this, hydrogen bonding between neighbouring carboxyl groups can occur when the group is fully protonated. Additionally the formation of dimers between carboxyl groups can introduce disorder in a larger scale<sup>149</sup>. Immersion of the SAM in an alkaline electrolyte will deprotonate the carboxyl group removing any favourable intermolecular hydrogen bonding and shift the energy balance of the SAM. CVs and SHG for MC16 and MHA are compared in figure 4.17. MC16 displays the characteristic double peaks, whereas MHA displays a single peak. The FWHM values for the desorption peaks are 37 mV and 88 mV for MHA and MC16 respectively. The readsorption peaks clearly show that the extent of readsorption is lower for MHA. MC16 has almost complete readsorption, while MHA has only partial readsorption. The SHG changes parallel the desorption and readsorption peaks in

both cases, and for MHA the SHG indicates that there is only a partial readsorption. The presence of the carboxylate group significantly changes the electrochemistry of the SAM. The MC16 first desorption peak occurs at  $-1145$  mV compared to  $-1090$  mV for MHA, MC16 desorbs at a potential 55 mV more negative than MHA, for this length of molecule this is equivalent to the potential shift for three methylene units. The carboxylate tail group has a destabilising influence on the overall energy balance of the thiol SAM. The desorption charge transfer values are compared, MHA has a charge transfer of  $102 \mu\text{C cm}^{-2}$ , compared to  $108 \mu\text{C cm}^{-2}$  established for alkane thiols in subchapter 4.1.1. There is a 6% difference in the total charge, suggesting a slight decrease difference in packing density for MHA. However, due to uncertainty in the capacitive charging influence of the polar tail group and the experimental errors it can not be unambiguously ascertained that there is a real difference in packing density.

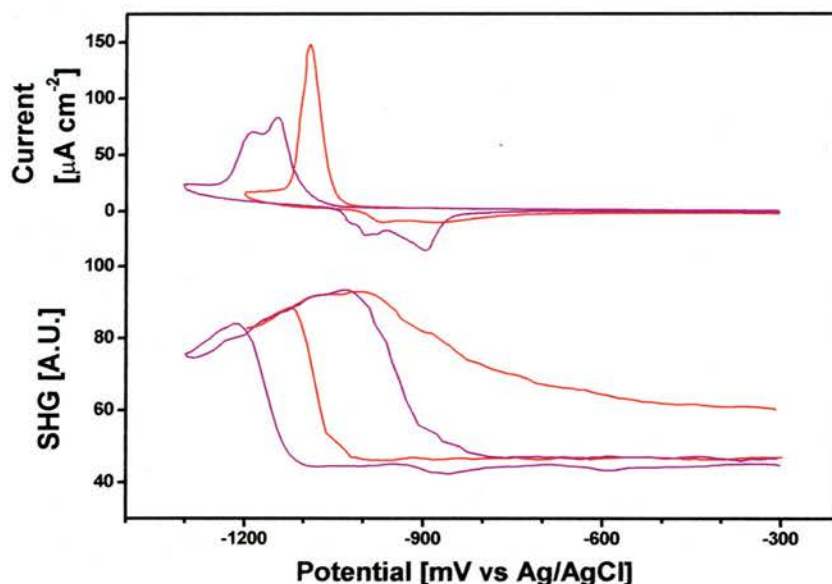


Figure 4.17: CV (top) and SHG (bottom) for MHA (red) and MC16 (purple) at 50 mV/second. Samples prepared at 22°C.

The SHG results are compared with the CVs. The SHG and CV for MHA both indicate the readsorption of MHA is incomplete. The SHG shows a very slightly lower coverage for MHA. The susceptibility tensors,  $\chi_{\text{Au}}$  and  $\chi_{\text{INT}}$  are calculated for MC16, assuming a coverage of 1 with SHG intensity of 44.8 units, and coverage of 0 has 84.1 units:  $\chi_{\text{Au}} = 9.171$  and  $\chi_{\text{INT}} = 2.477$ . The 'b' value (equation 2.14) is  $-0.27$ , this is in excellent agreement with the value of 'b' value of  $-0.28$  for the MC16 average in figure 3.15. The relative coverage for MHA with SHG intensity of 47.1 units, using the same

susceptibility tensors corresponds to a coverage of 0.93 relative to MC16. The MHA coverage based on SHG intensities is 7% lower than MC16 coverage. The MHA average SHG intensity is about two standard deviations away from the MC16 SHG intensity suggesting that there is only a 5% chance that the difference is due to a random statistical deviation. The two techniques both suggest that the coverage for MHA may be slightly lower than for MC16.

In summary, the MHA is less stable than MC16 by a factor equivalent to three or four methylene units. Both electrochemistry and SHG suggest there may be a slightly lower packing density for MHA, by about 5-10%. The presence of the carboxylate group significantly changes the electrochemistry of the SAM, it is likely that this is a consequence of repulsive interactions between negatively charged neighbouring carboxylate groups in an alkaline environment. The results here are in agreement with Kakiuchi and co-workers who report that there is an average shift of 110 mV between methyl terminated SAMs and carboxyl terminated SAMs at 20 mV/second<sup>143</sup>.

### 4.2.3 BP1 / DT

The chemical structures for BP1 and DT are given in figure 4.18. BP1 is compared with an analogous dithiol molecule. Dithiol molecules have two possible ways of attaching to the gold surface. They can attach with one sulfur and stand upright, or attach with two sulfurs lying flat, or a mixture of these two states.

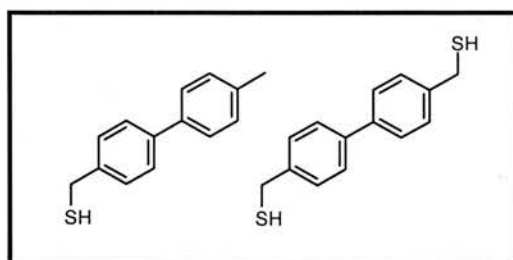


Figure 4.18: BP1 (left) and DT (right), DT has an additional sulfur atom in the tail group.

Figure 4.19 shows the cyclic voltammograms and SHG for the two molecules, DT and BP1, they both have single desorption peaks. The dithiol molecule desorbs at a potential more negative than the BP1 desorption potential, the dithiol molecule is significantly more stable to electrochemical desorption. The readsorption peaks for the two molecules show that BP1 readsorbs before DT. Qualitatively the DT CV shows a more

pronounced hydrogen evolution that is indicative of a roughened surface. The SHG increase parallels the desorption peak for both molecules, the starting intensities are comparable, but the DT intensity unusually decreases as the potential becomes more negative. The extra stability of the layer due to the thiol tail group will be discussed after the peaks are assessed.

The desorption position for DT is  $-1168 \pm 5$  mV compared to  $-1060 \pm 5$  mV for BP1, DT is substantially more stable to desorption. The additional sulfur atom in the molecule has a stabilising influence on the resulting SAM. The charge transfer associated with the desorption of a layer of these molecules can give an indication of the nature of the bonding. The desorption charge for DT is  $103 \pm 1 \mu\text{C cm}^{-2}$ . The error here is only the random error, however there is an uncertainty due to the hydrogen evolution. The charge for desorption of 22°C prepared BP1 is  $103 \pm 3 \mu\text{C cm}^{-2}$ , the two systems have comparable desorption charges, and hence a similar coverage. The peak areas for the dithiol molecules prepared at 22°C matches exactly the peak area for BP1 sample. This is a very strong indication that the molecules packing densities are very similar and therefore the DT molecules stand upright in their final state. For a flat lying dithiol molecule, due to geometric constraints, the two end sulfurs would be about 15 Angstroms apart. Even allowing for a two electron transfer process per molecule the resulting desorption charge would be of the order of half of the charge for BP1 desorption. The measured charge transfer magnitude clearly rules out this possibility. However, the dithiols may initially form a kinetically favourable flat lying configuration, which changes to an upright phase once the coverage is sufficient. The increase of the hydrogen evolution peak for DT compared to BP1 suggests the roughening of gold which is likely due to breaking of gold sulfur bonds. This suggests that dithiol molecules may initially bond with two sulfurs, before one bond is broken to maximise the close packing of molecules. It is interesting to note that no STM images have been published demonstrating molecular resolution for dithiols in an upright configuration. The reasons for this are unclear, the state of Au surface is therefore not known. This hypothesis is supported by work from another group, Morin and co-workers report that a dithiol molecule with one phenyl ring forms upright packing monolayers<sup>88</sup>. Morin also discussed<sup>88</sup> the possible formation of multilayers of dithiols. The formation of a multilayer cannot be excluded, however it is unlikely that well

ordered multilayers would form that would contribute to the increase in stability of the film.

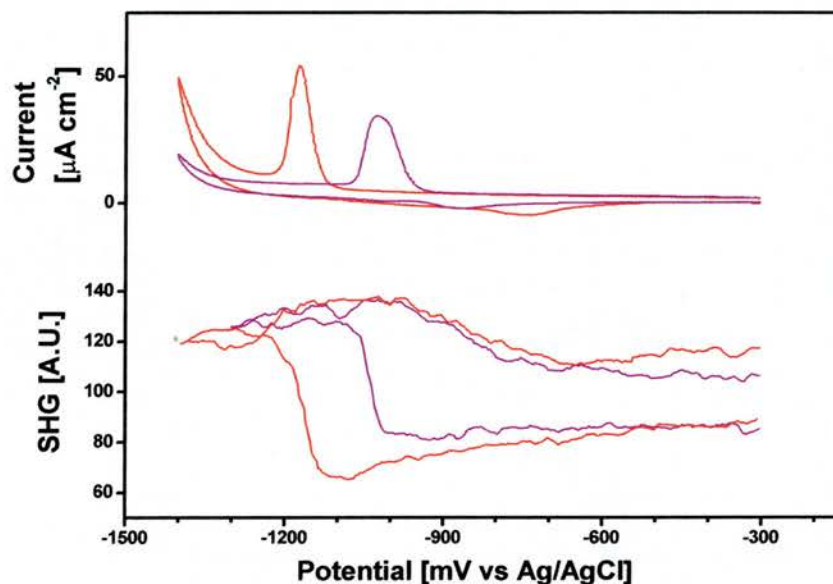


Figure 4.19: Cyclic voltammograms (top) and SHG (bottom) for DT (red) and BP1 (purple) at 20 mV/second. The CV and SHG for BP1 are from different experiments. The hydrogen evolution currents are very different. The scan range from  $-300$  to  $-1400$  mV was chosen to illustrate the different hydrogen evolution currents. Samples prepared at  $22^{\circ}\text{C}$ .

The FWHM values for DT and BP1 are compared, DT has a peak width of  $50 \pm 11$  mV, whereas BP1 has a peak width of  $39 \pm 9$  mV. The DT peak is on average slightly broader than the BP1 peak, but the error bars for the two desorption experiments overlap. Considering the coverage of the two systems is comparable, there is a remarkable difference in the electrochemical stability of 108 mV. The presence of the additional thiol moiety in the tail group increases the electrochemical stability. It is possible that adjacent sulfurs can bond to each other forming a disulfide once the molecules are positioned in the film. Thiol groups are held together in the SAM, two neighbouring thiols could react to form a disulfide and a hydrogen molecule, and the reaction is irreversible as molecular hydrogen is evolved. This would be consistent with all of the observations in the comparison between BP1 and DT. The normalised SHG for the two samples shows an equivalent SHG intensity in the first 200 mV of the scan, before the DT intensity decreases before desorption supporting the theory that there is a similar packing density of molecules. The decrease in SHG intensity for DT as the potential scans from  $-300$  mV to the desorption potential was unexpected, and its origin

is unclear at present. It may possibly reflect a change in the polarisability of the SAM due to the presence of the sulfur tail group.

#### 4.2.4 BP2 / PET

Phenyl ethyl thiol (PET) is compared with BP2. Factors such as coverage, charge transfer and desorption position are explored. Figure 4.20 shows the chemical structures.

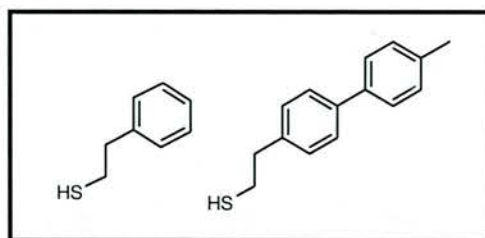


Figure 4.20: PET (left) and BP2 (right).

The stability of the two SAMs are compared, figure 4.21 depicts the voltammograms for the two systems. BP2 has a single desorption peak, PET has two desorption peaks. Qualitatively, the double peak feature for PET is of interest, the reason for the second peak is not immediately obvious. Similar features are observed for other short molecules, MC2, MC4, BPSe and to a small extent BP0. This is possibly due to the formation of a low density phase after some molecules desorb, or desorption from step edge sites. The BP2 desorption peak occurs at  $-985 \pm 22$  mV, the PET main desorption peak is at  $-830 \pm 40$  mV, PET has an additional peak at  $-955 \pm 1$  mV. BP2 is significantly more stable to desorption than PET, there is a difference of 155 mV which is comparable to a shift expected for about 4 or 5 methylene units, notably this is comparable with the difference in length of the two molecules.

The charge transfer for the desorption of PET was carefully evaluated. Experiments were performed at 50 mV/second and 100 mV/second for PET with thorough deoxygenation, the charge transfer is  $109 \pm 2 \mu\text{C cm}^{-2}$ . This compares to the charge transfer of  $92 \pm 6 \mu\text{C cm}^{-2}$  for BP2 under identical conditions. The charge transfer for PET is between 15% and 20% greater than for BP2.

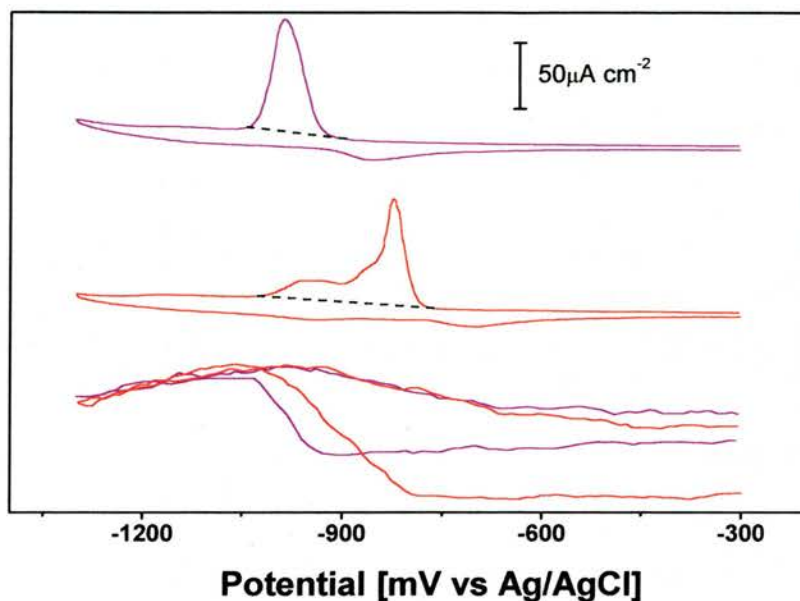


Figure 4.21: CV and SHG for BP2 (purple) and PET (red) at 50 mV/second. Baseline for integration is indicated by dashed line. The cell was degassed for one full hour in inert gas to eliminate the presence of oxygen. The SHG minimum is 50% of the SHG intensity at  $-1300$  mV. Samples prepared at  $22^{\circ}\text{C}$ .

The charge transfer for BP2 has previously been established during the homologous biphenyl thiol series investigation, the charge transfer for PET, however brings new information on the impact of the additional phenyl ring on the assembly of these films. The charge transfer of  $109 \pm 2 \mu\text{C cm}^{-2}$  initially seems a little large considering the sample was prepared at  $22^{\circ}\text{C}$ . Due to the broad multiple peaks for PET, the baseline selection for the PET integration could lead to a systematic overestimation of the peak area. This is a real possibility, the baseline spans 250 mV and the errors are therefore greater, an error of up to 25% could be accommodated, however this is the upper limit considering the extent of the inert gas purging. Based on the charge transfer values and allowing for errors it can be concluded that the packing density of molecules for PET is similar to, or greater than that of BP2. This is in contrast with Liu and co-workers who claim to have identified  $(\sqrt{3} \times 7)$  unit cell with two molecules per unit cell for PET. This corresponds to a coverage two times lower than a SAM with  $(\sqrt{3} \times \sqrt{3})$  unit cell. This would result in a desorption peak with a faradaic contribution of about  $36 \mu\text{C cm}^{-2}$  excluding any domain boundary effects. Considering the capacitive charge in the region of  $43 \mu\text{C cm}^{-2}$ , typical for the desorption of densely packed SAMs, the overall maximum desorption charge would be about  $79 \mu\text{C cm}^{-2}$ . This is clearly in contrast to

the observed results of  $109 \pm 2 \mu\text{C cm}^{-2}$  and cannot be explained in terms of errors alone. Disordered regions may have a higher density of packing than the ordered region, although this could not explain the large inconsistency. The unit cell reported by Liu and co-workers is incorrect<sup>150</sup>. The correct unit cell, determined by STM<sup>151</sup> is  $(\sqrt{3} \times 4)\text{rect}$  with 2 molecules per unit cell. This gives a packing density of  $28.7 \text{ \AA}^2/\text{molecule}$  and an expected faradaic charge of  $55 \mu\text{C cm}^{-2}$  and a total desorption charge consistent with the observed charge.

#### 4.2.5 BP3 / HBP3

BP3 and HBP3 molecules with different terminated tail groups are compared. Figure 4.22 illustrates the different molecules.

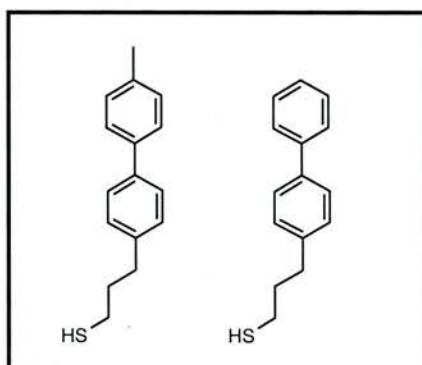


Figure 4.22: BP3 (left) and HBP3 (right).

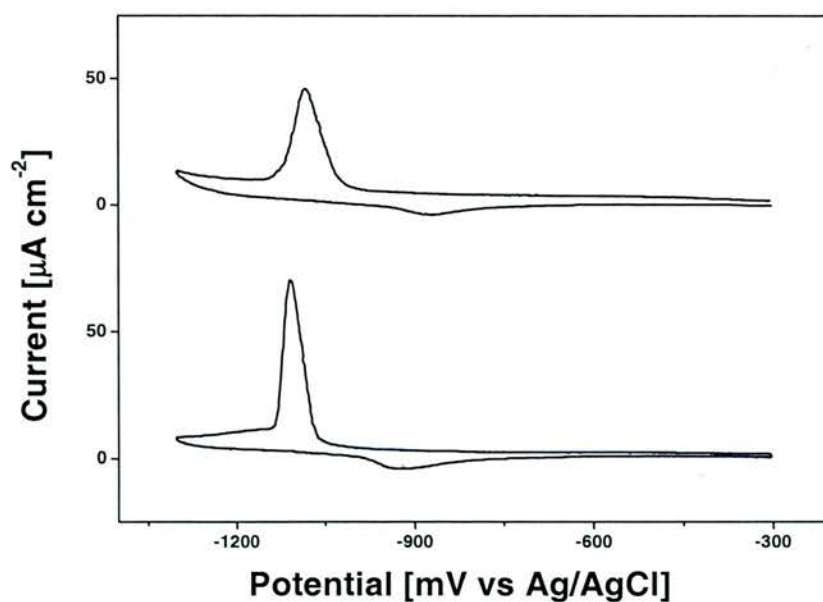


Figure 4.23: Cyclic voltammogram of HBP3 (top) and BP3 (bottom) at 20mV/second. Samples prepared at 22°C.

The SHG for HBP3 is similar to BP3 and is not presented. The CVs for HBP3 and BP3 prepared at room temperature are compared in figure 4.23, both have single desorption and readsorption peaks and the positions are reasonably close which is as expected. There are however small but systematic differences between BP3 and HBP3. The average position for BP3  $-1106 \pm 5$  mV compared to desorption position of  $-1073 \pm 15$  mV for HBP3. BP3 is more stable by 33 mV, this is comparable with the effect of between one and two methylene units for this type and length of molecule. The desorption charges are compared, BP3 has a desorption charge of  $101 \pm 4 \mu\text{C cm}^{-2}$  compared to a desorption charge of  $105 \pm 2 \mu\text{C cm}^{-2}$  for HBP3. The charge transfer is comparable for the two systems. This is an indication that the coverage is the same, and probably the same unit cell is adopted, the difference in capacitive charging is within the experimental uncertainty. The peak widths are examined, the FWHM values are compared, BP3 is  $38 \pm 2$  mV, HBP3 is  $62 \pm 14$  mV. HBP3 is systematically broader, by an average of 24 mV or 60%.

In summary, BP3 is slightly more stable, by 33 mV on average, this is equivalent to one or two methylene units for molecules of this type and length. The charge transfer is approximately equal for the two different systems. HBP3 peaks are systematically broader, the mean FWHM values are 62 mV and 38 mV for HBP3 and BP3 respectively. This is an interesting result which shows that small differences in the tail group can alter the overall SAM stability and properties.

#### 4.2.6 BP4 / HBP4 / BP4OH

BP4 and BP4 molecules with different terminated tail groups are compared. Figure 4.24 illustrates the different molecules.

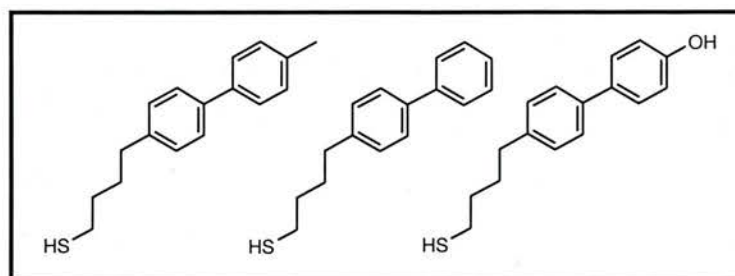


Figure 4.24: BP4 (left), HBP4 (middle) and BP4OH (right).

Figure 4.25 illustrates the CVs for BP4, HBP4 and BP4OH, and SHG for HBP4 and BP4OH.

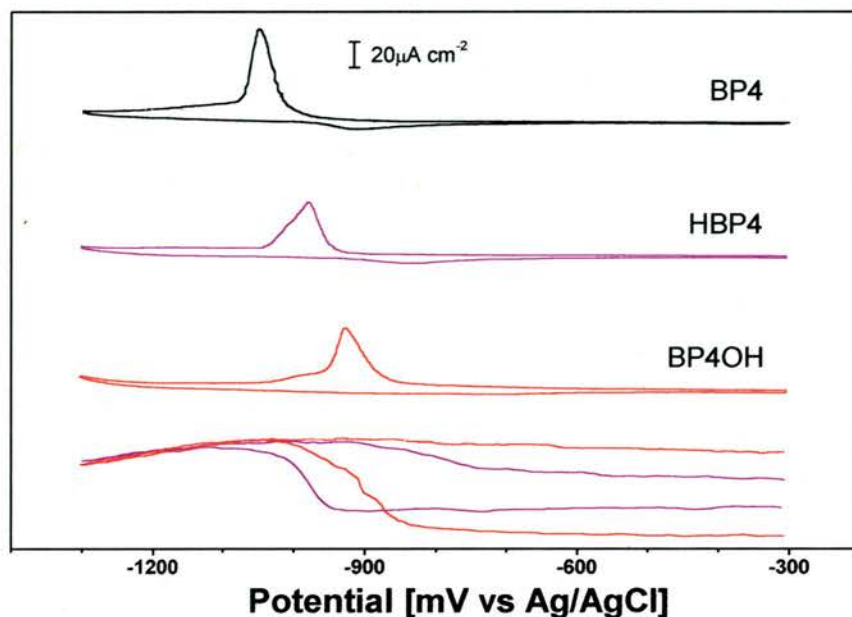


Figure 4.25: CVs for BP4 (black), HBP4 (purple) and BP4OH (red). SHG for HBP4 and BP4OH are compared. The SHG minimum is 33% of the intensity at  $-1300$  mV. Samples prepared at  $22^{\circ}\text{C}$ .

There is a clear stability trend observed for the three molecules increasing stability going from BP4OH to HBP4 to BP4, the desorption positions are  $-930$  mV,  $-980$  mV and  $-1040$  mV respectively. HBP4 is less stable than BP4 by  $60$  mV, BP4OH is less stable than BP4 by  $110$  mV. The tail group has a significant influence on the film stability. The desorption potentials for HBP3 and HBP4 are consistent with the odd-even effect in desorption potentials observed for BP $n$  thiols. The HBP4 desorption peak is broader than BP4 with an average FWHM of  $57$  mV compared to  $46$  mV for BP4. Interestingly the width of BP4OH is  $43$  mV, making it slightly narrower than the average BP4 width. BP4OH has an additional feature at  $-990$  mV, the origin of this feature is, at present, not understood. The desorption charge transfer for HBP4 is  $92 \mu\text{C cm}^{-2}$ , the average desorption charge for BP4 is  $90 \mu\text{C cm}^{-2}$ , the two values are equivalent within the experimental uncertainty. There were insufficient statistics to determine the desorption charge for BP4OH. The desorption charge transfers for HBP3 and HBP4 are consistent with the odd-even effect in charge observed for BP $n$  thiols. It should be noted that the biphenyl unit does dramatically contribute to the film stability, MC4 desorbs at a potential of  $-770$  mV, compared to  $-1040$  mV for BP4 and  $-975$  mV

for HBP4. Comparing MC4 and HBP4, the biphenyl unit accounts for a shift of 205 mV, and the additional methyl group adds a further 60 mV. Varying the tail group has a notable effect on the film stability with increasing stability going from BP4OH to HBP4 to BP4. The hydroxyl group destabilises the film, this may be due repulsive dipolar interactions between neighbouring molecules<sup>152</sup>, or related to the increased solubility of alcohol molecules. Interestingly, Poirier noted that for MC6 SAMs the introduction of an hydroxyl tail group changed the packing arrangement of molecules<sup>153</sup>. The desorption charges for BP4 and HBP4 indicate that an equivalent packing density is observed. The peak narrows for BP4OH. In general the peak width is a measure of the uniformity of the SAM, a broad peak, is expected for a more inhomogeneous film. However, there is an important exception to this general principle. Kakiuchi and co-workers presented cyclic voltammograms of SAMs of mercaptopropionic acid and propanethiol<sup>56</sup>, mercaptopropionic acid has a significantly narrower peak, suggesting the tail group of the film must also be considered. This is supported by Sur et al. who report that a hydrophobic gap at SAM / electrolyte interface exists for hydrophobic SAMs<sup>154,155</sup>. Furthermore, Morin and co-workers observe that the desorption peak shape for MC16 depends on the electrolyte cation, due to each cation having a different hydration shell<sup>59</sup>. Clearly, permeability of the SAM to the electrolyte is an important consideration in peak shape analysis. The results for BP4OH are consistent with the observation that hydrophilic surfaces have a narrower desorption peak<sup>56</sup>.

#### 4.2.7 Tail Group Summary

In summary, six different comparisons are made cataloguing a total of thirteen different SAM systems. The perfluorinated octanethiol SAM is less stable than the equivalent non-substituted alkane thiol. The carboxyl tail group has a destabilising effect on the film structure, an equivalent effect to removing five methylene units. BP1 and DT are compared, this is an example of a tail group which increases interactions between molecules further stabilising the SAM. BP2 and PET are compared, there is a notable difference in the electrochemistry due to the extra phenyl ring, with a shift of 180 mV. The removal of the methyl group from BP3 and BP4 has the effect of slightly decreasing the film stability, but the packing of the films appears to remain unchanged. Interestingly the magnitude of the change is different for BP3 to HBP3 and BP4 to HBP4. BP3 to HBP3 has a shift of 35 mV compared to the shift of 60 mV for BP4 to

HBP4. The peak positions and desorption charges for these SAMs are fully consistent with the established odd-even effect in the shift of the peaks for methyl terminated biphenyl thiols. However, without the full homologous range of HBP<sub>n</sub> molecules the odd-even effect can not be absolutely confirmed. Examining BP4OH demonstrates that the presence of the hydroxyl group decreases the film stability and that the desorption peak narrows. In two cases the presence of a functional tail group destabilises the SAM, carboxyl and hydroxyl groups. There are however two ways in which the group could cause a decrease in the SAM stability. Repulsive interactions, either through negatively charged carboxylate electrostatic repulsions or dipole repulsions between neighbouring hydroxyl groups could render the SAM less stable to desorption. Alternatively, the destabilisation could be due to some kind of solvation effect. The desorption requires counter ion penetration through the film in order to maintain charge neutrality. The counter ions have a solvation shell of water molecules. SAMs containing a carboxylate or hydroxyl group have a hydrophilic surface therefore, energetically, the counter ions are more likely to reside in and around the SAM | electrolyte region and penetrate the film as far as the tail group extends. On average, the counter ions will sit closer to the electrode surface and complete penetration of the SAM will be easier relative to the hydrophobic SAMs. In one case the presence of a functional tail group stabilises the SAM, a thiol. It is envisaged that disulfide formation can occur, this is in essence an increase in intermolecular interactions through a covalent bond. The overall increase in stability is equivalent to the stability realised for the addition of six methylene units. However, the energies can not be directly compared due to the fact that the molecules may have to slightly adjust their conformation and orientation to accommodate the disulfide bond. In every case, attractive intermolecular interactions in the tail group stabilise the SAM whereas repulsive intermolecular interactions in the tail group destabilise the SAM.

### 4.3 Head Group Influence

The head group to substrate interaction is the principal driving force for self assembly, it is a crucial aspect of the stability of SAMs. Two very different head group types are explored, head groups with a single point connecting the molecule to substrate and molecules with the potential to connect to the substrate at more than one point. SAMs with a single atom head group are the commonly known system, SAMs with a sulfur

head group are compared with their selenium head group analogue. Comparison of these systems reveals differences in stability<sup>41</sup> and conductivity<sup>42</sup> caused by the head group. These are important considerations for future development of molecular electronics, and rational design of SAM systems. This is followed by a look at molecules with multiple binding points, which have received less attention in literature<sup>7,156-162</sup>. Molecules could potentially bond to the substrate with two or three sulfur atoms while maintaining their upright close packed conformation.

### 4.3.1 Sulfur / Selenium Head Group

Both sulfur and selenium containing small molecules spontaneously form monolayers on gold substrates. Both head groups have similar properties although selenium is larger and more polarisable than sulfur. The hard / soft bonding concept described by Pearson<sup>41,163</sup> predicts that the interaction strength between gold, a soft acid, will be greater with a softer base. Selenium is softer than sulfur due to the increased polarisability. The strength of the bonding between Au-S and Au-Se is assessed using the peak position in cyclic voltammetry. Two different comparisons are made, a biphenyl disulfide is compared with a biphenyl diselenide and a perfluorinated thiol is compared with a perfluorinated diselenide. Figure 4.26 shows the structure for the biphenyl disulfide and the biphenyl diselenide.

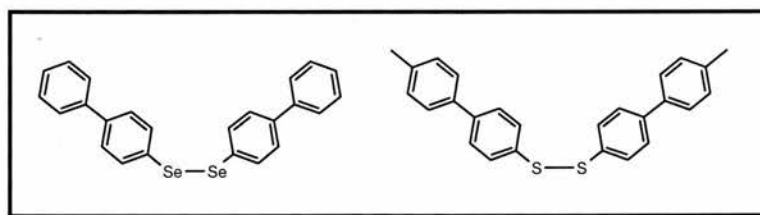


Figure 4.26: BPSe (left) and BPO (right), BPSe is a diselenide, BPO is a disulfide. BPSe and BPO have different tail groups, BPO has a methyl unit that is not present in the equivalent position on BPSe.

Comparing BPO with BPSe, there are differences in both the tail group and head group, the influence of the different tail group is discussed. The tail group difference is exactly the same as for HBP3 / BP3 and HBP4 / BP4 illustrated in subchapter 4.2. In both cases the methyl group increased the stability of the SAM. The additional methyl unit in the tail group of BPO contributes to the film stability, and this influence is considered in the

assessment. The methyl tail group is expected to increase the stability by approximately 35-60 mV for a molecule of this length.

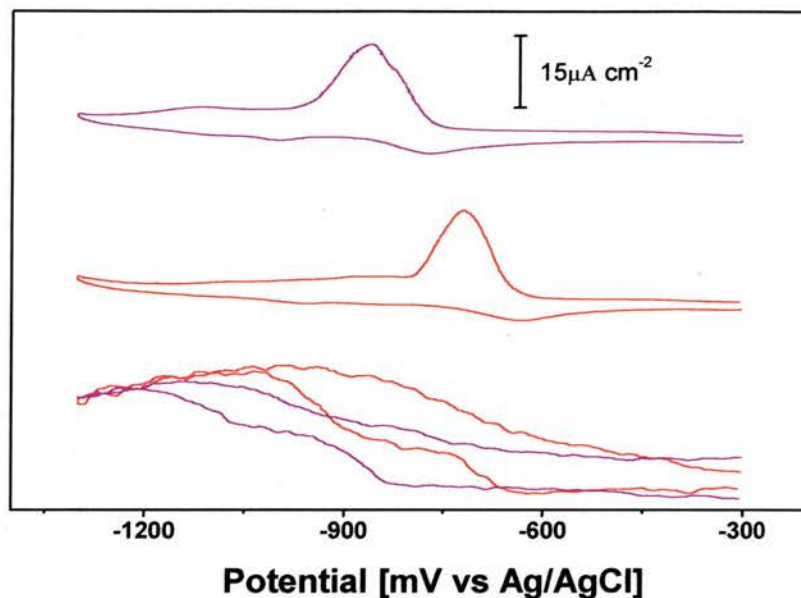


Figure 4.27: CV and SHG for BPSe (purple) and BP0 (red) at 20 mV/second. Both demonstrate unusual SHG features in the desorption and re-adsorption scan. The minimum SHG intensity is 30% of the intensity at  $-1300$  mV. Samples prepared at  $22^{\circ}\text{C}$ .

CVs and SHG for the two systems are shown in figure 4.27, the most prominent difference is the desorption position, BPSe desorbs at a more negative potential than BP0, BPSe is considerably more stable. The desorption potential for BPSe is  $-875 \pm 28$  mV, compared to BP0 desorption potential of  $-700 \pm 16$  mV. Noting that BP0 has an additional methyl unit stabilising the layer, the different tail group influence is considered. Were the exactly analogous molecules available, assuming the additional methyl group contributes to the film stability as it does for BP3 and BP4, the difference would be greater than 175 mV recorded here. The significant difference of 175 mV is therefore due to the difference in interaction between the head group and substrate. The selenium head group-substrate bond is considerably stronger than the sulfur head group-substrate bond. Close examination of the CVs reveals unusual features which are mirrored by SHG. For both BPSe and BP0, there is a reductive feature continuing past the main desorption peak. This is paralleled by the SHG which shows a step-wise intensity increase. On the anodic scan there are two well separated re-adsorption peaks which are, again, paralleled by the SHG. Similar results have been observed for other small molecules such as PET and MC4. The origin of this unexpected result is not clear.

Since this type of feature has only been observed for small molecules the phenomenon can be related to the size of the molecule. It could possibly be due to the formation of a flat lying phase after a partial desorption or it could be due to the relative increased interaction between the head group and substrate at step sites. These features are not observed for larger molecules with greater intermolecular interactions. Due to the non-ideal desorption peak shape, selection of a baseline and peak integration can not be performed. The desorption charge can not be established from these CVs. Interestingly, STM investigations have noted that BPSe forms well ordered films whereas BP0 does not<sup>151</sup>. Altering the head group has a profound effect on the long range ordering of molecules.

Another comparison of the S-Au bond with the Se-Au bond is made using another system with a perfluorinated octane chain. Figure 4.28 shows the chemical structures for the perfluorinated molecules, CFS and CFSe.

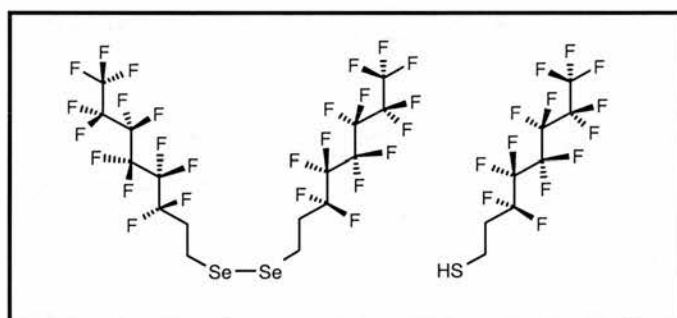


Figure 4.28: CFSe (left) and CFS (right), CFSe is a diselenide, CFS is a thiol.

Cyclic voltammograms for the two SAMs are shown in figure 4.29, CFS has a single peak whereas CFSe has an early reduction onset followed by a main peak with a distinct shoulder on the cathodic side. The peak positions for CFS is  $-940 \pm 8$  mV, CFSe peak position is  $-1040 \pm 16$  mV. CFSe desorbs at a potential 100 mV more negative than CFS. The selenium head group-substrate bond is considerably stronger than the sulfur head group-substrate bond. Qualitatively this is in good agreement with the biphenyl molecules described above, where the selenium to gold bond is stronger than the sulfur to gold bond. The peak width for CFS and CFSe are compared, the CFS peak width is  $44 \pm 2$  mV compared to the CFSe peak width of  $86 \pm 14$  mV. The peak width for CFS is approximately half of the CFSe peak width. The desorption charge for CFSe can not be

accurately determined due to the uncertainty in determining the baseline. The SHG changes parallel the desorption and readsorption peaks. The incomplete readsorption observed by voltammetry is supported by the SHG. Comparing the starting SHG intensities reveals that the starting intensity for CFS is significantly lower than for CFSe. Referring to the results and discussion in subchapter 4.2.1, where the SHG response for CFS is compared to MC8, it is noted that the MC8 starting intensity is comparable to the CFSe intensity. The similarity of starting SHG intensities for MC8 and CFSe indicate that CFS is a unique case. A diminished starting SHG intensity is observed when the perfluorinated moiety and a thiol head group are combined. This suggests there is a polarisation effect which can only occur through the thiol head group.

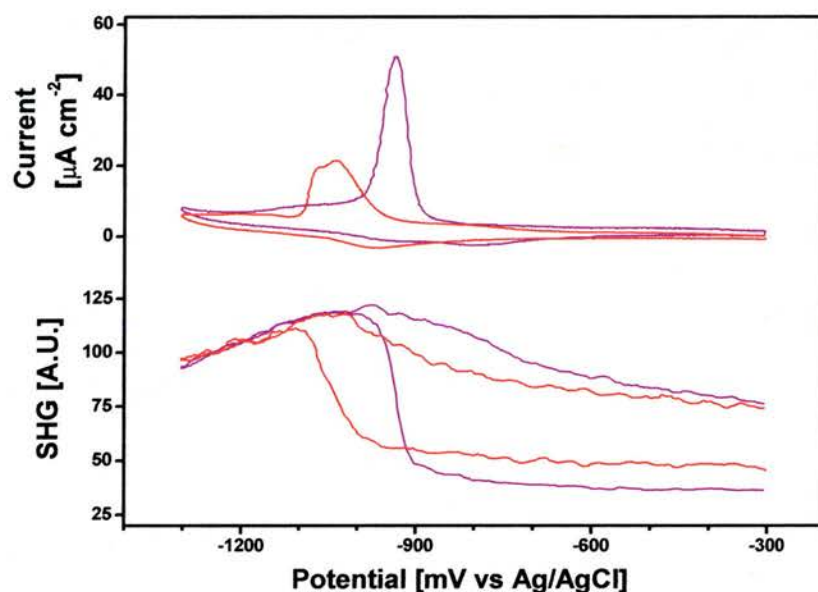


Figure 4.29: CV (top) and SHG (bottom) for CFS (purple) and CFSe (red) at 20 mV/second. Samples prepared at 22°C.

In summary, the Selenium to gold bond is stronger than the sulfur to gold bond. Selenols desorb at potentials more negative than thiols. For the biphenyl molecules the difference is 175 mV, for the perfluorinated system the difference is 100 mV. The influence of the head group-substrate interaction relative to the intermolecular interaction is greater for the biphenyl systems explaining the two different shifts. This is analogous to the difference that one methylene unit makes in an alkane thiol, for short molecules it shifts the desorption potential by 40 mV, but for long molecules it shifts it by only 13 mV. Cross referencing the desorption potentials with the alkane thiol of equivalent stability, figure 4.2, reveals that BP0 and MC1 have similar stability, BPSe

and MC5 have similar stability, CFS and MC6 have similar stability and CFSe and MC10 have similar stability. The difference in desorption potential due to the replacement of sulfur with selenium is equivalent to the potential shift provided by four extra methylene units. This result is in agreement with results from other groups where the Se-Au interaction is stronger than the S-Au interaction<sup>41,163</sup>.

### 4.3.2 Molecules with Multiple Binding Points

There is a class of molecules which potentially could attach to the gold surface with two<sup>7,156,157</sup> or three<sup>158-162</sup> sulfur atoms while maintaining the favoured upright conformation allowing close packing of molecules. Dipod and tripod molecules shown in figure 4.30 represent this unique class of molecule for SAM formation. BP2 is the mono-thiol that is structurally similar to dipod and tripod, and is used as a reference.

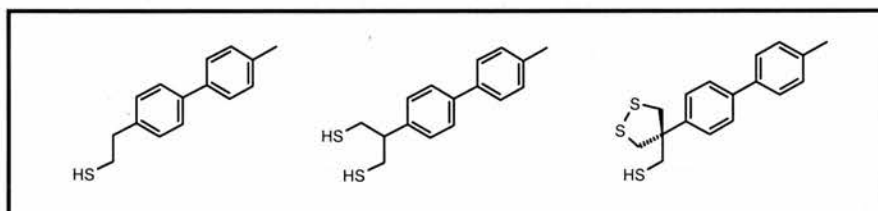


Figure 4.30: BP2 (left), dipod (middle), tripod (right). The molecules have one, two and three sulfur atoms respectively.

The structure of dipod and tripod SAMs are considerably more complicated than that of BP2 SAMs due to the interplay of many competing factors. The molecule-substrate interactions, Au-S-C bond angle, geometric constraints, intramolecular interactions and intermolecular interactions all add to a system that is rather complicated. Additionally, there is the possibility of intermolecular disulfide formation, either cross-linking of adsorbed molecules or tethering of molecules to the surface through an adsorbed molecule. The presence of a disulfide link between neighbouring molecules does not contribute to the desorption charge. Experiments on dithiol SAMs, subchapter 4.2.3, suggest that disulfide bonds link tail groups. The desorption charge indicates that the disulfide bond is not reduced during desorption. Previous work has been performed on these systems using XPS and IR spectroscopy<sup>164</sup>. XPS indicates that for both dipod and tripod SAMs there is a mixture sulfurs, some are bonded to gold, while others are not bonded to gold. IR spectroscopy indicates the biphenyl units are tilted away from the surface normal.

According to the generic SAM model, figure 1.1, where molecules contain a head group, spacer and tail group, dipod and tripod have their sulfur atoms in the head group only. This is the key difference to other dithiols reported in literature<sup>88</sup> and in this thesis (subchapter 4.2.3) where one sulfur atom is located in the tail group. It is envisaged that dipod and tripod molecules can bond to the surface through more than one sulfur atom while maintaining the upright conformation with close packing of molecules. Considering the preferred Au-S-C bond angle of  $104^\circ$ , tilting of the biphenyl unit relative to the surface normal is expected for both dipod and tripod SAMs. A maximisation of the number of Au-S bonds is favourable whereas other factors such as sterical hindrance and bond angle constraints can limit the number of Au-S bonds for an individual molecule. The structure of the thermodynamically most stable conformation for dipod and tripod SAMs is difficult to predict due to the complex interplay of energetics. Indeed, it is unclear if the thermodynamically most stable structure is even formed. It is likely that the kinetics of film formation plays a particularly crucial role in structure of dipod and tripod SAMs. Electrochemical experiments are performed with a view to gaining some understanding of the properties of dipod and tripod SAMs.

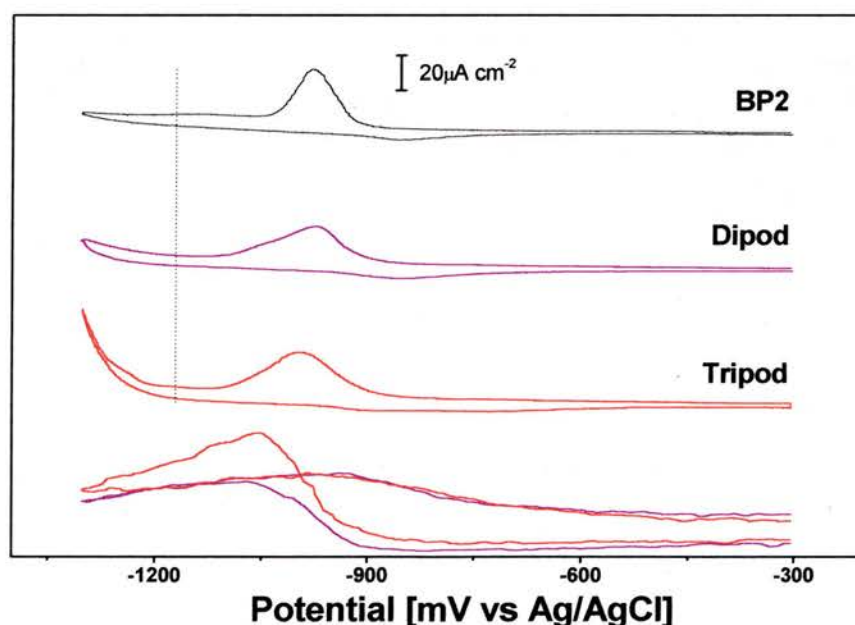


Figure 4.31: CVs for BP2 (black), dipod (purple) and tripod (red) on Au/mica at 20 mV/second. SHG for dipod (purple) and tripod (red), the minimum SHG is 60% of the dipod intensity at  $-1300$  mV. Samples prepared at  $22^\circ\text{C}$ . The SHG for BP2 is comparable to the SHG for dipod. The dotted line at  $-1170$  mV is referred to in the text.

Figure 4.31 shows the cyclic voltammograms for BP2, dipod and tripod. The desorption position for all three SAMs are within a 20 mV range from  $-995$  mV to  $-975$  mV indicating that the stability of the three SAMs are similar. There is a systematic tendency for tripod SAMs to desorb at slightly more negative potentials indicating a small increase in SAM stability relative to dipod and BP2 SAMs.

The peak shapes for BP2 and tripod show a single peak, for dipod there is a single peak with a small shoulder on the cathodic side of the peak maximum. BP2 has a peak width (FWHM) of  $59 \pm 9$  mV, this compares to 109 mV for dipod and 108 mV for tripod. The peak widths for the desorption of dipod and tripod are remarkably similar. The broad peaks indicate a gradual breakdown of the film structure suggesting that there may be a relatively inhomogeneous film. This is not surprising considering the complicated interplay of energetics involving molecule-substrate interactions, the gold-sulfur-carbon bond angle, geometric constraints, intramolecular interactions and intermolecular interactions.

The desorption charges for a SAM consisting of BP2, dipod and tripod are  $92 \pm 6$   $\mu\text{C cm}^{-2}$ ,  $106 \pm 1$   $\mu\text{C cm}^{-2}$  and  $127 \pm 6$   $\mu\text{C cm}^{-2}$  respectively. The desorption charge is clearly related to the number of binding points per molecule in the respective SAMs. The faradaic contribution to the desorption charge is linearly proportional to the overall number of Au-S bonds present in each SAM. The faradaic contribution is equal to the difference of the total desorption charge and the capacitive contribution. The total desorption charge is known and the capacitive contributions can be estimated. For BP2 prepared at  $22^\circ\text{C}$  the coverage, accounting for packing faults at domain boundaries is estimated to be about 88%. Using the methodology used in subchapter 4.1.2, the capacitive contribution is calculated. Noting that the faradaic charge is  $59$   $\mu\text{C cm}^{-2}$  for a BP(even) SAM with 100% coverage and assuming a coverage of 88% for a sample prepared at  $22^\circ\text{C}$  the faradaic charge is  $52$   $\mu\text{C cm}^{-2}$ . Subtracting the faradaic charge from the total charge for BP2 gives a capacitive charge of  $40$   $\mu\text{C cm}^{-2}$ . Dipod and tripod SAMs have a similar thickness and desorption potential, therefore, the capacitive contribution should be similar. However, it is possible that dipod and tripod SAMs have a greater porosity, and are more susceptible to counter ion penetration. The capacity of dipod and tripod SAMs are likely to be greater than that of BP2 SAM. The assumed capacitive contribution to the desorption charge of  $40$   $\mu\text{C cm}^{-2}$  for dipod and tripod must

therefore be considered an upper limit. Using the assumed capacitive contribution of  $40 \mu\text{C cm}^{-2}$  the faradaic contributions are calculated. The faradaic contributions for BP2, dipod and tripod are  $52 \mu\text{C cm}^{-2}$ ,  $66 \mu\text{C cm}^{-2}$  and  $87 \mu\text{C cm}^{-2}$  respectively. The faradaic contribution is linearly proportional to the total number of Au-S bonds present in the SAM. Therefore, the overall density of Au-S bonds for dipod and tripod SAMs are greater than observed for BP2. This aspect is discussed in more detail below for the individual SAMs relating the overall Au-S bond density to the number of Au-S bonds in individual molecules with a view to identifying the possible number of binding points per molecule.

The SHG results for dipod and tripod are examined. For tripod there is a characteristic overshoot upon desorption. The SHG maximum occurs at  $-1055 \text{ mV}$  before the end of the desorption peak at  $-1125 \text{ mV}$ . As discussed in subchapter 2.1.4, it is possible that some kind of local surface rearrangement or relaxation occurs when molecules adsorb on gold. The surface could adopt an arrangement different from the established  $(1 \times 1)$  or  $(\sqrt{3} \times \sqrt{3})$  structures, i.e. a more disordered or locally rearranged state. The overshoot is attributed to a surface rearrangement after desorption of molecules. After desorption the surface rearranges from the disordered or locally rearranged state to the  $(\sqrt{3} \times \sqrt{3})$  reconstructed state. SHG has previously probed the transition between  $(1 \times 1)$  and  $(\sqrt{3} \times \sqrt{3})$  surface structures for gold (111). Despite the fact that the experimental conditions are very different, a change in the SHG intensity by nearly two orders of magnitude was observed<sup>74</sup>. This is a clear demonstration that rearrangement of surface atoms can indeed result in a change in the SHG intensity. The magnitude of the observed SHG change assigned to a surface rearrangement after desorption of a tripod SAM is within a reasonable scale relative to the SHG change for a  $(1 \times 1)$  to  $(\sqrt{3} \times \sqrt{3})$  reconstruction. The SHG overshoot feature observed here is different to the feature observed for the desorption of long chain alkane thiols, figure 4.1, where the layer impedes counter ions from accessing the surface. The starting magnitude of the SHG for dipod and tripod can not be compared with other thiols due to the unknown effects of the SAM-metal interface.

The hydrogen evolution region for the three cyclic voltammograms shows considerable variation despite all three samples having identical experimental conditions. The ratio of the hydrogen evolution current at  $-1300 \text{ mV}$  to the measured current at  $-1170 \text{ mV}$  on

the cathodic scan is determined. -1170 mV is a potential close to the potential where the current maximum for oxygen reduction is observed, figure 3.10. This compensates for any slight differences in trace oxygen. The overall range of current densities at -1170 mV was less than  $2 \mu\text{C cm}^{-2}$  indicating that any oxygen influence is negligible. The results are as follows: BP2 has a ratio of 1.09, dipod has a ratio of 2.02, tripod has a ratio of 4.92. The increased hydrogen evolution is an indication of an increased step edge density and surface area, i.e. roughening of the electrode surface. It is possible that the kinetic barrier for hydrogen evolution is decreased as monatomic hydrogen can collect at step or kink sites. There are considerable differences in the roughness of samples considering that identical substrates were initially used. There is a substantial roughening of the surface during film assembly for dipod and to a greater extent tripod SAMs. The source of the roughening is the complex interaction of the molecules with the substrate. The maximisation of Au-S bond formation is in opposition to the optimisation of the Au-S-C bond angle of  $104^\circ$ . The Au-S interface may be reconstructed as the opposing forces are balanced. Reconstruction of the surface, in combination with making and breaking of Au-S bonds amounts to a disruption of the surface. Pits and adatoms are introduced, which on a larger scale leads to formation of small islands or pits and a greater number of step edges increasing the extent of hydrogen evolution. There are a few other occasions where such irreversible roughening like this is observed. Formation of a dithiol SAM increases the hydrogen evolution relative to the thiol SAM (subchapter 4.2.3) and for repeated electrochemical desorption and reabsorption cycling of MC16 on Au/mica. Additionally, Au/Si substrates, which are initially rougher than Au/mica (subchapter 3.3.2) produce larger hydrogen evolution currents (figure 4.33).

The voltammetric reabsorption features of BP2 and dipod are similar, whereas for tripod it occurs over a large range, from -950 to -600 mV. It should be noted that despite the similar SHG magnitudes during reabsorption, the SHG signal can not be relied on to measure the extent of reabsorption due to the unknown influence of the surface reconstruction. The reabsorption features for tripod are examined with a faster scan rate. For a scan performed at 50 mV/second the reabsorption features become much clearer, figure 4.32. There are two clear reabsorption peak maxima separated by about 200 mV. This type of double reabsorption feature is different to the double peaks observed for

MC16 where there is a complete readsorption. The double readsorption feature suggests that there are at least two sulfurs bonded to the gold surface for tripod.

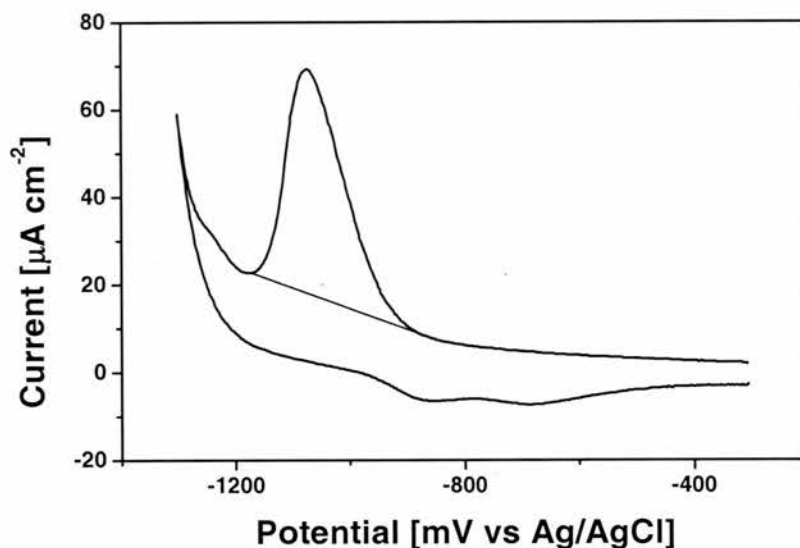


Figure 4.32: Cyclic Voltammogram for tripod molecule, scan rate 50 mV/second with thorough degassing. Two readsorption peak maxima are observed, at  $-850$  mV and  $-685$  mV. Sample prepared at  $22^\circ\text{C}$ .

The calculated faradaic contributions for the reductive desorption of dipod ( $66 \mu\text{C cm}^{-2}$ ) and BP2 ( $52 \mu\text{C cm}^{-2}$ ) are examined with a view to determining the number of sulfur atoms bonded to the gold per dipod molecule. For dipod, there is an increase in the number of Au-S bonds by 27% relative to BP2. It is known that BP2 forms a well ordered film, for dipod the structural information is limited. Three possible cases exist: all dipod molecules bond with one thiol only, all dipod molecules bond with two thiols or molecules bond with a mixture of one and two thiols. It is possible to exclude the possibility that all dipod molecules bond with one thiol only. This would require a space of about  $21 \text{ \AA}^2$  per dipod molecule, i.e. a packing density comparable to a  $(\sqrt{3}\times\sqrt{3})$  unit cell observed for alkane thiols. This is an unfeasible proposition due to sterical hindrance and bond angle constraints. An ordered film with each dipod molecule attaching to the surface through two sulfurs is now considered. The packing density of dipod molecules would be 64% of the BP2 packing density. This corresponds to an area of about  $42 \text{ \AA}^2$  per dipod molecule. The biphenyl unit would have to tilt away from the surface normal to accommodate the bond angle constraints on the molecule. However, it is unlikely as a relatively large area of gold would be prone to adsorption of additional dipod molecules. Additionally, this possibility is in conflict with the XPS data which

indicates that two different sulfur types are observed<sup>164</sup>. Therefore, the only possibility is that there is a mixture of binding points, with some molecules attached through one sulfur atom and others attached through two sulfur atoms. The film is likely to be relatively inhomogeneous. This is supported by the peak width, which suggests that there may be an inhomogeneous film with an average number of sulfurs bonded to the surface per molecule between one and two. The roughening of the surface evidenced by increased hydrogen evolution indicates that there is a significant disruption to the surface during dipod assembly. In order to gain a better insight into the film structure, further investigation by other techniques such as sum frequency generation and scanning tunnelling microscopy are required. Dipod SAMs represent a complicated example; tripod SAMs are similarly complicated by the nature of the head group.

The calculated faradaic contributions for the reductive desorption of tripod ( $87 \mu\text{C cm}^{-2}$ ) and BP2 ( $52 \mu\text{C cm}^{-2}$ ) are examined with a view to determining the number of sulfur atoms bonded to the gold per tripod molecule. For tripod, there is an increase in the number of Au-S bonds by 67% relative to BP2. Considering all of the logically possible cases, tripod could bond uniformly with one, two or three sulfur atoms, or there could a mixture involving a combination of one, two or three bonded molecules coexisting. The possibility that tripod molecules could all bond to the surface through one sulfur can be unequivocally excluded. The packing density would be about  $16 \text{ \AA}^2$  per tripod molecule, which is significantly lower than the area required for alkane thiols. Additionally, the double readsorption feature suggests that there are at least two sulfurs bonded to the gold surface. The possibility that tripod molecules could form a SAM with all molecules bonded to the surface with two sulfur atoms is considered. This would correspond to a packing density of about  $32 \text{ \AA}^2$  per tripod molecule. Intuitively, this is a plausible scheme, however, it raises two questions, why does dipod not adopt the same packing arrangement? And why is the tripod desorption charge transfer larger? Considering that the additional moiety in the tripod molecule should inhibit close packing, it is unclear if tripod adopts an ordered structure with two sulfurs bonded to the surface and dipod does not. The possibility that tripod molecules could form a SAM with all molecules bonded to the surface with three sulfur atoms is considered. This would correspond to a packing density of about  $48 \text{ \AA}^2$  per tripod molecule. If three sulfurs could all attach to the surface, then the head group would have to be symmetric, forcing molecules to stand upright. This case is extremely unlikely for a number of reasons. The preferred Au-S-C

bond angle of  $104^\circ$  is incompatible with the symmetrical geometry required by this binding mode. The XPS data indicates that there are two different types of sulfur<sup>164</sup>. IR data indicates that the biphenyl moiety is tilted from the surface normal. The possibility of this binding mode can be excluded. There is the possibility that molecules bind to the surface with a mixture of one or two sulfurs. This is supported by the peak width which suggests an inhomogeneous film is formed. The large hydrogen current points to considerable disruption to the gold surface during film assembly suggesting there is a competition between various binding modes. The picture is further complicated by the possibility that tripod molecules can cross-link or tether molecules to the surface through a disulfide link. Additionally there is a likelihood that some kind of gold surface rearrangement occurs which is linked to the interaction of the molecules with the surface.

The results for BP2, dipod and tripod molecules prepared at  $22^\circ\text{C}$  have been thoroughly examined. A few key points are noted in summary, the desorption potential for BP2 and dipod are very similar, about  $-985\text{ mV}$ . Tripod is more stable by about  $10\text{-}20\text{mV}$  for room temperature prepared samples, possibly due to disulfide cross-linking. The charge transfer for dipod and tripod are greater than for BP2, indicating that there are more sulfur to gold bonds. The peak shapes are broad, and in conjunction with the charge transfer values and the observed hydrogen evolution, the electrochemistry suggests the possibility of an inhomogeneous film for both structures with molecules bonding with varying numbers of sulfurs. Furthermore, the hydrogen evolution indicates a roughening of the gold surface during the film assembly. For tripod there is a large systematic overshoot in the SHG at the desorption potential. These factors point to a reconstruction of the gold surface. The reconstruction is facilitated by the interaction of the molecules with the gold surface. There is a conflict between the preferred Au-S-C bond angle which tends to tilt the biphenyl unit away from the surface normal and the maximisation of the number of Au-S bonds which requires the biphenyl unit to stand upright to maximise the packing. These competing factors result in a SAM structure that subjects strains on the surface. The apparent surface rearrangement is a result of the overall system minimising the surface energy. The fine details of the interface region are not clear, however, the structural properties are expected to be sensitively dependant on the preparation conditions. The data suggests that the kinetically favoured structures have been formed with  $22^\circ\text{C}$  preparation temperatures. Preparation of samples using lower

thiol concentrations, higher preparation temperatures or annealing steps could potentially produce a SAM with a more thermodynamically favoured structure. Relating the odd-even effect to the structure of dipod and tripod SAMs it is envisaged that well defined structures would be observed if the molecules were based on a BP3 molecule rather than BP2. Additionally, the structure on a silver substrate is expected to be remarkably different as the expected Ag-S-C bond angle is  $180^\circ$  allowing close packing of upright molecules.

Considering both the Selenium based molecules and the multiple binding points it has been demonstrated that the head group substrate interaction is a crucial aspect of the overall SAM stability, packing and order. The following subchapter examines the substrate influence on the SAM stability. The molecule-substrate interactions are the principal driving force for self assembly and both head group and substrate factors enter into the energy balance, their influence on the film stability and ordering is central to achieving high quality films.

## 4.4 Substrate Influence

The influence of various aspects of the substrate on the overall SAM stability is examined. There are three different variables that could be altered, the substrate element, the substrate roughness or the crystallographic orientation. Substrates of the same element but different roughness' or crystal orientations are to some extent overlapping cases because one manifestation of a rough sample is the presence of step edges or regions that are equivalent to the surface of another low index cut. In this subchapter two gold (111) substrates with different roughness' are compared, Au/Si and Au/mica. Additionally, surfaces of a different element, silver and gold are compared, the preparation conditions are very similar and it is expected that the roughness should be comparable.

### 4.4.1 Roughness

Two different gold substrates are compared, Au/mica with a roughness of 1.07 and Au/Si with a roughness of 1.19 as determined in subchapter 3.3.2. Figure 4.33 illustrates

the cyclic voltammogram and SHG for MC16 on Au/mica and Au/Si highlighting the influence of the substrate quality.

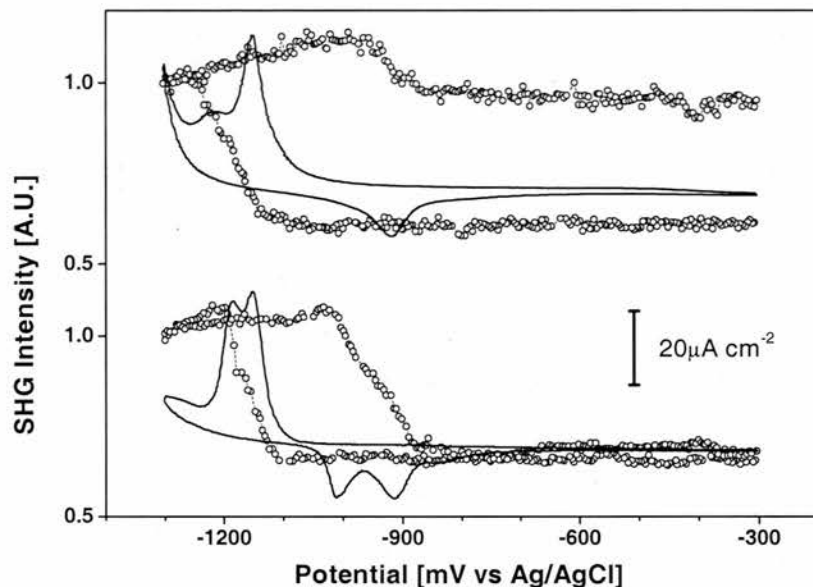


Figure 4.33: Cyclic voltammogram and SHG for MC16 on Au/Si (top) and Au/mica (bottom). Samples prepared at 22°C.

Hexadecane thiol samples were compared because cyclic voltammetry data for hexadecane thiol has been studied in detail on Au (111) single crystals. Cyclic voltammograms and SHG are pronouncedly different for the two substrates. For the (111) Au/mica the cyclic voltammogram shows double peaks both during reductive desorption and oxidative readsorption which are characteristic for a high quality Au (111) surface. In contrast, the Au/Si sample shows a cyclic voltammogram typical for a rough gold surface. A large desorption peak is followed by a small and broad second wave and a single readsorption peak. While the first peak for each cyclic voltammogram appears at the same potential irrespective of the substrate, the second peak is observed at more negative potentials for Au/Si compared to Au/mica, the peak separation is about 70 mV and 30-40 mV, respectively. This second wave on the Au/Si substrate is explained by the presence of steps, kinks, and crystal faces other than (111)<sup>81,141,165</sup>. Consistent with differences in surface quality of the two types of substrates is the larger hydrogen evolution from Au/Si. It is noted that multiple cycling of Au/mica substrates also increases the hydrogen background due to roughening of the gold surface through a disruption to the gold surface during desorption and readsorption. The difference in the substrate is also reflected in the readsorption. The Au/Si sample shows only one peak

while for Au/mica an additional wave precedes the one seen on both substrates. Comparison of the readsorption charges yields a significantly lower value for Au/Si ( $43 \mu\text{C cm}^{-2}$ ) than for Au/mica ( $81 \mu\text{C cm}^{-2}$ ). The result for Au/Si is not a kinetic phenomenon as the SHG signal does not decrease substantially over longer periods of time. This irreversibility is characteristic of the first cycle. In subsequent cycles the magnitude of the change of the SHG signal is equal for desorption and readsorption. This is in contrast to Au/mica substrates where a substantial readsorption is observed for several tens of cycles. The surface morphology has a critical role in the readsorption of long chain alkane thiols. The source of this effect is not clear.

The desorption of the thiols causes the SHG signal to increase. Taking the maximum SHG signal at  $-1250 \text{ mV}$  and  $-1210 \text{ mV}$  for Au/Si and Au/mica, respectively, as points of complete desorption, this corresponds to a change by about 65% from the value for the SAM covered substrate. Comparing this value with other data in literature it is noted that the increase in SHG intensity is in the same range as observed earlier for thiol film formation under non-electrochemical conditions<sup>118</sup> and is significantly different from other SHG studies of electrochemical desorption of alkane thiols<sup>55</sup>. In the latter experiments, however, the axis along the  $[\bar{1}10]$  direction of a Au (111) single crystal was chosen which involves different tensor elements and, thus, could alter the magnitude of  $\chi_{\text{int}}$ .

It is noted that for MC16 on Au/mica the SHG signal at  $-1210 \text{ mV}$  is slightly higher for the cathodic scan compared to the anodic one. Consequently, the slope of the potential dependent SHG signal is somewhat steeper. This overshoot is characteristic for MC16 on Au/mica. The hysteresis points to a change in the potential distribution across the Au-S/SAM/electrolyte interface between the potential immediately after desorption on the cathodic and anodic scan. This is interpreted as an indication that the layer stays largely intact, which impedes counter ion penetration to the metal surface for a short time before micelles are formed.

Comparison of the SHG with the CV data reveals that the currents are paralleled by the optical signal. Irrespective of the substrate, the SHG signal extends over both desorption peaks. Furthermore, the minimum between the two desorption peaks corresponds to a plateau in the SHG signal. Even though the number of data points together with the

signal to noise ratio might make the clear presence of a plateau questionable, the fact that it is observed in many separate experiments suggests that this is a real effect. The match between SHG and CV continues during readsorption. Similar to desorption, the minimum in the current in case of the Au/mica sample is expressed by a change in slope of the SHG signal.

Summarising this section, the roughness of Au/Si (1.19) and Au/mica (1.07) is shown to significantly influence the reductive desorption features of hexadecane thiol. The results for Au/mica display the characteristic double desorption and readsorption peaks which are characteristic for a well-defined Au (111) single crystal. This is in good agreement with the conclusions from the surface roughness experiments, subchapter 3.3.2. The extent of readsorption of hexadecane thiols onto Au/Si is significantly lower than on Au/mica substrate. This indicates that the surface morphology has an important influence on the electrochemical features. The different surfaces both have identical features on an atomic length scale, i.e. both have (111) terraces of gold atoms. However, due to the differing densities of step edges, stresses on the surfaces may result in a different surface response. The extent of rearrangement of surface atoms may differ, and hence the interaction energies between the surface and adsorbates may differ.

#### 4.4.2 Gold / Silver Substrate

The influence of the substrate material on the SAM properties is examined. Silver and gold surfaces are compared. Subchapter 2.1.2 highlights some of the similarities and differences between (111) Au/mica and (111) Ag/mica substrates. Both substrates are prepared using the same conditions and are expected to have identical topographic features. However, the substrate-thiol energy corrugation for silver is flatter than for gold<sup>8</sup> which has a profound difference on the properties of the resulting SAM.

Figure 4.34 compares the cyclic voltammograms. MC7 is chosen as a reference system because a characteristic double peak is reported for a Ag (111) single crystal<sup>10</sup>, and the peak is outwith the hydrogen evolution region allowing a desorption charge transfer determination. The double desorption peak feature is observed for the reductive desorption from Ag/mica confirming that the substrate is of a quality suitable for electrochemical investigation. The desorption peak for MC7 on gold and silver is at –

960 mV and -1180 mV respectively, a difference of 220 mV. Alkane thiol SAMs on silver are more stable than on gold. The desorption charge transfer for MC7 on silver is  $120 \mu\text{C cm}^{-2}$  compared to  $108 \mu\text{C cm}^{-2}$  for MC7 on gold. This is a strong indication that the packing density of alkane thiols on silver is greater than on gold and that the unit cells and tilt angles are different. Due to the flatter substrate-molecule interaction corrugation for silver the energy difference between an on top and hollow site is lower for silver substrates than gold substrates<sup>8</sup>. The interplay of chemisorption and chain-chain interactions determines packing of molecules, because on top to hollow site energy differences are lower for silver than gold the chain interactions can dominate the packing to a greater extent than on gold. The unit cell for alkane thiols on silver is  $(\sqrt{7}\times\sqrt{7})R19.1^\circ$  and it is accepted that the packing density of molecules is greater on silver compared to on gold<sup>8,10</sup>.

Examining biphenyl thiols, a clear difference in voltammetry is observed. The peak shapes are notably different for the two substrates. The desorption of BP(odd) SAMs from silver involves multiple peak features which span over 500 mV, whereas BP(even) SAMs produce narrower desorption peaks similar to those observed on gold surfaces. This is a striking difference to the desorption peaks on gold which all display peaks with a narrow desorption range.

The results for the desorption of SAMs from silver are a good illustration that not all multiple peaks are the same. Different types of multiple peaks are observed in figure 4.34. Firstly, BP6 and BP12 have desorption and readsorption double peak features similar to MC16 on gold where intermolecular interactions are a significant. Secondly, as noted earlier, MC7 has an established double desorption peak feature. However, this is attributed to a mismatch in the unit cell for MC7 and the Au surface resulting in desorption from two different adsorption sites<sup>10</sup>. Lastly, BP1, BP3 and BP5 SAMs display multiple peak features, which have a separation of over 500 mV. The readsorption for MC7, BP1, BP3 and BP5 SAMs is incomplete. This is a fundamental distinguishing feature from the double features observed for BP6 and BP12. However, the deviation in peak separation between MC7 and BP(odd) SAMs is not clear. Nevertheless, it is clear that not all multiple peaks can be considered equivalent.

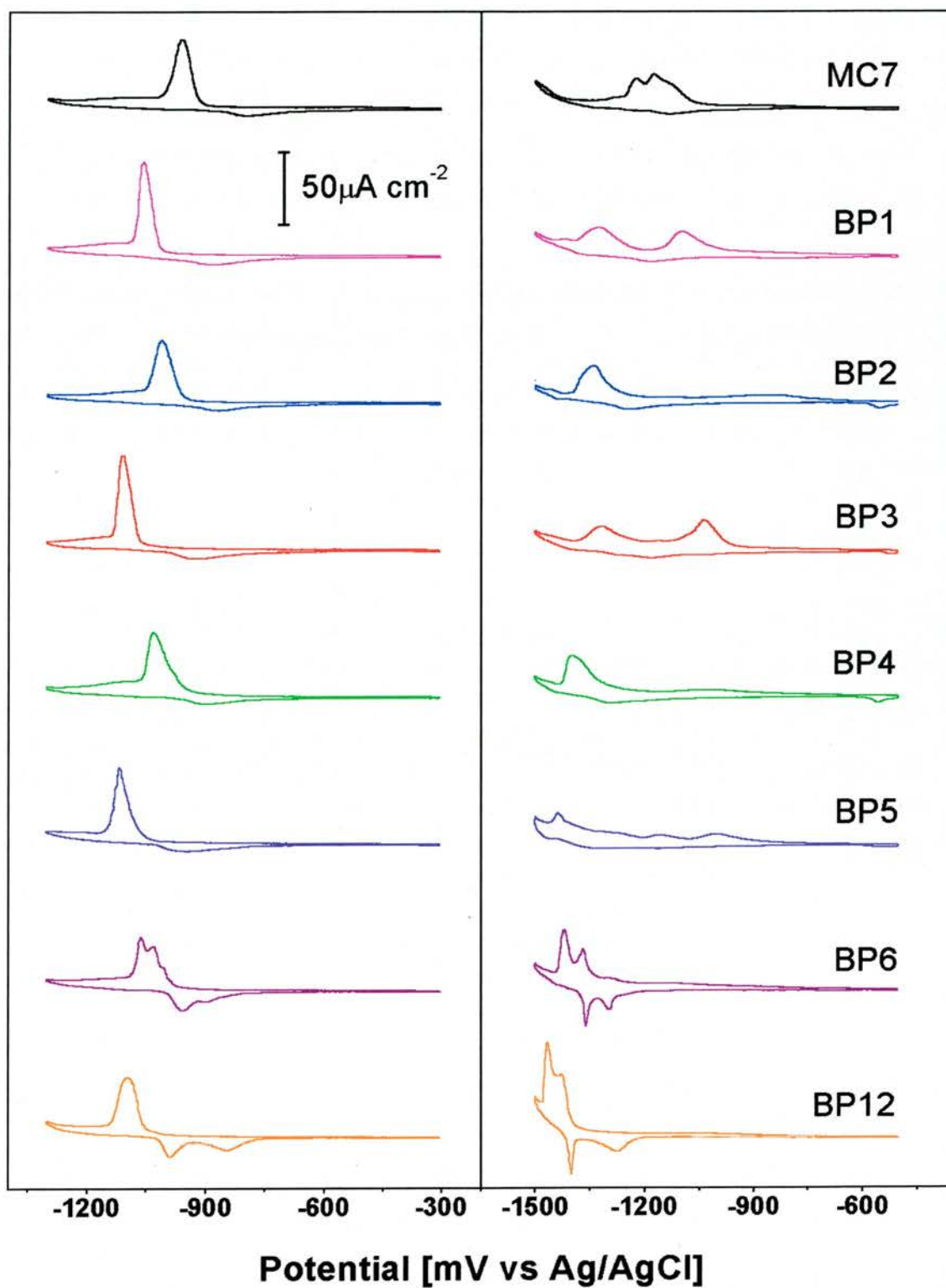


Figure 4.34: Cyclic voltammograms for MC7, BP1-6 and 12 on (111) Au/mica (left) and (111) Ag/mica (right). Samples prepared at 22°C.

One consequence of the desorption features spanning over 500 mV is the unreliability of the desorption charge determination. Selection of a baseline that spans over 500 mV introduces incredibly large errors. Moving the baseline by  $1 \mu\text{A cm}^{-2}$  results in a  $25 \mu\text{C cm}^{-2}$  change in the calculated charge transfer for samples acquired at 20 mV/second. This makes determination of the peak area, and hence the desorption charge impossible. Furthermore, due to the evolution of hydrogen, selection of the baseline is hindered for BP(even) SAMs as well as BP(odd) SAMs.

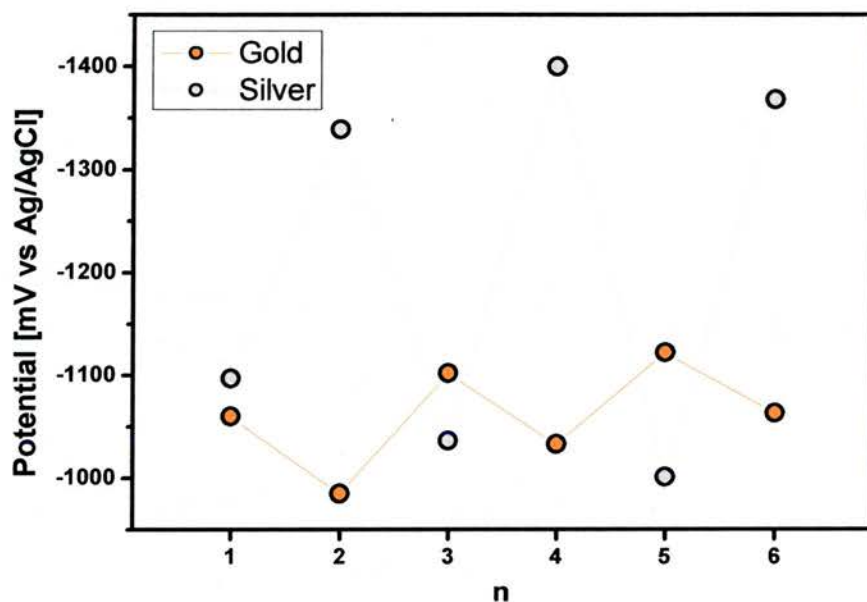


Figure 4.35: Comparison of the peak position for the BP series on gold and on silver.

Figure 4.35 highlights the reversal of the odd-even effect going between gold and silver surfaces. The trend for more negative desorption potentials is observed for these samples as the average desorption position on silver is 150 mV more negative than on gold. The reversal of the odd-even effect is clearly observed as BP(even) molecules are more stable than BP(odd) molecules. Additionally, the odd-even separation on silver is about 4-5 times greater than on gold. The reversal of the odd-even effect is attributed to a change in the hybridisation of the sulfur<sup>94</sup>. The hybridisation of sulfur on gold is  $sp^3$ , this causes a bond angle,  $\xi$  (appendix 4) of about  $104^\circ$ , on silver the sulfur is  $sp$  hybridised tending to give a bond angle,  $\xi$  of  $180^\circ$ .

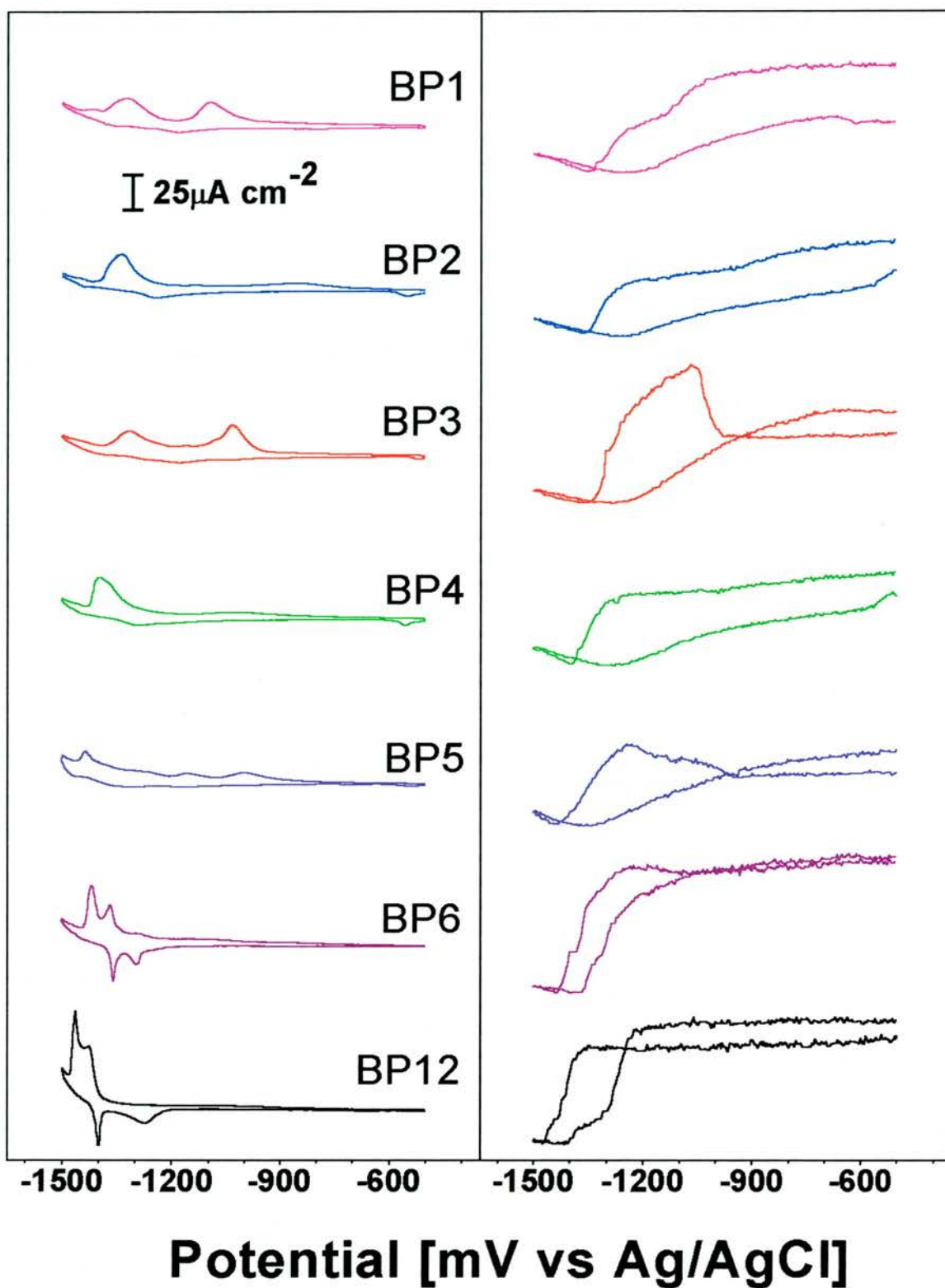


Figure 4.36: Cyclic voltammograms (left) and SHG (right) for BP1-6 and 12 on Ag/mica, the SHG scale is normalised, at  $-1500$  mV the SHG intensity is about 15% of the maximum intensity. Samples prepared at  $22^\circ\text{C}$ .

Comparison of the SHG results for the biphenyl thiol homologue series on the two different substrates reveals some very interesting points. The CVs and SHG for the desorption of biphenyl thiols from gold and silver are illustrated in figures 4.12 and 4.36 respectively. The SHG changes parallel the desorption peaks for both substrates. However, the SHG responses for gold and silver substrates are diametrically different. Firstly, there is a decrease in SHG intensity for the complete desorption of SAMs from silver compared to an increase in SHG for desorption from gold. Although, for BP3 and BP5 the SHG intensity increases over the first desorption peak, followed by a large decrease over the following peak. Additionally, the SHG intensity behaviour in the region where the molecules have desorbed is different, on gold the SHG decreases as the potential becomes more negative, whereas on silver the SHG intensity increases. The SHG contrast is much larger on silver compared to gold. On silver, the SHG intensity after desorption is only about 10% of the starting intensity, i.e. the signal intensity changes by an order of magnitude. With gold the SHG intensity after desorption is typically 165% of the starting intensity. There is a change in intensity by less than a factor of two. The SHG is about six times more sensitive to desorption on silver surfaces. The phase factors and optical constants for the two materials have profound influence on the SHG intensity. The difference in behaviour of the SHG vs. potential for the two substrates can be understood with respect to the phase factors. However, the SHG response for BP3 and BP5, which exhibit an increase in intensity prior to a decrease cannot be explained. Additionally, due to a lack of calibration for the  $\chi_{Ag}$  factor, the correlation of charge to coverage can not be examined.

## 4.5 Summary

The previous four subchapters examined the spacer, tail group, head group and substrate influences on the overall SAM stability sequentially. Reviewing the results reveals that all four factors contribute to the energy balance of SAMs and influence the stability and structure of these systems.

Subchapter 4.1 demonstrates the influence of the spacer group on the overall SAM stability, molecules with a greater number of methylene groups in the spacer have greater intermolecular interactions and more stable layers. Alkane thiols represent the simplest class of thiol SAMs and were examined. The charge for desorption is within

the experimental error, unaffected by the chain length, for samples prepared at 22°C the charge of desorption is  $108 \pm 3 \mu\text{C cm}^{-2}$ . The peak shape is dependent on the chain length, short molecules (MC7-MC10) display a single peak, MC16 has a double peak and MC22 has a single peak, this is explained in the following chapter with reference to the desorption mechanism. Biphenyl thiols prepared at 22°C and 70°C were examined, a clear odd-even effect was observed for these SAMs with differences in desorption potential, peak area, and peak width depending on the number of methylene units in the spacer group. BP(odd) SAMs have a greater packing density, more stable films, greater desorption charge and narrower peaks. Superimposed on the odd-even effect is the trend for longer molecules to have more stable SAMs. Additionally, BP6 is the first biphenyl thiol to consistently exhibit double desorption peaks and is also the first to exhibit insolubility mirroring the trend for alkane thiols between MC10 and MC16.

Subchapter 4.2 examines the influence of the tail group on the overall film stability. Six different comparisons are made. MC8 and CFS are compared, the perfluorinated SAM has a lower electrochemical stability by 50 mV, peak shape and areas are very similar. MC16 and MHA are compared, the carboxyl tail group produces instability in the SAM, a narrower desorption peak is observed. BP1 is compared with DT, the dithiol is shown to stand upright, the thiol tail group improves the film stability presumably through disulfide formation. BP2 is compared with PET, the additional phenyl ring and methyl group have a notable influence on the overall stability. HBP3 and HBP4 are compared with BP3 and BP4 respectively; there is a difference of around 50 mV in stability due to the additional methyl group. This is in the same magnitude region as the stability generated by an additional methylene group in the spacer of an alkane thiol. BP4OH is compared with BP4; the hydroxyl group decreases the electrochemical stability by 110 mV. It has been demonstrated that tail groups can improve (thiol) or worsen (carboxyl or hydroxyl) the overall stability of the SAM.

Subchapter 4.3 examines the influence of the head group on the overall film stability. Replacing a sulfur head group with a selenium head group increases the film stability by an equivalent of four additional methylene units. Head groups with two (dipod) and three (tripod) sulfur atoms were compared with the equivalent molecule with one sulfur in the head group (BP2). The stability of the three films were similar, although slightly larger desorption charges and broader peaks were observed for dipod and tripod

molecules, suggesting inhomogeneous films were formed. The hydrogen evolution was considerably greater for these systems indicating that the surface was roughened during film formation.

Subchapter 4.4 examined the influence of the substrate on the overall film stability and electrochemical behaviour. It has been demonstrated that the substrate type and quality have an extremely important influence on the stability and structure of SAMs. Au/mica was compared with the rougher Au/Si, notable differences in the cyclic voltammetry of hexadecane thiol SAMs on these substrates are observed. The flatter Au/mica substrate produced results comparable to gold single crystal results. Au/mica was compared with Ag/mica, with markedly different results. Despite the very similar nearest neighbour distance for gold and silver, 2.88 Å and 2.89 Å respectively<sup>8</sup>, the electrochemical behaviour is remarkably different. On average molecules desorbed from silver at more negative potentials than on gold, in agreement with results from literature<sup>166</sup>. The odd-even effect was reversed for the biphenyl series due to the change of hybridisation of the sulfur from  $sp^3$  for gold to  $sp$  for silver.

In summary, for a generic SAM consisting of a tail group, spacer, head group and substrate, the electrochemical film stability depends on all four constituent parts of the SAM. A total of twenty six different molecules have been investigated. Tailoring SAM properties can be achieved by proper selection of the constituent parts of the self-assembling molecule. Additionally, the preparation conditions play a crucial role on the properties of the resulting SAM. An example of SAM design would be combining a selenium head group with a docosane spacer / tail group, this should result in an extremely stable SAM. Another desirable SAM property is the conductivity; BP2 and BP3 offer a good structural quality while having a high conductivity. Similarly, terphenyl based SAMs are expected to have a high conductivity with good structural perfection. SAM properties can be tailored for a specific function by correct selection of the substrate, head group, spacer and tail group combination. This rational design approach is essential for processes such as metal deposition, molecule exchange or selective desorption. One area of particular relevance to this thesis is that of copper deposition on patterned SAMs, described in chapter 6. Selective copper deposition only occurs where there is an adequate difference in the blocking properties between two SAMs. Extending this work to deposit more active metals may require use of SAMs

with a higher stability. This work lays a foundation for understanding the properties of a large variety of SAM systems, and how their properties can relate to SAM design.

## Chapter 5

# DESORPTION MECHANISM

### 5.1 Background

Discussion on the desorption mechanism for alkane thiols has largely centred on the cyclic voltammogram for the desorption of long chain alkane thiols from gold such as MC16, where double peaks are observed in contrast to shorter molecules which have a single desorption peak. Figure 5.1 demonstrates the classic double peak features for MC16, two reductive desorption peaks A and B on a cathodic scan separated by about 20-70 mV, and two readsorption peaks A' and B' with a larger separation of 40-100 mV on the anodic scan.

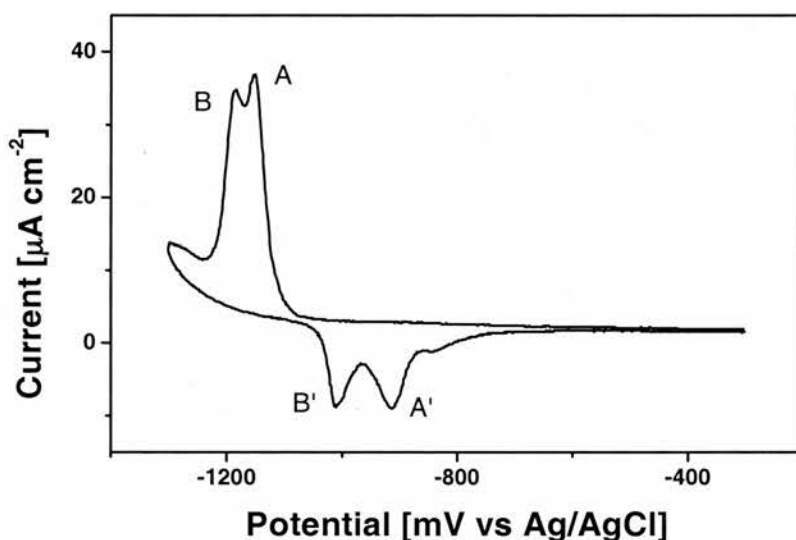


Figure 5.1: Cyclic voltammogram for the reductive desorption of MC16 at 20 mV/second. Peaks are labelled A and B for the first and second desorption peaks and B' and A' for the first and second readsorption peaks respectively. These labels are maintained and referred to throughout this chapter. The FWHM for the desorption peak is 70 mV, in contrast to 140 mV for the readsorption peak.

These double peak features are different from other multiple peak features, such as those observed for tripod SAMs on gold or MC7 / BP(odd) SAMs on silver. In this case the molecules are insoluble, double peaks occur on both desorption and readsorption scans and are observed over many cycles. The desorption mechanism responsible for the occurrence of double peak features has been of interest to understand basic

electrochemical processes at the molecular level. Several groups have investigated this phenomenon and have speculated about the origin of the source of the double peaks. A review of the literature discussing the double peak is summarised in a chronological fashion, with a view to highlighting the salient points made by various groups. The review begins with two theoretical papers describing surface confined redox species. In 1987 Matsuda et al reported that for surface confined redox species, a reversible reaction involving only one electron could produce a double peak. The condition was that the interaction between a reduced species-oxidised species pair was greater than the interaction between an oxidised species-oxidised species pair and a reduced species-reduced species pair, although SAMs were not explicitly mentioned<sup>110,111</sup>. In 1991 Porter and co-workers described the voltammetric behaviour for a series of alkane thiol SAMs: MC3 to MC18, on a variety of gold and silver surfaces, including annealed gold on mica<sup>144</sup>. However the plot for the reductive desorption of MC18 from gold on mica did not show double peaks for the desorption or re-adsorption process, and they observe “that the peak shape is not a strong function of [the chain length]”. In January 1997 Morin and co-workers published the first paper with double desorption peaks for MC16 and MC18 on a gold (111) single crystal<sup>59</sup>, the two peaks were suggested to be due to the presence of domains of different ionic permeabilities. Only two months later a paper by Porter and Zhong (claiming the first example of double peaks) was published containing a more comprehensive study of the desorption and re-adsorption processes observing double peak features for MC12 to MC16 on gold on mica<sup>135</sup>. The study was more systematic examining chain length, scan rate, scan range and pH influences, they note that the results are at least in part due to a difference in the chemical thermodynamics of the short and long chain systems. They note that peaks A and A' are linked, changing scan direction between peaks A and B results in only one re-adsorption peak at position A'. Furthermore, the double peak occurs only at high pH values. They speculate that the double peak could arise due to different hybridisation of sulfur at different binding sites, sp hybridised sulfur on top of gold or sp<sup>3</sup> hybridised sulfur in a three fold hollow site or differences in packing density, but do not make firm conclusions. In April 1998 Honeychurch and Rechnitz presented a review of the voltammetry of adsorbed molecules<sup>109</sup>, specifically reversible redox systems. In this review they discuss SAMs and crucially refer to the 1987 Matsuda papers making an implicit connection between SAMs and the double peak predictions made by Matsuda et al<sup>110,111</sup>. In June 1998 Kakiuchi and co-workers report on the reductive desorption of

MC16 on gold on mica<sup>56</sup>, they “observed no splitting of the reductive and oxidative peaks for [MC16]”, but did observe using STM the formation of aggregates at the surface after desorption, which disappeared after readsorption. In 1999, Badia et al present results for the reductive desorption of MC14 from gold (111) on mica, a cyclic voltammogram displays a single peak but they note that a double peak is observed for some samples<sup>167</sup>. Using a single crystal they present a cyclic voltammogram with double peaks for MC14, and present in-situ AFM images displaying aggregates at desorption potentials. Later that year Morin and co-workers proposed a two step model for the double peak structure observed for the reductive desorption of MC16 from gold (111) single crystal<sup>53</sup>. The peak A is a faradaic process involving the transition from chemisorbed thiols to physisorbed thiolates. Peak B is a capacitive process involving the transition from physisorbed thiolates in a lamellar structure to a micellar structure. The readsorption process is the reverse of the desorption process. The charge transfer for each peak is in general agreement with the expected charge for the process it is assigned to. They claim to rule out the possibility that two domains of different densities or that different adsorption sites are responsible for the double peak structure based on in-situ IR spectroscopy. The next month Azebara et al report that “splitting fine structure” was observed MC16 on a gold single crystal<sup>168</sup>. In April 2000, Morin and co-workers reported that the reductive desorption of alkane thiols from silver (111) single crystals produced double desorption peaks for short chain alkane thiols MC5 to MC8<sup>10</sup>, however, this is attributed to desorption from two different adsorption sites. In May 2000 Porter and Wong demonstrated the importance of the substrate surface morphology on the double peak occurrence, comparing smooth gold on mica with the rougher template stripped gold<sup>58</sup>, it was shown that flatter surfaces were essential for double peak formation. In June 2000 Calvente et al presented a theoretical paper that strengthens the links between double peak features for reductive desorption of alkane thiol SAMs and the theoretical calculations predicting double peaks based on pair interactions<sup>112</sup>. They cite papers by Morin and co-workers<sup>59</sup> and Porter and Zhong<sup>135</sup> which explicitly address the double desorption peaks, and Matsuda et al<sup>110</sup> which gives a detailed theoretical description based on pair interactions. They develop the theoretical description for surface redox processes which result in the formation of double peak structures. In 2001 Morin and co-workers report the temperature dependence of double peak structures<sup>54</sup>, increasing the temperature at which desorption occurs the double peaks to merge into a single peak, whilst the decrease of temperature causes a

separation of the two peaks. In 2002 Kakiuchi et al studied the reductive desorption of MC3 to MC14 from gold on mica, they present cyclic voltammograms with single peaks only but note that “sometimes, double peaks also appeared.” although do not stipulate which SAMs produced these<sup>76</sup>.

Summarising the review of literature, it emerges that the occurrence of the double peak is extremely sensitive to the experimental conditions as Porter and co-workers did not initially observe them<sup>144</sup> and Kakiuchi et al<sup>76</sup> and Badia et al<sup>167</sup> note that double peaks only sometimes appear. There is consensus that aggregates in the shape of micelles form after desorption of insoluble alkane thiols, Kakiuchi and co-workers observe micelles with STM<sup>56</sup>, Badia et al observes aggregates using AFM<sup>167</sup> and Morin and co-workers suggest micelle formation based on IR spectroscopy<sup>53,54</sup>. Despite the considerable attention in literature, the desorption mechanism is not certain. Reviewing the literature and considering the data, there are three models that could potentially explain the double peak formation.

1. The two step model proposed<sup>53</sup> and developed<sup>54</sup> by Morin and co-workers, where one peak corresponds to a faradaic process and the other to a capacitive process. There are questions about the two step model such as what is the driving force for micelles to unfold? If it is chemisorption then why is there a clear delay before chemisorption occurs?
2. A variation of the binding site model suggested by Porter and Zhong for gold<sup>135</sup> and Morin and co-workers for silver<sup>10</sup>. Instead of the double peaks corresponding to the selective desorption of coexisting  $sp^3$  and  $sp$  hybridised sulfur, the two peaks account for a step-wise  $sp^3$  to  $sp$  transition followed by a desorption of  $sp$  hybridised molecules. There is no detailed discussion in literature on the model involving the  $sp^3$  to  $sp$  transition prior to desorption, consequently there is no data that has ruled it out. The model is unlikely though, due to the difficulty in explaining the magnitude of the first peak in terms of this model.
3. A model involving the pair interactions described by Matsuda et al<sup>110,111</sup>, Honeychurch and Rechnitz<sup>109</sup> and Calvente et al<sup>112</sup>. All three papers predict the

occurrence of double peaks for a one electron redox process but do not assert that this is the mechanism for double peak formation for the reductive desorption of alkane thiols such as MC16.

Experiments are presented to challenge these models with a view to identifying one unifying model that is consistent with published data and all the data collected in this project.

## 5.2 Results

Various experiments using cyclic voltammetry with in-situ SHG, including complex cyclic voltammograms involving multiple scans and potential holding were performed. The two step model was tested first.

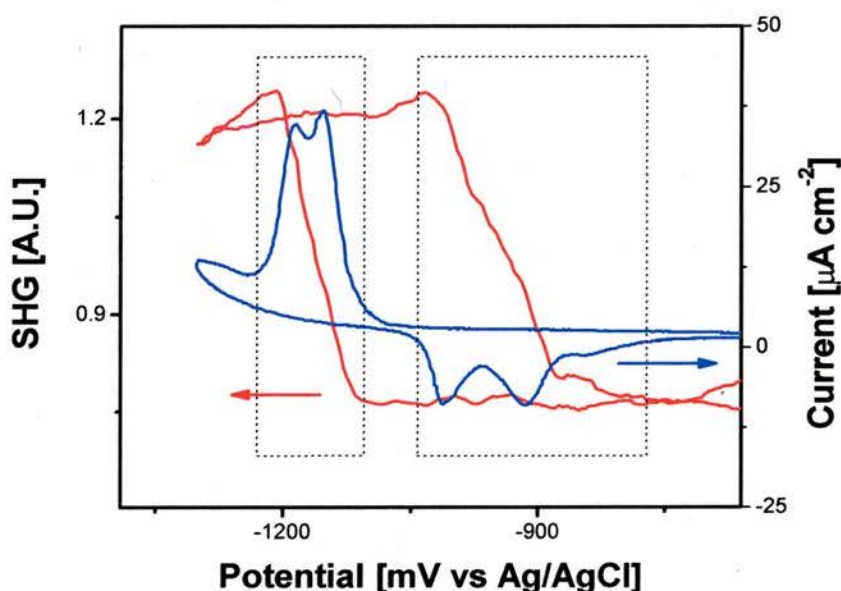


Figure 5.2: Cyclic voltammogram (blue) with in-situ SHG (red) for the reductive desorption of MC16 from Au/mica, sample prepared at 22°C. Dotted lines are provided to identify the boundaries for desorption and readsorption. On the cathodic scan the SHG begins to increase at the same potential as the onset of the desorption peak, the end of the desorption peak is marked by the dotted box. The point where the SHG deviates from a straight line going from -1300 mV towards -1200 mV on the cathodic scan is exactly at the dotted line. An overshoot of the SHG is systematically observed after desorption on the cathodic scan compared to the SHG intensity on the anodic scan.

Figure 5.2 is the cyclic voltammogram with in-situ SHG for MC16. The SHG changes occur in parallel with the charge transfer. The SHG changes parallel both desorption peaks and both readsorption peaks. For the readsorption peaks in particular, where there is a clear separation of the two peaks, the SHG changes clearly occur over both peaks. This is in conflict with the two step model where the SHG is only expected to probe faradaic processes. For the desorption peak, the coverage, determined by the SHG change, is correlated with the charge transfer, figure 5.3 illustrates the linear correlation. The line of best fit through the charge over coverage relation has a coefficient of determination of 0.993 indicating a very good linear correlation. Within experimental errors there is a linear correlation between charge and coverage, considering the two step model this is surprising result.

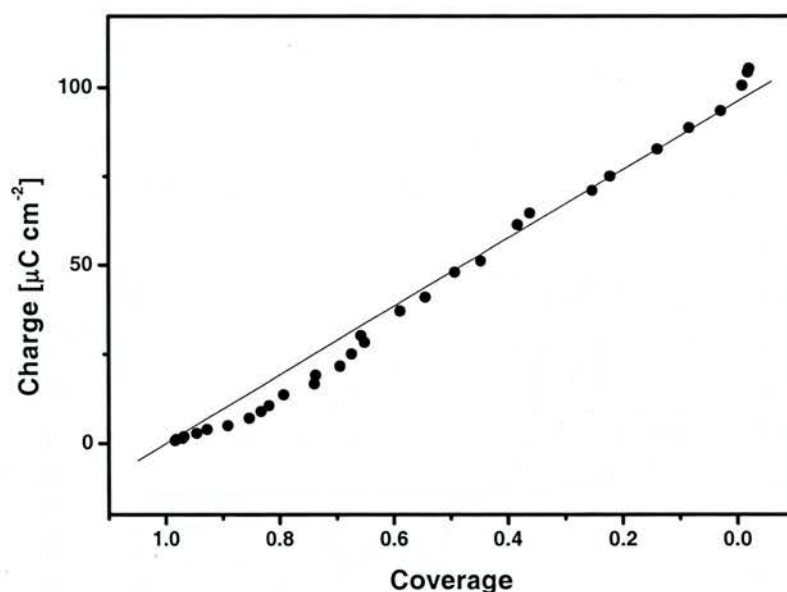


Figure 5.3: The charge over coverage ratio for MC16 where double peaks are observed. The line of best fit intersecting (1,0) is included and the  $R^2$  value is 0.993.

The SHG change for a faradaic process is not expected to be exactly the same as for a capacitive process. The SHG change is the same for both peaks, it is either an incredible coincidence that the SHG changes are identical for the two different processes or the model is incorrect. More results are presented that challenge the two step model. Porter<sup>135</sup> and Morin<sup>53</sup> have both presented cyclic voltammograms illustrating that peak A is related to peak A', reversing the scan direction between the desorption peaks A and B results in an anodic scan with peak B' absent. An equivalent experiment when the scan direction is reversed between the readsorption peaks is presented here, figure 5.4.

One cycle covering both desorption and readsorption peaks was first performed. Subsequently, three cycles were performed with a shorter scan range where the starting potential was between the readsorption peaks in the first cycle. The first cycle of the shorter scan range exhibited a double desorption peak. The following cycles include a single desorption peak, the second and third cycle of the shorter scan range are presented. The single desorption peak is observed in a position corresponding to peak A. The SHG fully supports the electrochemical data. This contradicts the two step model where peak B should not shift to less negative potentials. Another experiment continues this line of probing by holding the potential at  $-960$  mV for various fixed times between cycles.

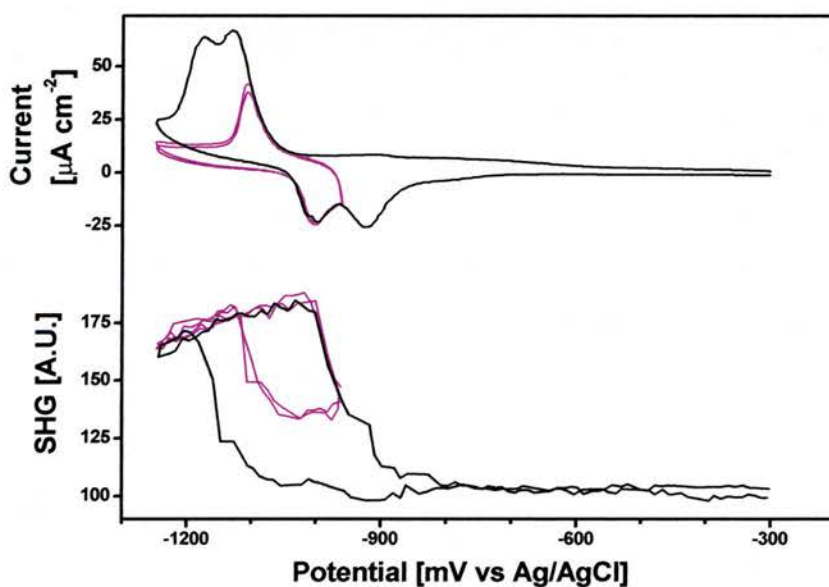


Figure 5.4: Cyclic voltammograms (top) and SHG (bottom) for MC16 at 50 mV/second. The black line is from  $-300$  to  $-1250$  mV, the purple line is from  $-960$  to  $-1250$  mV, experiments were performed consecutively, and cycles 2 and 3 of the shorter scan range are displayed.

Figure 5.5 illustrates the effect of holding the potential at  $-960$  mV, the current minimum between the readsorption peaks B' and A', for 5 seconds and 5 minutes. In both cases the resulting desorption peaks indicate a partial coverage, a complete layer was recovered in a subsequent experiment. Holding the potential at  $-960$  mV does not allow a complete readsorption but it does allow some rearrangement of molecules, after 5 minutes the desorption peak is 70 mV more negative indicating a significant increase in stability, there is an ordering during the holding time. The results of the two

experiments are difficult to explain in the terms of the two step model where a faradaic process and capacitive process are separated.

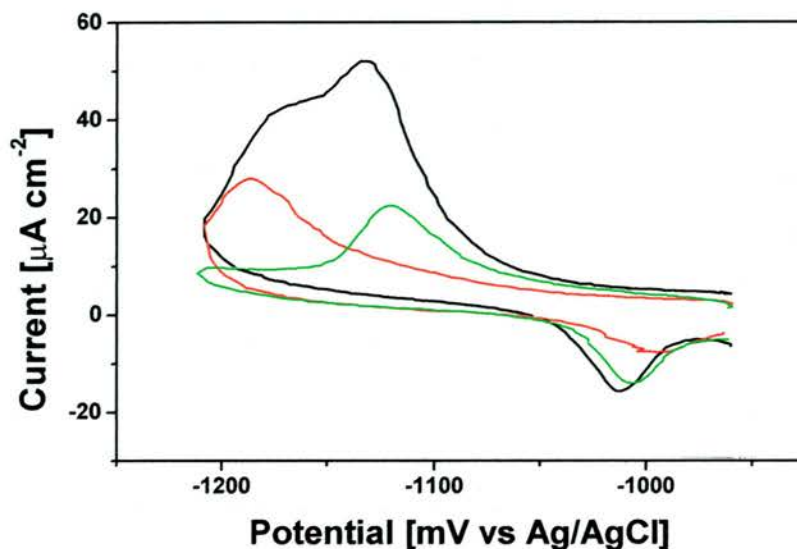


Figure 5.5: Cyclic voltammograms of MC16 at 50 mV/second from  $-960$  mV to  $-1210$  mV. The sample has been cycled several times prior to this experiment. The potential is held at  $-960$  between cycles. The black line is the CV for a complete layer, the green line is for a sample that has been held for 5 seconds at  $-960$  mV, the peak is at  $-1120$  mV. The red line is for a sample that has been held for 5 minutes at  $-960$  mV, the peak is at  $-1190$  mV.

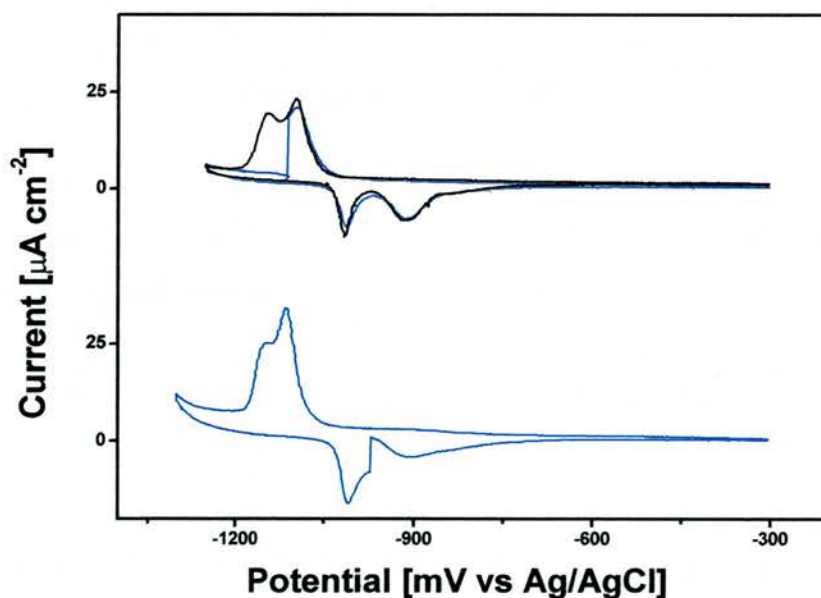


Figure 5.6: Cyclic voltammograms of MC16 at 20 mV/second. Black line has no holding, cycle is paused at  $-1110$  mV for 12 seconds (top) and paused at  $-970$  mV for 30 seconds (bottom) two different samples were used to acquire this data, overlaid results are from same sample.

Further experiments are performed involving holding during a cycle, figure 5.6. Pausing at  $-1110$  mV for a short time of 12 seconds allows a complete desorption, however pausing at  $-970$  mV for 30 seconds does not allow a complete readsorption. The charge of the readsorption peak observed immediately after holding at  $-970$  mV is  $35 \mu\text{C cm}^{-2}$  for 30 seconds of holding and  $27 \mu\text{C cm}^{-2}$  for 90 seconds of holding. In terms of the two step model, during desorption the folding of the micelle occurs rapidly after desorption of molecules, whereas during readsorption, after unfolding of the micelle the molecules do not rapidly chemisorb onto the electrode surface. Holding the potential at  $-970$  mV for 90 seconds does not fully adsorb molecules, what then is the driving force for the micelle to unfold? According to the two step model, the folding and unfolding of the micelle and corresponding capacitive charging has a lower energy barrier than the faradaic charge transfer. Considering the capacitive part involves movement and arrangement of molecules this is an unlikely scenario. The driving force for readsorption should be the formation of the Au-S bond so the result is in conflict with the two step model where the first readsorption peak is a capacitive process as the micelle unfolds and the second peak is a faradaic process as physisorbed thiolates chemisorb to the surface. The final part of testing the two step model involves comparing MC16 with MC22, figure 5.7.

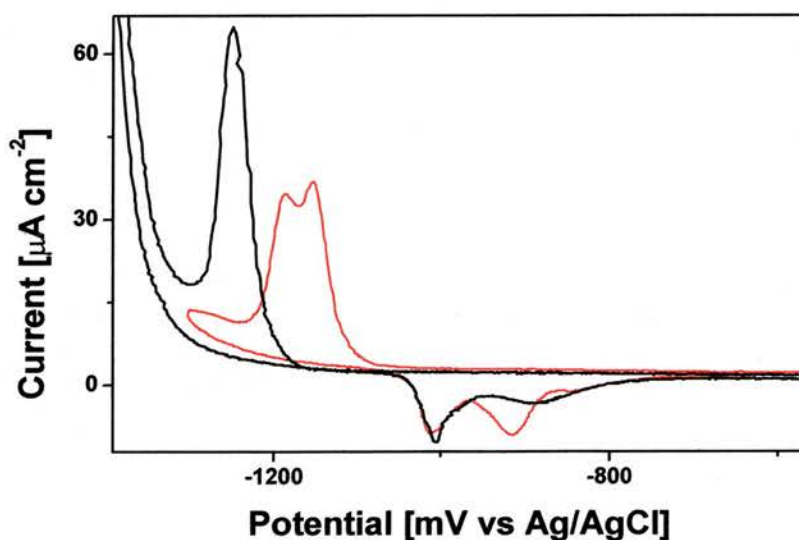


Figure 5.7: Cyclic voltammogram for MC22 (black) and MC16 (red) at 20 mV/second.

The voltammetric response for MC22 is compared with MC16, MC22 has a single desorption peak and a double readsorption peak. The peak shape for the MC22 desorption is inconsistent with the two step model, according to the model, alkane thiols

MC12 and longer produce double peaks, the observed single peak for MC22 is in conflict with the model. Additionally the readsorption peaks question the two step model. The readsorption peaks for MC16 occur at  $-1010$  and  $-915$  mV, compared to  $-1010$  and  $-890$  mV for MC22. Peaks B' have a very similar shape and position but peaks A' have dramatically different shapes and positions. Considering the two step model, peak B' is assigned to a capacitive current as micelles unfold to a lamellar structure expelling counter ions from the surface, peak A' is assigned to a faradaic process as molecules chemisorb onto the surface. Considering the shapes and positions for peak A' and B' for MC16 and for MC22 it is hard to imagine that these systems would have an identical rate of unfolding of micelles expelling ions from the double layer inferred from overlapping peak B', yet very different faradaic charge transfer processes. The readsorption mechanism in the two step model can not explain the discrepancies between the readsorption characteristics for MC22 and MC16. It is interesting to note that the shape of the readsorption peak for MC22 and BP12 are very similar, and that both molecules are of a similar length. Furthermore, the fact that MC22 has a single desorption peak and a double readsorption peak suggests the desorption and readsorption processes are not a straightforward reversal of each other. The molecules go from an ordered state to a disordered state during desorption, in contrast to going from a disordered to an ordered state during readsorption, the dynamics of the two processes are evidently different.

The two step model is incompatible with several of the results presented here.

1. The linear correlation of charge to coverage across both desorption and readsorption peaks is not expected for this model.
2. The desorption peak B position moves to less negative potentials when the scan range is such that a direction change occurs between peaks B' and A'. This is in conflict with the model.
3. Molecules will not fully readsorb within a few minutes when the potential is held between the two readsorption peaks. According to the model the second peak is due to bond formation, this is the driving force for readsorption. The readsorption should proceed rapidly to completion while the potential is held at this potential.

4. The MC22 desorption peak shape is inconsistent with the two step model which demands a double desorption peak.
5. The model cannot explain the discrepancies between the readsorption of MC22 compared to MC16.

These five factors decisively undermine the validity of the two step model. The model involving the transition from  $sp^3$  to  $sp$  hybridisation is now challenged using a BP6 on silver example. The sulfur head group on silver is  $sp$  hybridised, known from biphenyl thiol investigations<sup>94</sup>, in contrast to  $sp^3$  on gold. Figure 5.8 illustrates the CV and SHG for a BP6 on silver surface. The SHG parallels both desorption and readsorption peaks. The SHG intensity decreases for desorption of molecules from silver as described in subchapter 4.4. There is a clear plateau on the SHG change for desorption corresponding to the potential between the two peaks. On the readsorption scan the SHG rate of change is lower between the readsorption peaks. BP6 is the first SAM to display significant readsorption, this related to the insolubility of the molecules. Due to the insolubility of molecules, different interactions between molecules are encountered during the desorption process which results in the occurrence of double peak features. BP6 on gold is the first SAM to display double peak features, similarly on silver, BP6 is the SAM to display double peak features of the type observed on gold. For BP6 on silver, the double desorption peaks are 50 mV apart, readsorption peaks are 65 mV apart. This is typical of the separation of peaks for BP6 and MC16 molecules on gold. As discussed in subchapter 4.4.2, the multiple peaks for BP(odd) molecules on silver have a different origin from the features observed for BP6 on silver. For BP6 on gold and silver, the similarity of the double peak features and the fact that the same molecule is used indicates that the double peak features observed are due to the same process. Therefore, if it can be demonstrated that the double peaks observed for the desorption of BP6 on silver is not due to a change of hybridisation then the same applies for gold. The possibility that the desorption peaks from silver are due to a transition from  $sp$  to  $sp^3$  are examined. Due to the preferred Ag-S-C bond angle of  $180^\circ$  it is known that the BP6 molecules stand upright on silver allowing close packing of molecules. Due to the insolubility of BP6 it is known that during desorption of molecules the structural integrity of the SAM is largely maintained, i.e. thiolates remain within the SAM. It is therefore impossible for molecules to tilt to any significant extent as is the case for BP6 on gold due to spatial constraints. Were the sulfur hybridisation to change from  $sp$  to  $sp^3$

the SAM would be extremely unstable as the preferred bond angle of  $104^\circ$  could not be achieved. The presence of a second desorption peak indicates that the SAM is stabilised rather than destabilised during desorption. The possibility of a transition from  $sp$  to  $sp^3$  hybridisation on silver is therefore precluded; the double peak features on silver are not due to a change in the sulfur hybridisation. The double peak features for gold are due to the same process as those observed for silver, so neither are due to a change in hybridisation. In conclusion, double desorption peak features for insoluble SAMs on gold are therefore not due to a change in hybridisation from  $sp^3$  to  $sp$ .

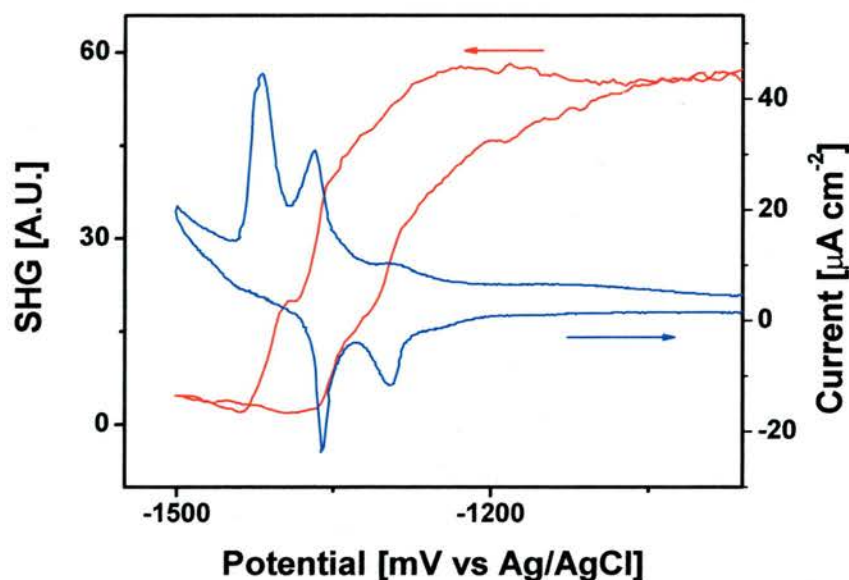


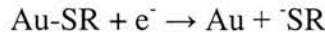
Figure 5.8: Cyclic voltammogram (blue) and SHG (red) for the reductive desorption and oxidative readsorption of BP6 on silver (111) substrate on mica at 20 mV/second.

The series of experiments above severely undermines the validity of the two step model and the  $sp^3$  to  $sp$  transition model. The third model, based on pair interactions, is described in detail and evaluated with reference to several experimental results.

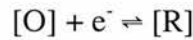
### 5.3 Pair interaction model

Several groups have proposed models for the behaviour of reversible redox reactions for surface confined species. Kakiuchi et al describe a theory that explains the shift in desorption potential for different length alkane thiols, but does not address the double peak features<sup>76</sup>. Three groups have described work involving pair interactions that generate double peaks under certain conditions for a one electron redox process<sup>109-112</sup>.

The theory described by Matsuda et al<sup>110,111</sup> using a statistical mechanical approach is outlined below. The conditions required for double peak formation due to intermolecular interactions between 6 coordinated surface confined species with strong lateral interactions are examined. For the reductive desorption of thiol molecules from a gold surface the following reaction occurs:



In terms of oxidised and reduced species the thiol bonded to gold is in the oxidised form [O], the thiolate is in the reduced form [R]:



The species briefly pass through a transition state,  $\neq$ . A two dimensional lattice is constructed, figure 5.9, with  $N$  vacancies for 6 coordinated species O, R or the transition species  $\neq$ . There is an overall number of species  $N$ , comprising  $N_{\text{O}}$  thiol molecules,  $N_{\text{R}}$  thiolate molecules and  $N_{\neq}$  transition species:

$$N = N_{\text{O}} + N_{\text{R}} + N_{\neq} \quad (5.1)$$

$N_{\neq}/N$  is assumed to be an infinitesimal quantity. There are  $3N$  pairs of nearest neighbours that can be one of five pairs, RR, RO, OO,  $\text{O}\neq$  and  $\text{R}\neq$ . Interactions between pairs of transition species are ignored due to the near zero probability of them occurring.

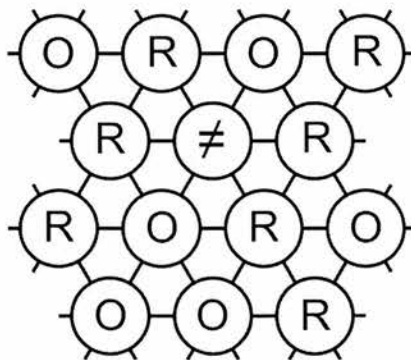


Figure 5.9: Two dimensional lattice model for thiol and thiolate surface bound species where O, R and  $\neq$  denote the thiol (oxidised form), thiolate (reduced form) and transition state respectively. Each surface bound species is surrounded by six other species. Figure is representative of a sample during the reduction process.

Denoting the numbers of pairs as  $N_{ij}$  where  $ij$  represents the pair, there are five pair types:  $N_{OO}$ ,  $N_{RR}$ ,  $N_{OR}$ ,  $N_{O\neq}$  and  $N_{R\neq}$ . Each pair has a particular intermolecular energy associated with it, the interaction energy for a pair  $ij$  has the form  $W_{ij}$ , the significant interactions are  $W_{RR}$ ,  $W_{OO}$  and  $W_{OR}$ . If the interaction energy  $W_{OR}$  is greater than  $W_{RR}$  and  $W_{OO}$ , the OR pair is more stable than OO and RR:

$$W = (W_{RR} + W_{OO}) - W_{OR} \quad (5.2)$$

$W$  is the interaction energy relating to the equilibrium potential, where there are approximately equal numbers of thiol and thiolate species. An attractive force is positive. If  $W_{OR}$  is more stable than  $W_{OO}$  plus  $W_{RR}$ , then  $W$  will be negative. When  $W/RT$  is sufficiently negative a double peak is predicted for a process involving only one electron. In cases where the interaction energy between a thiol and thiolate pair exceeds the interaction energy between a thiol-thiol pair and a thiolate-thiolate pair a double peak is therefore predicted. Describing the three relative interactions in more detail, the thiolate-thiolate pair has repulsive interactions from the head group due to electrostatic repulsions from the charges, but has attractive interactions from the alkane chains. The thiol-thiolate pair has attractive interactions between the alkane chains and attractive interactions between the head groups<sup>169</sup>. The thiol-thiol pair has favourable interactions between the alkane chains, and negligible interactions between the head groups, the forces between pairs can be considered as forces between neighbouring head groups and neighbouring chains:

$$W_{ij} = W_{ij, \text{head}} + W_{ij, \text{chain}} \quad (5.3)$$

Table 5.1 summarises the forces between neighbouring molecules.

Pair	Head group interactions	Alkane chain interactions
thiol-thiol	negligible	Attractive
thiolate-thiolate	repulsive	Attractive
thiol-thiolate	attractive	Attractive

Table 5.1: Interactions between head groups and alkane chains for OO, RR and OR pairs.

Assuming that all chains are in the all-trans conformation, the attractive force between neighbouring alkane chains is proportional to the chain length. The relative interactions between the chains are independent of the head group for surface confined species:

$$W_{OR, chain} = W_{OO, chain} = W_{RR, chain} = W_{chain} \quad (5.4)$$

The overall energy at equilibrium can be determined:

$$W = W_{RR, head} + W_{chain} - W_{OR, head} \quad (5.5)$$

Overall  $W$  contains a repulsive thiolate-thiolate force, an attractive force proportional to chain length and an attractive thiol-thiolate force. An attractive force is positive while a repulsive force is negative. The thiolate-thiolate interaction is negative which drives the overall  $W$  value to the negative. The positive thiol-thiolate interaction is subtracted so will drive the overall  $W$  value to the negative. The chain-chain interaction is positive in sign so will counter the influence of the head group interactions. If the  $W$  value is sufficiently negative a double peak is predicted. With increasing chain length, the chain-chain interactions will outweigh the thiolate-thiolate interactions, the  $W$  value will tend to positive values decreasing the likelihood of double peak features. In contrast, for shorter chain lengths, the  $W$  factor will tend to more negative values increasing the likelihood of double peak features. However, a condition for the model is that species are confined to the surface. For soluble molecules the head group interactions cease as molecules diffuse away from the surface on a time scale much shorter than the whole desorption process. The head group interactions are eliminated from the equation and the  $W$  factor becomes positive, a single peak is observed. This interpretation is consistent with the observed results for MC7 to MC22, MC7 to MC10 are soluble after desorption so repulsive thiolate-thiolate interactions are not a factor. MC16 is insoluble so thiolate-thiolate repulsions are a factor. Going to MC22 the longer chain stabilises the layer, and has a greater influence on the overall stability relative to the thiolate-thiolate repulsion. The chain interactions outweigh the thiolate-thiolate repulsion driving the  $W$  factor positive.

The above pair interaction description was based on a literature model. The pair interaction model describes faradaic charges for desorption only, whereas the readsorption process, capacitive processes and formation of micelles are not addressed. In the following paragraph a more general, molecular level mechanistic model incorporating the pair interaction model for hexadecane thiols SAMs is described. The model encompasses capacitive charging, readsorption processes and micelle formation, explaining the desorption and readsorption features of SAMs.

Starting with the pristine hexadecane thiol SAM modified electrode, the potential is scanned gradually to more negative potentials. At a sufficiently negative potential molecules begin to desorb as thiolates. Due to pair interactions between thiolate and thiol molecules the film is stabilised after approximately half of the molecules have desorbed. This results in a decrease in the rate of desorption and hence a dip in the faradaic contribution to the desorption current. This process corresponds to peak A, figure 5.1. The electrode potential is continually becoming more negative. The overpotential eventually becomes too great for the remaining molecules which then desorb, peak B. Counter ions are likely to be penetrating the film during the entire desorption process. There is a capacitive process occurring across both desorption peaks. Micelle formation begins once the majority of molecules have desorbed, and may last for a few seconds. The majority of the capacitive charging occurs before the faradaic process is complete. The molecules in a lamellar structure still impede counter ions accessing the surface. The remaining capacitive charging occurs after desorption as the micelles are formed. This hypothesis is supported by the SHG which measures an overshoot for MC16 indicating counter ions are impeded from accessing the surface. The potential continues becoming more negative until it reaches the point of inflection where the scan direction changes. Throughout this time the molecules remain close to surface in a disordered micellar structure. When the potential for readsorption is reached molecules begin to chemisorb onto the gold driving an unfolding of the micelle. Due to strong lateral interaction a degree of the micelle disorder is likely to be retained as the micelle unfolds and molecules adsorb onto the surface. Peak B' accounts for the thiolate moieties that were on the outermost sphere of the micelle, peak A' accounts for the molecules with thiolate moieties that were deeper inside the micelle. The capacity of the electrode decreases as the micelle unfolds and adsorbs onto the electrode surface. Counter ions are effectively displaced from the electrode double layer region by the

molecules. Capacitive discharging occurs in parallel to both peaks as counter ions are expelled from the interface region. Before the electrode potential reaches its final potential, but after the adsorption of molecules is complete there will be a period of rearrangement and ordering of molecules. During this period there will be a small capacitive discharging as remaining counter ions are expelled from the film. The steps for the molecular level mechanistic model are illustrated in figure 5.10.

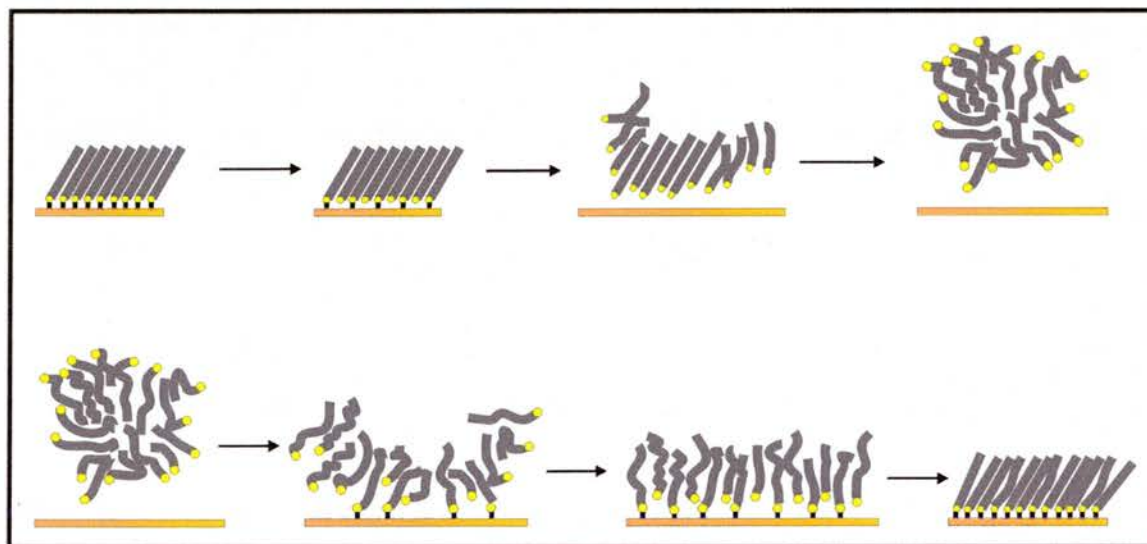


Figure 5.10: Schematic illustration of a molecular level desorption (top) and readsorption (bottom) model. A bold black line represents the gold-sulfur bond.

The validity of this model is checked by corroborating it with results in this chapter, other results in this thesis and with results from other groups. The desorption peak shapes for all alkane thiols are consistent with the pair interaction model. Readsorption peaks for MC16 and MC22 both demonstrate a broader readsorption peaks relative to the desorption peaks, figure 5.7. The time scale for readsorption is longer than for desorption due to the irregularity of the micelle. MC22 has readsorption peaks with a greater separation than MC16 suggesting entanglement of molecules becomes an increasingly significant factor. Voltammetric experiments involving holding potentials and altering the scan ranges are consistent with this model. The voltammetric data is consistent with this model. Similarly, the SHG data is consistent with this model, specifically the linear correlation of charge to coverage, figure 5.3. The experiment involving desorption of BP6 from silver is consistent with the desorption model. Examining results from previous chapters, the stability of DT compared to BP1 is

consistent with the pair interaction model. BP1 is soluble, however, a molecule that is attached to a neighbour through a disulfide link will be fixed at the surface, and the pair interaction energy becomes relevant for DT. Examining the results in literature, the influence of temperature on the desorption of molecules detailed by Morin is consistent with the pair interaction model<sup>54</sup>, when the temperature decreases, the magnitude of a negative  $W/RT$  value increases, making the double peak formation more likely. Morin reports that using SNIPTIRS spectroscopy the orientation of the molecules changes during peak B and B', this is in agreement with the model<sup>53</sup>. At lower electrolyte pH values the double peaks merge into a single peak<sup>59</sup>, in cases where solvent can penetrate through the film, protons will attach to the thiolate eliminating repulsive thiolate-thiolate interactions. The pH influence is consistent with the pair interaction model, and supports the theory that the capacitive process occurs in parallel to the faradaic process.

## 5.4 Summary

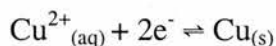
Three plausible models that could explain the desorption mechanism responsible for the double desorption and readsorption peaks for MC16 on gold are described. They are the two step model, the  $sp^3$  to  $sp$  transition model and the pair interaction model. Experiments were presented that challenged these models; two of the models were unable to explain the electrochemical and spectroscopic results. The two step model proposed by Morin is excluded; five key points that undermined the model were presented. The  $sp^3$  to  $sp$  transition model was already unlikely due to the difficulty in explaining the first desorption current and, based on a further experiment using silver, has been excluded. The pair interaction model has been described and satisfactorily explains the double peak behaviour. The model is consistent with SHG data and other electrochemical experiments. The pair interaction model, which originated from a paper published before the first double peak was observed, predicts that for a surface confined redox species, a reversible reaction involving only one electron could produce a double peak. The condition was that the interaction between a thiolate-thiol pair was greater than the interaction between a thiol-thiol pair and a thiolate-thiolate pair. A general model based on the pair interaction is described, accounting for faradaic and capacitive processes for desorption and readsorption, and is consistent with work presented in this thesis and elsewhere.

## Chapter 6

# METAL DEPOSITION

### 6.1 Introduction

Electrochemical metal deposition on SAM modified electrodes is a convenient technique to fabricate metal structures. A variety of metals have been deposited on electrode surfaces<sup>47</sup>, however, not all metals will be suited to deposition on SAM modified electrodes due to the considerable overpotentials required. Copper has successfully been used to deposit metal layers onto bare gold and thiol coated gold electrodes by many groups<sup>44,85,170-175</sup>, and due to the ease of use, is employed here. Copper is deposited from copper sulfate in sulfuric acid. The equilibrium reaction for copper deposition is as follows:



It is a two electron process, with an equilibrium potential of +0.337 vs. standard hydrogen electrode. Copper deposition on bare gold or gold modified with very small thiols<sup>176</sup> can begin with under potential deposition of copper where up to a monolayer of copper is deposited. At small overpotentials a single layer of copper is formed where the affinity of copper to the gold surface is greater than the affinity of copper to itself, with larger overpotentials multilayers of copper form. Multilayers are required to develop macroscopically detectable features on the electrode surface.

The substrate flatness and SAM properties, i.e. structural perfection and conductivity, are expected to have a profound influence on the structure of the copper deposits at the electrode interface. Modification of the SAM properties and fine tuning of the deposition conditions can tailor the structural properties of the copper deposit.

An advantage of having copper deposited on a SAM modified gold rather than on a bare gold surface is that it allows the detachment of the deposited metal. The adhesion

between the two metals is sufficiently low to allow separation of the two metals without notable disruption to the surface structure. An insulating substrate is attached to the metal deposit using an adhesive material, this is simply lifted off, shearing the metal deposit from the underlying substrate at the metal | thiol | metal interface. The face of the deposited metal layer that was buried at the interface of the two metals is now exposed. A similar process has previously been performed in combination with surface patterning by Salvarezza and co-workers<sup>177,178</sup>. Some exploratory experiments are performed to prove the feasibility of the detachment procedure for copper deposits on gold electrodes. Two examples are illustrated; surface patterning directed by SAMs using micro contact printing and metal detachment procedures using adhesives.

## 6.2 Copper Deposition and Patterning

Before more detailed and complicated electrodeposition experiments are performed the deposition / dissolution response for copper on a bare gold electrode is illustrated. A cyclic voltammogram for copper deposition and dissolution is displayed in figure 6.1. The copper deposition occurs on the cathodic scan, and dissolution on the anodic scan. For each cycle the deposition onset occurs at  $-40$  mV and the dissolution onset occurs at  $-40$  mV, the reaction is highly reversible. For the first cycle there is a current maximum of  $2.2 \text{ mA cm}^{-2}$  at  $-170$  mV for the deposition, with a current maximum of  $-17 \text{ mA cm}^{-2}$  at  $+110$  mV for the copper dissolution. With subsequent cycles the deposition, and hence dissolution peaks become gradually larger. This is likely due to a build up of copper ions in the vicinity of the electrode caused by the fact that during the experiment, for the majority of the time, ions are attracted to the electrode and will deposit onto it. There is a net migration of copper to the electrode surface. The deposition peak is typically much broader than the dissolution peak and is limited by diffusion to the electrode, the dissolution is kinetically limited and is much sharper. During repetitive deposition and dissolution the colour change of the electrode is clearly observed.

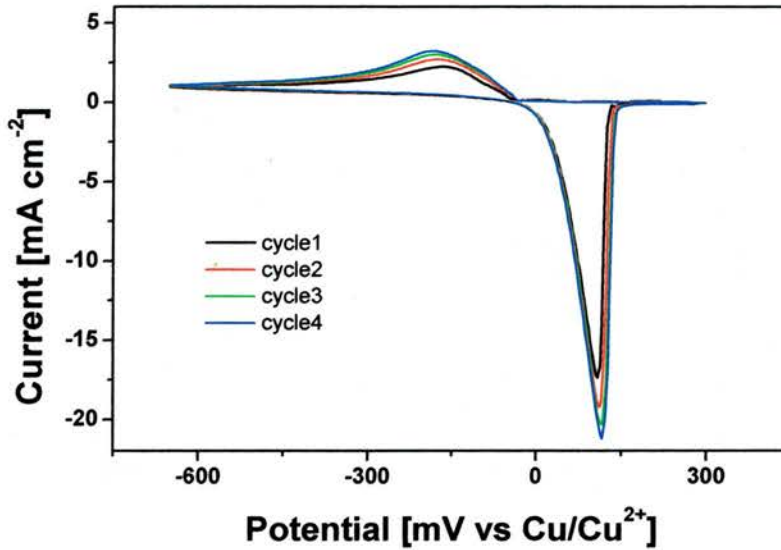


Figure 6.1: Cyclic voltammogram for repeated copper deposition / dissolution on bare Au/Si substrate, in 10 mM CuSO<sub>4</sub> / 0.5 M H<sub>2</sub>SO<sub>4</sub>, platinum wire counter electrode, copper wire reference electrode. Four cycles, starting at +300 mV, scanning to -650 mV at 50 mV/second.

The charge transfer for dissolution of the layer from the first cycle is  $19 \text{ mC cm}^{-2}$ , The copper dissolution is a two electron process, dividing by twice the charge of an electron gives a value of  $5.96 \times 10^{16}$  copper atoms per  $\text{cm}^2$ . For a single layer of copper, assuming close packing with six coordinated atoms of  $2.556 \text{ \AA}$  bond length, the area per copper atom is  $5.66 \times 10^{-16} \text{ cm}^2$ , and hence the number of atoms per  $\text{cm}^2$  is  $1.77 \times 10^{15}$ . There is therefore an average of about 34 layers of copper deposited on the first cycle. For the perfect face centred cubic crystal structure this corresponds to a depth of 5 nm. It is intuitive that a high degree of control over copper deposition could be achieved by varying electrode potential, deposition time and copper ion concentration. The depth of the copper deposit is related to the deposition time. The underlying substrate morphology and overpotential will likely influence the quality of the copper deposit in terms of flatness of the deposit and degree of crystallinity. Modification of the gold electrode has a profound effect on the copper deposition process. The influence of a monolayer of thiols on the gold electrode on the copper deposition is illustrated in figure 6.2.

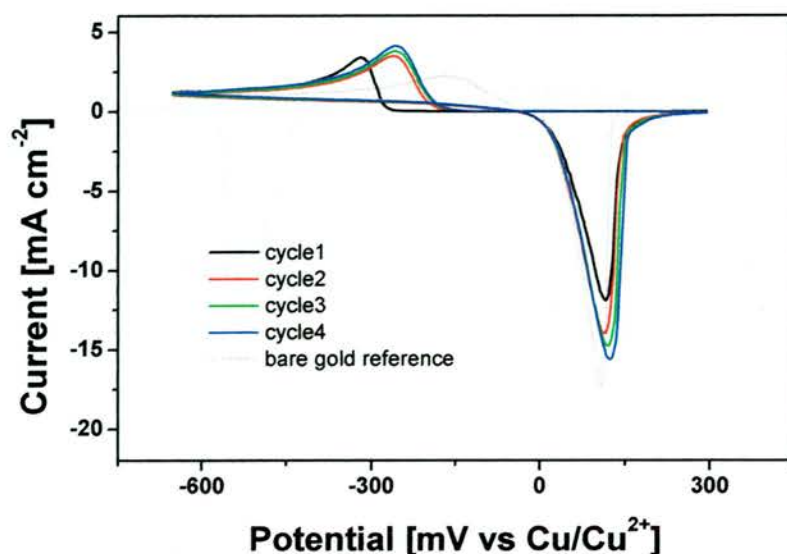


Figure 6.2: Cyclic voltammogram for repeated copper deposition / dissolution on a Au/Si electrode modified with BP4 at room temperature, in 10 mM  $\text{CuSO}_4$  / 0.5 M  $\text{H}_2\text{SO}_4$ , platinum wire counter electrode, copper wire reference electrode. Cycles 1 to 4 are displayed as well as cycle 1 of the bare gold sample, as used in figure 6.1 for reference. Starting at +300 mV, the potential is scanned between +300 mV and -650 mV at 50 mV/second.

The BP4 SAM has a profound effect on the electrochemistry of the metal deposition. There is a potential drop across dielectric SAM layer, the onset of the metal deposition occurs at -250 mV on cycle 1, this is in stark contrast to the onset at -40 mV for the control experiment with no thiol layer present, the BP4 layer inhibits copper deposition. The onset of copper dissolution is the same for BP4 covered gold and bare gold, but the dissolution maxima are slightly offset with the BP4 SAM hindering the dissolution to a small extent. The SAM layer significantly hinders the deposition, but only slightly alters the dissolution. With continued cycling the deposition peak shifts to less negative potentials indicating the blocking effectiveness of the SAM is decreased, the biggest shift happens between cycles 1 and 2 indicating irreversible structural changes occur during the first deposition / dissolution cycle. Peak areas gradually increase with continued cycling in agreement with bare gold. In terms of the deposition regimes (figure 1.4) it is likely that during the first cycle copper deposition is initiated at pinhole defect sites or domain boundaries where bare gold is exposed, and growth continues with mushroom shaped deposits. The build up of copper at the gold surface sites will irreversibly disrupt the nearest molecules, the subsequent cycles will proceed more easily as the defect site has now been enlarged by the initial deposition.

The influence of BP4 on the copper deposition is compared with the influence of the more insulating MC16, figure 6.3.

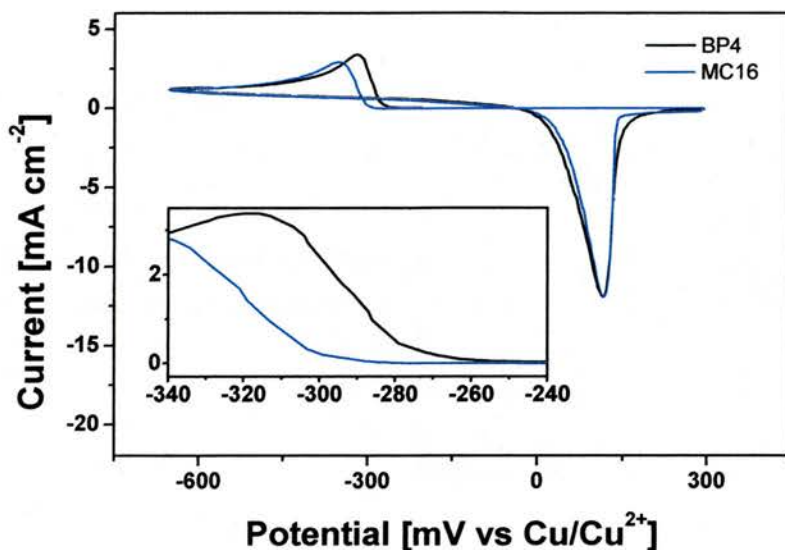


Figure 6.3: Cyclic voltammogram for one copper deposition / dissolution cycle on a Au/Si electrode modified with BP4 and one copper deposition / dissolution cycle on a Au/Si electrode modified with MC16, both immersed overnight at room temperature. The inset shows the region where the copper deposition onset occurs, there is a difference of about 30 mV in the deposition onset. Conditions were identical, 10 mM CuSO<sub>4</sub> / 0.5 M H<sub>2</sub>SO<sub>4</sub>, platinum wire counter electrode, copper wire reference electrode. Starting at +300 mV, the potential is scanned between +300 mV and -650 mV at 50 mV/second.

It is clear that both molecules impede copper deposition, however, MC16 impedes deposition to a greater extent than BP4. A small overpotential window exists where metal deposition on a conducting SAM can occur yet insulating SAMs still blocks the metal deposition. This feature of SAMs is exploited to develop patterns of metal deposits on SAM modified electrode surfaces with a resolution in the micron scale. BP2 conducts to a greater extent than BP4<sup>43</sup> so the deposition window for a sample patterned with BP2 and MC16 should be greater than a sample patterned with BP4 and MC16. Using micro contact printing, subchapter 3.1, a sample is patterned with BP2 and MC16. The substrate is stamped with MC16, then immersed in BP2 solution for 90 minutes, then annealed for 50 minutes at 70°C. The sample was quickly scanned to -300 mV to initiate the deposition, then cycled between 0 mV and -190 mV to develop the copper deposit. Figure 6.4 is an image of the sample after copper deposition on a patterned SAM, the definition achieved between MC16 and BP2 coated regions is

excellent. A control experiment using the same stamp, involving stamping the sample twice, with a  $90^\circ$  rotation between stamps confirmed that deposition occurs on the BP2 coated region and not MC16.



Figure 6.4: Photograph of a gold substrate stamped with MC16 then immersed in BP2 solution. Copper was subsequently deposited onto region coated with BP2. A periodicity of  $8\ \mu\text{m}$  is clearly defined.

The perfection of the respective conducting and insulating SAM and the electrochemical conditions are crucial parameters that must be fully explored to understand metal deposition processes on surfaces patterned with SAMs. Surface patterning with different SAM types and development of patterns with copper deposits has been achieved with a periodicity of  $8\ \mu\text{m}$  and a resolution around  $1\ \mu\text{m}$ . The potential to use patterned deposits of copper or other metals in applications is possible due to a detachment technique where the deposits are attached to an insulating substrate and lifted off the gold substrate.

### 6.3 Copper Detachment

The detachment of deposited metals from the underlying substrate can be performed on patterned or non-patterned samples. Separation of the layers with weak interaction is easily achieved, this concept has been previously demonstrated by Salvarezza and co-workers<sup>177,178</sup>. Figure 6.5 illustrates the steps for the preparation of a copper deposit then subsequent detachment from the original substrate. The detachment procedure is not possible for a copper layer deposited directly on gold, as the adhesion is too great. Presence of a thiol SAM between the gold electrode and copper layer means that there are only weak interactions between the two metals. For mushroom type growth the copper is only directly attached to the gold surface at a few pinhole sites, and for on top growth there is no direct contact (figure 1.4).

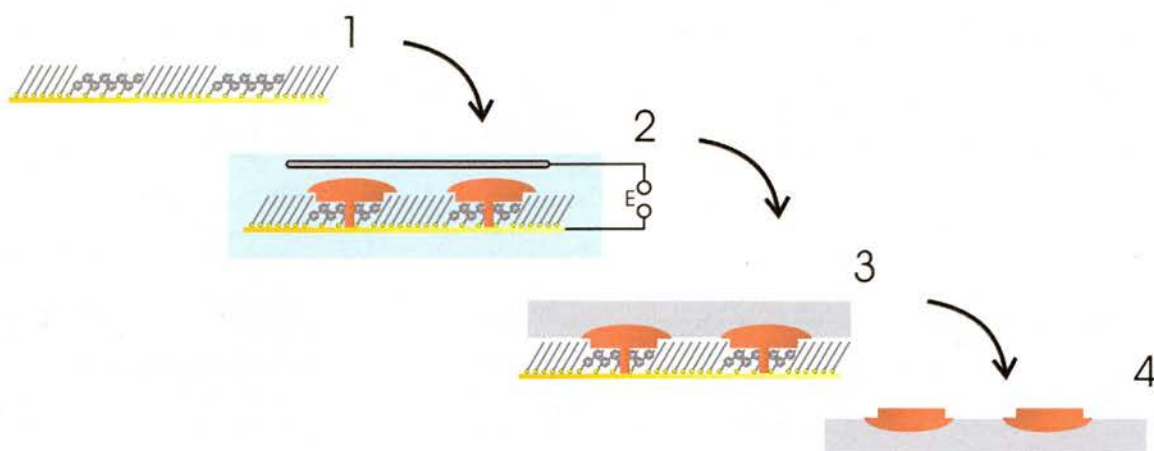


Figure 6.5: Schematic of metal deposition on a SAM patterned surface with subsequent adlayer detachment. The patterned sample (1) is assembled into an electrochemical cell where copper is deposited selectively onto one thiol type (2). The sample is removed from the cell, and using an adhesive material is attached to the sample (3), separating the top material from the gold substrate results in the copper deposits detaching from the gold surface (4).

A gold substrate is covered with thiols patterned or otherwise, the copper deposit is formed using the electrochemical method described in the previous subchapter. The electrode is removed from the cell and rinsed with water to remove sulfuric acid, then dried. An insulating substrate, such as a piece of glass is attached to the top of the copper deposit with a strong adhesive such as super glue. Once dried, the insulating substrate is detached from the gold substrate, the shear occurs at the gold | thiol | copper interface. Using a Au/Si substrate covered with hexadecane thiol a copper deposit is formed using the method described above. The deposit is removed from the gold substrate using the detachment procedure. Using STM, the newly exposed copper surface and the temporarily coated gold surface are examined, figure 6.6. Images of the two surfaces and cross sectional profiles are compared. The grain sizes for gold and copper are very similar, about 75 nm in diameter. An anisotropy of the gold and copper exists with small fingers extending from some grains, all in the same direction. This may be due to shear forces exerted during the separation of the two layers, possibly where copper–copper bonds have broken. At present, it is not clear if the fingers observed on the gold surface are remains of copper. Additional characterisation with XPS is required to elucidate this point. The cross sectional line profile shows the relative flatness of each surface, the cross section profile for the gold surface has a maximum peak to trough height of 7.5 nm compared to 14 nm for the deposited copper. The flatness of the deposited copper is comparable with the flatness of the underlying

gold surface. The copper surface is slightly rougher than the gold surface. The techniques described show promise to routinely fabricate metal microstructures on insulating substrates, with good control of thickness and surface flatness using an inexpensive and relatively straightforward technique. An excellent definition between species is observed, a resolution below 1  $\mu\text{m}$  is demonstrated. For Au/mica substrates even flatter copper deposits can be achieved, although adhesion becomes more critical with separation of the Au and mica layers during detachment. It is evident that design of suitable SAMs is central to the continued development of metal deposition and detachment techniques. The foundations have been laid for some more detailed experiments and some quite exquisite electrodeposition chemistry. The principles for bottom up production of well defined microstructures have been demonstrated using a simple and inexpensive technique.

Fine tuning of the metal deposition can be performed by modification of the SAM surface properties through introduction of functionality. Tail groups can be designed to modify wetting or complexation properties. From relatively simple tail groups such as carboxyl, hydroxyl, nitro, amino or nitriles to more complex tail groups such as terpyridyl or pyrazolylys, the surface properties can be modified to alter the interaction between the SAM and electrolyte.

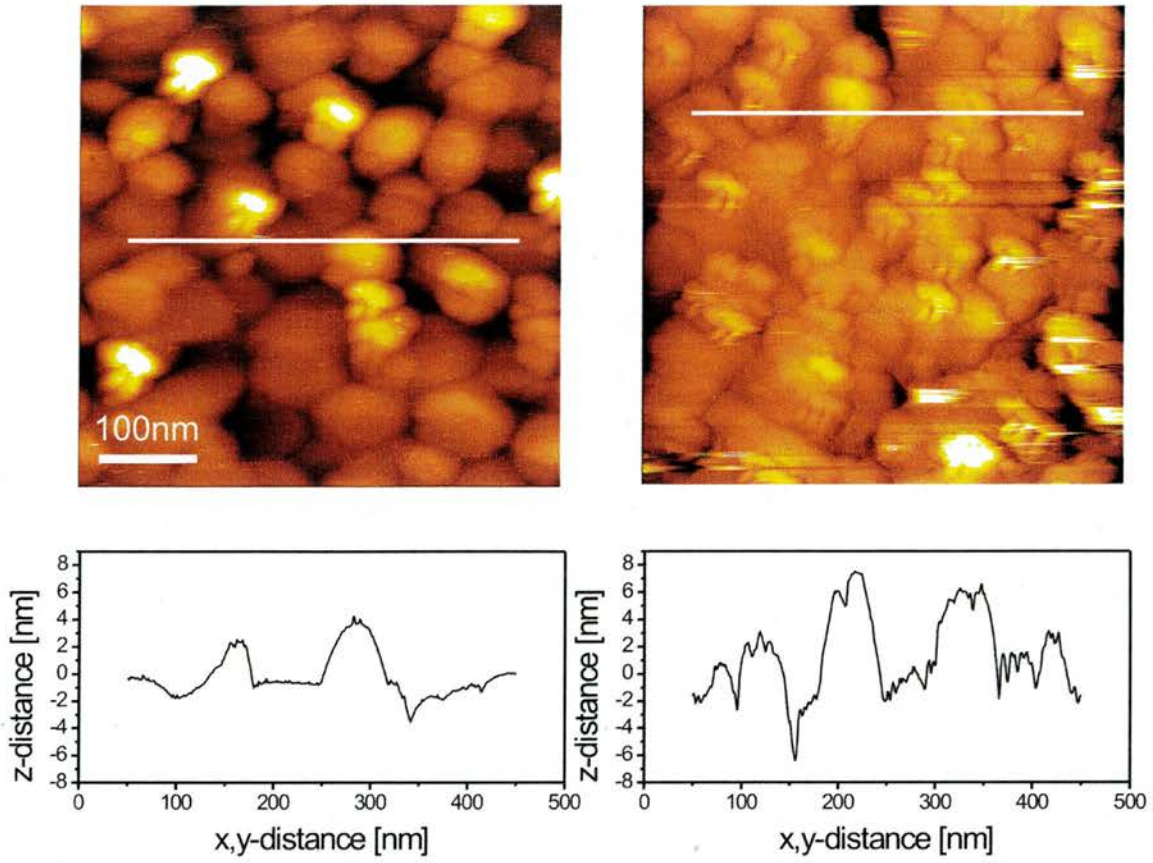


Figure 6.6: STM image of the surface of Au/Si after the copper deposit was removed (left) and the copper surface detached from the gold electrode (right), constant current mode ( $U = 1.1$  V;  $I = 200$  pA). The scale for both images is identical. The cross sectional profile corresponding to the white line for each sample is plotted directly below the respective image.

## Chapter 7

# CONCLUSIONS

A total of twenty six different SAMs on gold have been examined using cyclic voltammetry with in-situ second harmonic generation, an optical technique that probes the solid-liquid interface. The in-situ technique allows the discrimination of faradaic processes and capacitive processes. Electrochemistry measures capacitive and faradaic processes whereas second harmonic generation measures faradaic processes only. This is a particularly attractive technique for probing buried surfaces due to the fact that it is non-destructive and can be applied to atomically flat surfaces, unlike the electrochemical quartz crystal microbalance. The technique allows investigation of surfaces with a quality comparable to well defined single crystal surfaces. The techniques probe the electrochemical stability of SAMs and quantitatively analyse parameters such as desorption potential, desorption charge, peak shape and re-adsorption characteristics as well as allowing a correlation of voltammetry with optical second harmonic generation. A striking correlation between cyclic voltammetry and second harmonic generation was observed. Voltammetric features are always paralleled by SHG intensity changes. Despite the presence of double peaks for long chain alkane thiol SAMs, a linear correlation between charge and coverage was observed.

Collecting such a broad catalogue of results for a variety of different SAMs has allowed a significant picture of the forces involved in the overall SAM properties to emerge. With a view to designing electrochemical applications, their stability, which depends on the strength of the head group-substrate interaction and intermolecular interactions, was investigated. The interactions were examined by comparing the influence of the substrate and constituent parts of the molecule. It was shown that tail groups could decrease or increase the SAM stability. A carboxyl or hydroxyl tail group decreases the film stability whereas a thiol tail group increases the film stability. For alkane and biphenyl thiols, in general, increasing the length of the spacer increases the stability of the SAM. However, there is an odd-even effect for biphenyl thiols. Due to the tilt angle of the biphenyl unit, BP(odd) molecules pack closer together than BP(even) molecules allowing greater intermolecular interactions which produce more stable films. BP(odd) molecules have a stability comparable to alkane thiols of an equivalent length, whereas

BP(even) molecules, due to internal geometric constraints are less stable. Replacing the sulfur head group with a selenium head group resulted in a substantial increase in the film stability, equivalent to the increase in stability observed for four additional methylene units. Lastly, SAMs on silver are, on average, more stable than the equivalent SAM on gold. The SAM stability depend on the combination of intermolecular and intramolecular forces and it is concluded that the tail group, spacer, head group and the substrate all influence the film stability, i.e. every part of the SAM system contributes to the stability. However, the odd-even effect demonstrates that SAM design must consider the overall structural aspects such as geometric constraints of the molecules in a SAM. Properties are not obtained by simply comparing interactions between groups in isolation. Using the knowledge acquired from the broad cross section of SAMs investigated a rational design of SAMs can be undertaken. A framework for tailoring surface properties, such as stability, conductivity or permeability has been developed. For example, the conductivity of the SAM can be fine-tuned by combining conducting and non-conducting moieties. The stability could be maximised by combining a selenium head group with a docosane spacer / tail group. Another desirable property may be a porous SAM, the dipod and tripod SAMs would be relevant here, while a perfluorinated SAM prepared in solution at high temperature would intuitively create a SAM with low porosity. One interesting detail that emerged from the examination of different molecules was the possibility to describe the relative stabilities of two SAMs in terms of the equivalent number of methylene units. This is a measure that scales with the size of the molecule.

A significant proportion of the thesis involved analysis of double peak features. It was demonstrated that not all multiple peak features have the same scientific basis. Insoluble SAMs produce double desorption and readsorption peaks on gold and silver. Tripod SAMs have a double readsorption feature. BP(odd) SAMs and MC7 on silver produce double desorption peaks, although the peak separations are very different. There are therefore three or four different types of double peak feature. One particularly interesting double peak feature was that of hexadecane thiol SAM on gold, an example of an insoluble molecule. The peak features have provoked considerable discussion on the desorption mechanism (chapter 5). Of particular interest was the correlation of second harmonic generation with the double desorption and readsorption peaks. The linear correlation of charge to coverage across the double peaks indicates that a two step

model proposed in literature is incorrect. A model based on pair interactions is proposed and developed consistent with published data and data presented in this thesis.

Copper deposition experiments with surface patterning have successfully been performed. It was demonstrated that copper deposition can be performed selectively on a biphenyl thiol while a long chain alkane thiol blocks deposition. A novel detachment procedure has been demonstrated. By combining the understanding of film structural quality and film conductivity a promising route to depositing other, more active metals is demonstrated.

---

## Chapter 8

### REFERENCES

1. Bain, C. D. et al. Formation of Monolayer Films by the Spontaneous Assembly of Organic Thiols from Solution onto Gold. *Journal of the American Chemical Society* **111**, 321-335 (1989).
2. Patel, N. et al. Immobilization of protein molecules onto homogeneous and mixed carboxylate-terminated self-assembled monolayers. *Langmuir* **13**, 6485-6490 (1997).
3. Williams, L. M. et al. Kinetics of the unrolling of small unilamellar phospholipid vesicles onto self-assembled monolayers. *Langmuir* **13**, 751-757 (1997).
4. Kim, H. I., Koini, T., Randall Lee, T. & Perry, S. S. Molecular contributions to the frictional properties of fluorinated self-assembled monolayers. *Tribology Letters* **4**, 137-140 (1998).
5. Zhang, S. W. & Lan, H. Q. Developments in tribological research on ultrathin films. *Tribology International* **35**, 321-327 (2002).
6. Joyce, S. A., Thomas, R. C., Houston, J. E., Michalske, T. A. & Crooks, R. M. Mechanical Relaxation of Organic Monolayer Films Measured by Force Microscopy. *Physical Review Letters* **68**, 2790-2793 (1992).
7. Nuzzo, R. G. & Allara, D. L. Adsorption of Bifunctional Organic Disulfides on Gold Surfaces. *Journal of the American Chemical Society* **105**, 4481-4483 (1983).
8. Ulman, A. Formation and structure of self-assembled monolayers. *Chemical Reviews* **96**, 1533-1554 (1996).
9. Schreiber, F. Structure and growth of self-assembling monolayers. *Progress in Surface Science* **65**, 151-256 (2000).
10. Mohtat, N., Byloos, M., Soucy, M., Morin, S. & Morin, M. Electrochemical evidence of the adsorption of alkanethiols on two sites on Ag(111). *Journal of Electroanalytical Chemistry* **484**, 120-130 (2000).
11. Burleigh, T. D. et al. Self-assembled monolayers of perfluoroalkyl amideethanethiols, fluoroalkylthiols, and alkylthiols for the prevention of silver tarnish. *Corrosion* **58**, 49-56 (2002).

12. Vollmer, S. et al. Low-energy vibrational dynamics of ultrathin organic adlayers: alkanethiols adsorbed on copper. *Surface Science* **462**, 135-142 (2000).
13. Jennings, G. K. & Laibinis, P. E. Self-assembled monolayers of alkanethiols on copper provide corrosion resistance in aqueous environments. *Colloids and Surfaces a-Physicochemical and Engineering Aspects* **116**, 105-114 (1996).
14. Alonso, C., Lopez, M. F., Gutierrez, A. & Escudero, M. L. X-ray photoelectron spectroscopy study of thiols adsorbed on Pt(111) with and without the presence of a copper monolayer. *Surface and Interface Analysis* **30**, 359-363 (2000).
15. Love, J. C. et al. Formation and structure of self-assembled monolayers of alkanethiolates on palladium. *Journal of the American Chemical Society* **125**, 2597-2609 (2003).
16. Volmeruebing, M. & Stratmann, M. A Surface Analytical and an Electrochemical Study of Iron Surfaces Modified by Thiols. *Applied Surface Science* **55**, 19-35 (1992).
17. Cheng, L. C., Bernasek, S. L., Bocarsly, A. B. & Ramanarayanan, T. A. Adsorption and Decomposition of 1-Alkanethiols on the Fe(100) Surface. *Chemistry of Materials* **7**, 1807-1815 (1995).
18. Kataby, G. et al. Self-assembled monolayer coatings on amorphous iron and iron oxide nanoparticles: Thermal stability and chemical reactivity studies. *Langmuir* **13**, 6151-6158 (1997).
19. Kataby, G. et al. The adsorption of monolayer coatings on iron nanoparticles: Mossbauer spectroscopy and XANES results. *Thin Solid Films* **333**, 41-49 (1998).
20. Adlkofer, K., Eck, W., Grunze, M. & Tanaka, M. Surface engineering of gallium arsenide with 4-mercaptobiphenyl monolayers. *Journal of Physical Chemistry B* **107**, 587-591 (2003).
21. Yamamoto, H., Butera, R. A., Gu, Y. & Waldeck, D. H. Characterization of the surface to thiol bonding in self- assembled monolayer films of C<sub>12</sub>H<sub>25</sub>SH on InP(100) by angle- resolved X-ray photoelectron spectroscopy. *Langmuir* **15**, 8640-8644 (1999).
22. Madueno, R., Pineda, T., Sevilla, J. M. & Blazquez, M. An electrochemical study of the SAMs of 6-mercaptopurine (6MP) at Hg and Au(111) electrodes in alkaline media. *Langmuir* **18**, 3903-3909 (2002).

23. Calvente, J. J. et al. Formation and reductive desorption of mercaptohexanol monolayers on mercury. *Journal of Physical Chemistry B* **105**, 5477-5488 (2001).
24. Muskal, N. & Mandler, D. Thiol self-assembled monolayers on mercury surfaces: the adsorption and electrochemistry of omega-mercaptoalkanoic acids. *Electrochimica Acta* **45**, 537-548 (1999).
25. Schonherr, H. & Vancso, G. J. Lattice structure of self-assembled monolayers of dialkyl sulfides and calix 4 arene sulfide adsorbates on Au(111) revealed by atomic force microscopy. *Langmuir* **15**, 5541-5546 (1999).
26. Yee, C. K. et al. Alkyl selenide- and alkyl thiolate-functionalized gold nanoparticles: Chain packing and bond nature. *Langmuir* **19**, 9450-9458 (2003).
27. Venkataramanan, M., Skanth, G., Bandyopadhyay, K., Vijayamohanam, K. & Pradeep, T. Self-assembled monolayers of two aromatic disulfides and a diselenide on polycrystalline silver films: An investigation by SERS and XPS. *Journal of Colloid and Interface Science* **212**, 553-561 (1999).
28. Balgar, T., Bautista, R., Hartmann, N. & Hasselbrink, E. An AFM study of the growth kinetics of the self-assembled octadecylsiloxane monolayer on oxidized silicon. *Surface Science* **532**, 963-969 (2003).
29. Abdelghani, A., Hleli, S. & Cherif, K. Optical and electrochemical characterization of self-assembled octadecyltrichlorosilane monolayer on modified silicon electrode. *Materials Letters* **56**, 1064-1068 (2002).
30. Posthumus, W., Magusin, P., Brokken-Zijp, J. C. M., Tinnemans, A. H. A. & van der Linde, R. Surface modification of oxidic nanoparticles using 3-methacryloxypropyltrimethoxysilane. *Journal of Colloid and Interface Science* **269**, 109-116 (2004).
31. Hatton, R. A., Day, S. R., Chesters, M. A. & Willis, M. R. Organic electroluminescent devices: enhanced carrier injection using an organosilane self assembled monolayer (SAM) derivatized ITO electrode. *Thin Solid Films* **394**, 292-297 (2001).
32. Frydman, E., Cohen, H., Maoz, R. & Sagiv, J. Monolayer damage in XPS measurements as evaluated by independent methods. *Langmuir* **13**, 5089-5106 (1997).
33. Hickman, J. J. et al. Combining Spontaneous Molecular Assembly with Microfabrication to Pattern Surfaces - Selective Binding of Isonitriles to

- Platinum Microwires and Characterization by Electrochemistry and Surface Spectroscopy. *Journal of the American Chemical Society* **111**, 7271-7272 (1989).
34. Henderson, J. I., Feng, S., Bein, T. & Kubiak, C. P. Adsorption of diisocyanides on gold. *Langmuir* **16**, 6183-6187 (2000).
  35. Steiner, U. B., Caseri, W. R. & Suter, U. W. Adsorption of Alkanenitriles and Alkanedinitriles on Gold and Copper. *Langmuir* **8**, 2771-2777 (1992).
  36. Tao, Y. T. Structural Comparison of Self-Assembled Monolayers of N-Alkanoic Acids on the Surfaces of Silver, Copper, and Aluminum. *Journal of the American Chemical Society* **115**, 4350-4358 (1993).
  37. Taylor, C. E. & Schwartz, D. K. Octadecanoic acid self-assembled monolayer growth at sapphire surfaces. *Langmuir* **19**, 2665-2672 (2003).
  38. Mitsuya, M. & Sugita, N. Chemisorption of dicarboxylic acids on an Si(111) surface and subsequent chemical reactions at the surface of adsorbed molecular layers. *Langmuir* **13**, 7075-7079 (1997).
  39. Hurley, P. T., Ribbe, A. E. & Buriak, J. M. Nanopatterning of alkynes on hydrogen-terminated silicon surfaces by scanning probe-induced cathodic electrografting. *Journal of the American Chemical Society* **125**, 11334-11339 (2003).
  40. Linford, M. R., Fenter, P., Eisenberger, P. M. & Chidsey, C. E. D. Alkyl Monolayers on Silicon Prepared from 1-Alkenes and Hydrogen-Terminated Silicon. *Journal of the American Chemical Society* **117**, 3145-3155 (1995).
  41. Sato, Y. & Mizutani, F. Formation and characterization of aromatic selenol and thiol monolayers on gold: in-situ IR studies and electrochemical measurements. *Physical Chemistry Chemical Physics* **6**, 1328 - 1331 (2004).
  42. Patrone, L., Palacin, S. & Bourgoin, J. P. Direct comparison of the electronic coupling efficiency of sulfur and selenium alligator clips for molecules adsorbed onto gold electrodes. *Applied Surface Science* **212**, 446-451 (2003).
  43. Felgenhauer, T., Rong, H. T. & Buck, M. Electrochemical and exchange studies of self-assembled monolayers of biphenyl based thiols on gold. *Journal of Electroanalytical Chemistry* **550**, 309-319 (2003).
  44. Felgenhauer, T. et al. Electrode modification by electron-induced patterning of aromatic self-assembled monolayers. *Applied Physics Letters* **79**, 3323-3325 (2001).

45. Smith, R. K., Lewis, P. A. & Weiss, P. S. Patterning self-assembled monolayers. *Progress in Surface Science* **75**, 1-68 (2004).
46. Xia, Y. N. & Whitesides, G. M. Soft lithography. *Angewandte Chemie-International Edition* **37**, 551-575 (1998).
47. *Modern Electroplating* (eds. Mordechay Schlesinger & Paunovic, M.) (Wiley inter-science, New York, 2000).
48. Ulman, A. *An Introduction to Ultrathin Organic Films From Langmuir-Blodgett to Self-Assembly* (Academic Press Inc, San Diego, 1991).
49. Zharnikov, M. et al. The effect of sulfur-metal bonding on the structure of self-assembled monolayers. *Physical Chemistry Chemical Physics* **2**, 3359-3362 (2000).
50. Porter, M. D., Bright, T. B., Allara, D. L. & Chidsey, C. E. D. Spontaneously Organized Molecular Assemblies .4. Structural Characterization of Normal-Alkyl Thiol Monolayers on Gold by Optical Ellipsometry, Infrared-Spectroscopy, and Electrochemistry. *Journal of the American Chemical Society* **109**, 3559-3568 (1987).
51. Chidsey, C. E. D. & Loiacono, D. N. Chemical Functionality in Self-Assembled Monolayers - Structural and Electrochemical Properties. *Langmuir* **6**, 682-691 (1990).
52. Fenter, P., Eisenberger, P. & Liang, K. S. Chain-Length Dependence of the Structures and Phases of  $\text{CH}_3(\text{CH}_2)_N\text{-1SH}$  Self-Assembled on Au(111). *Physical Review Letters* **70**, 2447-2450 (1993).
53. Byloos, M., Al-Maznai, H. & Morin, M. Formation of a self-assembled monolayer via the electrospreading of physisorbed micelles of thiolates. *Journal of Physical Chemistry B* **103**, 6554-6561 (1999).
54. Byloos, M., Al-Maznai, H. & Morin, M. Phase transitions of alkanethiol self-assembled monolayers at an electrified gold surface. *Journal of Physical Chemistry B* **105**, 5900-5905 (2001).
55. Byloos, M., Rifai, S., Al-Maznai, H., Laferriere, M. & Morin, M. A second harmonic generation study of a physisorbed precursor to the electrodeposition of a monolayer of alkanethiols. *Langmuir* **17**, 2478-2484 (2001).
56. Hobara, D., Miyake, O., Imabayashi, S., Niki, K. & Kakiuchi, T. In-situ scanning tunneling microscopy imaging of the reductive desorption process of alkanethiols on Au(111). *Langmuir* **14**, 3590-3596 (1998).

57. Peterlinz, K. A. & Georgiadis, R. In situ kinetics of self-assembly by surface plasmon resonance spectroscopy. *Langmuir* **12**, 4731-4740 (1996).
58. Wong, S. S. & Porter, M. D. Origin of the multiple voltammetric desorption waves of long-chain alkanethiolate monolayers chemisorbed on annealed gold electrodes. *Journal of Electroanalytical Chemistry* **485**, 135-143 (2000).
59. Yang, D. F., Wilde, C. P. & Morin, M. Studies of the electrochemical removal and efficient re-formation of a monolayer of hexadecanethiol self-assembled at an Au(111) single crystal in aqueous solutions. *Langmuir* **13**, 243-249 (1997).
60. Yang, D. F. & Morin, M. Chronoamperometric study of the reductive desorption of alkanethiol self-assembled monolayers. *Journal of Electroanalytical Chemistry* **441**, 173-181 (1998).
61. Kim, D. H., Noh, J., Hara, M. & Lee, H. An adsorption process study on the self-assembled monolayer formation of octadecanethiol chemisorbed on gold surface. *Bulletin of the Korean Chemical Society* **22**, 276-280 (2001).
62. Qu, D. & Morin, M. The effect of concentration on the oxidative deposition of a monolayer of alkylthiolate on gold: from island formation to random adsorption. *Journal of Electroanalytical Chemistry* **565**, 235-242 (2004).
63. Himmelhaus, M., Eisert, F., Buck, M. & Grunze, M. Self-assembly of n-alkanethiol monolayers. A study by IR-visible sum frequency spectroscopy (SFG). *Journal of Physical Chemistry B* **104**, 576-584 (2000).
64. Yamada, R., Wano, H. & Uosaki, K. Effect of temperature on structure of the self-assembled monolayer of decanethiol on Au(111) surface. *Langmuir* **16**, 5523-5525 (2000).
65. Cyganik, P., Buck, M., Azzam, W. & Woll, C. Self-assembled monolayers of omega-biphenylalkanethiols on Au(111): Influence of spacer chain on molecular packing. *Journal of Physical Chemistry B* **108**, 4989-4996 (2004).
66. Gold single crystal prepared by Surface Preparation Laboratory, P. F., 1507 DE Zaandam, The Netherlands. Gold on mica and gold on silicon prepared by GA PVD, Angew. Physikalische Chemie, Im Neuenheimer Feld 253 D-69120, Heidelberg, Germany.
67. Czochralski, J. Ein neues Verfahren zur Messung des Kristallisationsgeschwindigkeit der Metalle. *Zeitschrift für physikalische Chemie* **92**, 219 (1918).
68. Cyganik, P. In preparation.

69. Woll, C., Chiang, S., Wilson, R. J. & Lippel, P. H. Determination of Atom Positions at Stacking-Fault Dislocations on Au(111) by Scanning Tunneling Microscopy. *Physical Review B* **39**, 7988-7991 (1989).
70. Poirier, G. E. Characterization of organosulfur molecular monolayers on Au(111) using scanning tunneling microscopy. *Chemical Reviews* **97**, 1117-1127 (1997).
71. Image is reproduced from the presentation of J Barth, surface science summer school CD.
72. Nichols, R. J., Nouar, T., Lucas, C. A., Haiss, W. & Hofer, W. A. Surface relaxation and surface stress of Au(111). *Surface Science* **513**, 263-271 (2002).
73. Strbac, S., Hamelin, A. & Adzic, R. R. Electrochemical Indication of Surface Reconstruction of (100), (311) and (111) Gold Faces in Alkaline-Solutions. *Journal of Electroanalytical Chemistry* **362**, 47-53 (1993).
74. Friedrich, A. et al. An Insitu Study of Reconstructed Gold Electrode Surfaces by 2nd Harmonic-Generation. *Chemical Physics Letters* **163**, 123-128 (1989).
75. Finklea, H. O. in *Electroanalytical Chemistry: A Series of Advances, Vol 19* 109-335 (1996).
76. Kakiuchi, T., Usui, H., Hobara, D. & Yamamoto, M. Voltammetric properties of the reductive desorption of alkanethiol self-assembled monolayers from a metal surface. *Langmuir* **18**, 5231-5238 (2002).
77. Vela, M. E. et al. Electrodesorption kinetics and molecular interactions in well-ordered thiol adlayers on Au(111). *Journal of Physical Chemistry B* **104**, 11878-11882 (2000).
78. Wano, H. & Uosaki, K. In situ, real-time monitoring of the reductive desorption process of self-assembled monolayers of hexanethiol on Au(111) surfaces in acidic and alkaline aqueous solutions by scanning tunneling microscopy. *Langmuir* **17**, 8224-8228 (2001).
79. Sumi, T., Wano, H. & Uosaki, K. Electrochemical oxidative adsorption and reductive desorption of a self-assembled monolayer of decanethiol on the Au(111) surface in KOH plus ethanol solution. *Journal of Electroanalytical Chemistry* **550**, 321-325 (2003).
80. Sumi, T. & Uosaki, K. Electrochemical oxidative formation and reductive desorption of a self-assembled monolayer of decanethiol on a Au(111) surface in KOH ethanol solution. *Journal of Physical Chemistry B* **108**, 6422-6428 (2004).

81. Kawaguchi, T., Yasuda, H., Shimazu, K. & Porter, M. D. Electrochemical quartz crystal microbalance investigation of the reductive desorption of self-assembled monolayers of alkanethiols and mercaptoalkanoic acids on Au. *Langmuir* **16**, 9830-9840 (2000).
82. Esplandiu, M. J., Hagenstrom, H. & Kolb, D. M. Functionalized self-assembled alkanethiol monolayers on Au(111) electrodes: 1. Surface structure and electrochemistry. *Langmuir* **17**, 828-838 (2001).
83. Loglio, F., Schweizer, M. & Kolb, D. M. In situ characterization of self-assembled butanethiol monolayers on Au(100) electrodes. *Langmuir* **19**, 830-834 (2003).
84. Wan, L. J., Terashima, M., Noda, H. & Osawa, M. Molecular orientation and ordered structure of benzenethiol adsorbed on gold(111). *Journal of Physical Chemistry B* **104**, 3563-3569 (2000).
85. Whelan, C. M., Smyth, M. R. & Barnes, C. J. HREELS, XPS, and electrochemical study of benzenethiol adsorption on Au(111). *Langmuir* **15**, 116-126 (1999).
86. Krings, N., Strehblow, H. H., Kohnert, J. & Martin, H. D. Investigations on the monolayer structure of thiol SAMs and the influence of conjugated pi-bonds on the electronic molecular conductivity. *Electrochimica Acta* **49**, 167-174 (2003).
87. Tao, Y. T., Wu, C. C., Eu, J. Y. & Lin, W. L. Structure evolution of aromatic-derivatized thiol monolayers on evaporated gold. *Langmuir* **13**, 4018-4023 (1997).
88. Rifai, S. et al. Electrodeposition of bilayers of dithiols. *Journal of Electroanalytical Chemistry* **531**, 111-118 (2002).
89. Janek, R. P., Fawcett, W. R. & Ulman, A. Impedance spectroscopy of self-assembled monolayers on Au(111): Sodium ferrocyanide charge transfer at modified electrodes. *Langmuir* **14**, 3011-3018 (1998).
90. Rifai, S. & Morin, M. Isomeric effect on the oxidative formation of bilayers of benzenedimethanethiol on Au(111). *Journal of Electroanalytical Chemistry* **550**, 277-289 (2003).
91. Long, Y. T., Rong, H. T., Buck, M. & Grunze, M. Odd-even effects in the cyclic voltammetry of self-assembled monolayers of biphenyl based thiols. *Journal of Electroanalytical Chemistry* **524**, 62-67 (2002).

92. Adams, D. M. et al. Charge transfer on the nanoscale: Current status. *Journal of Physical Chemistry B* **107**, 6668-6697 (2003).
93. MC4 was obtained from BDH. MC7 from Fluka. MC2, MC8, MC10, MC16, MHA and PET from Aldrich, BP4OH and MC22 were synthesised by J. Wallace (bromodocosane from Fluka). HBP3 and HBP4 were synthesised by J. Wilton-Ely. M. Zharnikov supplied BPSe and CFSe. S. Francis supplied CFS. M. Buck supplied all other BP thiols.
94. Rong, H. T. et al. On the importance of the headgroup substrate bond in thiol monolayers: A study of biphenyl-based thiols on gold and silver. *Langmuir* **17**, 1582-1593 (2001).
95. Sellers, H., Ulman, A., Shnidman, Y. & Eilers, J. E. Structure and Binding of Alkanethiolates on Gold and Silver Surfaces - Implications for Self-Assembled Monolayers. *Journal of the American Chemical Society* **115**, 9389-9401 (1993).
96. Yourdshahyan, Y., Zhang, H. K. & Rappe, A. M. n-alkyl thiol head-group interactions with the Au(111) surface. *Physical Review B* **6308**, art. no.-081405 (2001).
97. Beardmore, K. M., Kress, J. D., Gr[oslash]nbech-Jensen, N. & Bishop, A. R. Ab-initio calculations of the gold-sulfur interaction for alkanethiol monolayers. *Synthetic Metals* **84**, 317-318 (1997).
98. Hayashi, T., Morikawa, Y. & Nozoye, H. Adsorption state of dimethyl disulfide on Au(111): Evidence for adsorption as thiolate at the bridge site. *Journal of Chemical Physics* **114**, 7615-7621 (2001).
99. Vargas, M. C., Giannozzi, P., Selloni, A. & Scoles, G. Coverage-dependent adsorption of CH<sub>3</sub>S and (CH<sub>3</sub>S)<sub>2</sub> on Au(111): A density functional theory study. *Journal of Physical Chemistry B* **105**, 9509-9513 (2001).
100. Kondoh, H. et al. Adsorption of thiolates to singly coordinated sites on Au(111) evidenced by photoelectron diffraction. *Physical Review Letters* **90**, art. no.-066102 (2003).
101. Roper, M. G. et al. Atop adsorption site of sulphur head groups in gold-thiolate self-assembled monolayers. *Chemical Physics Letters* **389**, 87-91 (2004).
102. Molina, L. M. & Hammer, B. Theoretical study of thiol-induced reconstructions on the Au(111) surface. *Chemical Physics Letters* **360**, 264-271 (2002).
103. Poirier, G. E. Mechanism of formation of Au vacancy islands in alkanethiol monolayers on Au(111). *Langmuir* **13**, 2019-2026 (1997).

104. Poirier, G. E. & Tarlov, M. J. Molecular Ordering and Gold Migration Observed in Butanethiol Self-Assembled Monolayers Using Scanning-Tunneling-Microscopy. *Journal of Physical Chemistry* **99**, 10966-10970 (1995).
105. Bard, A. J. & Faulkner, L. R. *Electrochemical Methods: Fundamentals and Applications* (Wiley & Sons, 2001).
106. Schneider, T. W. & Buttry, D. A. Electrochemical Quartz-Crystal Microbalance Studies of Adsorption and Desorption of Self-Assembled Monolayers of Alkyl Thiols on Gold. *Journal of the American Chemical Society* **115**, 12391-12397 (1993).
107. Atkins, P. W. *Physical Chemistry* (Oxford University Press, Oxford, 1982).
108. Honeychurch, M. J. & Rechnitz, G. A. Voltammetry of adsorbed molecules. Part 2: Irreversible redox systems. *Electroanalysis* **10**, 453-457 (1998).
109. Honeychurch, M. J. & Rechnitz, G. A. Voltammetry of adsorbed molecules. Part 1: Reversible redox systems. *Electroanalysis* **10**, 285-293 (1998).
110. Matsuda, H., Aoki, K. & Tokuda, K. Theory of Electrode-Reactions of Redox Couples Confined to Electrode Surfaces at Monolayer Levels .2. Cyclic Voltammetry and Ac Impedance Measurements. *Journal of Electroanalytical Chemistry* **217**, 15-32 (1987).
111. Matsuda, H., Aoki, K. & Tokuda, K. Theory of Electrode-Reactions of Redox Couples Confined to Electrode Surfaces at Monolayer Levels .1. Expression of the Current Potential Relationship for Simple Redox Reactions. *Journal of Electroanalytical Chemistry* **217**, 1-13 (1987).
112. Calvente, J. J., Gil, M. L., Sanchez, M. D., Andreu, R. & de Pablos, F. Voltammetry of surface redox processes perturbed by a father- son reaction. *Electrochimica Acta* **45**, 3087-3097 (2000).
113. Aoki, K. & Kakiuchi, T. Probability theory of desorption kinetics of self-assembled alkanethiols stabilized with pair interaction. *Journal of Electroanalytical Chemistry* **452**, 187-192 (1998).
114. Mills, D. L. *Nonlinear Optics Basic Concepts* (Springer-Verlag, New York, 1991).
115. Butcher, P. N. & Cotter, D. *The Elements of Nonlinear Optics* (eds. Knight, P. L. & Firth, W. J.) (Cambridge University Press, Cambridge, 1991).
116. Williams, C. T. & Beattie, D. A. Probing buried interfaces with non-linear optical spectroscopy. *Surface Science* **500**, 545-576 (2002).

117. Corn, R. M. & Higgins, D. A. Optical 2nd-Harmonic Generation Ass Probe of Surface-Chemistry. *Chemical Reviews* **94**, 107-125 (1994).
118. Dannenberger, O., Buck, M. & Grunze, M. Self-assembly of n-alkanethiols: A kinetic study by second harmonic generation. *Journal of Physical Chemistry B* **103**, 2202-2213 (1999).
119. Franken, P. A., Hill, A. E., Peters, C. W. & Weinreich, G. Generation of Optical Harmonics. *Physical Review Letters* **7**, 118-119 (1961).
120. Bain, C. D. in *Modern Characterization Methods of Surfactant Systems* (ed. Binks, B. P.) 335-373 (Marcel Dekker, New York, 1999).
121. Buck, M., Eisert, F., Grunze, M. & Trager, F. 2nd-Order Nonlinear Susceptibilities of Surfaces - a Systematic Study of the Wavelength and Coverage Dependence of Thiol Adsorption on Polycrystalline Gold. *Applied Physics a-Materials Science & Processing* **60**, 1-12 (1995).
122. Binning, G., Rohrer, H., Gerber, C. & Weibel, E. Surface Studies by Scanning Tunneling Microscopy. *Physical Review Letters* **49**, 57-61 (1982).
123. Wiesendanger, R. *Scanning Probe Microscopy and Spectroscopy Methods and Applications* (Cambridge University Press, Cambridge, 1994).
124. Binnig, G. & Rohrer, H. Scanning Tunneling Microscopy - From Birth to Adolescence. Nobel Lecture. (1986).
125. Mishina, E., Tamura, T., Sakaguchi, H. & Nakabayashi, S. Kinetics of adsorption and self-assembling of thiophene and dodecanethiol studied by optical second harmonic generation. *Chemistry Letters* **32**, 652-653 (2003).
126. Ma, F. Y. & Lennox, R. B. Potential-assisted deposition of alkanethiols on Au: Controlled preparation of single- and mixed-component SAMs. *Langmuir* **16**, 6188-6190 (2000).
127. Brett, C. M. A., Kresak, S., Hianik, T. & Brett, A. M. O. Studies on self-assembled alkanethiol monolayers formed at applied potential on polycrystalline gold electrodes. *Electroanalysis* **15**, 557-565 (2003).
128. Cyganik, P. & Buck, M. Polymorphism in Biphenyl-Based Self-Assembled Monolayers of Thiols. *J. Am. Chem. Soc.* **126**, 5960-5961 (2004).
129. Angerstein-Kozłowska, H., Conway, B. E., Hamelin, A. & Stoicoviciu, L. Elementary steps of electrochemical oxidation of single-crystal planes of Au Part II. A chemical and structural basis of oxidation of the (111) plane. *Journal of Electroanalytical Chemistry* **228**, 429-453 (1987).

130. Angersteinkozłowska, H., Conway, B. E., Hamelin, A. & Stoicoviciu, L. Elementary Steps of Electrochemical Oxidation of Single-Crystal Planes of Au .1. Chemical Basis of Processes Involving Geometry of Anions and the Electrode Surfaces. *Electrochimica Acta* **31**, 1051-1061 (1986).
131. Uchida, H., Ikeda, N. & Watanabe, M. Electrochemical quartz crystal microbalance study of copper adatoms on gold electrodes .2. Further discussion on the specific adsorption of anions from solutions of perchloric and sulfuric acid. *Journal of Electroanalytical Chemistry* **424**, 5-12 (1997).
132. Losic, D., Shapter, J. G. & Gooding, J. J. Influence of surface topography on alkanethiol SAMs assembled from solution and by microcontact printing. *Langmuir* **17**, 3307-3316 (2001).
133. Iwami, Y., Hobara, D., Yamamoto, M. & Kakiuchi, T. Determination of the potential of zero charge of Au(111) electrodes modified with thiol self-assembled monolayers using a potential-controlled sessile drop method. *Journal of Electroanalytical Chemistry* **564**, 77-83 (2004).
134. Rodriguez, J. F., Mebrahtu, T. & Soriaga, M. P. Determination of the Surface-Area of Gold Electrodes by Iodine Chemisorption. *Journal of Electroanalytical Chemistry* **233**, 283-289 (1987).
135. Zhong, C. J. & Porter, M. D. Fine structure in the voltammetric desorption curves of alkanethiolate monolayers chemisorbed at gold. *Journal of Electroanalytical Chemistry* **425**, 147-153 (1997).
136. Schlenoff, J. B., Li, M. & Ly, H. Stability and self-exchange in alkanethiol monolayers. *Journal of the American Chemical Society* **117**, 12528-12536 (1995).
137. Hamelin, A., Sottomayer, M. J., Silva, F., Chang, S. C. & Weaver, M. J. Cyclic voltammetric characterization of oriented monocrystalline gold surfaces in aqueous alkaline solution. *Journal of Electroanalytical Chemistry* **295**, 291-300 (1990).
138. Walczak, M. M., Alves, C. A., Lamp, B. D. & Porter, M. D. Electrochemical and X-ray photoelectron spectroscopic evidence for differences in the binding sites of alkanethiolate monolayers chemisorbed at gold. *Journal of Electroanalytical Chemistry* **396**, 103-114 (1995).

139. Leopold, M. C., Black, J. A. & Bowden, E. F. Influence of gold topography on carboxylic acid terminated self-assembled monolayers. *Langmuir* **18**, 978-980 (2002).
140. Strbac, S. & Adzic, R. R. The influence of OH- chemisorption on the catalytic properties of gold single crystal surfaces for oxygen reduction in alkaline solutions. *Journal of Electroanalytical Chemistry* **403**, 169-181 (1996).
141. Yang, D. F., Wilde, C. P. & Morin, M. Electrochemical desorption and adsorption of nonyl mercaptan at gold single crystal electrode surfaces. *Langmuir* **12**, 6570-6577 (1996).
142. Buck, M., Grunze, M., Eisert, F., Fischer, J. & Trager, F. Adsorption-Kinetics of N-Alkyl Thiols on Gold Studied by 2nd- Harmonic Generation and X-Ray Photoelectron-Spectroscopy. *Journal of Vacuum Science & Technology a-Vacuum Surfaces and Films* **10**, 926-929 (1992).
143. Imabayashi, S. et al. Reductive desorption of carboxylic-acid-terminated alkanethiol monolayers from Au(111) surfaces. *Journal of Electroanalytical Chemistry* **428**, 33-38 (1997).
144. Widrig, C. A., Chung, C. & Porter, M. D. The Electrochemical Desorption of N-Alkanethiol Monolayers from Polycrystalline Au and Ag Electrodes. *Journal of Electroanalytical Chemistry* **310**, 335-359 (1991).
145. Azzam, W., Cyganik, P., Witte, G., Buck, M. & Woll, C. Pronounced odd-even changes in the molecular arrangement and packing density of biphenyl-based thiol SAMs: A combined STM and LEED study. *Langmuir* **19**, 8262-8270 (2003).
146. Azzaroni, O. et al. Electrodesorption kinetics and molecular interactions at negatively charged self-assembled thiol monolayers in electrolyte solutions. *Langmuir* **17**, 6647-6654 (2001).
147. Naud, C., Calas, P. & Commeyras, A. Critical influence of the fluorinated chain length in the self- assembly of terminally perfluorinated alkanethiol monolayers on gold surfaces. An electrochemical study. *Langmuir* **17**, 4851-4857 (2001).
148. Zharnikov, M. & Grunze, M. Spectroscopic characterization of thiol-derived self-assembling monolayers. *Journal of Physics-Condensed Matter* **13**, 11333-11365 (2001).

149. Arnold, R., Azzam, W., Terfort, A. & Woll, C. Preparation, modification, and crystallinity of aliphatic and aromatic carboxylic acid terminated self-assembled monolayers. *Langmuir* **18**, 3980-3992 (2002).
150. Yang, G. H. & Liu, G. Y. New insights for self-assembled monolayers of organothiols on Au(111) revealed by scanning tunneling microscopy. *Journal of Physical Chemistry B* **107**, 8746-8759 (2003).
151. Cyganik, P. (Private Communication).
152. Kang, J. F., Ulman, A., Liao, S. & Jordan, R. Mixed self-assembled monolayers of highly polar rigid biphenyl thiols. *Langmuir* **15**, 2095-2098 (1999).
153. Poirier, G. E., Pylant, E. D. & White, J. M. Crystalline structures of pristine and hydrated mercaptohexanol self-assembled monolayers on Au(111). *Journal of Chemical Physics* **104**, 7325-7328 (1996).
154. Sur, U. K. & Lakshminarayanan, V. A study of the hydrophobic properties of alkanethiol self-assembled monolayers prepared in different solvents. *Journal of Electroanalytical Chemistry* **565**, 343-350 (2004).
155. Sur, U. K. & Lakshminarayanan, V. Existence of a hydrophobic gap at the alkanethiol SAM-water interface: An interfacial capacitance study. *Journal of Colloid and Interface Science* **254**, 410-413 (2002).
156. Garg, N., Carrasquillo-Molina, E. & Lee, T. R. Self-assembled monolayers composed of aromatic thiols on gold: Structural characterization and thermal stability in solution. *Langmuir* **18**, 2717-2726 (2002).
157. Lee, Y. J., Jeon, T. C., Paik, W. K. & Kim, K. Self-assembly of 1,2-benzenedithiol on gold and silver: Fourier transform infrared spectroscopy and quartz crystal microbalance study. *Langmuir* **12**, 5830-5837 (1996).
158. Hirayama, D. et al. Large photocurrent generation of gold electrodes modified with 60 fullerene-linked oligothiophenes bearing a tripodal rigid anchor. *Journal of the American Chemical Society* **124**, 532-533 (2002).
159. Otsubo, T., Aso, Y. & Takimiya, K. Functional oligothiophenes as advanced molecular electronic materials. *Journal of Materials Chemistry* **12**, 2565-2575 (2002).
160. Yam, C. M., Cho, J. & Cai, C. Z. Preparation, characterization, and heck reaction of multidentate thiolate films on gold surfaces. *Langmuir* **19**, 6862-6868 (2003).

161. Chechik, V., Crooks, R. M. & Stirling, C. J. M. Reactions and reactivity in self-assembled monolayers. *Advanced Materials* **12**, 1161-1171 (2000).
162. Fox, M. A., Whitesell, J. K. & McKerrow, A. J. Fluorescence and redox activity of probes anchored through an aminotrithiol to polycrystalline gold. *Langmuir* **14**, 816-820 (1998).
163. Pearson, R. G. Hard and Soft Acids and Bases. *Journal of the American Chemical Society* **85**, 3533-3539 (1963).
164. Rong, H.-T. (Ruprecht Karls Universitaet Heidelberg, Heidelberg, 2000).
165. Arihara, K. et al. Multiple voltammetric waves for reductive desorption of cysteine and 4-mercaptobenzoic acid monolayers self-assembled on gold substrates. *Physical Chemistry Chemical Physics* **5**, 3758-3761 (2003).
166. Azzaroni, O. et al. Electrodesorption potentials of self-assembled alkanethiolate monolayers on copper electrodes. An experimental and theoretical study. *Journal of Physical Chemistry B* **107**, 13446-13454 (2003).
167. Badia, A. et al. Probing the electrochemical deposition and/or desorption of self-assembled and electropolymerizable organic thin films by surface plasmon spectroscopy and atomic force microscopy. *Sensors and Actuators B-Chemical* **54**, 145-165 (1999).
168. Azehara, H. et al. Investigation of the structure of self-assembled monolayers of asymmetrical disulfides on Au(111) electrodes by electrochemical desorption. *Journal of Electroanalytical Chemistry* **473**, 68-74 (1999).
169. Israelachvili, J. *Intermolecular and Surface Forces* (Academic Press Limited, London, 1991).
170. Hagenstrom, H., Schneeweiss, M. A. & Kolb, D. M. Modification of a Au(111) electrode with ethanethiol. 2. Copper electrodeposition. *Langmuir* **15**, 7802-7809 (1999).
171. Cavalleri, O., Bittner, A. M., Kind, H. & Kern, K. Copper electrodeposition on alkanethiolate covered gold electrodes. *Zeitschrift Fur Physikalische Chemie-International Journal of Research in Physical Chemistry & Chemical Physics* **208**, 107-136 (1999).
172. Nishizawa, M., Sunagawa, T. & Yoneyama, H. Underpotential deposition of copper on gold electrodes through self-assembled monolayers of propanethiol. *Langmuir* **13**, 5215-5217 (1997).

173. Eliadis, E. D., Nuzzo, R. G., Gewirth, A. A. & Alkire, R. C. Copper deposition in the presence of surface-confined additives. *Journal of the Electrochemical Society* **144**, 96-105 (1997).
174. SondagHuethorst, J. A. M. & Fokkink, L. G. J. Galvanic copper deposition on thiol-modified gold electrodes. *Langmuir* **11**, 4823-4831 (1995).
175. Kaltenpoth, G., Volkel, B., Nottbohm, C. T., Golzhauser, A. & Buck, M. Electrode modification by electron-induced patterning of self-assembled monolayers. *Journal of Vacuum Science & Technology B* **20**, 2734-2738 (2002).
176. Hagenstrom, H., Schneeweiss, M. A. & Kolb, D. M. Copper underpotential deposition on ethanethiol-modified Au(111) electrodes: kinetic effects. *Electrochimica Acta* **45**, 1141-1145 (1999).
177. Schilardi, P. L., Azzaroni, O. & Salvarezza, R. C. A novel application of alkanethiol self-assembled monolayers in nanofabrication: Direct molding and replication of patterned conducting masters. *Langmuir* **17**, 2748-2752 (2001).
178. Azzaroni, O., Schilardi, P. L. & Salvarezza, R. C. Templated electrodeposition of patterned soft magnetic films. *Applied Physics Letters* **80**, 1061-1063 (2002).

## APPENDICES

## Appendix 1 Biphenyl Thiols Unit Cells

The unit cells, figure A.1, are defined using a matrix, which relates vectors  $a_1$  and  $a_2$  for the gold lattice with  $b_1$  and  $b_2$  for the adsorbate unit cell.

$$\begin{bmatrix} b_1 \\ b_2 \end{bmatrix} = \begin{bmatrix} n_{11} & n_{21} \\ n_{12} & n_{22} \end{bmatrix} \begin{bmatrix} a_1 \\ a_2 \end{bmatrix}$$

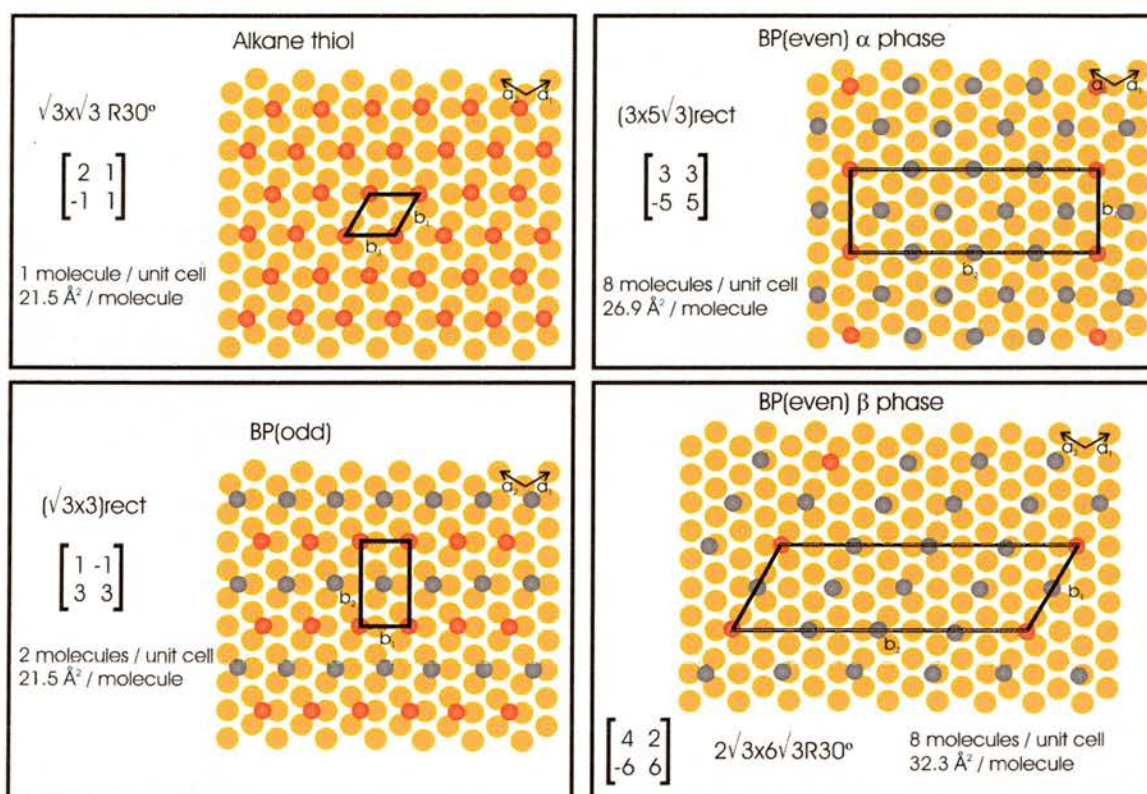


Figure A.1: unit cells for alkane thiols, and biphenyl thiols from references 65, 70 and 128. Red and grey circles identify “blobs” of different brightness in STM images. These indicate some type of difference in either the binding site or conformation of the adsorbed molecules.

The area per molecule is calculated using the determinant of the matrix.

$$\text{Area per molecule} = \frac{\text{Det} \begin{bmatrix} \end{bmatrix} \times 2.88^2 \sin 60}{\text{molecules per unit cell}}$$

---

## Appendix 2 Home-built Spectroelectrochemical Cell

All experiments involving electrochemistry with in-situ SHG were performed in a home-built spectroelectrochemical cell which consists of a Viton o-ring sandwiched between the sample and a cover glass. Considerable time has been invested in the design and development of the spectroelectrochemical cell. The procedures for construction and routine use have continuously been refined and optimised and the final versions are detailed below. Diagrams of the assembled cell are also shown. The following procedures are adhered to strictly to ensure that the quality of results is high and the greatest reproducibility is achieved.

1. Procedure for construction of the main unit of the cell.
2. Procedure for routine sample assembly.

The cell is composed of a main unit that stays intact once built and a top plate, which is removed every time a new sample is assembled. Spacers are placed between the plates which control the distance between the plates, and hence the pressure exerted on the gold samples. For Au/mica samples the spacers consist of a piece of glass slide, an o-ring and a piece of the silicon. The o-ring in the centre is compressed by the thickness of the Au/mica substrate. This provides a high degree of consistency in the pressure applied to different samples and adds to the high degree of reproducibility of experiments. For Au/Si samples the spacer consists of two glass slides and an o-ring, which compensates for the slightly thicker substrate. The components for cell construction are shown in figure A.2, the main unit of the cell (components 1 to 11) stays intact during routine use. Components 12 –16 are assembled and disassembled every time a new sample is tested.

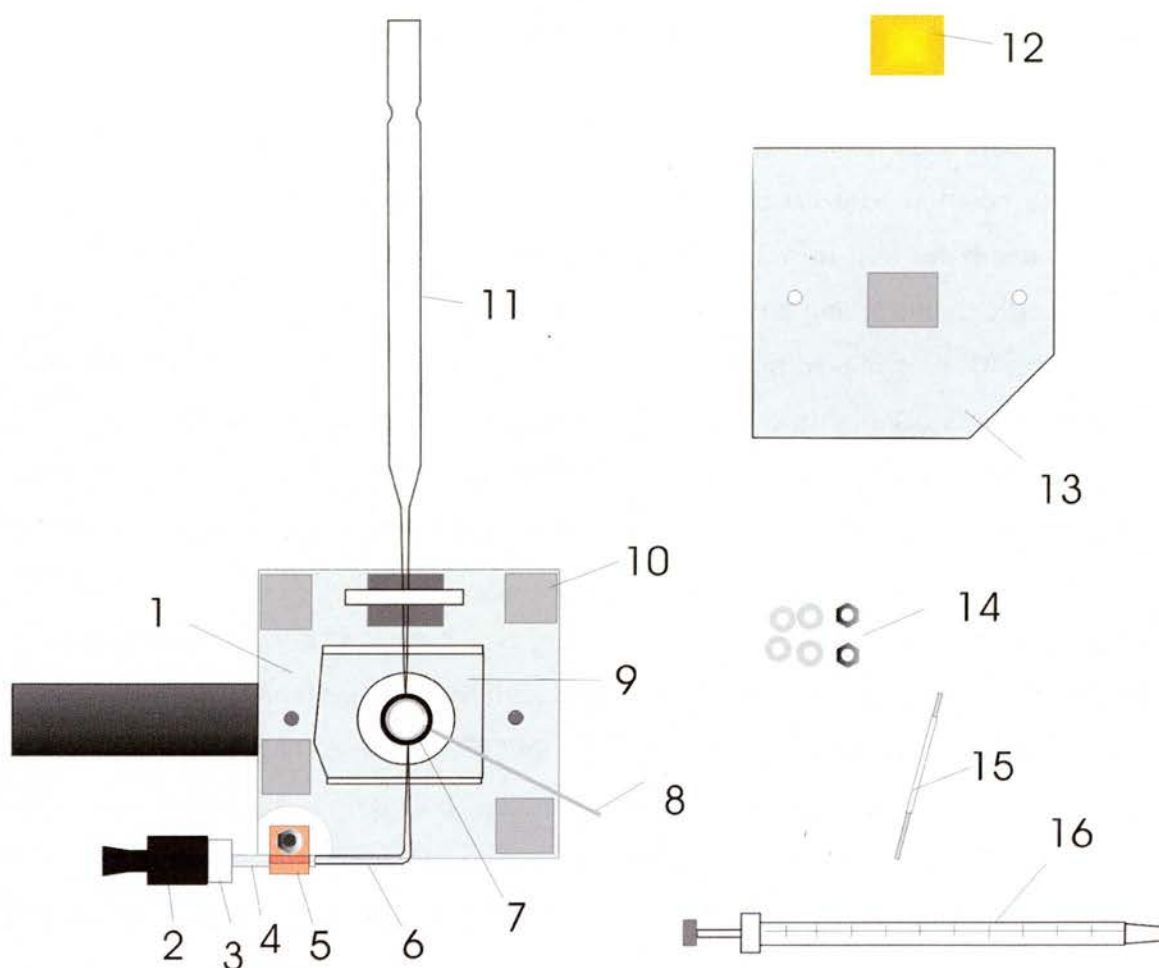


Figure A.2: Materials for the spectroelectrochemical cell, parts 1 to 11 show the main unit (left) in the assembled state. 1) adjustable mount base-plate, 2) female Luer Lock connection, 3) PTFE screw connection, 4) PTFE tubing, 5) small clamp, 6) bent and tapered capillary tube, 7) Viton o-ring (8 mm internal diameter, 11 mm outer diameter), 8) platinum wire (0.5 mm diameter), 9) glass microscope slide, 10) spacer unit, 11) tapered Pasteur Pipettes. Parts 12-16 are routinely assembled and disassembled. 12) gold sample, 13) top plate with silicon wafer spacer, 14) washers and nuts, 15) metal contact for working electrode, 16) syringe with male Luer Lock connection.

## Procedure for Construction of the Main Unit of the Cell

The adjustable mount base-plate is positioned flat in a clamp and the glass slide is secured in position with a small amount of tape. The Viton o-ring was prepared by drilling three holes in it in well defined positions as indicated in figure A.2. Each hole has a specific diameter and position with respect to each other. The hole for the pipette is the largest, allowing sufficient conductivity through this region to the reference electrode, this is 0.7 mm in diameter. The hole for the capillary has a diameter of 0.5 mm. The hole for the counter electrode has a diameter of 0.4 mm, it is positioned slightly below the centre of the o-ring so the platinum wire will be closer to the glass slide than the gold sample when the cell is assembled. Initially 0.4 mm holes are drilled in each position, these are widened as necessary. The o-ring is boiled in water for a few minutes then dried. The Pasteur Pipette and capillary tube are tapered in a flame, the flame is also used to bend the capillary tube by 90° and clean the platinum wire. The Luer lock connection and PTFE components are boiled in water, then dried and assembled. The dry o-ring is picked up with cleaned tools, the counter electrode and glass fittings are carefully pushed through the drilled holes, and any glass protruding through the holes is clipped off. The o-ring with all the fittings are carefully transferred to the base-plate and secured using the small clamp around the PTFE tube. The o-ring is positioned so that it is in the centre of the window in the base-plate, and the o-ring is flat on the glass slide. The pipette is secured over the small spacer on the base-plate with tape. The clamp stand supports the top end of the pipette. It is ensured that the o-ring and counter electrode are flush with the glass slide. Four spacers are positioned on each corner of the base-plate. The main unit is complete and ready for routine use. The procedure for the assembly of the gold sample into the cell is described below.

## Procedure for Routine Sample Assembly

Electrolyte, prepared using distilled water and high purity chemicals, typically 0.5 M  $\text{KOH}_{(\text{aq})}$ , was degassed for 45 minutes in pure argon, and transferred to an inert atmosphere glove box. The spectroelectrochemical cell was positioned flat in the clamp stand. The sample was placed very carefully upside down onto the cell as shown in figure A.3. The top plate was placed carefully onto the bottom plate ensuring it is flat. Two washers were put on each screw, nuts were put on and gradually tightened. Due to

the presence of the four corner spacers the nuts naturally became very tight when the top plate touched all four corner spacers. The cell is now in a secure state, it was rotated 90° in the clamp to an upright position. The working electrode contact was inserted between the plates and the sides of the cell were sealed with insulating tape leaving only a small gap at the top to allow flushing of inert gas between the plates. The cell and syringe were transferred to the inert atmosphere glove box, which was flooded with argon. The cell was gently flushed between the plates and inside the o-ring using the hose inside the glove box, this was repeated after forty five minutes of flooding. The syringe was filled with electrolyte and injected into the cell. The cell was transferred from the glove box to the position for laser probing. The reference electrode was inserted into the pipette, an inert gas line was added to continually flush between the plates during the experiment. The working electrode and counter electrode connections were made and a SHG signal was established. Electrochemical with in-situ second harmonic generation experiments were performed immediately.

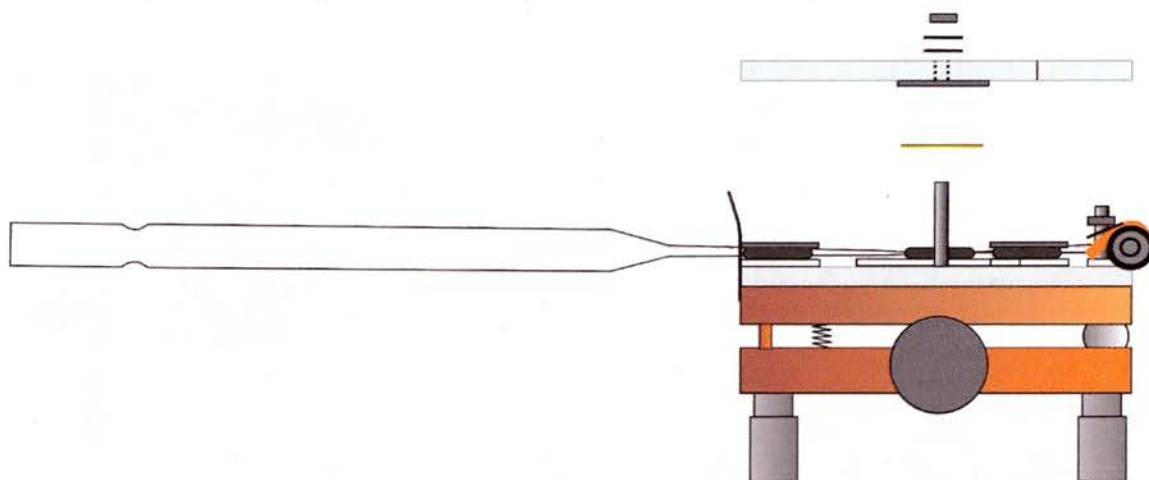


Figure A.3: Main unit of the cell is held flat, the sample is placed upside down onto the o-ring.

Diagrams of the fully assembled spectroelectrochemical cell are presented in figure A.4.

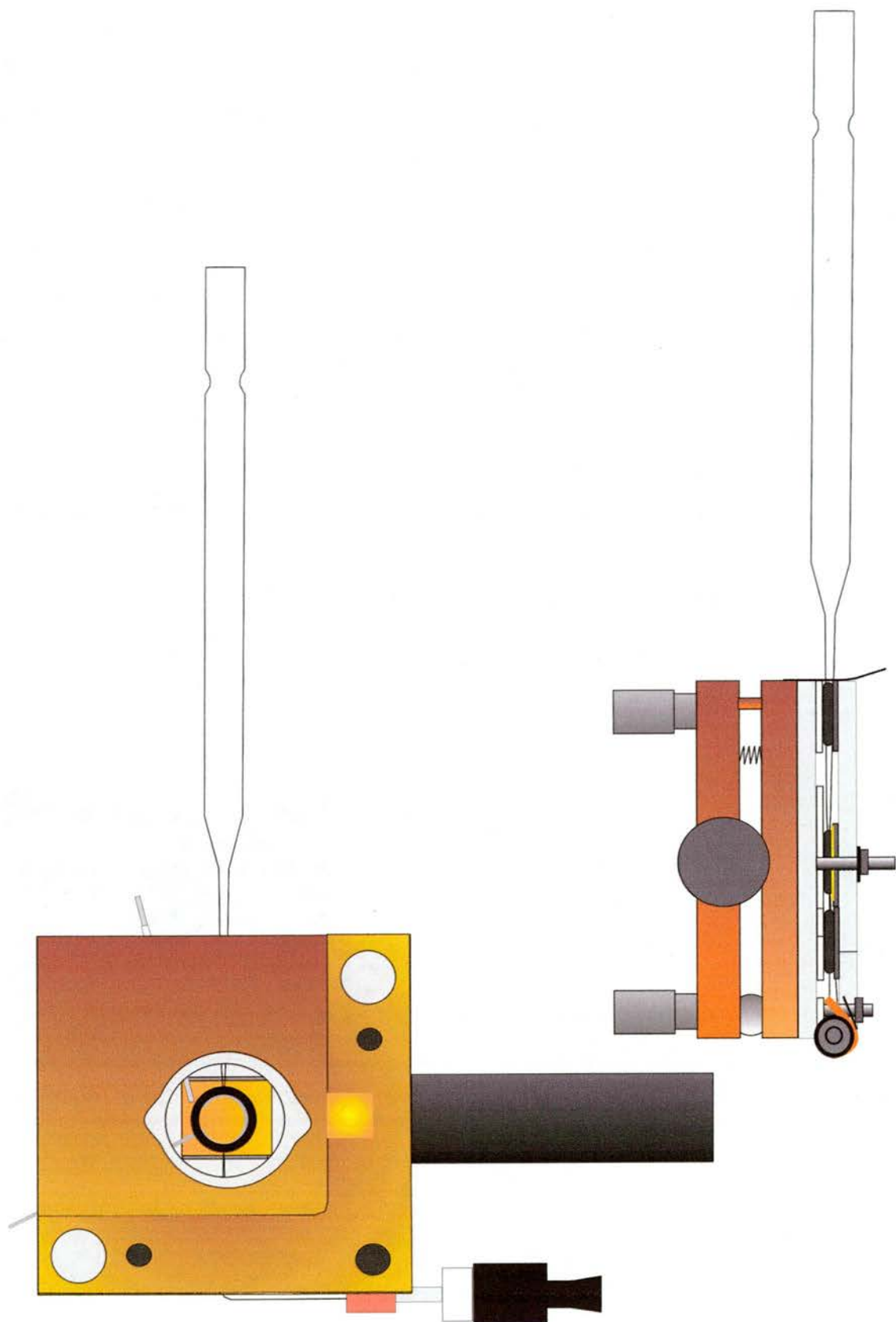


Figure A.4: Home-built spectroelectrochemical cell fully assembled, front view (left) and side view (right) drawn to actual size.

### Appendix 3 Statistical Analysis

There are two statistical analyses described here, standard deviation and the coefficient of determination. The standard deviation is used to assess a set of data with one variable, the standard deviation is a measure of the extent of variation of data points around the mean value. The standard deviation represents a range either side of the mean value that has a 68% likelihood of containing a result. There is a 95% likelihood of a value falling within two standard deviations. The coefficient of determination or  $R^2$  is used to assess a set of data that has two variables. The coefficient of determination is a measure of the extent of correlation between the two variables, a value of zero indicates no correlation, and a value of 1 indicates perfect correlation. The standard deviation is determined for a dataset with one variable, i.e.  $x_1, x_2, \dots, x_n$  where there are  $n$  members in the set. The standard deviation is calculated using the following equation.

$$\text{Standard deviation} = \sqrt{\frac{1}{n-1} \sum_{i=1}^n (x_i - \bar{x}_n)^2}$$

Where  $\bar{x}_n$  is the mean value of members in a dataset that has  $n$  members. Standard deviation is normally represented as error bars in plots,  $\pm$  one standard deviation either side of the mean value; small standard deviations indicate that there is a small variation in the data points.

The coefficient of determination is a measure of the extent of the correlation between independent and dependent variables. For a plot of variables,  $(x_1, y_1), (x_2, y_2), \dots, (x_n, y_n)$  the  $R^2$  value indicates how closely a regression line fits to the set of data. It is a measure of how close values lie to the regression, typically least squares line of best fit. The coefficient of determination is the ratio of the sum of squares due to the regression over the total sum of squares.

$$R^2 = \frac{SS_{\text{regression}}}{SS_{\text{total}}}$$

The sum of squares total comprises the sum of the sum of squares due the regression line and the sum of squares of the error, the error is the difference between the actual data point and the line of best fit.

$$SS_{\text{total}} = SS_{\text{regression}} + SS_{\text{error}}$$

$$R^2 = 1 - \frac{SS_{\text{error}}}{SS_{\text{total}}} = 1 - \frac{\sum_{i=1}^n (x_i - x_{\text{bf}})^2}{\sum_{i=1}^n (x_i - \bar{x})^2}$$

A coefficient of determination value of 1 means that there is perfect correlation, all values lie exactly on the line of best fit, a value of 0 means there is no correlation between the two variables.

## Appendix 4 Biphenyl Thiol Angles

The orientation of the biphenyl unit is described in terms of the tilt angle and twist, figure A.5.

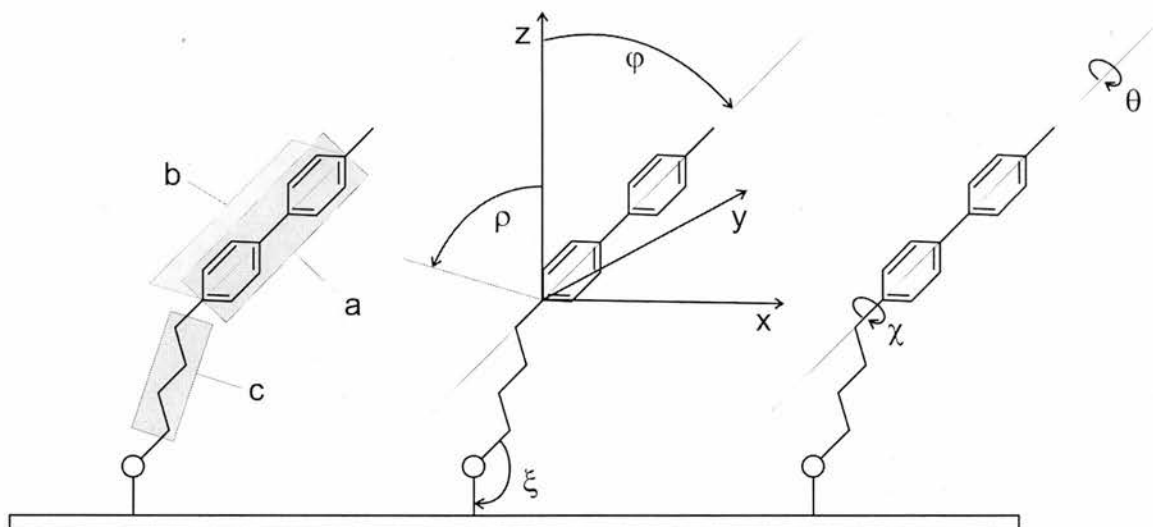


Figure A.5: Diagram of BP4 illustrating the conformation of the molecule in terms of tilt and twist with respect to the surface plane, the biphenyl unit and the molecule alkane backbone. Diagram adapted from figure 1 in reference 94.

Three planes a, b and c are identified, a is the plane of the biphenyl units, it is assumed that the two phenyl rings are coplanar. Plane b intersects the biphenyl backbone and is perpendicular to plane a. Plane c is the plane of the carbon atoms in the alkane chain assuming an all-trans conformation. A Cartesian co-ordinate system is defined by x, y and z with plane xy parallel with the surface and z defined as the surface normal. The angle of the gold-sulfur-carbon bond is denoted by  $\xi$ . The tilt of the biphenyl unit is defined by two angles  $\phi$  and  $\rho$ ,  $\phi$  defines the angle from the surface normal to the biphenyl unit backbone,  $\rho$  defines the angle between the surface normal and the line in plane b perpendicular to the biphenyl backbone. The twist of the biphenyl unit is defined with respect to the Cartesian co-ordinate system ( $\theta$ ) and to the plane of carbons in the alkane chain ( $\chi$ ).  $\theta = 0^\circ$  if  $\phi + \rho = 90^\circ$  and  $\chi = 0^\circ$  if planes a and c are perpendicular.